Tampere University

JUHA TIIHONEN

Thermal Effects in Atomic and Molecular Polarizabilities with Path Integral Monte Carlo

Tampere University Dissertations 35

Tampere University Dissertations 35

JUHA TIIHONEN

Thermal Effects in Atomic and Molecular Polarizabilities with Path Integral Monte Carlo

ACADEMIC DISSERTATION
To be presented, with the permission of
the Faculty Council of the Faculty of Engineering and Natural Sciences
of Tampere University,
for public discussion in the auditorium TB109
of Tietotalo building, Korkeakoulunkatu 1, 33720, Tampere,
on 5 April 2019, at 12 o'clock.

ACADEMIC DISSERTATION
Tampere University, Faculty of Engineering and Natural Sciences
Finland

Responsible supervisor and Custos	Professor Tapio Rantala Tampere University Finland	
Supervisor	Adjunct professor Ilkka Kylänpää Tampere University Finland	
Pre-examiners	Professor Juha Vaara University of Oulu Finland	Professor Michel Caffarel Centre National de la Recherche Scientifique France
Opponent	Professor Carlo Pierleoni Università degli Studi dell'Aquila Italy	

The originality of this thesis has been checked using the Turnitin OriginalityCheck service.

Cover design: Roihu Inc.

ISBN 978-952-03-1008-0 (print)
ISBN 978-952-03-1009-7 (pdf)
ISSN 2489-9860 (print)
ISSN 2490-0028 (pdf)
http://urn.fi/URN:ISBN:978-952-03-1009-7

PunaMusta Oy
Tampere 2019

To Ida

For every infinity there exists a way you renormalize me

PREFACE

This Thesis is a structured and self-contained introduction to everything I needed to know about the topic some four years ago, when I started my post-graduate journey. Of course, the message is painfully late. No ready-made piece was ever handed to the younger me. No, it took all my determination, most of my dedication, and countless hours of Finnish metal music to shed the remnants of my prodigal years and complete this work. But complete it I did, and for that I am proudly indebted to so many people.

I thank my university – teachers, administration and other staff – for supporting and educating me. I thank my colleagues at the Physics laboratory for their efforts in queueing for lunch and draining the coffee pot. Especially, I thank Janne and Joonas for making my shortcomings painfully apparent but always dragging me along towards salvation. I thank Ilkka for occasionally luring me out of imaginary time and Sami for making me sweat in positive ways. I thank Esa for showing me the way up also figuratively. I thank David, Paul and all the other friends from Champaign–Urbana for making the turning point of my scientific life. I thank the great personalities of Hiukkanen, NääsPeksi, Jaara and Wappuradio for marinating me in priceless transferable skills: responsibility and common sense, courage to perform, tolerance of imperfection, and borders of socially awkward. I thank my dear friends for all the days and nights, whose memories will easily outlive those spent with Fortran. I thank my family, relatives, in-laws and my dog for their constant cluelessness of my trade but approving of it nevertheless. From the bottom of my heart I thank my beloved wife Ida for making me sleep, smile, eat healthy and stay hopeful come what may.

I thank my brilliant pre-examiners, professors Juha Vaara and Michel Caffarel, for their constructive feedback. Most of all, I thank my supervisors and mentors, whose inspiration, dedication, support, and practical guidance have carried me through the years to this point and beyond: Ilkka Kylänpää for so many new ideas and professor Tapio T. Rantala for so many new beginnings.

Tampere, 26 February 2019

Juha Tiihonen

ABSTRACT

This Thesis is a review of polarizability and different means to estimate it from path-integral Monte Carlo (PIMC) simulations. Polarizability is the quantum mechanical equivalent of electric susceptibility: it describes the electric field response of atoms and molecules. The static and dynamic multipole polarizabilies are, arguably, the most important electronic response properties and multipurpose parameters for physical modeling. Computing them from first principles is challenging in many ways, and in this Thesis we focus on a few particular aspects: exact many-body correlations, nonadiabatic effects and thermal coupling.

The Thesis contains an introduction to polarizability in the framework of nonrelativistic Feynman path integrals and thermal density matrices. The electric field interactions due to electric multipoles is associated with causal time-correlation functions and nonlinear response theory. The original scientific contribution manifests in various strategies to obtain the polarizabilities from PIMC simulations: we demonstrate finite-field simulations, static field-derivative estimators, and analytic continuation of imaginary-time correlation functions. The required analytic continuation of Matsubara frequencies is a common but ill-posed numerical challenge, which we approach with the Maximum Entropy method.

For data, we provide the most important polarizabilities and hyperpolarizabilities of several one- or two-electron systems: H, H_2^+, H_2, H_3^+, HD^+, He, He^+, HeH^+, Li^+, Be^{2+}, Ps, PsH, and Ps_2. Our benchmark simulations within the Born–Oppenheimer approximation (BO) agree with the available literature and complement it in many cases. Beyond BO, we are able to demonstrate weak and strong thermal effects due to, *e.g.*, rovibrational coupling. We also estimate the first-order multipole spectra, dynamic polarizabilities and van der Waals coefficients. The simulations show unprecedented accuracy in terms of exact many-body correlations and fully nonadiabatic coupling of the electronic and nuclear quantum effects.

TIIVISTELMÄ

Väitöskirja käsittelee polarisoituvuutta ja erilaisia keinoja sen laskemiseksi polkuintegraali–Monte Carlo -menetelmällä (PIMC). Polarisoituvuus on kvanttimekaaninen suure, joka vastaa sähköistä suskeptibiliteettiä: se kuvaa atomien ja molekyylien vastetta sähkökenttään. Staattiset ja dynaamiset multipoli-polarisoituvuudet ovatkin yksiä tärkeimmistä elektronien vasteominaisuuksista ja näin ollen monikäyttöisiä parametrejä fysikaalisessa mallinnuksessa. Polarisoituvuuksien äärimmäisen tarkka laskeminen on kuitenkin haasteellista. Väitöskirjassa keskitytään siksi muutamaan erityiseen ongelmaan: tarkkaan monen kappaleen korrelaatiokuvaukseen, ei-adiabaattisiin efekteihin sekä lämpötilan vaikutuksiin.

Tässä työssä polarisoituvuuksien laskemista tarkastellaan ei-relativistisesti Feynmanin polkuintegraalien ja termisten tiheysmatriisien avulla. Sähkökentän ja sähköisten multipolien välinen vuorovaikutus kytketään kausaalisiin korrelaatiofunktioihin sekä epälineaarisen vasteen teoriaan. Uusi tieteellinen ansio muodostuu muutamasta erilaisesta keinosta määrittää polarisoituvuus PIMC-laskuista: äärellisen kentän simulointi, staattiset kenttä-derivaatan estimaattorit, sekä imaginääriajan korrelaatiofunktioiden analyyttinen jatkaminen. Vaadittu Matsubara-taajuuksien analyyttinen jatkaminen on yleisesti esiintyvä mutta huonosti määritelty numeerinen ongelma, jota lähestytään tässä työssä maksimientropiamenetelmällä.

Tärkeimmät laskennalliset tulokset ovat seuraavien yhden tai kahden elektronin systeemien polarisoituvuudet ja hyperpolarisoituvuudet: H, H_2^+, H_2, H_3^+, HD^+, He, He^+, HeH^+, Li^+, Be^{2+}, Ps, PsH, ja Ps_2. Born–Oppenheimer-approksimaatiossa (BO) lasketut referenssitulokset vastaavat tunnettuja kirjallisuuden arvoja ja monessa tapauksessa myös täydentävät niitä. BO-approksimaation ulkopuolelta voidaan osoittaa mm. rovibraatiosta johtuvia heikkoja sekä voimakkaita lämpötilaefektejä. Muut tulokset käsittävät multipoli-spektrejä, dynaamisia polarisoituvuuksia sekä van der Waals-vakioita. Simulaatioiden kvanttimekaaninen kuvaus monen kappaleen korrelaatioista sekä elektronien ja ytimien ei-ediabaattisesta kytkennästä on poikkeuksellisen tarkka.

CONTENTS

LIST OF SYMBOLS AND ABBREVIATIONS

AQ	all-quantum
BO	Born–Oppenheimer
CC	coupled cluster
CEIMC	coupled electron–ion Monte Carlo
CI	configuration interaction
CMD	centroid molecular dynamics
DFT	Density functional theory
DMC	diffusion Monte Carlo
DNC	derivative Numerov–Cooley
FSP	Fermion sign problem
IR	infrared
MaxEnt	maximum entropy
MD	molecular dynamics
MMC	Metropolis Monte Carlo
NMR	nuclear magnetic resonance
PIGS	path integral ground state
PIMC	path integral Monte Carlo
PIMD	path integral molecular dynamics
QMC	quantum Monte Carlo
RPIMC	Restricted path integral Monte Carlo
SOS	sum-over-states
vdW	van der Waals
VMC	variational Monte Carlo

$\hbar$	reduced Planck's constant
r	real-space position variable
p	real-space momentum variable
r, r'	radius
R	real-space variable for many-body positions
Ψ	wavefunction
$\psi_n(R)$	energy eigenstate in real space

$\hat{H}$	Hamilton operator
$\hat{H}_0$	Time-independent or unperturbed Hamilton operator
$\hat{h}(t)$	Time-dependent perturbation
$\hat{U}(t)$	propagator
$\hat{U}_\tau(\tau)$	imaginary-time propagator
E	total energy
E_n	energy eigenvalue
P	a physical property
$\hat{P}$	measurement operator for P
$\bar{P}$	expectation value of $\hat{P}$
$\langle P \rangle$	thermal average $\hat{P}$
$\hat{Q}_1, \hat{Q}_2, \hat{Q}_3$	perturbing interactions
$\mathscr{P}$	permutation operator
N	number of particles
N_V	number of particles in unit volume
$\hat{\rho}$	unnormalized thermal density operator
ρ	thermal density matrix
ρ^F	field-perturbed density matrix
ρ^K	free-particle kinetic density matrix
ρ_F / B	fermion/boson density matrix
β	inverse temperature
k_B	Boltzmann constant
T	Temperature
Z	partition function
δ_{nm}	Kronecker delta
$\delta(t)$	Dirac delta
$\hat{G}$	Green's function operator, correlator
G	Green's function
C_n	n-time correlation function
$\hat{C}_n$	n-time correlator
$C^{>/<}$	lesser/greater 1-time correlator
$C^{R/A}$	retarded/advanced 1-time correlator
$t, t', t'', \ldots$	real-time variables
$t_1, t_2, t_3, \ldots$	real time-differences
$\tau, \tau', \tau'', \ldots$	imaginary-time variables
$\tau_1, \tau_2, \tau_3, \ldots$	imaginary time-differences

$\mathscr{T}$	time-ordering operator
$\theta(t)$	Heaviside step function
$\omega, \omega_1, \omega_2, \ldots$	real frequencies
ω_{nm}	transition energy
ω_n	Matsubara frequency
S	action
U	potential action
V	potential energy
K	kinetic action
T	kinetic energy
M	Trotter number
$\mathbb{P}, \Pi$	Probability
$\mathbb{A}$	Acceptance probability
$\mathbb{T}$	Trial move probability
C	covariance matrix
σ^2	statistical variance
$\varkappa$	statistical correlation time
s	average sign
P_l	Legendre polynomial
$\mathbf{F}$	electric field (vector field)
F_α	electric field (tensor component)
χ	generalized susceptibility, electric susceptibility
$A(\omega)$	spectral function
η	positive infinitesimal
n	refractive index
μ, Θ, Ω	electric multipole moments: dipole, quadupole, octupole
Θ	electric quadrupole moment
Γ	natural linewidth
α	polarizability
$\alpha_l(\omega)$	dynamic multipole–multipole polarizabilities
β, γ	hyperpolarizabilities, see Table. 3.1
$A, B, C, \ldots$	field-gradient polarizabilities, see Table. 3.1
C_n^{AB}	van der Waals coefficient

ORIGINAL PUBLICATIONS

I. Tiihonen, J., Kylänpää, I., Rantala, T.T. (2015) Adiabatic and nonadiabatic static polarizabilities of H and H_2. Physical Review A 91, 062503

II. Tiihonen, J., Kylänpää, I., Rantala, T.T. (2016) General polarizability and hyperpolarizability estimators for the path-integral Monte Carlo method applied to small atoms, ions, and molecules at finite temperatures. Physical Review A 94, 032515

III. Tiihonen, J., Kylänpää, I., Rantala, T.T. (2017) Static field-gradient polarizabilities of small atoms and molecules in finite temperature. The Journal of Chemical Physics 147, 204101

IV. Tiihonen, J., Kylänpää, I., Rantala, T.T. (2018) Computation of dynamic polarizabilities and van der Waals coefficients from path-integral Monte Carlo. The Journal of Chemical Theory and Computation 14, 5750

AUTHOR'S CONTRIBUTION

Publication I

The Author, Juha Tiihonen, had the main responsibility over this work, which was based on his Master's thesis. The work was conceptualized by Tapio Rantala, and the code development was supervised by Ilkka Kylänpää. The simulations, analyses and postprocessing were performed by the Author, who also wrote most of the text. The Methods section was written by Kylänpää. Rantala and Kylänpää also consulted with the conclusions, presentation of the results and refining the text.

Publication II

The Author had the main responsibility. The work is focused on theoretical findings, which were inspired by David Ceperley and developed together with Kylänpää. The Author made the necessary code implementations and carried out all the simulations, analyses, postprocessing and writing. Rantala and Kylänpää also consulted with the theoretical background, conclusions, presentation and refining the text.

Publication III

The Author had the main responsibility. He wrote the code and carried out all the simulations, analyses, postprocessing and writing. The work is a follow-up of Publication II, but it contains more detailed theoretical background and interpretation of data, both of which involved all the authors. Rantala and Kylänpää also consulted with conclusions, presentation and refining the text.

Publication IV

The Author had the main responsibility, and he conceptualized and initiated the work. He also made the necessary code developments, and designed and carried out the simulations and extensive postprocessing of the raw data. The Author also made the conclusions and wrote the article. Rantala and Kylänpää were in supervising roles throughout the long process, and also helped with the theoretical work and the write-up.

1 INTRODUCTION

The last century has been a celebration of modern physics and technology. Quantum physics has redefined our understanding of the nature: quantization of light, matter and state – and fundamental uncertainty. The implications have unleashed a plethora of technologies, such as quantum chemistry, semiconductors, and materials design. Maybe the most important is the light–matter interaction: Optical fibers, spectroscopy, and lasers, to name a few, have become irreplaceable corner stones of modern science, communication and infrastructure. The eve of quantum computers and photonics only accentuates that this is the era of nonlinear optics.

The precursor of modern technology is the combination of scientific theory and computation. Most problems in electronic structure theory are so complex that a practical solution is only given by extensive computer simulations. Computing is often a cost-effective and complementary alternative to the experiment, and it can provide insight even beyond the measurable realm. Thus, there are supercomputers designed for the sole purpose of heavy scientific computation. The design of efficient simulation methods, algorithms and approximations is a universal challenge and also the future for most natural sciences.

This Thesis combines quantum mechanics, nonlinear optics and heavy computation. In particular, means are developed to study electric field response properties of quantum systems, atoms and molecules, using path integral simulations. The path integration is an accurate but computationally intensive way to approach quantum mechanics. On the other hand, the standard measure of electric field response is induced polarization: the polarizability.

1.1 The importance of polarizability

Polarizability is, arguably, the most important electronic response property. It models the effects of electric fields on microscopic quantum systems, such as atoms and small molecules. To give an exhaustive review is virtually impossible, but the following will hopefully outline the importance of polarizability and the main challenges it poses to computational sciences.

The famous evidence of polarizability was the discovery of Stark in 1914 [1]: the shifting of atomic energy levels in response to static electric fields. The Stark shift is still one of the standard ways to characterize a quantum system [2]. Namely, from early empirical models [3, 4] to the first quantum mechanical explanations [5], it was clear that the field-response was dominated by a characteristic constant: the polarizability. During the following decades, more advanced theories were established to account for higher order properties and more exotic symmetries [6, 7, 8, 9, 10]. Today, the fundamental theory of nonlinear optical properties has matured for almost 100 years. Since the discovery of laser, the endeavor to understand, calculate and utilize the polarizabilities has never ceased.

The first-order polarizability α is an important parameter in many physical models. Conceptually, α relates the response of a microscopic particle to the perturbing field, *i.e.*

$$\mathbf{P} = \alpha \mathbf{F}_{\text{loc}}, \tag{1.1}$$

where $\mathbf{P}$ is an induced electric polarization and $\mathbf{F}_{\text{loc}}$ is a local electric field. At the macroscopic level, the polarizability is related to the bulk electric susceptibility χ by

$$\chi \mathbf{F} = N_V \alpha \mathbf{F}_{\text{loc}}, \tag{1.2}$$

where N_V is the number of particles per unit volume and $\mathbf{F}$ denotes the applied electric field, which may differ from the local field. A familiar bulk property is the refractive

index n, which is related to the polarizability by the Lorentz–Lorenz relation

$$\frac{n^2-1}{n^2+2} = \frac{4\pi}{3} N_V \alpha. \tag{1.3}$$

Optical dispersion is only one illustrative example, however, a more comprehensive definition of polarizability is given in Ch. 3. Applications of the first-order polarizabilities include ultracold molecule alignment [11], diffusion of adatoms [12, 13], stellar spectroscopy [14, 15], atomic clocks [16], quantum information technology [17], and method benchmarking in general. On the other hand, polarizabilities can be used for empirical understanding and prediction of chemical properties, such as softness/hardness [18], acidity/basicity, and ionization potential [19, 20].

The higher-order response, the so-called hyperpolarizability, is even more diverse in terms of definitions and applications. It describes processes involving multiple fields, and in essence, lays foundations of the nonlinear optics. Particularly interesting phenomena are nonlinear spectroscopy and many-harmonic generation, that is, multiplying the frequency of a laser using optically active media. For instance, second-order polarizabilities are involved in the second-harmonic generation [21], birefringence [22], and Raman spectroscopy [9]. The third-order polarizabilities are involved in the Kerr effect [23, 24], four-wave-mixing [25], third-harmonic generation [26], piezo-electric phenomena [27], and so on.

In the end, polarizability is an emergent property, meaning that heavy quantum mechanical calculations can be efficiently replaced by a single object, a scalar or tensor α. In that sense polarizability resembles the bulk susceptibility. However, the polarizabilities are still inherently atomistic and therefore able to describe microscopic dielectric processes. Indeed, an important application of polarizability is related to atomic and molecular long-range interactions: the van der Waals forces (vdW). Multipole polarizabilities are involved in the attractive interaction between quantum fluctuating electric moments, called the London dispersion [28, 29]. The corrections due to the long-range attraction are important in large-scale simulation models of, *e.g.* biological systems [30, 31] and liquid water [32]. Indeed, effects of the first and higher-order dispersion can be crucial [33], and the research on polarizable force-field models has increased rapidly during the past few years [34, 35, 36, 37] .

1.2 Computational challenge

In this Thesis, polarizability is studied with computer simulations. The agreement between experiment and first-principles simulation is the foremost measure of theoretical integrity. However, while the experiments struggle to measure pure systems, the ongoing computational challenge is to make realistic simulations. Unfortunately, solving quantum mechanical problems is inherently challenging, and simulating the electric field response is no exception. Depending on the approach, the main difficulties are related to quantum many-body correlations, sensitivity of time evolution, and non-equilibrium nature of the field interaction. In any case, striving for better accuracy requires decomposition of the problem, method development and excessive amounts of computing.

Accurate polarizability is a powerful benchmark, and indeed a lot of literature exists on the computation of polarizabilities using the wide variety of electronic structure methods and their dedicated variations. Generally, the electric field response is more sensitive to electron density than total energy, while the latter is often used to optimize simulation methods [38]. The many-body correlation plays an important role [39], and thus, among the most popular high-accuracy approaches are the coupled-cluster method (CC) [40, 41, 42] and the configuration interaction method (CI) [43]. CI augmented with many-body perturbation theory (MBPT) has also been demonstrated [44, 45]. Furthermore, using CI with semi-empirical core potentials is relatively accurate, because the core only contributes several percents to the total polarizabilities [16]. Bigger systems can be studied, for instance, with the Derivative Hartree-Fock method, but the accuracy is not as good [46]. Alternatively, one can pursue better accuracy by developing basis sets that are adjusted for reference data [47]. Density functional theory (DFT) is a very popular approach for its high scalability [48, 49], and time-dependent DFT can be used to study the dynamic response properties and long-range dispersion [50]. However, DFT-based methods have fundamental problems with uncontrollable approximation, and the incorrect asymptotic behavior of xc-functionals is a particular problem for the polarizabilities [51]. Explicitly correlated methods, such as diffusion Monte Carlo (DMC) [52], are probably the most rigorous but computationally demanding ways to simulate quantum many-body systems. Finally, the most explicit way to study polarizability is the finite-field approach [53], which can be utilized with

almost any quantum mechanical simulation method.

This Thesis is focused on thermal and nonadiabatic effects on polarizabilities. For atoms, these effects are usually small, but the topic is also largely unexplored. On one hand, experimental data is difficult to obtain for other than inert species, such as xenon [54]. On the other hand, simulation with *ab initio* methods is restricted to the pure state, 0 Kelvin. Some studies exist that model the effects of finite density with confinement to a sphere [55] or harmonic potential [56].

Molecules are known to have strong electric field response due to orientational coupling [21, 29], which is also subject to thermal effects [57]. One usually studies this by making the adiabatic approximation, *i.e.*, decoupling of the nuclear and electronic degrees of freedom. This allows one to estimate electronic and rovibrational polarizabilities and their thermal coupling by various analytic approximations [10], explicit summation [58], and numerical methods such as the derivative Numerov–Cooley approach (DNC) [59]. Unfortunately, such approaches often become tedious and inaccurate for more complicated problems. The nuclear quantum effects give rise to microwave, infrared (IR) and Raman spectroscopy, which can be studied experimentally, but also with molecular dynamics (MD) [60]. Even better accuracy of quantum effects can be obtained with path integral MD (PIMD) [61, 62]. Yet, the lack of accurate electron–ion coupling is a fundamental limitation, which we aim to resolve in this work.

1.3 Objectives and structure of the Thesis

Objective of the Thesis is to study and utilize different means of estimating atomic and molecular polarizabilities with a particular computational method, path integral Monte Carlo (PIMC). We focus on exact thermal and nonadiabatic effects related to the polarizabilities, as they arise naturally from PIMC simulations. In particular, we study how the electron–ion coupling and the nuclear degrees of freedom – the molecular rovibration – respond to electric fields in higher orders of perturbation. The problem is often decoupled in the Born–Oppenheimer approximation, but in this Thesis we aim for the exact coupling.

Apart from a few studies, the computation of polarizabilities is a novel feat in the com-

munities of path integral methods and quantum Monte Carlo. For instance, Caffarel *et al.* successfully used DMC to study real and imaginary-domain polarizabilities and van der Waals coefficients at the ground state [52]. A PIMC approach was demonstrated by Shin *et al.* [63], but only in the imaginary domain. Neither of the studies involved quantized nuclei or electron–nucleus coupling. On the other hand, many PIMD studies exhibit nuclear quantum phenomena [61, 62, 64], but they mainly neglect the electronic response and nonadiabatic effects. The nonadiabatic response properties have been simulated with the coupled electron–ion Monte Carlo (CEIMC) [65, 66, 67, 68], but not the polarizabilities.

There are many variations of PIMC, and the one used in this work [69, 70, 71, 72] is fully nonadiabatic and extremely accurate in terms of exact Coulomb interactions. The biggest challenge is the usual difficulty of all the real-space QMC methods: the so-called Fermion sign problem (FSP), which arises from the quantum statistics of identical particles. However, this work is not focused on developing the core method, and thus, the study is limited to few-electron systems.

Instead, we focus on estimating the field-response, *i.e.*, multipole polarizability from PIMC simulations. We demonstrate three approaches: finite field simulation, static field-derivative estimators, and transformation of imaginary-time correlation functions. The field-derivative estimators are efficient in the estimation of the static higher-order polarizabilities. The correlation functions are the most capable approach, providing an interface to dynamic properties. However, the required analytic continuation is an ill-posed numerical problem and a challenge of its own. We provide an ample demonstration and a workflow description for a particular approach called the Maximum Entropy method (MaxEnt) [73, 74].

Besides advances in the methodology, we report static and dynamic multipole polarizabilities of a range of one- and two-electron systems: H, He, H_2^+, H_2, H_3^+, He^+, Li^+, Be^{2+}, Ps, Ps_2, PsH, HeH^+ and HD^+. We successfully benchmark our approaches against pre-existing data, but we also complement them at unprecedented accuracy. Especially, we provide exact numerical evidence to some thermal effects, which used to be known only at a qualitative or approximate level.

The Thesis is structured as follows: In Chapter 2, we establish the basic definitions of quantum mechanics, path integrals and linear response theory. In Chapter 3 we spec-

ify perturbation due to electric field and consider the emergence of polarizabilities and their basic properties. In Chapter 4 we outline some of the more practical aspects of the PIMC simulation and emphasize the different strategies to obtain polarizabilities. In Chapter 5 we discuss thermal effects in atomic and molecular higher-order polarizabilities using the proposed static estimators. In Chapter 6 the focus is on the properties of dynamic response functions: correlation functions, analytic continuation and van der Waals coefficients. We conclude with a summary and outlook. Comprehensive sets of results are found in the original publications, whose reprints are provided at the end.

2 QUANTUM MECHANICS AND PATH INTEGRALS

Quantum physics is the foundation of most properties of matter. The purpose of this chapter is to view generalized dynamic susceptibilities in the framework of nonrelativistic quantum mechanics. The narrative is dedicated to understanding the connection between ground state wavefunctions and the Feynman path-integral formalism for thermal density matrices. In particular, we are focused on associating linear and nonlinear response properties with quantum time-correlation functions, whose definitions and analytic properties we consider in both real and imaginary times.

This chapter lays the abstract and theoretical foundations of this Thesis. It is based on, *e.g.*, Refs. [72, 75, 76, 77, 78], which also allow for more verbose and educational introduction for nonexpert readers.

2.1 The Schrödinger equation

Throughout this Thesis we are concerned with a quantum state and its time evolution. In nonrelativistic quantum mechanics, the time-evolution is defined by the time-dependent Schrödinger equation

$$\hat{H}|\Psi(t)\rangle = i\,\hbar\,\frac{\partial}{\partial t}|\Psi(t)\rangle, \tag{2.1}$$

where $\hat{H}$ is the Hamilton operator and $|\Psi(t)\rangle$ is a normalized wavefunction. The Hamiltonian in Eq. (2.1) is a Hermitian operator and independent of the basis. The wavefunction is a solution to Eq. (2.1) in an abstract vector space, and it uniquely defines the state of the system.

In the following, we denote by $\hat{H}_0$ that the Hamiltonian is independent of time and unperturbed. The stationary eigenstates of $\hat{H}_0$ are given by the time-independent Schrödinger equation

$$\hat{H}_0|n\rangle = E_n|n\rangle, \tag{2.2}$$

where E_n is an eigenenergy associated with an eigenstate $|n\rangle$. The eigenstates span a

complete and orthonormal basis set. That is, the set of eigenstates obeys orthonormality

$$\langle n|m\rangle = \delta_{nm}, \tag{2.3}$$

where δ is the Kronecker delta, and resolution of the identity

$$\sum_n |n\rangle\langle n| = \hat{1}, \tag{2.4}$$

where $\hat{1}$ is the identity operator, for which $\hat{1}\hat{P} = \hat{P}$ for any operator $\hat{P}$.

2.1.1 Propagator

Let us now consider the propagation of the wavefunction to another time t'. The time-evolution is given by

$$|\Psi(t')\rangle = \hat{U}(t,t')|\Psi(t)\rangle, \tag{2.5}$$

where the propagator $\hat{U}(t,t')$ is a unitary operator that satisfies $\hat{U}(t,t) = \hat{1}$, $\hat{U}(t,t') = \hat{U}^\dagger(t',t)$ and $\hat{U}(t,t') = \hat{U}(t,t'')\hat{U}(t'',t')$. Its explicit form can be solved from Eq. (2.1) as

$$\hat{U}(t,t') = \mathrm{e}^{-i/\hbar \int_t^{t'} \mathrm{d}\bar{t}\hat{H}_0(\bar{t})} \tag{2.6}$$

$$= \mathrm{e}^{-i(t'-t)\hat{H}_0/\hbar} \tag{2.7}$$

$$\equiv \hat{U}(t'-t), \tag{2.8}$$

provided that $\hat{H}_0$ is time-independent. That is, the propagation only depends on the time differences, and an arbitrary t can be chosen without loss of generality.

Let us consider a general operator $\hat{P}$ and its expectation value, which is denoted $\bar{P}(t)$ at a given time and defined by

$$\bar{P}(t) = \langle\Psi(t)|\hat{P}|\Psi(t)\rangle \tag{2.9}$$

$$\equiv \langle\Psi|\hat{P}(t)|\Psi\rangle. \tag{2.10}$$

Equation (2.9) is called the *Schrödinger picture*, where we propagate the wavefunction. It is equivalent to Eq. (2.10), which is the *Heisenberg picture*, where the time-propagation

is encoded in the operator $\hat{P}(t) \equiv \hat{U}(t)\hat{P}\hat{U}(-t)$. In the following, the standard convention will be the Heisenberg picture.

2.1.2 Representation of the wavefunction

So far, the wavefunction $|\Psi(t)\rangle$ has been treated in the abstract vector space. However, the actual mechanical problem is usually treated in the Hilbert space $\mathscr{H}$, such that $R \in \mathscr{H}$, where R is a set of real-space coordinates that span the phase-space of the system. Projection of the wavefunction is denoted

$$\Psi(R,t) \equiv \langle R|\Psi(t)\rangle = \langle \Psi(t)|R\rangle. \tag{2.11}$$

For practical reasons, R represents degrees of freedom of the mechanical system, such as the positions and generalized momenta of the particles. In quantum mechanics, positions $\hat{r}$ and momenta $\hat{p}$ are connected by the canonical commutation relations

$$[\hat{r}_i, \hat{p}_j] \equiv \hat{r}_i\hat{p}_j - \hat{p}_j\hat{r}_i = i\hbar\delta_{ij}, \tag{2.12}$$

where the brackets denote a commutator. Consequently, only either set of coordinates is needed to fully express the state. We can thus summarize the choices of basis in the resolution of the identity

$$\sum_n |n\rangle\langle n| = \int \mathrm{d}R\,|R\rangle\langle R| = \int \mathrm{d}p\,|p\rangle\langle p| = \hat{1}. \tag{2.13}$$

This also implies orthonormality, *i.e.*

$$\langle n|m\rangle = \langle R_n|R_m\rangle = \langle p_n|p_m\rangle = \delta_{nm}. \tag{2.14}$$

For the remainder of this work, we will denote a many-body state in real space by $R \equiv \{\mathbf{r}_1 \ldots \mathbf{r}_N\}$, where $\mathbf{r}_n$ are the Cartesian coordinates of N distinguishable particles. The real-space projection of the Schrödinger equation is written as [72]

$$H(R)\Psi(R,t) = i\hbar\frac{\partial}{\partial t}\Psi(R,t), \tag{2.15}$$

and the projection of any operator as

$$P(R) \equiv \langle R|\hat{P}\rangle. \tag{2.16}$$

So far, we have omitted the spin degree of freedom, which is critical for the complete quantum-mechanical representation of state. Adding the spin is straightforward, but also redundant for the purposes of this Thesis.

2.1.3 Fermion, boson and boltzmannon statistics

Let us briefly consider the many-body wavefunction of identical, indistinguishable particles. By indistinguishability it is implied that we cannot tell apart $\Psi(R)$ and $\Psi(\mathscr{P}R)$, where the permutation operator $\mathscr{P}$ has permuted some of the one-particle coordinates: *e.g.* $\mathscr{P}\{\mathbf{r}_1,\mathbf{r}_2,\ldots\} \rightarrow \{\mathbf{r}_2,\mathbf{r}_1,\ldots\}$. The statistical properties of identical particles arise from the particle density measurement. The probability amplitude ρ is given by the squared norm of the wavefunction:

$$\rho(R) = |\Psi(R)|^2 = \langle\Psi(R)|\Psi(R)\rangle, \tag{2.17}$$

which leads to a conclusion

$$\Psi(R) = \mathrm{e}^{i\phi}\Psi(\mathscr{P}R), \tag{2.18}$$

whose square solves ϕ either as 0 or π. Based on experiments, those particles obeying $\phi = 0$ are defined as *bosons* (integer spin; *e.g.* photons, gluons and composites with an even number of fermions) and those obeying $\phi = \pi$ as *fermions* (half-integer spin; *e.g.* electrons, protons and neutrons). The consequence can be summarized in

$$\Psi(R) = (\pm 1)^{\mathscr{P}}\Psi(\mathscr{P}R), \tag{2.19}$$

where plus is for bosons, minus is for fermions and $\mathscr{P}$ in the exponent refers to the total number of permutations.

The seemingly simple property of Eq. (2.19) has vast implications in both the theoretical and practical aspects of quantum mechanical simulations. In large systems, the number of identical particles increases inevitably, and thus, the number of permutations also grows rapidly. Many approaches related to explicit integration over spatial dimensions

R or permutation determinants suffer from the exclusive nature of the minus sign of fermions: subtraction of almost but not quite identical permutations leads to numerical problems that are commonly referred to as the Fermion sign problem (FSP). While FSP is a significant challenge, we make no attempts to solve it or further study its consequences in this Thesis. This is a major trade-off, which is made for convenience and the focus on response properties – for now.

Consequently, we only study small systems that obey the so-called *boltzmannon* statistics. There is no need to consider identical fermions, if all the particles are distinguishable: either they are different species or opposite spins. Thus, up to two electrons or identical nuclei are allowed to appear in one simulation. We elude this restriction in a few simulations, because the interaction of identical nuclei is negligible at high temperatures. Mostly, it is natural to simulate two-electron systems as boltzmannons, because the *singlet* spin state is also the ground state.

2.1.4 Density matrix and thermal ensemble

The wavefunction $\Psi(R,t)$ represents a pure quantum state, but a density matrix ρ represents a state that is mixed in the statistical sense. The normalized density matrix is defined by the density operator

$$\hat{\rho} = \sum_n \mathbb{P}_n |n\rangle\langle n|, \tag{2.20}$$

where $\mathbb{P}_n$ is a nonnegative probability describing the relative occupation at the given pure state n. The dynamics of a density matrix are given by the von Neumann equation

$$i\hbar \frac{\partial}{\partial t}\hat{\rho}(t) = \left[\hat{H}(t), \hat{\rho}\right]. \tag{2.21}$$

If $\hat{H} = \hat{H}_0$ is time-independent, the solution is $\hat{\rho}(t) = \mathrm{e}^{-it\hat{H}_0/\hbar}\rho(0)\mathrm{e}^{it\hat{H}_0/\hbar}$.

An expectation value of some physical property P is given by a weighted trace:

$$\langle P \rangle = Z^{-1}\mathrm{Tr}\left[\hat{\rho}\hat{P}\right], \tag{2.22}$$

where

$$Z = \mathrm{Tr}[\hat{\rho}] = \sum_n \mathbb{P}_n \tag{2.23}$$

is the partition function.

A usual mixed state is the Boltzmann distribution in thermal equilibrium:

$$\hat{\rho}(\beta) \equiv \mathrm{e}^{-\beta \hat{H}_0/\hbar}, \tag{2.24}$$

where $\beta = 1/k_B T$ is the inverse temperature. The partition function is then given by

$$Z \equiv \mathrm{Tr}[\hat{\rho}] = \sum_n \mathrm{e}^{-\beta E_n}. \tag{2.25}$$

Clearly, the equilibrium density matrix $\hat{\rho}(\beta)$ commutes with $\hat{H}_0$ and $\hat{U}$: the equilibrium is time-invariant.

In real-space projection, the normalized density matrix is defined and denoted

$$\rho(R, R'; \beta) \equiv Z^{-1} \langle R|\hat{\rho}(\beta)|R'\rangle = Z^{-1} \sum_n \psi_n(R) \psi_n^*(R') \mathrm{e}^{-\beta E_n}, \tag{2.26}$$

where $\psi_n(R) = \langle R|n\rangle$. Analogous to Eq. (2.21), the thermal density matrix uniquely solves the Bloch equation [72]

$$\left[\hat{H}_0 + \tfrac{\partial}{\partial \beta}\right] \rho(R, R'; \beta) = \delta(\beta)\delta(R - R') \tag{2.27}$$

for a set of boundary conditions.

2.1.5 Measurements and observables

A quantity is an observable, if it can be measured. That is, if P is an observable, there exists a self-adjoint operator $\hat{P} = \hat{P}^\dagger$ that produces real-valued results P out of the wavefunction:

$$\hat{P}|\Psi(R,t)\rangle = P|\Psi_P(R,t)\rangle, \tag{2.28}$$

where the system has collapsed to an eigenstate $\Psi_P(R,t)$ of $\hat{P}$. This is the widely debated Copenhagen interpretation of the quantum measurement. Nevertheless, empirical evidence suggests that the expectation value $\bar{P}(t)$ taken over repeated measurements follows Eq. (2.9). If the state is time-invariant, *i.e.*, $|\Psi(R,t)\rangle \equiv |\Psi(R)\rangle$, we can without loss of generality choose $t = t'$, which leads to

$$\begin{aligned}\bar{P}(t') &= \langle\Psi(R,t')|\hat{P}|\Psi(R,t')\rangle && (2.29)\\ &= \langle\Psi(R)|\hat{P}|\Psi(R)\rangle && (2.30)\\ &\equiv \bar{P}, && (2.31)\end{aligned}$$

that is, the expectation value is also time-independent.

A particular stationary state is the thermal equilibrium. According to Eq. (2.22), a one-time observable yields a *thermal expectation value*

$$\begin{aligned}\langle P(t')\rangle &= Z^{-1}\mathrm{Tr}[\hat{\rho}(\beta)\hat{U}(t')\hat{P}\hat{U}^{\dagger}(t')]\\ &= Z^{-1}\mathrm{Tr}[\hat{U}^{\dagger}(t')\hat{\rho}(\beta)\hat{U}(t')\hat{P}]\\ &= Z^{-1}\mathrm{Tr}[\hat{\rho}(\beta)\hat{U}^{\dagger}(t')\hat{U}(t')\hat{P}]\\ &= \langle P\rangle, && (2.32)\end{aligned}$$

which is also time-invariant. That is, based on the cyclic property of the trace and the fact that $\hat{\rho}$ and $\hat{U}$ commute. The same equation in the coordinate representation is

$$\begin{aligned}\langle P\rangle &= Z^{-1}\mathrm{Tr}[\hat{\rho}(\beta)\hat{P}] && (2.33)\\ &= Z^{-1}\int \mathrm{d}R\,\mathrm{d}R'\,\langle R|\hat{\rho}(\beta)|R'\rangle\langle R'|\hat{P}|R\rangle] && (2.34)\\ &= Z^{-1}\int \mathrm{d}R\,\mathrm{d}R'\,\rho(R,R';\beta)\langle R'|\hat{P}|R\rangle. && (2.35)\end{aligned}$$

Moreover, if $\hat{P}$ is an operator that is local or *diagonal* in R, it follows that

$$\langle R'|\hat{P}|R\rangle = P(R)\langle R'|R\rangle = P(R)\delta(R-R'),$$

and thus,

$$\langle P \rangle = Z^{-1} \int \mathrm{d}R\, \rho(R,R;\beta) P(R). \tag{2.36}$$

Most operators are diagonal in the coordinate space R except, *e.g.*, the Hamiltonian $\hat{H}_0$ and the momentum $\hat{p}$. For the remainder of this Thesis, we prefer the thermal expectation value for density matrices. Transformation to the wavefunction representation is possible in some cases by taking the limit $\beta \to \infty$, but that is not always straightforward or rigorous.

2.1.6 Causal time-correlation and Green's functions

Diagonal observables are time-independent in the equilibrium, but the situation is more complicated for correlated measurements: when two or more events occur in succession, they affect each other. In the following, we summarize the most important definitions of 1-time correlators and beyond. The higher-order formalism is rare in the literature, but we will follow Ref. [79]. The framework may appear daunting, but the motivation is recovered in Sec. 2.2, where the general n-time correlators are associated with higher-order response functions.

Let us adopt a notation for a series of consecutive interactions, according to Fig. 2.1. That is, operator $\hat{P}(t)$ in the Heisenberg picture denotes the final measurement of P, which responds to interactions $\hat{Q}_1(t')$, $\hat{Q}_2(t'')$, *etc*, whose indices are ordered backwards in time. The reverse ordering may appear confusing at first, but it allows adding an arbitrary number of steps. It turns out that the process only depends on the relative

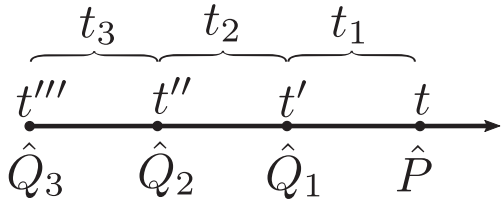

Figure 2.1 Denotation of the few lowest real-time arguments and the associated interactions and time-differences in causal scenario.

time-differences, which are denoted $t_1 = t - t'$, $t_2 = t'' - t'$, $t_3 = t''' - t''$, and so on.

Thus, let us define the correlator, or the Green's function operator, between $\hat{P}$ and $\hat{Q}$:

$$\hat{G}(t;t') = \frac{1}{i\hbar}\mathscr{T}\hat{P}(t)\hat{Q}(t') \tag{2.37}$$

where $\mathscr{T}$ is a time-ordering operator on the so-called Keldysh contour [78]. A proper way to implement the time-ordering is to define lesser and greater correlators, *i.e.*

$$\hat{G}^{>}(t;t') = \frac{1}{i\hbar}\hat{P}(t)\hat{Q}(t') \tag{2.38}$$

$$\hat{G}^{<}(t;t') = \pm\frac{1}{i\hbar}\hat{Q}(t)\hat{P}(t'), \tag{2.39}$$

where the latter plus/minus refer correlators of bosonic/fermionic symmetry, respectively. Observable measurements in this Thesis are categorically bosonic, and we will use the bosonic sign from this point on. We can further define the retarded and advanced correlators as

$$\hat{G}^{R}(t;t') = \theta(t-t')\Big[\hat{G}^{>}(t;t') - \hat{G}^{<}(t;t')\Big] = \theta(t-t')\frac{1}{i\hbar}\Big[\hat{P}(t),\hat{Q}(t')\Big] \tag{2.40}$$

$$\hat{G}^{A}(t;t') = \theta(t'-t)\Big[\hat{G}^{>}(t;t') - \hat{G}^{<}(t;t')\Big] = \theta(t'-t)\frac{1}{i\hbar}\Big[\hat{Q}(t'),\hat{P}(t)\Big] \tag{2.41}$$

where $\theta(t)$ is the Heaviside step function. The retarded correlator is also causal: $\hat{P}$ happens after $\hat{Q}$.

The correlator $\hat{G}(t,t')$ is associated with the thermal Green's function

$$\begin{aligned} G(t;t') &= Z^{-1}\mathrm{Tr}\Big[\hat{\rho}(\beta)\hat{G}(t;t')\Big] \\ &= Z^{-1}\mathrm{Tr}\Big[\hat{\rho}(\beta)\tfrac{1}{i\hbar}\mathscr{T}\hat{P}(t)\hat{Q}(t')\Big] \\ &= Z^{-1}\mathrm{Tr}\Big[\hat{\rho}(\beta)\tfrac{1}{i\hbar}\mathscr{T}\hat{P}(0)\hat{Q}(t'-t)\Big] \\ &= Z^{-1}\mathrm{Tr}\Big[\hat{\rho}(\beta)\hat{G}(0,-t_1)\Big] \qquad (2.42) \\ &\equiv G_1(t_1), \qquad (2.43) \end{aligned}$$

where the *1-time Green's function* $G_1(t_1)$ only depends on the time-difference $t_1 = t - t'$.

Similarly, an n-time correlator

$$\hat{G}_n\left(t;t',\ldots,t^{(n)}\right)=\frac{1}{(i\hbar)^n}\mathscr{T}\hat{P}(t)\hat{Q}_1\left(t'\right)\ldots\hat{Q}_n\left(t^{(n)}\right), \tag{2.44}$$

produces an n-time Green's function

$$\begin{aligned}G_n\left(t;t',\ldots,t^{(n)}\right)&=Z^{-1}\mathrm{Tr}\left[\hat{\rho}(\beta)\hat{G}_n\left(t;t',\ldots,t^{(n)}\right)\right]\\&=Z^{-1}\mathrm{Tr}\left[\hat{\rho}(\beta)\hat{G}_n\left(0;t'-t,\ldots,t^{(n)}-t\right)\right]\\&\equiv G_n(t_1,\ldots,t_n).\end{aligned} \tag{2.45}$$

That is, the $n+1$ instances of time can be reduced to n time-differences.

Causality in higher orders

We are interested in the retarded n-time Green's function, so let us construct one using the advanced correlators. The advanced 1-time correlator $\hat{G}_1^A(t,t')$ starts from $\hat{P}(t)$ and reverts back in time to $\hat{Q}_1(t')$. Now, according to Eq. (2.41), the advanced 2-time correlator is defined with respect to $\hat{G}_1^A(t,t')$:

$$\hat{G}_2^A(t,t',t'')=\theta(t''-t')\frac{1}{i\hbar}\left[\hat{Q}_2(t''),\hat{G}_1(t,t')\right] \tag{2.46}$$

$$=\theta(t'-t)\theta(t''-t')\frac{1}{(i\hbar)^2}\left[\hat{Q}_2(t''),\left[\hat{Q}_1(t'),\hat{P}(t)\right]\right]. \tag{2.47}$$

It is easy to generalize this by repeating n times:

$$\begin{aligned}\hat{G}_n^A\left(t;t',\ldots,t^{(n)}\right)=&\frac{1}{(i\hbar)^n}\theta\left(t'-t\right)\ldots\theta\left(t^{(n)}-t^{(n-1)}\right)\\&\times\left[\hat{Q}_n\left(t^{(n)}\right),\left[\ldots\left[\hat{Q}_1\left(t'\right),\hat{P}(t)\right]\ldots\right]\right].\end{aligned} \tag{2.48}$$

Finally, the retarded n-time correlation function is obtained by flipping the arguments of θ-functions, and shifting the time by $-t$ inside the trace:

$$
\begin{aligned}
&G_n^R\left(t;t',\ldots,t^{(n)}\right)\\
&=\frac{1}{(i\hbar)^n}\theta\left(t-t'\right)\ldots\theta\left(t^{(n-1)}-t^{(n)}\right)\mathrm{Tr}\left[\hat{\rho}(\beta)\left[\hat{\mathrm{Q}}_n(t^{(n)}),\left[\ldots\left[\hat{\mathrm{Q}}_1(t'),\hat{P}(t)\right]\ldots\right]\right]\right]\\
&=\frac{1}{(-i\hbar)^n}\theta(t_1)\ldots\theta(t_n)\left\langle\left[\ldots\left[\hat{P},\hat{\mathrm{Q}}_1(-t_1)\right],\ldots\hat{\mathrm{Q}}_n(-(t_1+\ldots+t_n))\right]\right\rangle \qquad (2.49)\\
&\equiv G_n^R(t_1,\ldots,t_n), \qquad (2.50)
\end{aligned}
$$

where flipping all the commutators produces and extra factor of $(-1)^n$.

Correlation functions and frequency domain

In dynamic simulations, it is sometimes more natural to consider time-correlation functions instead of the Green's functions. The difference is a small matter of definition: the time-correlation function is based on correlator

$$\hat{C}(t,t')=\mathscr{T}\hat{P}(t)\hat{\mathrm{Q}}(t'), \qquad (2.51)$$

and thus, it is easy to see that the thermal n-time correlation functions are defined as

$$C_n(t,t',\ldots,t^{(n)})\equiv C_n(t_1,\ldots,t_n)=(i\hbar)^n G_n(t_1,\ldots,t_n). \qquad (2.52)$$

The same also holds for the retarded and advanced variations.

In physical understanding, the point of interest is usually in the frequency domain. This calls for Fourier transform, which is defined for the 1-time correlation function as

$$C_1(\omega_1)=\mathscr{F}C_1(t_1)\equiv\int_{-\infty}^{\infty}\mathrm{d}t\,\mathrm{e}^{-i\omega_1 t_1}C_1(t_1). \qquad (2.53)$$

and, generally to an n-time correlation function as

$$C_n(\omega_1,\ldots,\omega_n) = \mathscr{F} C_n(t_1,\ldots,t_n) \tag{2.54}$$

$$= \int_{-\infty}^{\infty} \mathrm{d}t_1 \ldots \int_{-\infty}^{\infty} \mathrm{d}t_n \, \mathrm{e}^{-i\omega_1 t_1} \ldots \mathrm{e}^{-i\omega_n t_n} C_n(t_1,\ldots,t_n). \tag{2.55}$$

The same definition applies to retarded functions, whose lower integration limit is zero instead of negative infinity.

2.2 Linear response theory

We are now equipped to consider the response of the system to weak perturbations. The general idea is that the linear response of a property P to a perturbing field F is

$$\delta P = \chi F, \tag{2.56}$$

where δP is the linear deviation, F is the field strength and χ is a generalized susceptibility. For convenience, we will consider responses that are *normal ordered*, *i.e.* $\delta P = \langle P \rangle - \langle P \rangle_0$, where $\langle P \rangle_0$ denotes an unperturbed expectation value. That is, we consider the induced fluctuations of properties with respect to their equilibrium values.

2.2.1 External perturbation

Let us consider the case, where an arbitrary number of weak time-dependent perturbations $\hat{h}$ are introduced to the equilibrium Hamiltonian $\hat{H}_0$. The total Hamiltonian is then written as

$$\hat{H}(t) = \hat{H}_0 + \hat{h}(t) = \hat{H}_0 + \sum_{n=1}^{\infty} \hat{h}_n(t) \tag{2.57}$$

where

$$\hat{h}_n(t) = -\hat{Q}_n \cdot F_n(t), \tag{2.58}$$

and the minus sign follows the standard convention. Q and F are typically vector fields or tensor fields, whose evaluation involves inner products and spatial integrals, in principle. It is not relevant for this Thesis, and thus, the interaction will be treated in simple real-space projection given by

$$h_n(R;t) = -Q_n(R;t)\cdot F_n(R;t), \tag{2.59}$$

whose evaluation out of a real-space state R will be considered later.

The interaction according to Eq. (2.57) leads to a non-equilibrium density matrix $\rho(t)$. It can be solved from the von Neumann equation (2.21) with the boundary condition $\rho(-\infty) = \rho_0$. Writing a perturbation expansion in the powers of the field amplitudes F_n, the solution is [79]

$$\rho(t) = \rho_0 + \sum_{n=1}^{\infty} \rho^{(n)}(t), \tag{2.60}$$

where

$$\begin{aligned}\rho^{(n)}(t) = \frac{1}{(i\hbar)^n} \int_{-\infty}^{t} \mathrm{d}t' \int_{-\infty}^{t'} \mathrm{d}t'' \cdots \int_{-\infty}^{t^{(n-1)}} \mathrm{d}t^{(n)} \\ \times \mathrm{Tr}\Big[\hat{h}(t'),\Big[\hat{h}\left(t''\right),\ldots\Big[\hat{h}\left(t^{(n)}\right),\rho_0\Big]\ldots\Big]\Big],\end{aligned} \tag{2.61}$$

where the time-arguments follow the definitions from Sec. 2.1.6.

2.2.2 Response function

According to Eq. (2.56), the linear and normal ordered response to a set of perturbations is given by

$$\delta P(t) = P(t) - P(0) = Z^{-1}\mathrm{Tr}\Big[\hat{P}\hat{\rho}(t)\Big] - \langle P\rangle_0 = Z^{-1}\mathrm{Tr}\Big[\hat{P}(\rho(t)-\rho_0)\Big].$$

Using Eq. (2.60), the difference becomes

$$\delta P(t) = \sum_n P^{(n)}(t), \tag{2.62}$$

where

$$
\begin{aligned}
P^{(n)}(t) =& Z^{-1}\frac{1}{(i\hbar)^n}\int_{-\infty}^{t}\mathrm{d}t'\int_{-\infty}^{t'}\mathrm{d}t''\cdots\int_{-\infty}^{t^{(n-1)}}\mathrm{d}t^{(n)} \\
&\times \mathrm{Tr}\Big[\hat{P}\hat{h}\left(t'\right),\Big[\hat{h}\left(t''\right),\ldots\Big[\hat{h}\left(t^{(n)}\right),\rho_0(t)\Big]\ldots\Big]\Big] \qquad (2.63)\\
=& Z^{-1}\frac{1}{(i\hbar)^n}\int_{-\infty}^{\infty}\mathrm{d}t'\int_{-\infty}^{\infty}\mathrm{d}t''\cdots\int_{-\infty}^{\infty}\mathrm{d}t^{(n)}\,\theta(t-t')\ldots\theta\left(t^{(n-1)}-t^{(n)}\right) \\
&\times \mathrm{Tr}\Big[\hat{P}(-t)\hat{h}(t'-t),\Big[\hat{h}(t''-t),\ldots\Big[\hat{h}(t^{(n)}-t),\rho_0(0)\Big]\ldots\Big]\Big]. \qquad (2.64)
\end{aligned}
$$

Usually, one does not study the full summation at once, but the term of a particular order n. At each degree, we can separate a linear response property

$$
\begin{aligned}
P^{(n)}(t) =& Z^{-1}\frac{1}{(-i\hbar)^n}\int_{-\infty}^{\infty}\mathrm{d}t'\int_{-\infty}^{\infty}\mathrm{d}t''\cdots\int_{-\infty}^{\infty}\mathrm{d}t^{(n)}\,\theta\left(t-t'\right)\ldots\theta\left(t^{(n-1)}-t^{(n)}\right) \\
&\times \mathrm{Tr}\Big[\hat{P}(-t)\hat{Q}_1\left(t'-t\right),\Big[\hat{Q}_2\left(t''-t\right),\ldots\Big[\hat{Q}_n\left(t^{(n)}-t\right),\rho_0\Big]\ldots\Big]\Big] \\
&\times F_1(t')\ldots F_n(t^{(n)}) \qquad (2.65)\\
=& \int_0^{\infty}\mathrm{d}t_1\int_{t_1}^{\infty}\mathrm{d}t_2\ldots\int_{t_{n-1}}^{\infty}\mathrm{d}t_n\,\chi^{(n)}(t_1,\ldots,t_n)F(t-t_1)\ldots F(t-t_n), \qquad (2.66)
\end{aligned}
$$

where we have substituted $t_1 = t-t'$, …, $t_n = t^{(n-1)} - t^{(n)}$. Furthermore, we have identified the causal response function as

$$
\begin{aligned}
&\chi^{(n)}(t_1,\ldots,t_n) \\
&=Z^{-1}\frac{1}{(-i\hbar)^n}\theta(t_1)\ldots\theta(t_n) \\
&\quad\times \mathrm{Tr}\Big[\hat{P}(0)\Big[\hat{Q}_1(-t_1),\Big[\hat{Q}_2(-t_1-t_2),\ldots\Big[\hat{Q}_n(-(t_1+\ldots+t_n)),\rho_0\Big]\ldots\Big]\Big]\Big] \\
&=Z^{-1}\frac{1}{(i\hbar)^n}\theta(t_1)\ldots\theta(t_n)\left\langle\Big[\ldots\Big[\hat{P}(0),\hat{Q}_1(-t_1)\Big],\ldots,\hat{Q}_n(-(t_1+\ldots+t_n))\Big]\right\rangle \qquad (2.67)\\
&=(-1)^n\,G_n^R(t_1,\ldots,t_n), \qquad (2.68)
\end{aligned}
$$

where G_n^R is the retarded n-time Green's function from Eq. (2.49). This is rather a design than a coincidence: the retarded Green's functions in equilibrium are interesting precisely because they are associated with out-of-equilibrium properties, the causal response functions.

2.2.3 Frequency-dependent response

For physical applications, $\chi^{(n)}$ is most interesting in the frequency representation. Let us define

$$F(\omega_1) = \mathscr{F}F(t_1) = \int_{-\infty}^{\infty} \mathrm{d}t_1\, \mathrm{e}^{i\omega_1 t_1} F(t_1) \tag{2.69}$$

$$F(t_1) = \mathscr{F}^{-1}F(\omega_1) = \int_{-\infty}^{\infty} \frac{\mathrm{d}\omega_1}{2\pi}\, \mathrm{e}^{i\omega_1 t_1} F(\omega_1). \tag{2.70}$$

Then, Eq. (2.66) can be rewritten as

$$\begin{aligned}
\delta P(t) = & \int_{-\infty}^{\infty} \frac{\mathrm{d}\omega_1}{2\pi} \ldots \int_{-\infty}^{\infty} \frac{\mathrm{d}\omega_n}{2\pi} \int_0^{\infty} \mathrm{d}t_1 \ldots \int_0^{\infty} d\, t_n \\
& \times \chi^{(n)}(t_1, \ldots, t_n) \mathrm{e}^{i\omega_1(t-t_1)} \ldots \mathrm{e}^{i\omega_1(t-t_n)} F(\omega_1) \ldots F(\omega_n) && (2.71) \\
= & \int_{-\infty}^{\infty} \frac{\mathrm{d}\omega_1}{2\pi} \ldots \int_{-\infty}^{\infty} \frac{\mathrm{d}\omega_n}{2\pi} \chi^{(n)}(\omega_1, \ldots, \omega_n) \mathrm{e}^{i(\omega_1 + \ldots + \omega_n)t} F(\omega_1) \ldots F(\omega_n) && (2.72) \\
\equiv & \int_{-\infty}^{\infty} \frac{d\,\omega}{2\pi} \mathrm{e}^{i\omega t} P(\omega) && (2.73)
\end{aligned}$$

where $\omega = \omega_1 + \ldots + \omega_n$ and we have defined the frequency-dependent susceptibility

$$\chi^{(n)}(\omega_1, \ldots, \omega_n) = \int_0^{\infty} \mathrm{d}t_1 \ldots \int_0^{\infty} \mathrm{d}t_n\, \mathrm{e}^{-i\omega_1 t_1} \ldots \mathrm{e}^{-i\omega_n t_n} \chi^{(n)}(t_1, \ldots, t_n). \tag{2.74}$$

The composition of Eqs. (2.68) and (2.74) is the foundation of the general order linear response theory.

2.2.4 Explicit formulas

For reference, let us define the susceptibility in the eigenstate basis $|n\rangle$ of the equilibrium system. The first-order response is given by

$$\begin{aligned}
\chi^{(1)}(\omega_1) &= \int_0^\infty \mathrm{d}t_1\, \mathrm{e}^{i\omega_1 t_1} \chi^{(1)}(t_1) \\
&= \frac{1}{i\hbar} \int_0^\infty \mathrm{d}t_1\, \mathrm{e}^{i\omega_1 t_1} \left\langle \hat{P} \mathrm{e}^{i\hat{H}_0 t_1/\hbar} \hat{Q}_1 \mathrm{e}^{-i\hat{H}_0 t_1/\hbar} - \hat{Q}_1 \mathrm{e}^{i\hat{H}_0 t_1/\hbar} \hat{P} \mathrm{e}^{-i\hat{H}_0 t_1/\hbar} \right\rangle \\
&= Z^{-1} \sum_{n,m} \frac{1}{i\hbar} \int_0^\infty \mathrm{d}t_1\, \mathrm{e}^{i\omega_1 t_1} \\
&\quad \times \mathrm{Tr}\Big[\exp(-\beta E_n) \langle n|\hat{P}|m\rangle \langle m|\hat{Q}_1|n\rangle \exp(-i(E_m - E_n)t_1/\hbar) \\
&\quad - \exp(-\beta E_n) \langle n|\hat{Q}_1|m\rangle \langle m|\hat{P}|n\rangle \exp(i(E_m - E_n)t_1/\hbar) \Big] \\
&= Z^{-1} \sum_{m \neq n} \mathrm{e}^{-\beta E_n} \left(\frac{P^{nm} Q_1^{mn}}{\omega_1 - \omega_{mn}} + \frac{Q_1^{nm} P^{mn}}{\omega_1 + \omega_{mn}} \right),
\end{aligned} \tag{2.75}$$

where $\omega_{mn} = (E_m - E_n)/\hbar$ is a transition frequency and $A^{nm} = \langle n|\hat{A}|m\rangle$ denotes a matrix element. Similarly, the second-order response function can be written as

$$\begin{aligned}
\chi^{(2)}(\omega_1, \omega_2) &= \int_0^\infty \mathrm{d}t_1 \int_{t_1}^\infty \mathrm{d}t_2\, \mathrm{e}^{i(\omega_1 t_1 + \omega_2 t_2)} \chi^{(2)}(t_1, t_2) \\
&= Z^{-1} \sum_{n,m,k} \int_0^\infty \mathrm{d}t_1\, \mathrm{e}^{i(\omega_1 + \omega_2)t_1} \mathrm{e}^{-\beta E_n} \\
&\quad \times \left(\frac{P^{nm} Q_1^{mk} Q_2^{kn}}{\omega_2 - \omega_{kn}} - \frac{Q_1^{nm} P^{mk} Q_2^{kn}}{\omega_2 - \omega_{kn}} - \frac{Q_2^{nm} P^{mk} Q_1^{kn}}{\omega_2 - \omega_{nm}} + \frac{Q_2^{nm} Q_1^{mk} P^{kn}}{\omega_2 - \omega_{nm}} \right) \\
&= Z^{-1} \sum_{n \neq m, n \neq k} \mathrm{e}^{-\beta E_n} \left(\frac{P^{nm} Q_1^{mk} Q_2^{kn}}{(\omega_2 - \omega_{kn})(\omega - \omega_{mk})} - \frac{Q_1^{nm} P^{mk} Q_2^{kn}}{(\omega_2 - \omega_{kn})(\omega - \omega_{nm})} \right. \\
&\quad \left. - \frac{Q_2^{nm} P^{mk} Q_1^{kn}}{(\omega_2 - \omega_{nm})(\omega - \omega_{kn})} + \frac{Q_2^{nm} Q_1^{mk} P^{kn}}{(\omega_2 - \omega_{nm})(\omega - \omega_{mk})} \right),
\end{aligned} \tag{2.76}$$

where $\omega = \omega_1 + \omega_2$, and the third-order response is

$$\begin{aligned}
\chi^{(3)}(\omega_1,\omega_2,\omega_3) &= \int_0^\infty \mathrm{d}t_1 \int_{t_1}^\infty \mathrm{d}t_2 \int_{t_2}^\infty \mathrm{d}t_3\, \mathrm{e}^{i(\omega_1 t_1+\omega_2 t_2+\omega_3 t_3)}\chi^{(3)}(t_1,t_2,t_3) \\
&= Z^{-1} \sum_{n\neq m, n\neq k, n\neq l} \mathrm{e}^{-\beta E_n} \\
&\times \left[\frac{P^{nm}Q_1^{mk}Q_2^{kl}Q_3^{ln}}{(\omega_3-\omega_{ln})(\omega_3+\omega_2-\omega_{kl})(\omega-\omega_{mk})} - \frac{Q_1^{nm}P^{mk}Q_2^{kl}Q_3^{ln}}{(\omega_3-\omega_{ln})(\omega_3+\omega_2-\omega_{kl})(\omega-\omega_{nm})} \right. \\
&- \frac{Q_2^{nm}P^{mk}Q_1^{kl}Q_3^{ln}}{(\omega_3-\omega_{ln})(\omega_3+\omega_2-\omega_{nm})(\omega-\omega_{kl})} + \frac{Q_2^{nm}Q_1^{mk}P^{kl}Q_3^{ln}}{(\omega_3-\omega_{ln})(\omega_3+\omega_2-\omega_{nm})(\omega-\omega_{mk})} \\
&- \frac{Q_3^{nm}P^{mk}Q_1^{kl}Q_2^{ln}}{(\omega_3-\omega_{nm})(\omega_3+\omega_2-\omega_{ln})(\omega-\omega_{mk})} + \frac{Q_3^{nm}Q_1^{mk}P^{kl}Q_2^{ln}}{(\omega_3-\omega_{nm})(\omega_3+\omega_2-\omega_{ln})(\omega-\omega_{mk})} \\
&\left. + \frac{Q_3^{nm}Q_2^{mk}P^{kl}Q_1^{ln}}{(\omega_3-\omega_{nm})(\omega_3+\omega_2-\omega_{mk})(\omega-\omega_{ln})} - \frac{Q_3^{nm}Q_2^{mk}Q_1^{kl}P^{ln}}{(\omega_3-\omega_{nm})(\omega_3+\omega_2-\omega_{mk})(\omega-\omega_{kl})} \right],
\end{aligned} \tag{2.77}$$

where $\omega = \omega_1+\omega_2+\omega_3$. Clearly, the explicit formulas build up in a hierarchical manner and become rather complicated at higher orders. On the other hand, if the eigenstate basis and the matrix elements are accurate, the response of arbitrary degree can be calculated just by deriving the proper sum-over-state formulas. This will be briefly discussed in Sec. 3.2.3.

2.2.5 Additional properties of response functions

In the previous, we have summarized the fundamentals of general order linear response theory. Not all the properties will be used in this Thesis, but comprehensive references are hopefully useful for future endeavors. For this reason, let us briefly discuss a few additional properties of the response functions.

First, formulas for the higher order perturbations can be sensitive to definitions and assumptions. In the first order, the familiar zero Kelvin limit is reproduced by taking the limit $\beta \to \infty$. This is demonstrated in Publication IV and Sec. 3.2.3. In higher orders, linking the linear response framework at finite temperature to the time-dependent perturbation theory of pure states is neither straightforward nor relevant, which can be seen by studying different derivations in the literature, *e.g.* Refs. [7, 77, 79]. Another

particular feature is the treatment of symmetry: whether the higher-order interactions are distinguishable or not affects the way they are symmetrized. Using the symmetry properties one can reduce the number of terms involved in the explicit formulas.

Second, a typical way to enforce boundary conditions is to add a small imaginary factor to the exponential propagators. It then appears in the denominators of the spectral representations, Eqs. (2.75)-(2.77), and models phenomenological damping. The intuition of the damping is that the system eventually recovers its equilibrium state.

Third, the physical spectra are always bounded from above, which suggests a sum rule over the total spectral moment. If one is able to derive what is called an f-sum rule [79], it can be used to renormalize a spectrum that may otherwise be ill-behaving or incomplete.

2.3 Path integrals and imaginary time

The exact many-body density matrices are formidable to evaluate in any representation of the basis. However, it turns out that the so-called path integral formalism is well suited for describing the many-body correlation in thermal conditions. The name stems from the famous interpretation by Richard Feynman: a quantum particle traveling in space and time not only takes the shortest trajectory – the classical path of extremal action – but in fact goes through every path simultaneously within the limits of quantum uncertainty [75]. The path integral is the evaluation of this process. Integrating over infinite paths is obviously challenging in its own ways, but it also provides unique perspective and an interface for stochastic approximations.

First, let us derive the path integral formalism from the Schrödinger equation. However, it could be done the other way, too [80]; for the purposes of this Thesis, the two are equivalent descriptions of the quantum physics. We quickly proceed to so-called imaginary time, because it turns out to be a stable domain for numerical recipes and controllable approximations. Especially, we will consider the computation and analytic properties of the time-correlation functions in imaginary time.

2.3.1 Discrete path integral

The Feynman path integrals are based on a postulate, which states that the quantum-mechanical propagation amplitude is proportional to an integral of the exponential action [75]

$$\rho(R,R';t) = \int \mathrm{d}q(R,R';t)\,\mathrm{e}^{iS(R,R';t)/\hbar}, \tag{2.78}$$

where $\mathrm{d}q(R,R';t)$ is a differential of paths q with the given boundary conditions: from R to R' in time t. The classical action is

$$S(R,R';t) = \int_0^t \mathrm{d}\bar{t}\,L(q(\bar{t}),\dot{q}(\bar{t})), \tag{2.79}$$

where $L = \frac{1}{2}m\dot{q}^2 - V(q)$ is the Lagrangian function. The classical limit arises as $\hbar \to 0$, and only the paths with extremal action, *i.e.* the *classical trajectories*, persist. That is, the exact quantum propagation involves integral over all possible paths in the order of $\hbar$.

Generally, the quantum propagation amplitude can be equated with Eq. (2.6):

$$\rho(R,R';t) = \left\langle R \left| \mathrm{e}^{-it\hat{H}_0/\hbar} \right| R' \right\rangle = \left\langle R \left| \mathrm{e}^{-it(\hat{T}+\hat{V})/\hbar} \right| R' \right\rangle, \tag{2.80}$$

where we have distinguished the kinetic energy $\hat{T}$ and the potential energy $\hat{V}$. This is often reasonable, because the kinetic part is known analytically. Unfortunately, $\hat{T}$ and $\hat{V}$ do not generally commute. A usual way to separate the exponential is using the Trotter's formula [81, 82]

$$\mathrm{e}^{-it(\hat{T}+\hat{V})/\hbar} = \lim_{M\to\infty} \left[\mathrm{e}^{-i\Delta t\hat{T}/\hbar} \mathrm{e}^{-i\Delta t\hat{V}/\hbar} \right]^M. \tag{2.81}$$

The separation is exact at the limit of short time-step $\Delta t = t/M \to 0$, where M is the Trotter number. Thus, using Eq. (2.81), one can redefine the path integral in Eq. (2.78)

over a discrete path [75]:

$$\rho(R,R';t) = \lim_{M\to\infty} (4i\pi\lambda\Delta t)^{-dNM/2} \int \mathrm{d}R_1 \ldots \mathrm{d}R_{M-1} \times \exp\left[\frac{i\Delta t}{\hbar}\sum_{j=0}^{M-1}\left[-\frac{\hbar^2(R_{j+1}-R_j)^2}{4\lambda\Delta t} - \Delta t\, V(R_j)\right]\right], \tag{2.82}$$

where $\lambda = \hbar^2/2\pi m$, d is spatial dimensionality, and N is the number of distinguishable particles. To simplify the expression, we have assumed that the particles are distinguishable with the same mass, but the definition is straightforward to generalize, if necessary.

2.3.2 Imaginary-time propagator and thermal density matrix

The quantum real-time propagator with the exponential $i\hat{H}t$ is difficult to utilize in probabilistic schemes, because it is complex-valued and spuriously oscillating. On the other hand, analytic continuation to imaginary time $t - t' \to -i\hbar\tau$ makes for a much better behaving propagator

$$\hat{U}(t-t') \to \hat{U}_\tau(-i\hbar\tau) = \exp\left(-\tau\hat{H}\right), \tag{2.83}$$

which is always real and positive-semidefinite. A physical interpretation arises, when we choose $\tau = \hbar\beta = \hbar/k_B T$, *i.e.*, we associate the (unnormalized) thermal density operator with a retarded imaginary-time propagator

$$\hat{\rho}(\beta) = \theta(\beta)\exp\left(-\beta\hat{H}\right) \equiv U_\tau^R(\beta), \tag{2.84}$$

where $\theta(\beta)$ follows from $\beta > 0$ at finite temperature, $T > 0$. Similarly, we can define the Heisenberg picture for operators in the equilibrium as [76]

$$\hat{P}(\tau) \equiv \mathrm{e}^{\tau\hat{H}}\hat{P}\mathrm{e}^{-\tau\hat{H}} = \hat{\rho}(\tau)\hat{P}\hat{\rho}(-\tau) \tag{2.85}$$

where $0 \leq \tau \leq \beta$.

We can further rewrite the thermal propagator in the Trotter expansion:

$$\hat{\rho}(\beta) = \lim_{M\to\infty} \left(\mathrm{e}^{-\Delta\tau \hat{K}} \mathrm{e}^{-\Delta\tau \hat{V}} \right)^M, \tag{2.86}$$

where $\Delta\tau = \hbar\beta/M$. This is called the primitive approximation, and it is valid, when $\hat{K}$ and $\hat{V}$ are self-adjoint operators and bounded from below [82]. A controllable error in the order of $\mathcal{O}(\Delta\tau^2)$ arises, when one uses finite but sufficiently large M instead of $M \to \infty$, which is the exact limit.

Now, we can define the thermal partition function as a discrete imaginary-time path integral over closed paths, *i.e.* $R = R'$:

$$Z = \mathrm{Tr}[\hat{\rho}(\beta)] \tag{2.87}$$

$$= \lim_{M\to\infty} \int \mathrm{d}R_0 \ldots \mathrm{d}R_{M-1} \left\langle R_0 \left| \mathrm{e}^{-\Delta\tau \hat{K}} \mathrm{e}^{-\Delta\tau \hat{V}} \right| R_1 \right\rangle \ldots \left\langle R_{M-1} \left| \mathrm{e}^{-\Delta\tau \hat{K}} \mathrm{e}^{-\Delta\tau \hat{V}} \right| R_0 \right\rangle, \tag{2.88}$$

where it generally holds for potentials bounded from below [82] that

$$\left\langle R_i \left| \mathrm{e}^{-\Delta\tau \hat{K}} \mathrm{e}^{-\Delta\tau \hat{V}} \right| R_{i+1} \right\rangle = \rho^K(R_i, R_{i+1}; \Delta\tau) \mathrm{e}^{-\Delta\tau V(R_i)}, \tag{2.89}$$

since $\hat{V}$ is diagonal. The free-particle density matrix is

$$\rho^K\left(R_i, R_{i+1}; \Delta\tau\right) = (4\pi\lambda\Delta\tau)^{-dN/2} \exp\left[-\frac{(R_{i+1} - R_i)^2}{4\lambda\Delta\tau} \right], \tag{2.90}$$

which contains no many-body interactions by definition. The total action is then given by

$$S(R_i, R_{i-1}; \Delta\tau) = \frac{dN}{2} \ln(4\pi\lambda\Delta\tau) + \frac{(R_{i+1} - R_i)^2}{4\lambda\Delta\tau} + \Delta\tau V(R_i), \tag{2.91}$$

which reproduces the imaginary-time counterpart of the path integral in Eq. (2.82).

Pair approximation

In order to evaluate the potential action for a propagation between many-body configurations R and R', let us consider the pair approximation. That is, let us assume that the full interaction is a sum of pairwise interactions, *i.e.*

$$U(R,R';\Delta\tau)=\sum_{i>j}u\left(\mathbf{r}_i,\mathbf{r'}_i,\mathbf{r}_j,\mathbf{r'}_j,\Delta\tau\right), \tag{2.92}$$

and thus, the many-body density matrix is a product of pairwise density matrices:

$$\rho(R,R';\Delta\tau)\approx\prod_{i<j}\rho_{ij}\left(\mathbf{r}_i,\mathbf{r'}_i,\mathbf{r}_j,\mathbf{r'}_j,\Delta\tau\right), \tag{2.93}$$

where i and j refer to different particles and $\mathbf{r}$ to their coordinates. The pair approximation is motivated by the fact that all natural interactions, such as Coulomb forces are fundamentally pairwise. The pair approximation is also exact for a pair of particles, and in the limit $\Delta\tau\to 0$. Yet, a many-body error emerges from correlated propagations of three or more particles [72, 83].

2.3.3 Measurement over the discrete path

Measurement over the discrete imaginary-time path is straightforward, and it involves some important symmetry properties. First, the thermal expectation value of a static observable $\hat{P}$ is given by

$$\begin{aligned}\langle P\rangle &= \mathrm{Tr}\left[\hat{\rho}(\Delta\tau)^M\hat{P}\right] &(2.94)\\ &= Z^{-1}\int \mathrm{d}R_0\ldots\mathrm{d}R_{M-1}\langle R_0|\hat{\rho}(\Delta\tau)|R_1\rangle\ldots\langle R_{M-1}|\hat{\rho}(\Delta\tau)|R_0\rangle P(R_0) &(2.95)\\ &= Z^{-1}M^{-1}\sum_{m=1}^{M}\int \mathrm{d}R_0\ldots\mathrm{d}R_{M-1}\,\rho(R_0,R_1;\Delta\tau)\ldots\rho(R_{M-1},R_0;\Delta\tau)P(R_m), &(2.96)\end{aligned}$$

where the last line utilizes the symmetry properties of equilibrium. Thus, all the time-slices are equivalent, *i.e.* $\langle P(\tau)\rangle=\langle P(0)\rangle=\langle P\rangle$, and their average can be used to produce a more precise estimate of the measurement.

The Green's functions are also defined for imaginary-time arguments. An n-time correlator analogous to Eq. (2.44) is [76]

$$\hat{G}_n\left(\tau;\tau',\ldots,\tau^{(n)}\right)=\left(-\frac{1}{\hbar}\right)^n \mathscr{T}_\tau \hat{P}(\tau)\hat{Q}_1(\tau_1)\ldots\hat{Q}_n(\tau_n), \tag{2.97}$$

where $\mathscr{T}_\tau$ is time-ordering operator in imaginary time and $0\leq\tau\leq\hbar\beta$ must hold for $\tau,\tau'\ldots\tau^{(n)}$. The associated Green's function is

$$\begin{aligned} G_n\left(\tau;\tau',\ldots,\tau^{(n)}\right) &= Z^{-1}\left(-\frac{1}{\hbar}\right)^n \mathrm{Tr}\left[\mathscr{T}_\tau\hat{\rho}(\beta)\hat{P}(\tau)\hat{Q}_1\left(\tau'\right)\ldots\hat{Q}_n\left(\tau^{(n)}\right)\right] && (2.98)\\ &= Z^{-1}\left(-\frac{1}{\hbar}\right)^n \mathrm{Tr}\left[\mathscr{T}_\tau\hat{\rho}(\beta)\hat{P}\hat{Q}_1(-\tau_1)\ldots\hat{Q}_n(-(\tau_1+\ldots+\tau_n))\right] && (2.99)\\ &\equiv G_n(\tau_1,\ldots,\tau_n) && (2.100)\end{aligned}$$

where we have made a shift of $-\tau$ and defined $\tau_1=\tau-\tau'$, $\tau_2=\tau''-\tau'$, and so on. Moreover, we have imposed causal conditions, *i.e.* $\tau_1\ldots\tau_n\geq 0$ and also $\tau_1+\ldots\tau_n\leq\hbar\beta$. This is only necessary, if the interactions $\hat{P},\hat{Q}_1,\ldots,\hat{Q}_n$ are distinguishable.

The n-time Green's functions defined in Eq. (2.99) are diffusive and real-valued, as opposed to the complex and oscillating real-time correlators from Eq. (2.49). Let us incorporate the time-ordering and expansion to the discrete path:

$$\begin{aligned} G_n(\tau_1,\ldots,\tau_n) \equiv& Z^{-1}\theta(\tau_1)\ldots\theta(\tau_n)\mathrm{Tr}\left[\hat{\rho}(\beta)\hat{P}\hat{Q}_1(-\tau_1)\ldots\hat{Q}_n(-(\tau_1+\ldots+\tau_n))\right]\\ =& Z^{-1}\theta(\tau_1)\ldots\theta(\tau_n)\mathrm{Tr}\left[\hat{\rho}(\beta-(\tau_1+\ldots+\tau_n))\hat{P}\hat{\rho}(\tau_1)\hat{Q}_1\ldots\hat{\rho}(\tau_n)\hat{Q}\right].\\ =& Z^{-1}\int \mathrm{d}R_0\ldots\mathrm{d}R_{M-1}\rho(R_0,R_1;\Delta\tau)\ldots\rho(R_{M-1},R_0;\Delta\tau)\\ &\times P(R_p)Q_1(R_{q_1})\ldots Q_n(R_{q_n}) && (2.101)\\ =& Z^{-1}\int \mathrm{d}R_0\ldots\mathrm{d}R_{M-1}\rho(R_0,R_1;\Delta\tau)\ldots\rho(R_{M-1},R_0;\Delta\tau)\\ &\times M^{-1}\sum_{m=1}^{M} P(R_{m+p})Q_1(R_{m+q_1})\ldots Q_n(R_{m+q_n}) && (2.102)\end{aligned}$$

where $R_j=R_{j \bmod M}$, $q_n=0$, and $m,p,q_1,\ldots,q_{n-1}$ are nonnegative integers with $p+\sum_n q_n\leq M$. The indexing may appear complicated until it is implemented in a tractable algorithm for measuring the sample trajectory R.

The imaginary-time correlation function is defined in terms of the n-time correlator

$$\hat{C}_n(\tau,\tau',\ldots,\tau^{(n)}) = \mathscr{T}_\tau \hat{P}(\tau)\hat{Q}_1(\tau')\ldots\hat{Q}_n(\tau^{(n)}), \tag{2.103}$$

and the associated n-time correlation function is

$$C_n(\tau_1,\ldots,\tau_n) = \left\langle \hat{C}_n(\tau,\tau',\ldots,\tau^{(n)}) \right\rangle, \tag{2.104}$$

whose connection to the Green's function is simply

$$C_n(\tau_1,\ldots,\tau_n) = \hbar^n G_n(\tau_1,\ldots,\tau_n), \tag{2.105}$$

which also inherits the causality of G_n.

2.3.4 Fourier transform and imaginary time

Imaginary-time Green's functions are only defined for time-arguments between 0 and $\hbar\beta$. However, the symmetry property $G_n(\ldots,\tau+\beta,\ldots) = \pm G_n(\ldots,\tau,\ldots)$ applies to each of the arguments, where plus and minus refer to bosonic and fermionic correlators, respectively. As a consequence of this (anti)symmetry, the Fourier transform is given by

$$G_1(i\omega_n) = \mathscr{F}_\beta G_1(\tau) \equiv \int_0^{\hbar\beta} \mathrm{d}\tau\, \mathrm{e}^{-i\tau\omega_n} G_1(\tau), \tag{2.106}$$

where $i\omega_n$ are discrete *Matsubara frequencies* given by

$$\omega_n = \frac{2\pi}{\beta\hbar} n \qquad \text{bosons}$$

$$\omega_n = \frac{2\pi}{\beta\hbar}(n+\tfrac{1}{2}) \qquad \text{fermions}$$

where n is an integer. In this Thesis, we will only consider correlators that obey the bosonic distribution. Without going into details, this follows from the fact that the representation of the measurement operators in the framework of second quantization is even in terms of creation and annihilation operators.

2.3.5 Analytic properties and the spectral function

So far we have considered Green's functions in terms of arguments that are either strictly real or imaginary. However, the causal or retarded Green's function is analytic for any argument in the upper complex plane, $\mathrm{Im}[z] \geq 0$. This is a well-known and important isomorphism: causality in the real time implies correlation in the imaginary time [84].

A useful consequence of the analytic property is the Kramers–Kronig relation [6]:

$$G_1^R(\omega) = \mathscr{P} \int_{-\infty}^{\infty} \frac{\mathrm{d}\omega'}{i\pi} \frac{G_1^R(\omega')}{\omega' - \omega},$$

where $\mathscr{P}$ denotes Cauchy principal value. A practical implementation of the Cauchy Principal value is [73]

$$G_1^R(\omega) = \int_{-\infty}^{\infty} \frac{\mathrm{d}\omega'}{\pi} \frac{\mathrm{Im}[G_1^R(\omega')]}{\omega' - \omega - i\eta} \tag{2.107}$$

where η is a positive infinitesimal. Now, let us define the *spectral function*:

$$A(\omega) = i\left[G_1^>(\omega) - G_1^<(\omega)\right] = i\left[G_1^R(\omega) - G_1^A(\omega)\right] = -2\mathrm{Im}[G_1^R(\omega)], \tag{2.108}$$

which follows from the fact that $G_1^R = \left(G_1^A\right)^\dagger$. Equations (2.107) and (2.108) lead to

$$G_1^R(\omega) = -\int_{-\infty}^{\infty} \frac{\mathrm{d}\omega'}{2\pi} \frac{A(\omega')}{\omega' - \omega - i\eta}. \tag{2.109}$$

The important physical relevance of the spectral function is related to the absorptive properties associated with the perturbation, and it will be discussed in more detail later.

The definition Eq. (2.109) can be extended to imaginary arguments, which gives [73]

$$G_1(i\omega_n) = \int_{-\infty}^{\infty} \frac{\mathrm{d}\omega'}{2\pi} \frac{A(\omega')}{i\omega_n - \omega'}, \tag{2.110}$$

where causality of the imaginary-domain correlation function is implicit, and the infinitesimal η can be neglected. Using the properties of Matsubara frequencies and Fourier

series, an equivalent definition in the imaginary-time domain is [73]

$$G_1(\tau) = \int_{-\infty}^{\infty} \frac{\mathrm{d}\omega'}{2\pi} \frac{\mathrm{e}^{-\tau\omega'}}{1 \pm \mathrm{e}^{-\beta\omega'}} A(\omega'). \tag{2.111}$$

That is, the real-frequency spectrum $A(\omega)$ can be mapped to imaginary time. Unfortunately, the inverse mappings from $G_1(\tau)$ or $G_1(i\omega_n)$ to $A(\omega)$ are ill-posed numerical problems.

Alternatively, the mapping between real- and imaginary-time correlation functions is called the Kubo transform [85]. It is given in the first order by

$$G_1(t) = \int_0^{\hbar\beta} \mathrm{d}\tau \left\langle \left[\hat{Q}(-\tau), \hat{H}_0 \right] \hat{P}(t) \right\rangle. \tag{2.112}$$

The Kubo transform is useful for approaches that utilize complex propagators. It is used in centroid molecular dynamics (CMD) also in higher orders [86, 87], but such approaches will not be pursued in this Thesis.

3 ELECTRIC FIELD RESPONSE

It is time to focus on the response to a specific perturbation: external electric field. The electric field is one of the fundamental interactions in the standard model, and, as already noted, central to numerous physical phenomena. Interaction with a finite electric field is formally a difficult out-of-equilibrium problem. However, it is quite tractable and even straighforward to consider within the framework of linear response theory. Thus, we shall start by briefly discussing the virtues and limitations of the perturbative approach.

However, the main purpose of this chapter is to introduce and define the concept of multipole polarizability. The standard way to define polarizability arises from the multipole expansion of electric moments: it is in essence a multipole–multipole susceptibility. The multipole expansion is a common and practical way to treat localized quantum systems, such as atoms and small molecules. This is exactly the scope of this Thesis, and thus, the multipole polarizability remains the standard unit of electric field response from this point on.

The chapter is rather a glossary of labels and definitions related to polarizability. There are different combinations of multipoles, computation strategies, and various consequences of symmetry and thermal averaging. The reader is not expected to memorize all the different combinations, but rather refer back to this chapter in order to understand the results and developments to come.

3.1 Electric field perturbation

In real-space, a general field-interaction is given in the form of Eq. (2.59). Let us assume that a perturbing electric field is spatially invariant within the size scale of atoms and small molecules, *i.e.* $\mathbf{F}(R) = \mathbf{F}$. Thus, the interaction for a given configuration R can be

conveniently encoded in terms of electric multipole moments [88]:

$$h(R) = -\sum_{n=0}^{\infty} \frac{2^n n!}{(2n)!} \left[\mathbf{Q}^{(n)}(R)\right](n)\left[\nabla^n \mathbf{F}\right], \tag{3.1}$$

where $\mathbf{Q}^{(n)}(R)$ is the nth electric moment and ∇ is the gradient operator. The terms are vector or tensor fields, and the (n)-product means an element-wise inner product. In the following, it will be treated using the Einstein notation, *i.e.* $\mu_\alpha F_\alpha \equiv \mu_x F_x + \mu_y F_y + \mu_z F_z$, and so on. The first four elements of the series are thus

$$h(R) = -q\phi - \mu_\alpha(R) F_\alpha - \frac{1}{3}\Theta_{\alpha\beta}(R) F_{\alpha\beta} - \frac{1}{15}\Omega_{\alpha\beta\gamma}(R) F_{\alpha\beta\gamma} - \ldots, \tag{3.2}$$

where q is the net charge, and μ, Θ and Ω are the dipole, quadrupole and octupole moments, respectively. Similarly, ϕ is the electrostatic potential, which is usually chosen to be zero. F_α is a homogeneous field and $F_{\alpha\beta\ldots}$ denote field-gradient components, *e.g.* $F_{\alpha\beta} \equiv \frac{\partial}{\partial\beta} F_\alpha$. As argued earlier, all the field components are independent of R. Assuming a discrete set of point charges q^i at positions r^i, traceless forms of the four first moments are calculated as

$$q(R) = \sum_i q^i(\mathbf{r}_i) = q \tag{3.3}$$

$$\mu_\alpha(R) = \sum_i r^i_\alpha q^i(R) \tag{3.4}$$

$$\Theta_{\alpha\beta} = \sum_i \tfrac{q^i}{3}\left(3 r^i_\alpha r^i_\beta - \delta_{\alpha\beta} r^2\right) \tag{3.5}$$

$$\Omega_{\alpha\beta\gamma} = \sum_i \tfrac{q^i}{2}\left(5 r^i_\alpha r^i_\beta r^i_\gamma - r^2\left(r^i_\alpha \delta_{\beta\gamma} + r^i_\beta \delta_{\alpha\gamma} + r^i_\gamma \delta_{\alpha\beta}\right)\right), \tag{3.6}$$

where $r = (r_x^2 + r_y^2 + r_z^2)$ and $\delta_{\alpha\beta}$ is the Kronecker delta. The choice of origin is important, because it affects the magnitudes of all the higher moments beyond the first non-zero moment. The standard choice is the center-of-mass, or in case of fixed-nuclei simulations, the center-of-mass of the nuclei.

Let us consider the time-dependence of the field. The physical field is required to be Hermitian and solve the classical wave-equation. In fact, any such field can be superposed

out of standing harmonic waves of the form [89]

$$F(\mathbf{r},t) = F(\mathbf{r})\left[\mathrm{e}^{i\omega t} + \mathrm{e}^{-i\omega t}\right]/2. \tag{3.7}$$

Thus, the spectrum of the actual perturbation can be arbitrary, but for convenience we will characterize it in terms of the harmonic frequency ω. When $\omega \to 0$, the field is *static* and it is denoted F, *i.e.*, without the ω-argument.

Last, let us briefly acknowledge the main limitations of our approach. In this Thesis, we only consider perturbations due to weak electric fields, since the linear response theory diverges in strong perturbations. We also assume that in absorptive processes there are no cascade effects or meaningful occupations of the excited states [7]. This is generally a safe assumption in atomic and molecular problems. Furthermore, the field is treated as semiclassical, as opposed to quantized field, while the latter is more rigorous in describing absorption. More comprehensive models include Hopfield dielectric [90] or similar frameworks involving quantum electrodynamics [91] and path integrals [92].

3.2 Multipole polarizability

The dynamic response properties that are defined in terms of Eq. (3.2) are called multipole polarizabilities or simply polarizabilities. The polarizabilities are tensorial properties, whose magnitude maps particular perturbations to induced electric moments, such as those in Eqs. (3.4)–(3.6). Generally, many different definitions exist for the multipole polarizabilities, some of which have emerged more popular than others. In the following, we are not trying to give an exhaustive display, but rather define the polarizabilities as they are used and labeled throughout this Thesis.

3.2.1 Foundations and common notation

In the static limit, one often uses the Buckingham notation [8]. Expressions for the induced dipole, quadrupole and octupole moments are respectively the following:

$$\begin{aligned}\mu_\alpha^{(1)} =& \mu_\alpha^{(0)} + \alpha_{\alpha,\beta}F_\beta + \tfrac{1}{2}\beta_{\alpha,\beta,\gamma}F_\beta F_\gamma + \tfrac{1}{6}\gamma_{\alpha,\beta,\gamma,\delta}F_\beta F_\gamma F_\delta \\ &+ \tfrac{1}{3}A_{\alpha,\beta\gamma}F_{\beta\gamma} + \tfrac{1}{3}B_{\alpha,\beta,\gamma\delta}F_\beta F_{\gamma\delta} + \tfrac{1}{15}E_{\alpha,\beta\gamma\delta}F_{\beta\gamma\delta} + \dots \end{aligned} \tag{3.8}$$

$$\Theta_{\alpha\beta}^{(1)} = \Theta^{(0)} + A_{\alpha\beta,\gamma}F_\gamma + C_{\alpha\beta,\gamma\delta}F_{\gamma\delta} + \tfrac{1}{2}B_{\gamma,\delta,\alpha\beta}F_\gamma F_\delta + \dots \tag{3.9}$$

$$\Omega_{\alpha\beta\gamma}^{(1)} = \Omega^{(0)} + E_{\alpha\beta\gamma,\delta}F_\delta + G_{\alpha\beta\gamma,\delta\epsilon\zeta}F_{\delta\epsilon\zeta} + \dots \tag{3.10}$$

where $^{(0)}$ denotes a permanent moment. Other symbols denote different multipole polarizabilities, whose common nomenclature is found in Table 3.1. The effects of induced multipole moments affect the total energy, too. The Stark energy shift can be written in the static limit as [8, 93]

$$\begin{aligned}E^{(1)} =& E^{(0)} - \mu_\alpha^{(0)}F_\alpha - \tfrac{1}{2}\alpha_{\alpha,\beta}F_\alpha F_\beta - \tfrac{1}{6}\beta_{\alpha,\beta,\gamma}F_\alpha F_\beta F_\gamma - \tfrac{1}{24}\gamma_{\alpha,\beta,\gamma,\delta}F_\alpha F_\beta F_\gamma F_\delta \\ &- \tfrac{1}{3}\Theta_{\alpha\beta}^{(0)}F_{\alpha\beta} - \tfrac{1}{3}A_{\alpha,\alpha\beta}F_\alpha F_{\beta\gamma} - \tfrac{1}{6}B_{\alpha,\beta,\gamma\delta}F_\alpha F_\beta F_{\gamma\delta} - \tfrac{1}{15}E_{\alpha,\beta\gamma\delta}F_\alpha F_{\beta\gamma\delta} \\ &- \tfrac{1}{6}C_{\alpha\beta,\gamma\delta}F_{\alpha\beta}F_{\gamma\delta} - \tfrac{1}{15}\Omega_{\alpha\beta\gamma}^{(0)}F_{\alpha\beta\gamma} - \tfrac{1}{30}G_{\alpha\beta\gamma,\delta\epsilon\mu}F_{\alpha\beta\gamma}F_{\delta\epsilon\mu} - \dots \end{aligned} \tag{3.11}$$

Appending the series to arbitrary degrees is very systematic. Main reason for the given truncation is that the interaction beyond the aforementioned terms is usually weak and scarcely covered in the literature.

The dynamic polarizabilities are usually defined in terms of the generalized susceptibilities. Essentially, they can be produced by populating Eqs. (2.75)–(2.77) with combinations of the multipole operators $\hat{\mu}$, $\hat{\Theta}$, $\hat{\Omega}$. Most studies, including this Thesis, only consider first-order correlators that are also symmetric, *i.e.*, $\hat{P} = \hat{Q}$. The resulting polarizabilities are denoted $\alpha_1(\omega)$ for dipoles, $\alpha_2(\omega)$ for quadrupoles, $\alpha_3(\omega)$ for octupoles, and so on. We will omit the tensorial notation for convenience. One should note that using this definition, the static properties are related to the corresponding dynamic properties by $\alpha_1(0) = \alpha$, $\alpha_2(0) = 3C$ and $\alpha_3(0) = 15G$.

Table 3.1 Names and definitions of the most common static multipole polarizabilities.

Polarizability	Symbol	Operators	Definition
Dipole	$\alpha_{\alpha,\beta}$	$\hat{\mu}_\alpha, \hat{\mu}_\beta$	$\frac{\partial}{\partial F_\beta}\langle\mu_\alpha\rangle$
First hyper-	$\beta_{\alpha\beta\gamma}$	$\hat{\mu}_\alpha, \hat{\mu}_\beta, \hat{\mu}_\gamma$	$\frac{\partial}{\partial F_\beta}\frac{\partial}{\partial F_\gamma}\langle\mu_\alpha\rangle$
Second hyper-	$\gamma_{\alpha,\beta,\gamma,\delta}$	$\hat{\mu}_\alpha, \hat{\mu}_\beta, \hat{\mu}_\gamma, \hat{\mu}_\delta$	$\frac{\partial}{\partial F_\beta}\frac{\partial}{\partial F_\gamma}\frac{\partial}{\partial F_\delta}\langle\mu_\alpha\rangle$
Dipole–quadrupole	$A_{\alpha,\beta\gamma}$	$\hat{\mu}_\alpha, \hat{\Theta}_{\beta\gamma}$	$\frac{\partial}{\partial F_{\beta\gamma}}\langle\mu_\alpha\rangle$
Dipole–dipole–quadrupole	$B_{\alpha,\beta,\gamma\delta}$	$\hat{\mu}_\alpha, \hat{\mu}_\beta, \hat{\Theta}_{\gamma\delta}$	$\frac{\partial}{\partial F_\beta}\frac{\partial}{\partial F_{\gamma\delta}}\langle\mu_\alpha\rangle$
Quadrupole–quadrupole	$C_{\alpha\beta,\gamma\delta}$	$\hat{\Theta}_{\alpha\beta}, \hat{\Theta}_{\gamma\delta}$	$\frac{\partial}{\partial F_{\gamma\delta}}\langle\Theta_{\alpha\beta}\rangle$
Octupole–octupole	$G_{\alpha\beta\gamma,\delta\epsilon\zeta}$	$\hat{\Omega}_{\alpha\beta\gamma}, \hat{\Omega}_{\delta\epsilon\zeta}$	$\frac{\partial}{\partial F_{\delta\epsilon\zeta}}\langle\Omega_{\alpha\beta\gamma}\rangle$
Dipole–octupole	$E_{\alpha,\beta\gamma\delta}$	$\hat{\mu}_\alpha, \hat{\Omega}_{\beta\gamma\delta}$	$\frac{\partial}{\partial F_{\beta\gamma\delta}}\langle\mu_\alpha\rangle$

3.2.2 Correlation functions

The response property is by definition a measurement of induced polarization: Based on Eqs. (2.55) and (2.68) the polarizability is readily obtained from correlation functions. For instance, the first-order multipole–multipole polarizability can be presented in alternative forms as

$$\alpha(\omega) = \chi^{(1)}(\omega) = -\mathscr{F} G_1^R(t_1) = \frac{i}{\hbar}\mathscr{F} C_1^R(t_1) \tag{3.12}$$

where the functions are defined in terms of electric multipole operators. The retarded correlation functions at arbitrary orders, $C_n^R(t_1,\ldots,t_n)$, are most easily obtained from real-time simulations. In that case, the polarizability is given by a simple Fourier transform, as shown in Eq. (2.74). The numerical transformation is straightforward, but the time-dependent simulation is not: the real-time propagator $\hat{U}(t) = \exp(-i\hat{H}t/\hbar)$ is complex and oscillatory in the coordinate basis. This is a problem for stochastic methods that rely on positive-semidefinite probability amplitudes [94, 95]. In 0 Kelvin, the Fourier transform requires an infinite time, in principle, yet in thermal conditions the real-time correlation eventually dissipates back to the equilibrium and the simulation can be truncated. For instance PIMD has been successful in capturing quantum effects in real-time thermal simulations [64, 96]. However, we shall not consider the real-time

propagation or popular real-time methods more deeply in this work.

However, the equilibrium response properties are also contained in the imaginary-time correlation. Based on Eqs. (2.99) and (2.105) the first-order polarizability in the imaginary domain can be expressed as

$$\alpha(i\omega_n) = \chi^{(1)}(i\omega_n) = \mathscr{F}_\beta G_1(\tau_1) = \frac{1}{\hbar}\mathscr{F}_\beta C_1(\tau_1), \tag{3.13}$$

where $\omega_n = \frac{2\pi n}{\beta}$ are the bosonic Matsubara frequencies. The real- and imaginary-time polarizabilities coincide at the static limit, *i.e.* $i\omega_n = \omega = 0$. The causal response properties are analytic [84], and thus, the real-time response properties can be obtained by using suitable integral transformations.

Especially, the 1-time Green's functions produce the associated spectral functions, if Eqs. (2.110) or (2.111) are inverted. The inversion is an infamous numerical problem, which is discussed more in Sec. 6.3.1 and Appendix A. Based on Eq. (2.109), the polarizability can also be expressed in terms of the spectral function:

$$\alpha(\omega) = \int_{-\infty}^{\infty} \frac{\mathrm{d}\omega'}{\pi} \frac{A(\omega')}{\omega' - \omega - i\eta}, \tag{3.14}$$

where ω' is a real frequency variable and η is a real positive infinitesimal. Equation (3.14) gives away some general properties of the dynamic polarizability. Since $A(\omega)$ is positive-semidefinite, $\alpha(\omega)$ must be complex-valued. The real part dominates at off-resonant frequencies, giving the dielectric response in terms of virtual excitations. This is the *dispersive* or non-absorptive picture of polarizability: the magnitude of induced electric moment. The imaginary part emerges straight from the spectrum and is indeed related to the absorption and emission of a particular kind of radiation.

3.2.3 Sum-over-states definition

The sum-over-states (SOS) definitions of polarizability follow, when electric multipole operators defined in Eqs. (2.75)–(2.77) are correlated in the eigenstate basis $|n\rangle$. For

example, the dynamic dipole polarizability is defined by

$$\alpha_{\alpha,\beta}(\omega) = Z^{-1} \sum_{n \neq m} \mathrm{e}^{-\beta E_n/\hbar} \left[\frac{\langle n|\hat{\mu}_\alpha|m\rangle\langle m|\hat{\mu}_\beta|n\rangle}{\omega - \omega_{nm}} + \frac{\langle n|\hat{\mu}_\beta|m\rangle\langle m|\hat{\mu}_\alpha|n\rangle}{\omega + \omega_{nm}} \right]. \quad (3.15)$$

The first term is the so-called resonant polarizability, which peaks at positive frequencies corresponding to the eigenenergies. The second term is the anti-resonant polarizability, which is purely dispersive. Usually, the incident waves are Hermitian, and thus, they consist of positive and negative frequencies symmetrically. In the 0 Kelvin limit, $\beta \to \infty$, we recover a familiar definition

$$\begin{aligned} \alpha_{\alpha,\beta}(\omega) = \sum_m & \frac{\left\langle 0 \left| \hat{\mu}_\alpha - \mu_\alpha^{(0)} \right| m \right\rangle \left\langle m \left| \hat{\mu}_\beta - \mu_\beta^{(0)} \right| 0 \right\rangle}{\omega - \omega_{0m}} \\ & + \frac{\left\langle 0 \left| \hat{\mu}_\beta - \mu_\beta^{(0)} \right| m \right\rangle \left\langle m \left| \hat{\mu}_\alpha - \mu_\alpha^{(0)} \right| 0 \right\rangle}{\omega + \omega_{0m}} \end{aligned} \quad (3.16)$$

where ω_{0m} is transition energy to the ground state. We refrain from displaying the higher-order formulas for polarizabilities, but they can be found elsewhere, *e.g.* Refs. [7, 77].

Instead, let us briefly review the main features of the SOS approach. As the name suggests, the formulas involve sums over energy eigenstates, whose number is, in principle, infinite. In practice, the summation must be truncated, and the main contribution often comes from the few lowest energy eigenstates [16, 97, 98]. As the system grows, solving for the many-body eigenstates becomes increasingly difficult or approximate. The SOS approach is relatively stable for low-ω response, but the near-resonant regions and the continuum (*i.e.* continuous spectrum beyond the first dissociation energy) are very sensitive to the exact spectral properties. A phenomenological way to deal with the resonant divergences is to introduce a complex denominator $\omega_{nm} \to \omega_{nm} + i\Gamma/2$. If Γ is the natural line width, this models the natural spectral broadening. In higher-order denominators, there are also secular divergences, which must be dealt with by other means [7].

3.2.4 Static field-derivative polarizability

The so-called field-derivative approach stems from identifying

$$\chi = \lim_{\mathbf{F}\to 0} \frac{\partial}{\partial F}\langle P\rangle, \tag{3.17}$$

where χ denotes an arbitrary polarizability associated with P and responding to F. Equation (3.17) or its higher-order variations can be readily generalized to extract specific polarizabilities from Eqs. (3.8)–(3.11). For instance,

$$\alpha_{\alpha\beta} = -2\frac{\partial}{\partial F_\alpha}\frac{\partial}{\partial F_\beta}\langle E\rangle = \frac{\partial}{\partial F_\beta}\langle \mu_\alpha\rangle.$$

Field-derivative definitions for the rest of the static polarizabilities are presented in Table 3.1. The estimators thus produced are original contributions of this Thesis, so they are presented in the following in ample detail.

The idea is to perform the differentiation analytically, and thus obtain an estimator for the equilibrium. Let us consider a perturbed density operator

$$\hat{\rho}^F(\beta) = \mathrm{e}^{-\hat{S}^F(\beta)/\hbar}$$

where

$$\hat{S}^F(\beta) = \beta\hat{H} = \beta\hat{H}_0 - \beta\hat{Q}_\alpha F_\alpha \tag{3.18}$$

is the imaginary-time action operator perturbed by the static field. Now, taking the

derivative of the perturbed expectation value of P_α is given by Eq. (2.36) as

$$\begin{aligned}
\chi_{\alpha,\beta} &= \frac{\partial}{\partial F_\beta}\langle P_\alpha\rangle \\
&= \frac{\partial}{\partial F_\beta}\frac{\mathrm{Tr}\left[\mathrm{e}^{-S^F(\beta)/\hbar}\hat{P}_\alpha\right]}{\mathrm{Tr}\left[\mathrm{e}^{-S^F(\beta)/\hbar}\right]} \\
&= \frac{\mathrm{Tr}\left[\left(\frac{\partial}{\partial F_\beta}\hat{\rho}^F(\beta)\right)\hat{P}_\alpha\right]}{Z} - \frac{\mathrm{Tr}\left[\left(\frac{\partial}{\partial F_\beta}\hat{\rho}^F(\beta)\right)\right]\mathrm{Tr}\left[\hat{\rho}^F(\beta)\hat{P}_\alpha\right]}{Z^2} \\
&= -\frac{\mathrm{Tr}\left[\hat{\rho}^F(\beta)\left(\frac{\partial S^F(\beta)}{\partial F_\beta}\right)\hat{P}_\alpha\right]}{Z} + \frac{\mathrm{Tr}\left[\hat{\rho}^F(\beta)\left(\frac{\partial S^F(\beta)}{\partial F_\beta}\right)\right]\mathrm{Tr}\left[\hat{\rho}^F(\beta)\hat{P}_\alpha\right]}{Z^2}.
\end{aligned} \tag{3.19}$$

Furthermore, let us consider the short time-step expansion of the density operator, Eq. (2.86). The total field-derivative is the sum over all time-slices

$$\begin{aligned}
\tfrac{\partial}{\partial F_\beta}\hat{\rho}^F(\beta) &= \tfrac{\partial}{\partial F_\beta}\left(\hat{\rho}^F(\Delta\tau)\right)^M \\
&= \sum_{i=1}^{M}\left(\hat{\rho}^F(\Delta\tau)\right)^i\left(-\tfrac{\partial S^F(\Delta\tau)}{\partial F_\beta}\right)\left(\hat{\rho}^F(\Delta\tau)\right)^{M-i} \\
&= \sum_{i=1}^{M}\left(\hat{\rho}^F(\Delta\tau)\right)^i\left(\Delta\tau\hat{\mathrm{Q}}_\beta\right)\left(\hat{\rho}^F(\Delta\tau)\right)^{M-i} \\
&\equiv \hbar\beta\hat{Q}_\beta^{\delta\tau},
\end{aligned} \tag{3.20}$$

where we denote by $\partial\tau$ the sample average over differential time-slices. Next, we take the limit $F \to 0$, which has the following consequences:

$$\lim_{\mathrm{F}\to 0}\begin{cases}\hat{H}(F) & = \hat{H}_0 \\ \rho^F(\beta) & = \rho(\beta)\end{cases}. \tag{3.21}$$

Combining Eqs. (3.19), (3.20) and (3.21), we conclude that

$$\chi_{\alpha,\beta} = \hbar\beta\left[\langle P_\alpha Q_\beta^{\partial\tau}\rangle - \langle P_\alpha\rangle\langle Q_\beta^{\partial\tau}\rangle\right], \tag{3.22}$$

where the sample average over time-slices is indeed

$$Q_\beta^{\partial\tau}(R) = \Delta\tau \sum_{m=0}^{M-1} Q_\beta(R_m). \tag{3.23}$$

At the limit $M \to \infty$, the operator $\hat{Q}$ is to be integrated over the imaginary-time trajectory from 0 to $\hbar\beta$. The second term in Eq. (3.22) arises from the fact that the normal ordering of observables, *i.e.* $\langle P\rangle_0 = \langle Q\rangle_0 = 0$, was never enforced in this definition.

Using the symmetry property Eq. (2.96), similar averaging can be utilized with P, so that Eq. (3.22) can be conveniently written as

$$\chi_{\alpha,\beta} = \hbar\beta\Big[\Big\langle \hat{P}_\alpha^{\partial\tau}\hat{Q}_\beta^{\partial\tau}\Big\rangle - \Big\langle \hat{P}_\alpha^{\partial\tau}\Big\rangle\Big\langle \hat{Q}_\beta^{\partial\tau}\Big\rangle\Big]. \tag{3.24}$$

Higher-order expressions can be worked out systematically, for instance

$$\begin{aligned}
\chi_{\alpha,\beta,\gamma} =& \tfrac{\partial}{\partial F_\gamma}\tfrac{\partial}{\partial F_\beta} P_\alpha \\
=& \tfrac{\partial}{\partial F_\gamma}\chi_{\alpha,\beta} \\
=& \tfrac{\partial}{\partial F_\gamma}\beta\Big[\langle \hat{P}_\alpha^{\partial\tau}\hat{Q}_\beta^{\partial\tau}\rangle - \langle \hat{P}_\alpha^{\partial\tau}\rangle\langle \hat{Q}_\beta^{\partial\tau}\rangle\Big] \\
=& (\hbar\beta)^2\Big[\langle \hat{P}_\alpha^{\partial\tau}\hat{Q}_\beta^{\partial\tau}\hat{Q}_\gamma^{\partial\tau}\rangle + 2\langle \hat{P}_\alpha^{\partial\tau}\rangle\langle \hat{Q}_\beta^{\partial\tau}\rangle\langle \hat{Q}_\gamma^{\partial\tau}\rangle \\
& -\langle \hat{P}_\alpha^{\partial\tau}\hat{Q}_\gamma^{\partial\tau}\rangle\langle \hat{Q}_\beta^{\partial\tau}\rangle - \langle \hat{P}_\alpha^{\partial\tau}\hat{Q}_\beta^{\partial\tau}\rangle\langle \hat{Q}_\gamma^{\partial\tau}\rangle - \langle \hat{P}_\alpha^{\partial\tau}\rangle\langle \hat{Q}_\beta^{\partial\tau}\hat{Q}_\gamma^{\partial\tau}\rangle\Big],
\end{aligned}$$

and so on. Static field-derivative estimators of the most important polarizabilities can be found in Table 3.2.

Finally, let us consider the basis dependence of the field-derivatives. While computing the trace in some incomplete basis $|\tilde{R}\rangle$, we end up differentiating terms of the form

$$\tfrac{\partial}{\partial F}\Big\langle \tilde{R}\Big|\hat{\rho}^F\Big|\tilde{R}\Big\rangle = \Big(\tfrac{\partial}{\partial F}\Big\langle \tilde{R}\Big|\Big)\hat{\rho}^F\Big|\tilde{R}\Big\rangle + \Big\langle \tilde{R}\Big|\Big(\tfrac{\partial}{\partial F}\hat{\rho}^F\Big)\Big|\tilde{R}\Big\rangle + \Big\langle \tilde{R}\Big|\hat{\rho}^F\Big(\tfrac{\partial}{\partial F}\Big|\tilde{R}\Big\rangle\Big). \tag{3.25}$$

The formulas found in Table 3.2 only consider the middle term and regard the rest as zero: the basis has no field-dependence. This is analogous to the Hellman–Feynman theorem [99]. It holds true for complete and variational bases, such as the real-space $|R\rangle$, which is mostly used in quantum Monte Carlo. On the other hand, truncated bases require corrections for the left and right-hand side terms of Eq. (3.25). These are

Table 3.2 Field-derivative estimators for the most common static multipole polarizabilities from Publications II and III. All the multipole operators measure the sample average, although the notation with $^{\partial\tau}$ is omitted for convenience. The names and definitions are found in Table 3.1.

Polarizability	Formula
$\alpha_{\alpha,\beta}$	$\hbar\beta\Big[\langle\mu_\alpha\mu_\beta\rangle-\langle\mu_\alpha\rangle\langle\mu_\beta\rangle\Big]$
$\beta_{\alpha,\beta,\gamma}$	$(\hbar\beta)^2\left[\langle\mu_\alpha\mu_\beta\mu_\gamma\rangle+2\langle\mu_\alpha\rangle\langle\mu_\beta\rangle\langle\mu_\gamma\rangle-\sum_{\alpha\beta,\gamma}\langle\mu_\alpha\mu_\beta\rangle\langle\mu_\gamma\rangle\right]$
$\gamma_{\alpha,\beta,\gamma,\delta}$	$(\hbar\beta)^3\Big[\langle\mu_\alpha\mu_\beta\mu_\gamma\mu_\delta\rangle-6\langle\mu_\alpha\rangle\langle\mu_\beta\rangle\langle\mu_\gamma\rangle\langle\mu_\delta\rangle-\sum_{\alpha\beta\gamma,\delta}\langle\mu_\alpha\mu_\beta\mu_\gamma\rangle\langle\mu_\delta\rangle-\sum_{\alpha\beta,\gamma\delta}\langle\mu_\alpha\mu_\beta\rangle\langle\mu_\gamma\mu_\delta\rangle+2\sum_{\alpha\beta,\gamma,\delta}\langle\mu_\alpha\mu_\beta\rangle\langle\mu_\gamma\rangle\langle\mu_\delta\rangle\Big]$
$A_{\alpha,\beta\gamma}$	$\hbar\beta\Big[\langle\Theta_{\alpha\beta}\mu_\gamma\rangle-\langle\Theta_{\alpha\beta}\rangle\langle\mu_\gamma\rangle\Big]$
$B_{\alpha,\beta,\gamma\delta}$	$(\hbar\beta)^2\Big[\langle\Theta_{\alpha\beta}\mu_\gamma\mu_\delta\rangle+2\langle\Theta_{\alpha\beta}\rangle\langle\mu_\gamma\rangle\langle\mu_\delta\rangle-\langle\Theta_{\alpha\beta}\mu_\gamma\rangle\langle\mu_\delta\rangle-\langle\Theta_{\alpha\beta}\mu_\delta\rangle\langle\mu_\gamma\rangle\Big]$
$C_{\alpha\beta,\gamma\delta}$	$\frac{\hbar\beta}{3}\Big[\langle\Theta_{\alpha\beta}\Theta_{\gamma\delta}\rangle-\langle\Theta_{\alpha\beta}\rangle\langle\Theta_{\gamma\delta}\rangle\Big]$
$E_{\alpha,\beta\gamma\delta}$	$\hbar\beta[\langle\mu_\alpha\Omega_{\beta,\gamma,\delta}\rangle-\langle\mu_\alpha\rangle\langle\Omega_{\beta,\gamma,\delta}\rangle]$
$G_{\alpha\beta\gamma,\delta\epsilon\zeta}$	$\frac{\hbar\beta}{15}[\langle\Omega_{\alpha,\beta,\gamma}\Omega_{\delta,\epsilon,\zeta}\rangle-\langle\Omega_{\alpha,\beta,\gamma}\rangle\langle\Omega_{\delta,\epsilon,\zeta}\rangle]$

called the Pulay forces [100], and they must be taken into account, *e.g.*, in fixed-node schemes [101].

3.2.5 Finite-field simulation

The finite-field approach (FF) is also based on Eq. (3.17), but it utilizes the electric field explicitly. That is, the actual response P of the system is simulated in an external potential due to an actual finite field $F \neq 0$. Usually, the simulation is repeated for variable field-strengths, and then fitted to a curve or otherwise extrapolated to the zero-field limit [53].

One characteristic of the FF approach is the full account of all orders of the response: there is no error from truncation of the perturbative expansion. On the other hand, it becomes increasingly difficult to tell apart different orders of the response. Practically, the number of independent samples for F must be higher than that of the meaningful polarizabilities. For instance, at least three values of F_z are needed to fit

$$\mu_z^{(1)} = \alpha_{z,z} F_z + \gamma_{z,z,z,z} F_z^3 + \mathcal{O}(F_z^5), \tag{3.26}$$

where the odd terms (in terms of the tensorial indices) are assumed to be zero and the terms proportional to F_z^5 and beyond are assumed to be negligible. This only holds true, if the fields are weak enough: in strong static fields the FF simulation is bound to break down due to a truncated basis or dissociation, *i.e.* irreversible separation of charges. Isolated quantum systems in static homogeneous fields are pathological problems, which can only be solved within the metastable regime.

Overall, the FF approach is not the most straightforward, but it is very explicit and suitable for complex environments [102, 103]. We only exercise the FF approach in Publication I, but some more details can be found in Refs. [53, 104].

3.3 Scalar and tensorial polarizability

The susceptibility and polarizability are tensorial quantities, whose tensorial rank depends on the induced property and the incoming perturbation. The rank equals to the number of lower indices α, β, γ *etc*. Naturally, it follows that the response tensor of a particular system follows its symmetry properties: a system with high symmetry has a low number of independent tensor elements. The ultimate limit is the spherical symmetry, where the number is one, *i.e.*, the tensor becomes scalar. For general purposes, a comprehensive review on symmetry point groups and independent polarizability tensors is given in Ref. [8].

3.3.1 Internal and laboratory coordinates

Let us make distinction between the so-called internal coordinates and laboratory coordinates. The *internal coordinates* will be denoted by lowercase x, y and z, referring to specific orientations of the system. For instance, atoms are always spherically symmetric and thus independent of the choice of z. On the other hand, diatomic molecules are defined by their principal axis of rotation, which is by convention denoted by z. Less symmetric molecules generally have more independent tensor components.

The internal orientation of a molecule may or may not be known to an external observer. The *laboratory coordinates* will be denoted by capital X, Y and Z. For instance, the orientation of a crystal structure or a surface are bulk quantities that can be fixed in the laboratory. Indeed, condensed matter and interfaces are generally more diverse and interesting in terms of nonlinear optical phenomena. On the other hand, species in isolation or fluid phases are always isotropic, because their orientation in thermal conditions is random on average. That is, regardless of the internal geometry, all results in the laboratory coordinates reduce to spherical symmetry, denoted with Z.

However, internal anisotropy of spherically symmetric systems can be inherited to the higher orders in perturbation. This is crucial for the understanding of the results of this Thesis. Let us consider a homonuclear diatomic molecule, which has two independent terms in the dipole polarizability tensor: $\alpha_{z,z}$ (along the principal axis) and $\alpha_{x,x} = \alpha_{y,y}$.

The measure of anisotropy is given by

$$\Delta\alpha = \alpha_{z,z} - \alpha_{x,x}.$$

That is, the electric moment induced in response to a field F_α is not centrosymmetric. Due to the anisotropic induced moment, there is an energetically favorable orientation for the coupling of another incident field. Thus, if more fields should emerge, they would cause a strong orientational effect in the favor of the optimal orientation. This is a qualitative explanation of a large orientational effect, which is discussed in better detail in Chapters 5 and 6.

3.3.2 Isotropic averaging

The internal coordinates can be important for the holistic understanding of the electric field response. For practical purposes, such as FF simulation or benchmarking, it is often convenient and insightful to fix the molecule in space and calculate the full internal polarizability tensor. However, the experiments are restricted to the laboratory coordinates, and thus, the ultimate aim should be at the measurable realm. For this reason, isotropic averaging of high-rank tensor, such as polarizabilities, has been studied in great detail [105, 106].

The trace and parity of the tensor has important consequences in terms of the isotropic averaging. First, the order of the tensor coincides with its rank. The isotropic averages are always zero by symmetry for the odd-ordered electric moments and polarizabilities, such as μ_α, $\beta_{\alpha,\beta,\gamma}$ and $A_{\alpha,\beta\gamma}$. The quadrupole moment $\Theta_{\alpha\beta}$ is also zero even though it has even parity, because it is defined as traceless. The induced moments are not traceless, and thus, the even-ordered polarizabilities are nonzero. However, their diagonal elements are symmetric and the response is essentially scalar.

The isotropic average can be calculated from properties of the internal coordinates. The spherically symmetric properties are trivially $\chi_{Z\cdots} = \chi_{\alpha\cdots}$, where $\alpha\cdots$ denotes an arbitrary diagonal element. For diatomic molecules, the isotropic averages of the most

important polarizabilities are [10]

$$\alpha_{Z,Z} = \tfrac{1}{3}(2\alpha_{x,x} + \alpha_{z,z}) \tag{3.27}$$

$$\gamma_{Z,Z,Z,Z} = \tfrac{1}{15}\left(3\gamma_{z,z,z,z} + 12\gamma_{x,x,z,z} + 8\gamma_{x,x,x,x}\right) \tag{3.28}$$

$$B_{ZZ,Z,Z} = \tfrac{2}{15}\left(B_{zz,z,z} + 4B_{xz,x,z} + B_{xx,z,z} + 4B_{xx,x,x}\right) \tag{3.29}$$

$$C_{ZZ,ZZ} = \tfrac{1}{15}\left(C_{zz,zz} + 8C_{zx,zx} + 8C_{xx,xx}\right). \tag{3.30}$$

The expressions become more complicated for more exotic symmetries, but it is not the intention of this Thesis to provide an exhaustive reference. Using Eqs. (3.27)–(3.30) and alike, one can easily estimate the average polarizability based on a single fixed-nuclei simulation. However, a word of caution is in order: the fixed-nuclei simulation only yields the average electronic polarizability. However, the total polarizability also involves diverse contributions from nuclear quantum phenomena.

3.4 The adiabatic approximation

The adiabatic approximation stems from the complete separation of the electronic and nuclear degrees of freedom: reaction of the electronic structure to changes in the nuclear geometry is assumed to be immediate, or rather, adiabatic. Loosely, the adiabatic approximation is also known as the clamped-nuclei approach or the Born–Oppenheimer approximation. However, detailed treatment of the perturbation is complicated and somewhat unambiguous [107], and thus, this section serves as a qualitative background for understanding the results to come.

In the following, we will denote the adiabatic approximation by BO for Born–Oppenheimer, and the exact nonadiabatic simulation with AQ for *all-quantum*. Generally, BO is a good approximation, but not perfect. Light nuclei, such as protons, show nonadiabatic effects, meaning that the electronic and nuclear motions are coupled. The magnitude is related to the reduced mass: thus, the effect is roughly 1/2000 for an electron–proton pair and less for heavier nuclei. Indeed the nonadiabatic effects usually show up in the fourth meaningful digit. For the remainder of this section, we will neglect the aforementioned nonadiabatic recoil effect and focus on the remaining degrees of freedom: the nuclear rovibration.

3.4.1 Polarizability of a diatomic molecule

The following is an outline of a detailed review on rovibrational effects on polarizabilities given in Refs. [10, 108]. Let us consider the polarizability of a diatomic molecule in the adiabatic approximation. The wavefunction is $|\Phi_{vJM}\rangle = |v(J)\rangle Y_J^M(\theta,\phi)$, where v, J and M are, respectively, quantum numbers for vibration, total angular momentum, and magnetic moment. $Y_J^M(\theta,\phi)$ is a spherical harmonic function. The ket $|v(J)\rangle$ is the ground state electronic wavefunction for a particular rovibrational state $v(J)$.

Using perturbation theory, one can show that the dynamic dipole polarizability can be written as

$$\alpha(v,J,M;\omega) = \alpha^e(v,J,M;\omega) + \alpha^v(v,J,M;\omega) + \alpha^r(v,J,M;\omega), \tag{3.31}$$

where ω is the incident frequency and the separate terms are electronic, vibrational and rotational polarizabilities, respectively. They are given by

$$\alpha^e(v,J,M;\omega) = \langle v(J)|\alpha_{x,x}(\omega)|v(J)\rangle + (C_{JM}+D_{JM})\langle v(J)|\Delta\alpha(\omega)|v(J)\rangle \tag{3.32}$$

$$\alpha^v(v,J,M;\omega) = \sum_{v'\neq v} 2C_{JM}\frac{|\langle v(J)|\hat{\mu}|v'(J+1)\rangle|^2}{E_{v',J+1}-E_{v,J}-\hbar\omega} + 2D_{JM}\frac{|\langle v(J)|\hat{\mu}|v'(J-1)\rangle|^2}{E_{v',J-1}-E_{v,J}-\hbar\omega} \tag{3.33}$$

$$\alpha^r(v,J,M;\omega) = 2C_{JM}\frac{|\langle v(J)|\hat{\mu}|v(J+1)\rangle|^2}{E_{v,J+1}-E_{v,J}-\hbar\omega} + 2D_{JM}\frac{|\langle v(J)|\hat{\mu}|v(J-1)\rangle|^2}{E_{v,J}-E_{v,J-1}-\hbar\omega} \tag{3.34}$$

where

$$C_{JM} = \frac{(J+1)^2-M^2}{(2J-1)(2J+3)}$$
$$D_{JM} = \frac{J^2-M^2}{(2J-1)(2J+1)}.$$

For the thermal expectation value, let us consider the Boltzmann distribution over the rotational states:

$$\rho(v,J) = \frac{(2J+1)g_J e^{-(E_{vJ}-E_{v0})\beta}}{\sum_{J'}(2J'+1)g'_J e^{-(E_{vJ'}-E_{v0})\beta}}, \tag{3.35}$$

where g_J is the nuclear spin-degeneracy factor needed for homonuclear diatomics. This approximation neglects the possibility of electronic and vibrational excitations, but it

will enable us to write the ensemble polarizability as

$$\begin{aligned}\langle\alpha(v;\omega)\rangle &= \sum_J \frac{\rho(v,J)}{2J+1}\sum_M \alpha(v,J,M;\omega) \\ &= \langle\alpha^e(v;\omega)\rangle + \langle\alpha^v(v;\omega)\rangle + \langle\alpha^r(v;\omega)\rangle,\end{aligned} \tag{3.36}$$

where

$$\langle\alpha^e(v;\omega)\rangle = \tfrac{1}{3}\sum_J \rho(v,J)\langle v(J)|\alpha_{z,z}(\omega)+2\alpha_{x,x}(\omega)|v(J)\rangle \tag{3.37}$$

$$\begin{aligned}\langle\alpha^v(v;\omega)\rangle = \tfrac{1}{3}\sum_J \frac{2\rho(v,J)}{2J+1}\sum_P\sum_{v'\neq v} \\ \left[\frac{(J+1)|\langle v(J)|\hat{\mu}_\alpha|v'(J+1)\rangle|^2}{E_{v',J+1}-E_{v,J}-\hbar\omega}+\frac{J|\langle v(J)|\hat{\mu}_\alpha|v'(J-1)\rangle|^2}{E_{v',J-1}-E_{v,J}-\hbar\omega}\right]\end{aligned} \tag{3.38}$$

$$\begin{aligned}\langle\alpha^r(v;\omega)\rangle = \tfrac{1}{3}\sum_J\sum_P \frac{2\rho(v,J)}{2J+1} \\ \left[\frac{|(J+1)\langle v(J)|\hat{\mu}_\alpha|v(J+1)\rangle|^2}{E_{v,J+1}-E_{v,J}-\hbar\omega}+\frac{J|\langle v(J)|\hat{\mu}_\alpha|v(J-1)\rangle|^2}{E_{v,J}-E_{v,J-1}-\hbar\omega}\right],\end{aligned} \tag{3.39}$$

where $\sum_P$ denotes a permutation between ω and $-\omega$. The argument v emphasizes that the vibrational and electronic levels are considered unchanged. At this point, it is apparent that the rotational and vibrational effects require a permanent dipole moment to be non-zero in the first place.

One is able to study the effects of rovibration in the SOS approach simply by computing a sufficient number of energies, wavefunctions and matrix elements. In practice, such pragmatic approach grows tedious very quickly, because of the complexity of the quantum many-body problem.

3.4.2 Thermal limits

Without further ado let us make a few approximations in order to study some thermal limits of the given polarizabilities. First, one can make a semiempirical approximation

[10]

$$\langle v(J)|P(r)|v(J)\rangle = \langle v(0)|P(r)|v(0)\rangle + 4J(J+1)\left(\frac{B_e}{\omega_e}\right)^2 \frac{\mathrm{d}P}{\mathrm{d}\zeta}, \tag{3.40}$$

where B_e and ω_e are the rotational constant and harmonic vibrational frequency, respectively. Furthermore,

$$\zeta = (r - r_e)/r_e,$$

where r_e is the equilibrium distance. Using the high-temperature approximation

$$\sum_J \rho(v,J)J(J+1) \approx \frac{kT}{\hbar B_e}, \tag{3.41}$$

one can estimate that the high-temperature limit for the electronic polarizability is

$$\begin{aligned}\langle \alpha^e(v;\omega)\rangle_T = {} & \langle v(0)|(\alpha_{z,z}(\omega) + 2\alpha_{x,x}(\omega))|v(0)\rangle \\ & + \frac{4J(J+1)}{3}\left(\frac{B_e}{\omega_e}\right)\frac{\mathrm{d}}{\mathrm{d}\zeta}[\alpha_{z,z}(\omega) + 2\alpha_{x,x}(\omega)]T.\end{aligned} \tag{3.42}$$

Dependence on $\frac{\mathrm{d}}{\mathrm{d}\zeta}[\alpha_{z,z} + 2\alpha_{x,x}]T$ indicates a centrifugal effect: since the electronic polarizability varies as a function of r, there is a corresponding change in polarizability. For example, the static dipole polarizabilities of H_2 is known to increase as a function of r [109], and thus, their centrifugal coupling is also positive.

For the vibrational polarizability, we can make a high-temperature approximation, namely $|v(J+1)\rangle \approx |v(J-1)\rangle \approx |v(J)\rangle$ and also $E_{v,J+1} \approx E_{v,J-1} \approx E_{v,J}$. We obtain

$$\langle \alpha^v(v;\omega)\rangle_T = \tfrac{1}{3}\sum_P \sum_{v\neq v'} \frac{\left|\left\langle v(0)\left|\langle n\left|\hat{\mu}_z\right|n\right\rangle\right|v'(0)\right\rangle\right|^2}{E_{v',0} - E_{v,0} - \hbar\omega}.$$

Thus, the vibrational contribution only appears, if there is a permanent dipole moment. Even then, the effect is rather small apart from the resonance.

Finally, the high-temperature approximation for the rotational polarizability is given

by [10]

$$\langle \alpha^r \rangle = \frac{\left(\mu^{(0)}\right)^2}{3kT} \left\langle \frac{2J+2}{2J+1} \frac{(E_{J+1}-E_J)^2}{(E_{J+1}-E_J)^2-(\hbar\omega)^2} \right\rangle. \tag{3.43}$$

Clearly, when $\hbar\omega \gg 0$, the rotational effect fades away. Classically, this means that the molecule cannot orient itself in a field that oscillates very rapidly. At the static limit $\omega = 0$, we get a high-temperature limit proportional to

$$\langle \alpha^r \rangle \propto \frac{\left(\mu^{(0)}\right)^2 \hbar\beta}{3}, \tag{3.44}$$

which is also Debye's classical limit [110]. This is one of the most important explanations to the results of later chapters.

Question of the low-temperature region remains open. One can say that the total polarizability is finite-valued at 0 Kelvin, but precise evaluation of the limit requires numerical methods. At low but finite temperatures the thermal coupling is governed by the lowest rotational states. It is possible to calculate them explicitly as long as the number of contributing states remains reasonable. At some point the region between low and high temperatures becomes nontrivial for simulation, unless the thermal ensemble is treated implicitly. This is exactly what will be demonstrated in the coming chapters.

3.4.3 Total higher-order polarizabilities

Similar derivations can be carried out for higher-order polarizabilities and systems with less symmetry. The general framework and many useful practices are found in Ref. [10]. However, the equations quickly become cumbersome, and the number of approximations makes the results questionable. Besides, we should emphasize that the separation to electronic, rotational and vibrational polarizability is an approximation on its own. There is no way to obtain the exact total polarizability other than calculating it with a fully explicit method. Thus, we make no further attempts to induce and decompose thermal effects from the analytical foundations.

Generally, there can be many simultaneous thermal effects that are scaled and activated in different ways. There is the average electronic polarizability, which is linearly cou-

pled to high temperatures due to centrifugal distortion. Then there are orientational effects, which follow Eq. (3.44) or something similar and saturate at 0 Kelvin. In the second order, the orientational effect is inverted [29]. The coupling of all the aforementioned effects is nontrivial, and we will later use only effective models for the total polarizability. Such models are proposed and discussed In Ch. 5 and Publications II and III.

4 PATH INTEGRAL MONTE CARLO

Regardless of the electric field response, computation of the thermal density matrix is a challenge on its own. This chapter is devoted to a particular method designed to do it, namely path integral Monte Carlo (PIMC). Along variational Monte Carlo (VMC) [111] and diffusion Monte Carlo (DMC) [112], PIMC is one of the most popular flavors of real-space Quantum Monte Carlo (QMC). The common principle for different QMC approaches is that they use stochastic processes to solve quantum many-body problems, which are otherwise hard or even intractable.

Contrary to most quantum mechanical simulation methods, PIMC features implicit account of thermal statistics and explicit many-body correlations. The many-body nature can in principle be extended to any degrees of freedom; the PIMC algorithm is flexible to be utilized in many kinds of problems [76, 113, 114, 115, 116, 117]. An optimal problem for PIMC is a balance between quantum phenomena (low temperature) and the classical limit (high temperature).

Yet, one of the most important features of PIMC is the straightforward possibility of nonadiabatic simulation. We refer to such simulation as all-quantum (AQ), because it treats electrons and nuclei on an equal footing, as quantum particles. AQ is a complementary approach to the Born–Oppenheimer approximation (BO), which involves a decomposition to rovibrational and electronic parts. The nonadiabatic approach is categorically more truthful than BO, but it can be computationally heavy. Yet, the most important results of this Thesis are unique and original because of the nonadiabaticity, which arises naturally from the AQ simulation.

In the following, we will outline the main features of the traditional PIMC method for exact Coulomb interactions. The primary focus is on the implementation of polarizability estimators, whereas better detail on the common techniques can be found in, *e.g.* Refs. [72, 83, 89, 118].

4.1 The computational problem

A recipe for the computational problem is given in Eq. (2.87): the quantum many-body partition function is a discrete path integral over the full phase-space of closed many-body trajectories. Evaluation of such multidimensional integral is a formidable challenge for a few reasons. First of all, the number of paths in the continuous space is infinite. Doing quadrature on finite grids in so many dimensions is impractical and still likely to suffer from biases and self-cancellations [72]. A viable solution is Monte Carlo integration: estimating the integral by providing a finite number of randomly generated samples from the true distribution.

In PIMC, the thermal density matrix is sampled in the canonical or NVT ensemble by a Markovian walker. The walker is a snapshot of the many-body trajectory, denoted R. Many good practices and optimizations have been developed for PIMC, but the main workflow can be summarized as follows:

1. Defining the system and parameters;
2. Computing and tabulating pairwise interactions;
3. Converging the walker;
4. Sampling and measuring the walker.

Let us briefly review the steps.

In step 1 we choose the number and quality of particles: masses and charges. We also define the environment, such as the spatial dimensions, temperature, boundary conditions, *etc*. In this Thesis, we carry out NVT simulations, so all the aforementioned parameters remain constant. The most definitive parameter is the finite time-step $\Delta\tau$. As we shall see, it dictates the accuracy of many-body interactions but also some estimators. It is advisable to repeat the simulation at several different time-steps to probe for time-step errors. The time-step is also inversely proportional to the Trotter number M, and thus, it is increasingly heavy to run simulations at lower temperatures or smaller time-steps.

Step 2 is rather an optimization and not always done. However, extremely accurate pair-actions can be used, if they are pre-calculated and saved to the memory. Some important details on the handling of pair-density matrices will be given in Sec. 4.3.

Step 3 consists of generating initial configuration for the walker, and then converging it to the thermal equilibrium. In the Markovian process the walker is randomly mutated, until it reaches equilibrium. The equilibrium is not a specific set of coordinates, but rather a subspace of the phase-space with low free energy. The process is maintained by the Metropolis algorithm [119]. The Metropolis Monte Carlo sampling (MMC) is discussed in Sec. 4.4.1. Convergence to the equilibrium is often referred to as the transient.

Finally, step 4 is that of the biggest computational intensity. The idea is to keep sampling the path integral with the MMC algorithm, and thus, gather data for the thermal partition function. The longer this is done, the more accurate statistical estimates are acquired. The error is at the same time controllable and inevitable: there is always a little statistical imprecision, but it can be decreased indefinitely by producing more data samples. The measurement is a problem of its own: Section 4.5 is dedicated to different estimators relevant to this Thesis.

Nevertheless, the scaling of computation is clearly an important question. Within the scope of this Thesis, there are two well-known numerical obstacles: First, the Fermion sign problem arises, if the simulation involves exchange of indistinguishable Fermions. This is briefly discussed in Sec. 4.7. Second, the estimation of dynamic properties involves numerical inversions, whose feasibility is strongly dependent on the quality of the QMC data. For these reasons, it is very important to optimize the whole computational procedure.

The PIMC simulations of this Thesis have been carried out with privately developed software. The main program is written in Fortran 90. Currently, it utilizes MPI parallelization for scalable MMC sampling, but OpenMP is also supported for some features. The latest branches mainly use HDF5 (v. 1.10) for file I/O. As of today, the software is being planned and refined for open source publication. The high-performance computation has been carried out in using SLURM environments and HPC resources provided by IT Center of Science Ltd. (CSC) and Tampere Center of Scientific computing (TCSC).

4.2 Atomic units

For the remainder of this Thesis, we use atomic units for convenience. That is, most of the relevant natural constants are given a unitary measure:

$$\hbar \equiv 1, \quad k = \frac{1}{4\pi\varepsilon_0} \equiv 1, \quad 1\,\mathrm{Ha} \equiv 1, \quad m_e \equiv 1, \quad e \equiv 1, \quad a_0 \equiv 1.$$

For instance, the units of length, charge, mass and energy are respectively the Bohr radius a_0, the elementary charge e and the electron mass m_e and Hartree. The unit of temperature is Kelvin and the Boltzmann constant is approximately $k_B = 3.166\,18 \times 10^{-6}$ in the atomic units. Scaling of the results, such as the polarizabilities, arises naturally from the above definitions, and will not be explicitly stated in the tables and figures. If necessary, conversion to SI units or some other commonly used system can be done according to Ref. [10].

4.3 Action

The most important part in terms of accuracy is the treatment of action. The path integral consists of link-propagators of the form

$$\left\langle R_{i-1} \left| \hat{\rho}(\Delta\tau) \right| R_i \right\rangle = \rho\left(R_{i-1}, R_i; \Delta\tau\right), \tag{4.1}$$

where the link action is defined as the negative natural logarithm of the density matrix:

$$S\left(R_{i-1}, R_i; \Delta\tau\right) = -\ln \rho\left(R_{i-1}, R_i; \Delta\tau\right). \tag{4.2}$$

Based on Eq. (2.91), the action can be separated into kinetic an interaction parts

$$S\left(R_{i-1}, R_i; \Delta\tau\right) = K\left(R_{i-1}, R_i; \Delta\tau\right) + U\left(R_{i-1}, R_i; \Delta\tau\right), \tag{4.3}$$

where the former is the free-particle kinetic action

$$K\left(R_{i-1}, R_i; \Delta\tau\right) = \frac{dN}{2} \ln(4\pi\lambda\Delta\tau) + \frac{\left(R_{i-1} - R_i\right)^2}{4\lambda\Delta\tau}. \tag{4.4}$$

The interaction part can be defined in the combination of primitive and semi-classical approximations: $U(R_{i-1},R_i;\Delta\tau) = \frac{\Delta\tau}{2}[V(R_{i-1}) + V(R_i)]$ in the limit of $\Delta\tau \to 0$. However, a finite time-step produces and error of $\mathcal{O}(\Delta\tau^2)$. The error comes from kinetic contributions in higher orders of $\Delta\tau$. There exists higher-order propagators for improved action, but they can be more tedious to use [82, 120]. Therefore, let us for a moment use an exact definition for the interaction part:

$$\begin{aligned} U\left(R_{i-1},R_i;\Delta\tau\right) &= S\left(R_{i-1},R_i;\Delta\tau\right) - K\left(R_{i-1},R_i;\Delta\tau\right) \\ &= -\ln\frac{\rho\left(R_{i-1},R_i;\Delta\tau\right)}{\rho^K\left(R_{i-1},R_i;\Delta\tau\right)}, \end{aligned} \tag{4.5}$$

where ρ^K is the free-particle density matrix from Eq. (2.90).

4.3.1 Coulomb pair action

Let us consider the pair approximation defined in Eq. (2.93). Density matrix for a pair of particles can be written as

$$\rho\left(\mathbf{r}_1,\mathbf{r}_2,\mathbf{r'}_1,\mathbf{r'}_2;\tau\right) = \rho^{\mathrm{cm}}\left(\bar{\mathbf{r}}_{12},\bar{\mathbf{r}}'_{12};\Delta\tau\right)\rho^{\mathrm{rel}}_{12}\left(\mathbf{r}_{12},\mathbf{r}'_{12};\Delta\tau\right), \tag{4.6}$$

where $\bar{\mathbf{r}}_{12} = (m_1\mathbf{r}_1 + m_2\mathbf{r}_2)/(m_1+m_2)$, $\mathbf{r}_{12} = \mathbf{r}_1 - \mathbf{r}_2$, *cm* refers to center-or-mass and *rel* to the relative motion. We are not concerned with ρ^{cm}, because it only involves kinetic contributions. On the other hand, we will next expand the relative pair-density matrix in partial waves [83]:

$$\rho_{\mathrm{rel}}\left(\mathbf{r},\mathbf{r}';\Delta\tau\right) = \frac{1}{4\pi r\, r'}\sum_{l=0}^{\infty}\rho_l(r,r';\Delta\tau)P_l(\cos\theta), \tag{4.7}$$

where r and r' are the norms of the respective displacement vectors, and θ is the angle between them. In the case of Coulomb interaction, the relative motion density matrix can be obtained using only the $l = 0$ channel [121]:

$$\rho_{\mathrm{rel}}\left(\mathbf{r},\mathbf{r}';\Delta\tau\right) = -\frac{1}{8\pi s}\frac{\partial}{\partial s}\rho_0(z+s,z-s;\Delta\tau) \tag{4.8}$$

$$\rho_{\mathrm{rel}}\left(\mathbf{r},\mathbf{r};\Delta\tau\right) = -\frac{1}{8\pi s}\frac{\partial^2}{\partial s^2}\rho_0(z+s,z-s;\Delta\tau)|_{s=0}, \tag{4.9}$$

where $z=(x+y)/2$, $s=(x-y)/2$, $x=(r+r'+|\mathbf{r}-\mathbf{r}'|)/2$ and $x=(r+r'-|\mathbf{r}-\mathbf{r}'|)/2$. This is the so-called s-wave miracle.

4.3.2 Matrix squaring

A technique called matrix squaring can be used to compute the pair-density matrix, such as $\rho_0(r,r';\Delta\tau)$ at a very high precision [121]. It is based on the following general identity:

$$\rho(R,R';2\Delta\tau)=\langle R|\hat{\rho}^2(\Delta\tau)|R'\rangle=\int \mathrm{d}R''\,\rho(R,R'';\Delta\tau)\rho(R'',R';\Delta\tau), \tag{4.10}$$

that is, a convolution of thermal density matrix can be used to produce one at half the temperature. At the limit of high temperature or small $\Delta\tau$, the primitive approximation and the semi-classical approximation are very accurate and can be safely used. Thus, successive use of the squaring property Eq. (4.10) can be used to calculate a very accurate pair-density matrix even at low temperatures.

In particular, components of the pair density matrix can be calculated by

$$\rho_l(r,r';\Delta\tau)=\int_0^\infty \mathrm{d}r''\,\rho_l(r,r'';\Delta\tau/2)\rho_l(r'',r';\Delta\tau/2). \tag{4.11}$$

However, the numerical procedure can be technically challenging, and further revisions are advised for extreme accuracy. For instance, one can define

$$\rho_l(r,r';\Delta\tau)=\rho_l^K(r,r';\Delta\tau)\mathrm{e}^{-u_l(r,r';\Delta\tau)}, \tag{4.12}$$

where $u_l(r,r';\Delta\tau)$ is the effective pair potential and the kinetic part is known analytically [72, 83]:

$$\rho_l^K(r,r';\Delta\tau)=\frac{4\pi r\,r'}{(4\pi\lambda\Delta\tau)^{3/2}}\exp\left(-\frac{(r-r')^2}{4\lambda\Delta\tau}m_l\left(\frac{r\,r'}{2\lambda\Delta\tau}\right)\right), \tag{4.13}$$

where $m_l(z)=i_l(z)\mathrm{e}^{-z}$ and $i_l(z)$ is the modified Bessel function of the first kind. One

can use this knowledge to calculate

$$u_l(r,r';2\Delta\tau) = -\ln\left[\int_0^\infty \mathrm{d}r''\,\frac{\rho_l^K(r,r'';\Delta\tau)\rho_l^K(r'',r';\Delta\tau)}{\rho_l^K(r,r';\Delta\tau)} \times \exp\left[-u_l(r,r'';\Delta\tau)-u_l(r'',r';\Delta\tau)\right]\right].$$

Another important practice is to use nonlinear grid for r, which promotes the resolution near the strongest kinetic mixing, *i.e.*, near the origin $r = 0$. At the limit of large r, $u_l(r,r') \to \frac{\Delta\tau}{2}[v(r)+v(r')]$, where $v(r)$ is the radial potential energy function. For more comprehensive details, see Ref. [72].

The matrix squaring process can be heavy, but it offers a great benefit: the exact Coulomb pair-potential matrix can be stored in an actual matrix, a 2D array. That is, instead of heavy on-site computation of the interaction, it suffices to read it from the memory. The pair-potential data has smooth but nontrivial shape, and thus, the storage and interpolation are conveniently implemented using cubic splines.

4.3.3 Generalized interaction

Let us briefly discuss interactions more generally. The combination of partial wave decomposition, Eq. (4.7), and matrix squaring works as is for any radial potential $v(r)$. The main difference is that generally one needs $l \to \infty$ channels, while the Coulomb action only requires $l = 0$. Practically, the summation can be truncated and approximated [122]. Still, aiming for extremely high accuracy is numerically challenging and likely to require caution with floating point arithmetic. Another issue is that the partial wave decomposition is a three-variable function, not a 2D matrix. A particular way to reduce the dimensions is to change some variables and make polynomial fits [83, p. 320].

The principle of matrix squaring can be utilized to three-body density matrices and higher. However, the number of variables escalates quickly: for instance, the complete three-body density matrix has 12 independent coordinate variables plus the time-step [83]. Most of these coordinates are small, yet the implementation of matrix squaring for many-body density matrices is a tedious task. There is a looming motivation, though: the biggest source of systematic error in this Thesis is due to the pair approximation.

4.4 Sampling

While action defines the accuracy, the algorithmic efficiency is strongly dependent on sampling. In Metropolis Monte Carlo, the task is to probe the phase-space of the system one sample at a time. The samples have statistical weights according to the partition function: the probability for finding the system in a state R is

$$\Pi(R) = Z^{-1}\rho(R,R;\beta). \tag{4.14}$$

The relative probability of an arbitrary configuration R is small, and thus, completely random sampling is highly inefficient. Indeed a better strategy is to pick samples near the maximum probability, the thermal equilibrium. This is readily achieved by the Metropolis Monte Carlo algorithm [119].

4.4.1 Metropolis Monte Carlo

According to the principle of detailed balance, in equilibrium the total rate of transitions from state R to R' equals that of the reverse rate, *i.e.*

$$\mathbb{P}(R \to R')\Pi(R) = \mathbb{P}(R' \to R)\Pi(R'). \tag{4.15}$$

Let us suppose that the transition rate is the product of an *a priori* sampling probability $\mathbb{T}(R \to R')$ and the acceptance probability $\mathbb{A}(R \to R')$. The conditional acceptance bias can then be written as [72]

$$q(R'|R) = \frac{\mathbb{A}(R \to R')}{\mathbb{A}(R' \to R)} = \frac{\mathbb{T}(R' \to R)\rho(R',R';\beta)}{\mathbb{T}(R \to R')\rho(R,R;\beta)} \geq 0. \tag{4.16}$$

The actual process of performing $\mathbb{T}(R \to R')$ is referred to as *making a move*. The probability for accepting or rejecting the move is written as

$$\mathbb{A}(R \to R') = \min[1, q(R'|R)], \tag{4.17}$$

which allows us to write out the generalized Metropolis Monte Carlo algorithm [72]:

- sample a possible new configuration R' using $\mathbb{T}(R \to R')$
- calculate $q(R'|R)$
- if $\mathbb{A}(R \to R') > u(0,1)$, where $u(0,1)$ is a uniformly distributed random number, accept the move and set $R(n) = R'$
- otherwise, reject the move and set $R(n+1) = R$

Repeating this procedure ultimately leads to the equilibrium regardless of the initial state $R(0)$, as long as the sampling is ergodic, meaning that any R and R' can be connected by a finite number of sampling steps. Converging, or equilibrating the system may take some time and it is one of the basic steps of MMC calculations.

In practice, ergodicity is sometimes difficult to ensure. For instance, the system can be complex or involve stiff constraints, such as strong potentials or nodal restrictions. This manifests in undesirable simulation characteristics, such as slow convergence and high correlation times of observables. To some extent, low ergodicity can be improved by extending the palette of different sampling algorithms. Generally, the Metropolis algorithm is flexible to purposeful sampling schemes, as long as the detailed balance is maintained. This can make a huge difference in terms of the algorithmic efficiency. The principle is to visit all the relevant subsets of the phase-space within a reasonable amount of simulation time. A rule of thumb is to make as large moves as possible while maintaining a good acceptance ratio. A few examples will be given in later sections.

On the other hand, one may wish to run simulations, which are inergodic by design: metastable equilibria. For instance, simulating charged particles in a finite electric field involves a finite risk of dissociation: opposite charges break apart, and the simulation gets out of equilibrium. Even the simulation of a loosely bound compound is at the risk of dissociation in infinite space at finite temperature. Without proper regulation or boundary conditions, metastable simulations are formally a malpractice. Practically they are shortcuts to the limits of low temperature and perturbation, but one must be cautious when initializing, running and analyzing such simulations.

4.4.2 The PIMC walker

The PIMC walker is the trajectory R consisting of M time-slices, each of which contains the Cartesian coordinates of N particles. That is, the walker consists of N times M real-space coordinates, which are called beads. The total memory footprint is that of the current configuration R and the trial R'.

Multilevel bisection

Converging such a multidimensional walker can be tedious, but there is a particularly efficient algorithm designed for such a walker: the bisection method is *de facto* popular, and the one also used in this work. One writes the acceptance probability as

$$\frac{\mathbb{T}(R' \to R)\rho(R', R'; \beta)}{\mathbb{T}(R \to R')\rho(R, R; \beta)} = \frac{\mathbb{T}(R' \to R)}{\mathbb{T}(R \to R')} \mathrm{e}^{-\Delta K} \mathrm{e}^{-\Delta U},$$

where ΔU and ΔK are the respective differences in the many-body interactions and the free-particle kinetic actions. Let us choose the coordinate of a random particle and a random time-slice i, $\mathbf{r}_i$. The bisection means defining the trial coordinate as

$$\mathbf{r}'_i = \tfrac{1}{2}\left(\mathbf{r}'_{i-1} + \mathbf{r}'_{i+1}\right) + \mathbf{n}(0, \sqrt{\lambda \Delta \tau}), \tag{4.18}$$

where $\mathbf{n}$ is normally distributed Cartesian vector, with zero mean and the standard deviation of $\sqrt{\lambda \Delta \tau}$. It is easy to show that this exactly counters the free-particle kinetic action [72, 104] and leads to

$$\frac{\mathbb{T}(R' \to R)}{\mathbb{T}(R \to R')} \mathrm{e}^{-\Delta K} = 1,$$

and thus, the acceptance probability only depends on the interaction difference. Algorithmically, this is both appealing and efficient, but moving only one coordinate at a time is still slow. One can implement the bisection method in nested multilevel stages, which enable to move a segment of $2^L + 1$ beads with the effective thermal wavelength of $\sqrt{2^{L-1} \lambda \Delta \tau}$. The multilevel bisection method is described in better detail in Ref. [72].

Permutation sampling

Let us briefly mention another important degree of freedom: permutation sampling. The permutation of trajectories is one of the fundamental characteristics of the simulation of identical particles, bosons or fermions. Equilibrating and sampling the full permutation determinants for all time-slices makes for a rather formidable walker. A more tractable approach is to only allow one permutation at a time, and then allow for it to change according to the principles of MMC. Depending on the number of identical particles, the trial permutation can involve relabeling of two or more one-particle trajectories. Permutation sampling can be optimized and combined with the multilevel bisection method [123]. The parity of permutation has important consequences on fermions, because the odd permutations cause the density matrix to have a negative sign. Thus, in constrained approaches such as RPIMC, only even permutations are allowed. If the permutation sampling is missing, inefficient or otherwise incomplete, it reflects badly to the results. In this work, we do not simulate identical particles or permutations in this sense.

Orientational sampling

Finally, let us briefly consider simple orientational sampling. By orientational sampling we refer to a trial move, where the whole many-body trajectory is randomly rotated to a different orientation:

$$R' = T_{\mathrm{rot}}(R),$$

where T_{rot} simply refers to the process of rotation using *e.g.* Euler angles, rotation matrices or quaternions. In order to maintain the detailed balance, the rotation must always be done with respect to the same origin. In the free-nuclei simulations of this work, the origin is always the mean center-of-mass of the trajectory. In fixed-nuclei simulations, the rotational averaging is seldom motivated, but if it were, we would use the laboratory origin.

Reorientation of the full trajectory may seem trivial and meaningless, but it is a cheap way to boost the efficiency of rotational averaging. The internal coordinates of the sys-

tem remain unchanged, and thus, no interaction calculations are needed: the move is automatically accepted, unless the system is in a finite field. In that sense, a full rotation such as this is rather a routinely procedure than an actual trial move. Rotational averaging is associated to all the tensorial properties, such as electric moments and polarizabilities. Doing it explicitly may not be the most elegant approach, but it is simple to use and interpret even in higher orders. Besides, the rotational averaging naturally arises from free-nuclei simulation. The bisection method will eventually cover the full orientational space, but the process is very slow, when the thermal wavelengths associated with the multilevel algorithm are small compared to the system radius. This is a typical feature in multiscale PIMC simulation, where both the electrons and the nuclei are explicitly simulated.

4.5 Calculation of properties

Calculation of properties is done according to Eq. (2.35), where MMC sampling does the integration over R. A measurement is the process of estimating the given property out of the sample trajectory. This is easy for properties that are local in space, such as the Coulomb potential, and more involved for those that are not, such as the momentum [83, p. 339]. In Eq. (2.96), we have already devised formulas for diagonal measurements over discrete imaginary-time paths. The result is obtained by calculating $A(R_0)$ at the reference configuration. Moreover, if the symmetry properties allow, the result can be averaged over each time-slice R_i to get better statistics. In the following, we will consider estimators that can be measured in the coordinate representation R. For instance, electric multipole moments are standard diagonal properties, which are easy to calculate according to their definitions, Eqs. (3.3)–(3.6). The actual polarizability estimators are only a little more involved.

A practical question remains: how often should one make the measurement? The answer is in the balance between sampling efficiency and the cost of a measurement. In terms of computation, both the measurement and a unit of sampling have a cost. Ideally, MC samples should be uncorrelated, and making a lot of sampling moves before consecutive measurements reduces the statistical *correlation time*. On the other hand, sampling without measurements is redundant. Thus, a finite stride, or interval should

be employed and optimized: *e.g.* 1 measurement in 100 bisection moves. Another practical concern is the memory footprint of cumulative data (especially the large correlation functions): a result could be averaged over billions of values before writing to disk. One ends up defining a bin, or a block, which is large number of measurements to be averaged over.

4.5.1 Energy estimators

The Hamiltonian $\hat{H}$ is a nondiagonal operator, but it can be recovered from R by using thermodynamic identities. All measurements of total energy can be symmetrized over the path, because $\hat{H}$ commutes with the propagators.

The thermal estimator, or the primitive estimator, can be defined as [72]

$$\begin{aligned}\langle E_T\rangle &= -Z^{-1}\frac{\partial Z}{\partial \beta}\\ &= \frac{1}{M}\sum_{k=1}^{M}\left\langle \frac{\partial S(R_{k-1},R_k;\Delta\tau)}{\partial \Delta\tau}\right\rangle\\ &= \frac{1}{M}\sum_{k=1}^{M}\left\langle \frac{dN}{2\Delta\tau}-\frac{(R_{k-1}-R_k)^2}{4\lambda\Delta\tau^2}+\frac{\partial U(R_{k-1},R_k;\Delta\tau)}{\partial \Delta\tau}\right\rangle.\end{aligned}$$

In the primitive and semiclassical approximation, $\frac{\partial U(R_{i-1},R_i;\tau)}{\partial \Delta\tau}=\frac{1}{2}[V(R_{i-1})+V(R_i)]$. However, the accuracy of $\Delta\tau$-derivative can be significantly improved by using matrix squaring for it, too. The implementation used in this work is described in great detail in Ref. [72].

Alternatively, the virial estimator for a minimal window size is given by [72]

$$\langle E_V\rangle = \frac{1}{M}\sum_{k=1}^{M}\left\langle \tfrac{1}{2}R_k\nabla V(R_k)+V(R_k)\right\rangle, \tag{4.19}$$

where ∇ denotes a spatial gradient over the potential energy function. For Coulomb potential, $R_k\nabla V(R_k)=-V(R_k)$, and Eq. (4.19) simplifies to

$$\langle E_V\rangle = \langle V\rangle/2. \tag{4.20}$$

The virial estimator is generally preferred over the thermal, because it has less fluctuation. However, neither gives an upper bound estimate of the energy. The upper bound energy is a useful property for variational benchmarking. For instance, the Hamiltonian estimator gives the upper bound [124], but it is heavier to evaluate and was not implemented for this Thesis.

In FF simulations such as those in Publication I, a correction due to the finite field is in order [104]. The energy correction is easy to calculate from Eq. (3.2):

$$\langle V_{\mathbf{F}} \rangle = -\sum_{k=1}^{M} \Big[\mu_\alpha(R_k) F_\alpha + \frac{1}{3} \Theta_{\alpha\beta}(R_k) F_{\alpha\beta} + \frac{1}{15} \Omega_{\alpha\beta\gamma}(R_k) F_{\alpha\beta\gamma} + \ldots \Big], \tag{4.21}$$

where care has been taken to consider each time-slice separately. Sample-averaged values cannot be used, because electric moments beyond the dipole order are nonlinear. The finite-field correction can be added as it is to the thermal estimator value. Correction to the virial estimator involves a potential gradient, which is [104]

$$-\tfrac{1}{2} R_k \nabla \mu_\alpha(R_k) F_\alpha = \tfrac{1}{2} \langle V_\mu \rangle \tag{4.22}$$

in case of the dipole moment. The higher multipoles are omitted, because they are not used in this Thesis and the tracelessness makes them more laborious to derive.

4.5.2 Imaginary-time correlation functions

Calculating imaginary-time correlation functions is straightforward in PIMC. Based on Eq. (2.105), the correlation functions are practically analogous to the Green's functions, and the former will be used for the remainder of this Thesis. According to Eq. (2.102), the measurements are averaged along the discrete sample path. That is, for a given reference $P(R_p)$, we compute the preceding measurements $Q_1(R_{q_1})$, $Q_2(R_{q_2})$ *etc*, where the time-slice indices are positive and ordered: $p \geq q_1 \geq q_2 > \ldots$. In case of symmetric correlators, *i.e.* $\hat{P} = \hat{Q}_1 = \hat{Q}_2 = \ldots$, it is maybe more intuitive to consider forward-

propagation. That is, for a given reference time-slice p, one evaluates *e.g.*

$$\begin{aligned}
G_2(0,0) &= P(R_p)P(R_p)P(R_p) \\
G_2(0,\Delta\tau) &= P(R_p)P(R_p)P(R_{p+1}) \\
G_2(\Delta\tau,0) &= P(R_p)P(R_{p+1})P(R_{p+1}) \\
G_2(\Delta\tau,\Delta\tau) &= P(R_p)P(R_{p+1})P(R_{p+2}) \\
&\cdots \\
G_2((M-1)\Delta\tau,0) &= P(R_p)P(R_{p-1})P(R_{p-1}),
\end{aligned}$$

and so on. The final estimate is the average over all indices p.

Clearly, measurement and storage of the correlation functions can be intensive: the correlation must be measured for all time-differences, that is, all $n \times M$ combinations in multiples of $\Delta\tau$. Symmetry can be utilized in order to reduce the required amount of computation and memory, and an optimized pseudocode for 1-time correlation functions is indeed provided in Publication IV. In this Thesis, we only calculate symmetric 1-time correlation functions, while the higher orders remain an interesting future avenue. The higher orders are also implicitly present in the static field-gradient estimators.

4.5.3 Sample-average estimators

In Sec. 3.2.4 we encountered expectation values in the form of $\langle P^{\partial\tau} Q_1^{\partial\tau} \dots Q_n^{\partial\tau} \rangle$, where $\partial\tau$ denotes an average over the imaginary-time sample trajectory. For two or more operators the measurement is generally correlated, *i.e.* $\langle P^{\partial\tau} Q_1^{\partial\tau} \dots Q_n^{\partial\tau} \rangle \neq \langle P Q_1 \dots Q_n \rangle$ for all $n \geq 1$. The path-averaging feature is a direct consequence of differentiation and cannot be turned off, unless the operator commutes with $\hat{H}$.

However, it has apparent benefits in the second and higher-order terms, namely

$$\begin{aligned}
P^{\partial\tau}(R) Q_1^{\partial\tau}(R) \dots Q_n^{\partial\tau}(R) &= (\Delta\tau)^{n+1} \sum_{p=0}^{M-1} P(R_p) \cdot \sum_{q_1=0}^{M-1} Q_1(R_{q_1}) \dots \sum_{q_n=0}^{M-1} Q_n(R_{q_n}) \\
&= (\Delta\tau)^{n+1} \sum_{p=0}^{M-1} \sum_{q_1=0}^{M-1} \dots \sum_{q_n=0}^{M-1} P(R_p) Q_1(R_{q_1}) \dots Q_n(R_{q_n}),
\end{aligned}$$

where the former sum only requires $n \cdot M$ operations, whereas M^n are involved in the latter sum, which arises naturally from the correlation functions.

To illustrate this, let us consider the dipole polarizability $\alpha_{z,z}$, which is the correlation function of the normal-ordered dipole operator, $\hat{P} = \hat{\mu}_z - \bar{\mu}_z$ and $\hat{Q} = \hat{\mu}_z$, where $\bar{\mu}_z = \langle \mu_z \rangle$ is the unperturbed expectation value. The associated polarizability is approximated as the discrete Fourier transform

$$\begin{aligned}\alpha_{z,z}(i\omega_n) &= \int_0^\beta \mathrm{d}\tau\, \mathrm{e}^{i\omega_n \tau} \langle\langle (\mu_z - \bar{\mu}_z)\mu_z(-\tau)\rangle\rangle \\ &\approx \sum_{m=0}^{M-1} \Delta\tau \mathrm{e}^{i\omega_n \Delta\tau} \left[\langle \mu_z \mu_z(-m\Delta\tau)\rangle - \langle \mu_z \rangle^2\right],\end{aligned}$$

which yields in the static limit $i\omega_n = 0$

$$\begin{aligned}\alpha_{z,z}(i\omega_n) &= \sum_{m=0}^{M-1} \Delta\tau \left[\langle \mu_z(m\Delta\tau)\mu_z\rangle - \langle \mu_z\rangle^2\right] \\ &= \beta\left[\langle \mu_z^{\partial\tau} \mu_z^{\partial\tau}\rangle - \langle \mu_z^{\partial\tau}\rangle^2\right],\end{aligned}$$

where $\langle \mu_z \rangle = \langle \mu_z^{\partial\tau} \rangle$, and the result is exactly the static field-gradient estimator. One also recognizes that the first-order polarizability equals to the statistical *variance* of the sample quantity in equilibrium. Similar exercise grows more laborious in higher order and is omitted here.

4.5.4 Error estimation

The usual unit of error in stochastic sampling is the standard error of the mean (SEM). For a series of uncorrelated samples A_i SEM is defined as [72]

$$\mathrm{SEM} = \frac{\sigma}{\sqrt{N}}, \tag{4.23}$$

where N is the number of samples, and σ is the standard deviation given by

$$\sigma^2 = \frac{1}{N-1} \sum_{i=1}^{N} \left(P_i - \bar{P}\right)^2, \tag{4.24}$$

where $\bar{P}$ is the mean. However, in Markovian processes that samples are usually correlated. The sample-correlation can be taken into account with a correction $\varkappa$ due to the average correlation time:

$$\mathrm{SEM} = \sigma \sqrt{\frac{\varkappa}{N}}, \tag{4.25}$$

which can be approximated for a finite set as

$$\varkappa \approx 1 + 2 \sum_{n=1}^{N} \frac{1}{(N-n)\sigma^2} \sum_{k=1}^{N-n} \left[(P_k - \bar{P})(P_{k+n} - \bar{P}) \right]. \tag{4.26}$$

In this work, we typically give 2SEM estimates, *i.e.*, twice that of Eq. (4.25), which gives statistical confidence of 95% for normally distributed random variables.

For other kinds of estimation, such as polynomial and nonlinear fitting, the error is usually 1SEM, often readily estimated by the fitting algorithm. More details are given in the associated publications.

4.6 Finite field simulation

A straightforward way to study the electric field response is to simulate the field itself. We have done this in case of static homogeneous field. The potential action due to a finite field F_α is in the primitive approximation

$$U(R, R'; \Delta\tau) = \int_0^{\Delta\tau} \mathrm{d}\Delta\tau \left\langle R \left| -\hat{\mu}_\alpha F_\alpha \right| R' \right\rangle \approx -\frac{\mu_\alpha(R) + \mu_\alpha(R')}{2} \Delta\tau F_\alpha, \tag{4.27}$$

and the last term is valid in the semi-classical approximation at the limit of short time-step $\Delta\tau$. In general, going beyond the primitive approximation is difficult, because the field cannot be easily incorporated in the matrix squaring of the Coulomb pair potential. The time-step error can be studied with time-step extrapolation, but since F is usually quite small, it is usually negligible. In the bisection sampling of charged particles, a special *drift* correction must be taken into account to compensate for a potential bias [104].

The FF simulation actually breaks the confines of perturbation theory: it contains all

the orders of static perturbation. On the downside, the simulation is only metastable, meaning that there is a finite possibility for the system to dissociate. That is, a charged particle, such as electron, could get loose in the field and never recombine with the original ion. This depends on the field magnitude: only relatively weak fields can be used. Remarkably, the orientational effect of the field becomes apparent in an AQ simulation. In Publication I we study it using an orientation parameter

$$S = \tfrac{1}{2}\langle 3\cos^2\theta - 1\rangle, \tag{4.28}$$

where θ is the angle between the field and molecular axis.

We could also study coupling to field-gradients. That would mean a non-homogeneous field, which then would need to be fixed in space. Furthermore, studying field-gradients would involve more orders of Cartesian components to study. However, we did not pursue to exercise finite-field simulation in the gradient order. Dynamic fields cannot be simulated directly, unless the PIMC propagator, sampling and measurements are fundamentally changed.

4.7 The Fermion sign problem

Let us briefly review the infamous challenge of the FSP for PIMC simulations. Based on the permutation property from Eq. (2.19) the thermal density matrices for N identical particles are defined as [118, 125]

$$\rho(R,R';\beta)_{F/B} = \frac{1}{N}\sum_{\mathscr{P}}(\pm 1)^{\mathscr{P}}\rho(R,\mathscr{P}R';\beta),$$

where F/B and $+/-$ refer to fermions/bosons, respectively. The bosonic simulation is straightforward, because the sign is always positive definite. One must still consider the permutations, which can become tedious for large N. However, instead of N explicit permutations, one can sample the permutation space and the phase-space simultaneously.

With fermions, all the odd permutations have negative signs. If the measure of the density matrix is not positive definite, stochastic sampling cannot be done directly. One can

still sample the boltzmannon distribution, including permutations, but have explicit account of the sign s. Then, an observable expectation value is evaluated as [126]

$$\langle P \rangle = \frac{\langle s\hat{P} \rangle}{\langle s \rangle},$$

which is plausible if the average sign $\langle s \rangle$ is *large enough*; if not, the denominator vanishes and the statistical fluctuation explodes. The numerical sign problem is NP-hard [127] and generally gets worse as N or β are increased [118, 126].

There have been different attempts to solve the Fermion sign problem, such as the configuration PIMC (CPIMC) [128] or permutation-blocking PIMC [129], and the so-called Majorana algorithms [130]. One of the most popular is the fixed-node approach, also known as the Restricted PIMC (RPIMC) [118, 131]. It is based on the identity

$$\rho_F(R_\beta, R_*; \beta) = \int \mathrm{d}R_0 \rho_F(R_0, R_*; 0) \oint_{R_0 \to R_* \in \Gamma(R_*)} \mathrm{d}R_\tau \mathrm{e}^{-S[R_\tau]}, \tag{4.29}$$

meaning, briefly, that only such paths are sampled that are node-avoiding with respect to the reference bead R_*. Then, the nodes become the most decisive factor in terms of accuracy and ergodicity of the simulation. Calculation of the nodal surface is often cumbersome and approximate, although controllable schemes, such as the free-particle nodes exist [72, 131].

There is a hardship related to estimation of polarizabilities and correlation functions in the fixed-node scheme. Namely, if the nodes are only accurate for the reference bead, one is unable to correlate two or more arbitrary time-slices without some sort of error. Alternatively, the perturbation can be coupled to the definition of the nodal surface. Unfortunately, detailed analysis and benchmarking of the RPIMC approach could not be included in this Thesis. The entity of Fermion statistics and the sign problem is still highly important and should be looked into in the future.

5 THERMAL EFFECTS IN STATIC POLARIZABILITIES

Thermal coupling has various effects on the different components of polarizability, as already seen in Chapter 3. On one hand, most atomic systems are practically invariant of the temperature, and are thus suitable for benchmarking against 0 Kelvin results. On the other hand, molecular systems with rovibrational degrees of freedom show strong thermal effects in the polarizabilities of all orders.

In this Chapter, we present and discuss static polarizabilities of various atoms and molecules using the PIMC method as described in Chapter 4. The static response is estimated with the field-derivative estimators, but also the finite-field approach is used to show the orientational effect. The most special feature is the fully nonadiabatic AQ simulation of molecules. It provides the exact total polarizability, which is approximately but not quite equal to the sum of its constituents: the electronic, rovibrational and nonadiabatic components.

In the following, we show examples of the most important thermal phenomena and benchmark data, whose complete details are found in Publications I–III. In the temperature range of 25–3200 Kelvin, the most important phenomena are related to centrifugal distortion and thermal decay of the orientational effect. We propose a semiempirical model to study the rotationally active polarizabilities over the full temperature range. Furthermore, we provide comprehensive benchmarking data, which agree with the literature but also complement it for many exotic systems, such as H_3^+, HeH^+ and Ps_2.

5.1 Static atomic polarizability

In the following, we consider the static polarizabilities of isolated atoms, atomic ions and positron systems. They are characterized by spherical symmetry and the apparent lack of thermal effects, since there are no low-energy excitations. That is, even relatively high-temperature simulations, *e.g.* $T \sim 4000$ Kelvin, correspond to the electronic ground states and the results be compared to 0 Kelvin values from the literature. Thus,

the atomic data is mostly studied for benchmark purposes, but we also present some novel data: higher-order polarizabilities of some positron systems and notable thermal effects in H^-.

5.1.1 Benchmarking with atoms

Table 5.1 contains the static polarizabilities and hyperpolarizabilities of several atoms and atom-like species in BO simulation. Due to the spherical symmetry, the number of independent tensors is small – in fact, the polarizabilities are scalar. However, we use the laboratory coordinate denotation Z for consistency with later tables. Some 0 Kelvin literature references are provided, when available, and the match is generally excellent. Not only does it mean that the PIMC estimators are working fluently, but that the simulation is a powerful black box. More discussion and better detail on the simulation parameters are given in Publications I-IV.

5.1.2 Thermal effects

The thermal effects of atomic polarizabilities are mostly negligible within the numerical accuracy, but the hydrogen negative ion H^- is a curious exception. Figure 5.1 shows that the static dipole polarizability and second hyperpolarizability show a notable drop

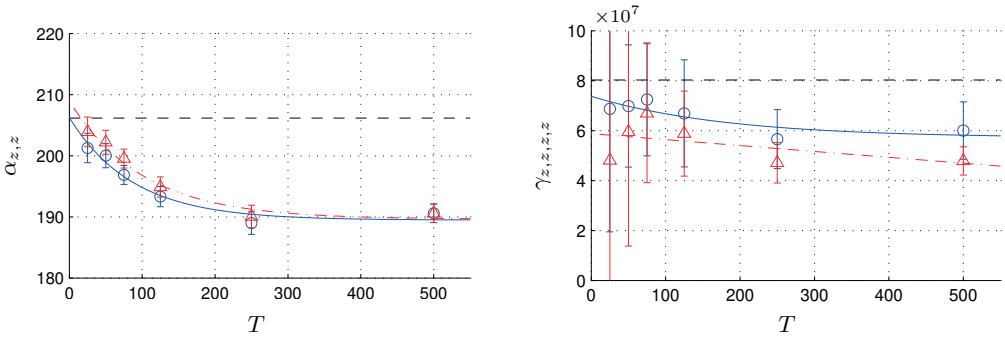

Figure 5.1 Thermal dependence of static polarizability $\alpha_{z,z}$ and hyperpolarizability $\gamma_{z,z,z,z}$ of H^- (BO) using static field-gradient estimators. Modified from Publication II.

Table 5.1 Total energies, static dipole polarizabilities, hyperpolarizabilities and some field-gradient polarizabilities of atoms or systems with atom-like symmetry. 2SEM error estimates are given in the parentheses and the values are in atomic units.

Atom	E	$\alpha_{z,z}$	$\gamma_{z,z,z,z}$	$B_{zz,z,z}$	$C_{zz,zz}$
H	-0.49997(5)[a]	4.496(23)[a]	1586(184)[a]		
	-0.49996(2)[b]	4.502(4)[b]	1331(28)[b]		
	-0.49995(3)[c]			-106.5(3)[c]	5.003(4)[c]
	-0.49993(2)[d]	4.5023(9)[d]			5.004(3)[d]
	-0.5[f]	4.5[f]	1333.33[f]	-106.5[f]	5.0[f]
H^-	-0.52781(7)[b]	209(5)[b]	5.9×10^{7}[b]		
	-0.52781(7)[c]			$-4.78(87)\times10^{5}$[c]	2568(136)[c]
	-0.52775[g,b]	206.15[i]	8.03×10^{7}[i]	-4.843×10^{5}[j]	2591.6[j]
He	-2.9036(2)[b]	1.382(4)[b]	42(6)[b]		
	-2.9032(2)[c]			-7.32(9)[c]	0.814(2)[c]
	-2.90372[b]	1.38319217[k]	43.104[k]	-7.3267[l]	0.8150[l]
Li^+	-7.2810(4)[b]	0.1923(4)[b]	0.24(8)[b]		
	-7.2800(7)[c]			-0.121(3)[c]	0.03797(9)[c]
	-7.279913[m]	0.192453[m]	0.2429[l]	-0.1214[l]	0.05694[l]
Be^{2+}	-13.647(12)[c]	0.05223(6)[e]	0.008(2)[e]	-0.0083(3)[c]	0.005106(15)[c]
	-13.655566[m]	0.052269[l]	0.008476[l]	-0.008393[l]	0.007660[l]
Ps	-0.24999(2)[b]	36.00(4)[b]	$1.70(4)\times10^{5}$[b]		
	-0.25[f]	36[f]	$1.7067(4)\times10^{5}$[f]		
Ps_2	-0.51597(7)[c]			0[c]	460(7)[c]
	-0.51598(8)[d]	71.57(8)[d]			463(7)[d]
	-0.5160038[n]				
PsH	-0.78932(7)[b]	42.27(7)[b]	$1.60(8)\times10^{5}$[b]		
	-0.7893(3)[c]			5300(260)[c]	260(3)[c]
	-0.78913[p]	42.2836[q]			

[a]Publication I; [b]Publication II; [c]Publication III; [d]Publication IV; [e]This thesis with $\Delta\tau = 0.002$; [f] exact, Bishop *et al* [132]; [g]Lin [133]; [h]Nakashima *et al* [134]; [i]Kar [135]; [j]Pipin *et al* [136]; [k]Cencek *et al.* [137]; [l]Bishop *et al.* [138]; [m]Johnson *et al.* [139]; [n]Bubin *et al.* [140]; [p]Frolov *et al.* [141]; [q]Yan [142]

due to the temperature. The polarizabilities have been modeled with an exponential fit. Unlike the neutral atoms and positive ions, the electronic density of H^- is very diffuse, and thus, its polarizability is very high. The drop due to thermal coupling is caused by activation of low-lying electronic excitations. Alternatively, the delocal character is decreased by thermal decoherence, or contraction of the thermal wavelength.

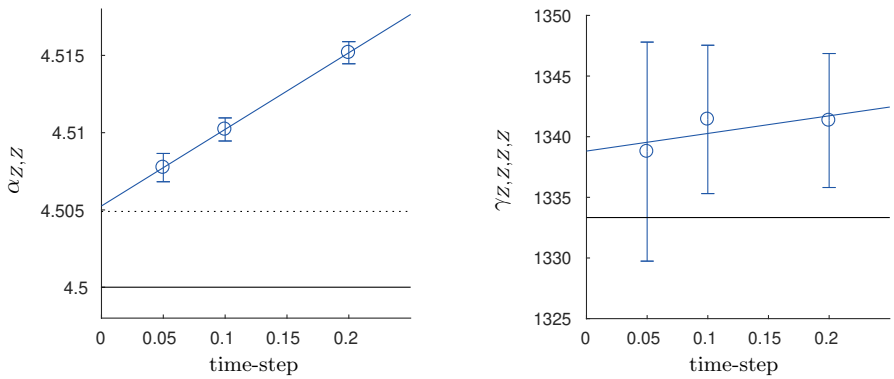

Figure 5.2 Nonadiabatic effects in the static dipole polarizability and second hyperpolarizability of H using static field-gradient estimators. The solid lines indicate the adiabatic BO values, and the dotted line is the analytic reference value for $\alpha_{Z,Z}$.

5.1.3 Nonadiabatic effect

Let us study the nonadiabatic effect of the Hydrogen atom, whose reduced mass is approximately $0.999456 m_e$. An AQ simulation produces $\alpha_{Z,Z} = 4.505(1)$ and $\gamma_{Z,Z,Z,Z} = 1339(7)$. The values clearly differ from the BO results ($\alpha_{z,z} = 4.5$ and $\gamma_{z,z,z,z} = 1333.3$), but they agree with the analytic finite-mass correction, which gives $\alpha_{Z,Z} = 4.50490275$ [143]. This is shown in Fig. 5.2, which also contains a linear time-step extrapolation. Namely, a finite time-step error is purely due to the static field-derivative estimators, because the pair-density matrix of H is exact. This is the only dedicated indication of the estimator error, because usually a bigger error is accumulated from other sources.

Overall, the nonadiabatic effect is present in all AQ simulations and realistic systems. On one hand, the effect is obviously smaller in magnitude and more difficult to extract for nuclei heavier than proton. On the other hand, the combined recoil effects of more than one electron cancel out to some extent. Most importantly, the effects due to rotation and zero-point vibration are orders of magnitude larger. Yet, more dedicated studies on the nonadiabatic effect are called for, because the phenomenon is increasingly significant in the research of, *e.g.*, isotope effects, proton transfer, and chemical reaction pathways [144, 145]. For the moment, let us rest assured that the AQ simulations contain the proper account of the effect.

5.1.4 Positron systems

Positrons are the antiparticles of electrons. Their masses are equal and the recoil effect is at maximum: positron simulation is in a way the ultimate nonadiabatic limit. Positron are known to form compounds, such as positronium Ps (electron and positron), dipositronium Ps_2 and PsH. We will not consider the annihilation, although the annihilation rate can be extracted from PIMC simulations [72]. Instead, we focus on the dielectric properties that are important in positron spectroscopy.

In Publications II and III we report original benchmark data for various polarizabilities of Ps, Ps_2 and PsH. This data is also presented in Table 5.1. The table indicates that no prior data exist for higher-order polarizabilities, to the best of our knowledge. Furthermore, inspired by the question, whether PsH is an atom or a molecule [146], we also projected the internal dipole moment of the system: $\mu^{(0)} = 0.0305(6)$.

5.2 Static molecular polarizability

Due to the inertia of the nuclei, molecular systems have less symmetry, and thus, more polarizability tensors that are independent. The dielectric response of molecules is more diverse than that of atoms. In BO simulation, we only sample the electronic state at the equilibrium nuclear geometry. Thus, we do not expect thermal coupling. We study the molecule at its internal coordinates, which is awkward in terms of experiment, but motivated for benchmarking and wholesome understanding of the dielectric response.

On the other hand, in AQ simulation we enable nuclear degrees of freedom and the nonadiabatic effect. The rovibrational motions resonate at different energies, which leads to low-lying thermal effects also in the static limit. Especially, we can observe and explain centrifugal and orientational effects due to temperature, which are also associated with microwave, IR, or Raman activity depending on the degree of perturbation. Complementary views on the dynamic spectrum are given in Chapter 6.

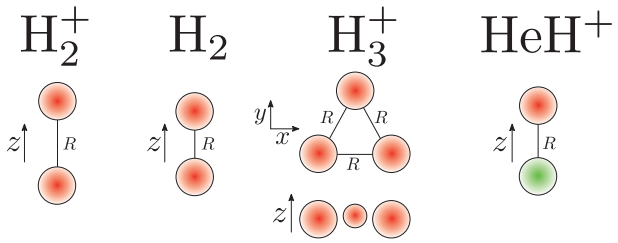

Figure 5.3 Orientations of the molecules with respect to z-axis.

5.2.1 Benchmarking with fixed molecules

Again, we start by benchmarking the results against known values in the BO approximation. That is, the nuclei are fixed at the equilibrium geometries and aligned with respect to z-axis, according to Fig. 5.3. Consequently, the rovibrational motion and thermal effects are suppressed. The result corresponds to the ground state electronic polarizability at a fixed orientation: the tensorial property in the internal molecular coordinates.

Table 5.2 contains some results of total energies and independent tensorial polarizabilities. The number of independent tensors for different symmetry point groups is reviewed in Ref. [8]. In addition, there are some more special independent properties, such as $\mu_z = 0.6788(1)$ for HeH^+ and $\beta_{y,y,y} = 1.12(14)$ for H_3^+. Comparison with some of the available references shows great agreement. Small discrepancies exist due to various reasons, such as statistical fluctuation and time-step error of the pair-approximation – but also erroneous references. Again, complementary data and technical details are found in the original Publications.

The BO simulation could be pushed further in many aspects, such as using potential energy surfaces to study rovibrational effects. However, the objectives of this Thesis are quite the opposite: studying the exact total polarizability in a straightforward nonadiabatic simulation.

Table 5.2 Total energies, static dipole polarizabilities, hyperpolarizabilities and some field-gradient polarizabilities of fixed molecules and molecular ions. 2SEM error estimates are given in the parentheses and the values are in atomic units.

Molecule	R	E	μ_z	$\alpha_{z,z}$	$\alpha_{x,x}$
H_2	1.4	-1.17434(18)[a]		6.382(13)	4.577(10)
	1.4	-1.1746(4)[b]		6.388(7)	4.574(5)
		-1.17447477[c]		6.387493[d]	4.57861[d]
H_2^+	2.0	-0.60259(10)[b]		5.080(4)	1.7586(8)
		-0.602634214[e]		5.0776490[f]	1.757648[f]
H_3^+	1.65	-1.3438(3)[b]		2.202(2)	3.549(3)
		-1.3438356[b]		1.7322[i]	3.2923[i]
HeH^+	1.46	-2.9785(6)[b]	0.6788	1.544(21)	0.8515(7)
		-2.978706[j]	0.655[j]	1.5421[k]	0.85070[k]

Molecule	$\gamma_{z,z,z,z}$	$\gamma_{x,x,x,x}$	$\gamma_{z,z,x,x}$	$\gamma_{z,x,z,x}$
H_2	787(100)[a]	640(73)	211(10)	191(7)
	700(49)[b]	572(26)		
	682.5[d]	575.9[d]		
H_2^+	-43(17)[b]	73(2)	27(2)	24.2(5)
	-193.76[g]	83.87[g]	29.73[g]	
H_3^+	51(4)[b]	58(11)	19(2)	19(3)
HeH^+	11(507)[b]	7.2(8)	3(8)	2.4(2)

Molecule	Θ_{zz}	$C_{zz,zz}$	$C_{xx,xx}$	$C_{xz,xz}$
H_2	0.4563(2)[q]	5.99(2)	4.930(13)	4.176(6)
	0.45684[l]	5.983[d]	4.927[d]	4.180[d]
H_2^+	1.53071(8)[q]	1.913(12)	1.268(5)	1.1946(7)
	1.5307[m]	1.9113[n]	1.2670[n]	1.1945[n]
H_3^+	-0.91953(10)[q]	1.557(10)	2.078(6)	1.2441(10)
	-0.92613[p]			
HeH^+	1.24956(13)[q]	0.59(2)	0.396(6)	0.3382(5)

[a]Publication I; [b]Publication II; [c]Kolos *et al.* [147]; [d]Bishop *et al.* [148]; [e]Turbiner *et al.* [149]; [f]Tsogbayar *et al.* [150]; [g]Bishop *et al.* [151]; [h]Turbiner *et al.* [152]; [i]Kawaoka [153]; [j]Pachucki [154]; [k]Pavanello *et al.* [155]; [l]Poll *et al.* [156]; [m]Bates *et al.* [157]; [n]Bishop *et al.* [158]; [p]Carney *et al.* [159] ($R = 1.6504$); [q]Publication III

5.2.2 Nonadiabatic simulation

In the nonadiabatic AQ simulation the electrons and the nuclei are treated on an equal footing: as fully quantized particles. As discussed in Sec. 4.4.2, the PIMC interface is very straightforward: the nuclei, too, are expanded into imaginary-time trajectories. The computational penalty is increased sampling, which is elevated by the mass difference between electrons and ions. Another essential feature is the evident isotropic sampling: free nuclei probe the full orientational space, unless some external constraint or projection is used. Most importantly, all the thermal and nonadiabatic effects are simultaneously activated.

It should be noted that the nuclei are simulated as boltzmannons, *i.e.*, distinguishable particles. This does not produce entirely truthful thermal occupation of different nuclear spin isomers, such as ortho/para-H_2. The spin isomers have different rotational activation, which may also affect the orientational coupling of polarizabilities at low temperatures. The effect becomes negligible, when the thermal wavelength $\lambda_{\mathrm{th}} = \sqrt{2\lambda\beta}$ of the nuclei becomes small compared to the nuclear separation, *i.e.* at high temperatures. For protons in the hydrogen systems, this is $\sim 100\,\mathrm{K}$. The issue is discussed *e.g.* in Refs. [160, 118].

In this Thesis, we only provide the isotropic averages of the polarizabilites, denoted with the laboratory coordinate Z. Table 5.3 contains a compilation of results extrapolated to 0 Kelvin. Agreement with the literature is mostly good, but many of the nonadiabatic results are also novel in the literature. There are small discrepancies, whose origins include statistical fluctuation, time-step error of the pair-approximation, and error in the extrapolation to 0 Kelvin. Better details are given in Publications I-IV. Need for the extrapolation to 0 Kelvin emerges from the apparent thermal effects. In the following, let us briefly discuss their cause and nature.

Vibrational effect

The effect of zero-point vibration can be seen from the total energy. The energy differences between BO and AQ energies (extrapolated to 0 K) are approximately $\Delta E \sim$ 10mHa for H_2, $\Delta E \sim 5.4$mHa for H_2^+, $\Delta E \sim 21$mHa for H_3^+ and $\Delta E \sim 12$mHa for

Table 5.3 Total energies, static dipole polarizabilities, hyperpolarizabilities and field-gradient polarizabilities extrapolated to 0 Kelvin. 2SEM error estimates are given in the parentheses and the values are in atomic units.

	E	$\alpha_{Z,Z}$	$\gamma_{Z,Z,Z,Z}$	$B_{ZZ,Z,Z}$	$C_{ZZ,ZZ}$	$G_{ZZZ,ZZZ}$
H_2	-1.16239(2)[a]	5.42(4)[a]	2678(300)[a]			
	-1.16239(2)[b]	5.424(3)[b]	2839(894)[b]			
	-1.1625(11)[c]			160(35)[c]	32(6)[c]	
	-1.1633(8)[d]	5.42(3)[d]			17.8(3)[d]	7.9(2)[d]
	-1.164025[e]	5.4139[f]	1763[g]			
H_2^+	-0.5975(12)[b]	3.168(49)[b]	12750(1403)[b]			
	-0.596(2)[c]			3000(580)[c]	580(150)[c]	
	-0.597193[b]	3.168725[b]	11479.805[b]		457.30[b]	1.55983[b]
HD^+	-0.5968(3)[d]	43.6(4)[d]			200(5)[d]	28.4(6)[d]
	-0.597898[b]	395.306328[b]	-3.356560[b]		683.41[b]	51.562[b]
H_3^+	-1.3233(3)[b]	3.873(24)[b]	3728(642)[b]			
	-1.323(5)[c]			860(720)[c]	157(39)[c]	
	-1.323568[i]					
HeH^+	-2.9827(3)[b]	528(23)[b]	$-1.202(11)\times10^{9}$[b]			
	-2.9670(8)[c]			3.4×10^{6}[c]	406(110)[c]	
	-2.96627[j]					

[a] Publication I; [b] Publication II; [c] Publication III; [d] Publication IV (300 K); [e] Bishop *et al*; [f] Kolos [147]; [g] [58]; [h] Tang *et al* [161]; [i] Kylänpää [71]; [j] Calculated from Refs. [154] and [162]

HeH^+. Obviously, the zero-point motion affects the total polarizability, too, but the effect is marginal. Thus, we have not made effort to extract or quantify it from the results. A dedicated study of the nonadiabatic coupling to zero-point vibration remains an interesting challenge.

Centrifugal effect

At higher temperatures, the rotational ensemble shifts to higher states, *i.e.*, the incorporation of higher centrifugal effects. Consequently, the average bond length is increased, which also increases the electronic polarizability. This is in agreement with fixed-nuclei studies, which imply that a system closer to dissociation is also more polarizable [109]. PIMC results of the centrifugal increment are displayed in Fig. 5.4. Nonpolar species H_2^+, H_2 and H_3^+ exhibit an increment in the dipole polarizability $\alpha_{Z,Z}$, which is around 0.5% at room temperature and between 6—10% at 1600 Kelvin. The 0 Kelvin limit has

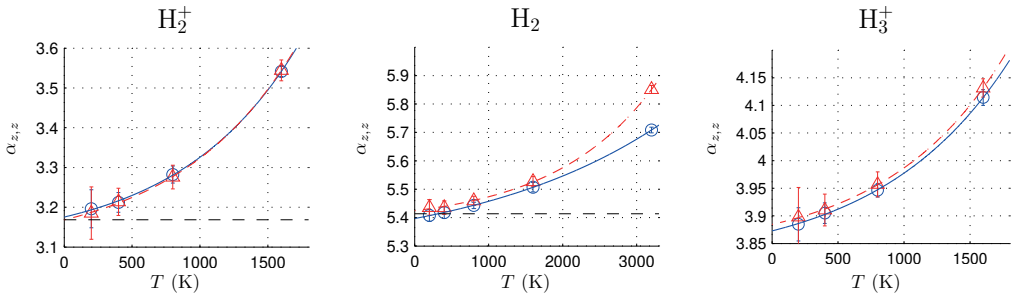

Figure 5.4 Nonadiabatic dipole polarizabilities $\alpha_{Z,Z}$ of molecules (AQ) against the temperature using two time-steps (blue and red) using static field-gradient estimators. Modified from Publication II.

been obtained with a phenomenological quadratic fit. However, the high-temperature limit of the effect is approximately linear, as discussed in Sec. 3.4.2. Of course, at very high temperatures, the approximate model breaks down, as the molecules dissociate and the total polarizability becomes a sum of the constituent particles.

Exact recovery of the centrifugal phenomenon, including the nonadiabatic effects, is difficult from approximate models, such as the rigid rotor. Yet, the effect is already notable and should perhaps be better appreciated in modeling and parameterization.

Orientational effect

Orientational coupling is the most important of the rotational effects. The requirement of favorable orientation emerges from degrees of anisotropy in electric moments. For instance, dipole moment couples to a homogeneous field, causing large orientational effects to the associated dipole polarizability. Thus, the systems with permanent moments, *i.e.* polar molecules, are rotationally active in the first order of perturbation. Yet, even nonpolar molecules have rotational effects in higher orders: if the first-order polarizability is anisotropic, so are the induced moments responding to further perturbations. That is, all non-spherical systems are bound to have rotational effects in the higher-order response, the hyperpolarizabilities. For instance, the values for the second hyperpolarizability γ can be compared between the BO result from Tables 5.2 and AQ results from Table 5.3: the values are off by several orders of magnitude.

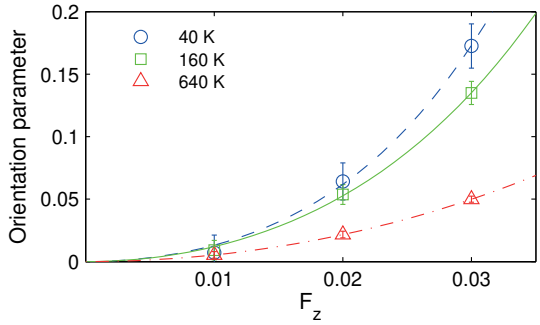

Figure 5.5 Orientation parameter of H_2 (AQ) against finite field strength F_z and temperature from Publication I. The orientational effect increases in stronger fields and lower temperatures.

There are several ways to understand the quantitative foundation of the orientational effect. According to Sec. 3.4.2, the rotational polarizability is proportional to the inverse temperature. Indeed, the same β-dependence can be seen from the estimators of Table 3.2: nonzero and invariant electric moments, such as the permanent $\mu^{(0)} = \langle\mu\rangle$, will dominate the higher-order polarizabilities in some power of β. Generally $\alpha_{\mathrm{rot}}(\beta) \propto \Delta\alpha\beta^n$, where n is some integer power depending on the degree of polarizability α. However, it turns out that additional perturbations over rotationally active response properties do counter the orientational effects and change the sign. Well-known "laws" [29] such as this are used very liberally to explain the results of this Thesis, while their rigorous foundations are omitted.

Thermal decay of the orientational polarizability is most directly understood as an interference due to the thermal bath. This is seen in Fig. 5.5, where the orientation parameter S from Eq. (4.28) has been obtained from finite-field simulations of H_2. S indicates a clear orientational effect due to the field, but the effect fades off as a function of temperature.

5.2.3 Total polarizability

Finally, let us summarize and appreciate the total molecular polarizability and its thermal coupling. First, the obvious component is the electronic polarizability, whose thermal value is the isotropic average. The electronic state is effectively invariant of the tem-

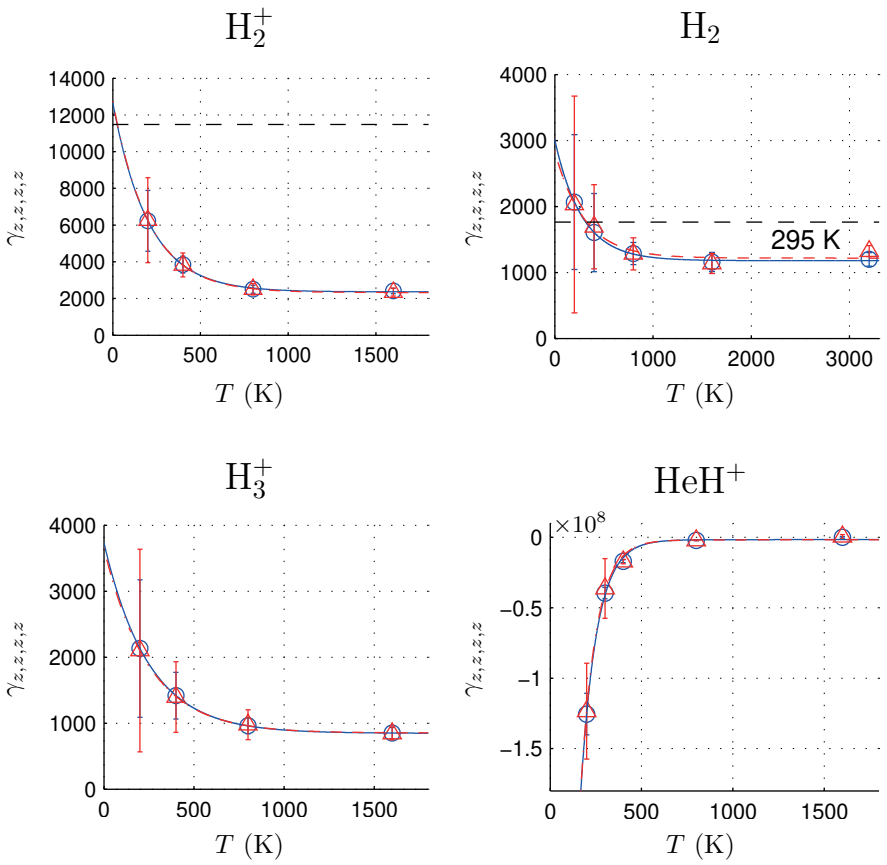

Figure 5.6 Nonadiabatic second hyperpolarizabilities $\gamma_{Z,Z,Z,Z}$ of several molecules (AQ) against the temperature using two time steps (blue and red) using static field-gradient estimators. Modified from Publication II.

perature, but the centrifugal distortion affects the electronic structure, and thus, the polarizability. An additional dominant rotational polarizability emerges, if and only if the system has anisotropies, such as permanent moments. Lastly, small nonadiabatic corrections due to finite nuclear masses are involved in all of the aforementioned effects. The conventional decomposition to electronic and rovibrational polarizabilities is only approximately correct.

For example, the total second hyperpolarizability γ is shown in Fig. 5.6 as a function of temperature for four molecules: H_2^+, H_2, H_3^+ and HeH^+. The first three species are nonpolar, so the orientational effect is positive; HeH^+ has a strong orientational

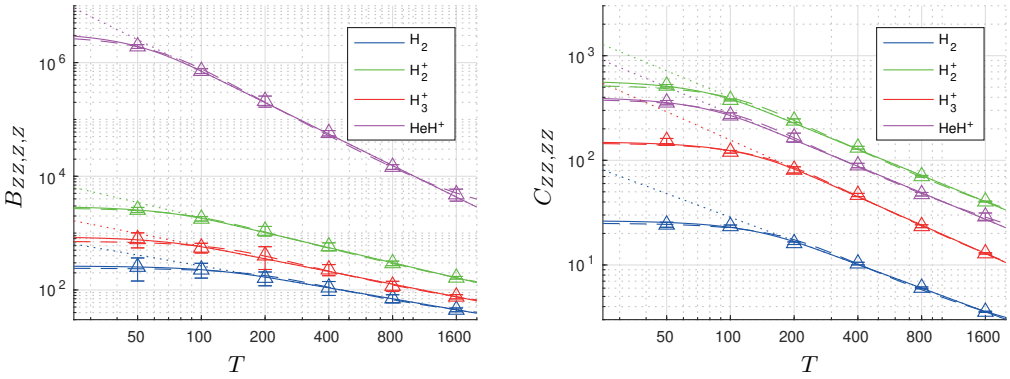

Figure 5.7 Logarithmic plot of the field-gradient polarizabilities B and C for some molecules (AQ) from Publication III.

effect already in the first order α, which reflects as a negative correction for γ. The first hyperpolarizability β is zero due to its symmetry against isotropic averaging. The strength of the orientational effect depends, loosely, on the magnitude of anisotropy: out of the nonpolar molecules, the low-temperature γ is largest for H_2^+ and smallest for H_2, and so are their internal anisotropies $\Delta\alpha = \alpha_{z,z} - \alpha_{x,x}$. Thus, the internal quantities do have indirect experimental significance. In Publication II, we proposed an *ad hoc* fit

$$\alpha(T) = a_1 \exp(a_2 T) + a_3, \tag{5.1}$$

where α is the total polarizability and a_i are characteristic factors. Equation 5.1 was used to extrapolate polarizabilities to 0 Kelvin.

However, closer inspection suggests that the orientational effect scales as T^{-x} rather than $\exp(-x)$ at high temperatures. On the other hand, the low-temperature limit should converge to a finite value, due to thermal activation of the rotational states. Thus, in Publication III we propose a better fit, namely

$$\alpha(T) = \left(\frac{a_1 \cdot \mathrm{erf}(a_2 T)}{T} \right)^x + a_3, \tag{5.2}$$

which obeys both limits. Natural choices for the exponent x are 1 for first-order orientational effects, such as $C_{ZZ,ZZ}$ of H_2, and 2 for second-order orientational effects, such as $B_{Z,Z,ZZ}$ of HeH^+. However, optimizing x yields an exponent somewhat smaller than

the integer. That is because the approximate formula merges all the thermal effects, including centrifugal distortion, into simple empirical trends. The thermal saturation is illustrated in Fig. 5.7, where the solid lines are the actual fits and in the dotted lines the erf-function has been replaced by unity. More discussion on the fits can be found in Publications II and III. Generally, the transition between low-T to high-T limits is non-trivial, and in that sense, the PIMC results featured in this Thesis are uniquely accurate.

6 DYNAMIC POLARIZABILITY AND VAN DER WAALS COEFFICIENTS

Studying dynamic polarizability is more challenging but also more rewarding than the static limit. The whole spectrum of electric field response – both dispersive and absorptive – is encoded in the frequency-dependent susceptibility. The spectral phenomena of small molecules are commonly decomposed into separate wavelengths, such as radiowaves (Rayleight dispersion), microwaves (rotation), infrared (vibration), x-ray (electronic), and beyond (scattering cross-section). However, the aim of this Thesis is to go beyond such decompositions and provide exact mixing of the full spectrum.

In the following, we consider the dynamic response in terms of first-order polarizabilities $\alpha_1(\omega)$, $\alpha_2(\omega)$, $\alpha_3(\omega)$, corresponding to the three lowest electric multipoles. The real-time correlation involves an out-of-equilibrium many-body problem – a formidable challenge for any numerical method. The PIMC method solves the many-body problem, but the time-correlation is only measured in the imaginary time. The imaginary-time correlation contains in principle all the spectral information, which can be recovered using analytic continuation. Unfortunately, the practical numerical transforms are ill-posed. The challenging inversion problem calls for special means, and in this Thesis, we utilize a popular method called Maximum Entropy method (MaxEnt) [73, 74].

This chapter is organized as follows: we start by considering the multipole correlation in the imaginary domain. We briefly go through some practical details on the workflow, such as optimization and Fourier transform. Especially, we demonstrate the use of Matsubara data in the estimation of van der Waals coefficients. Finally, we use MaxEnt inversion to estimate and analyze dynamic multipole spectra and first-order polarizabilities of various systems: H, He, H_2 and HD^+. The thermal effects encountered are familiar and complementary to those observed earlier.

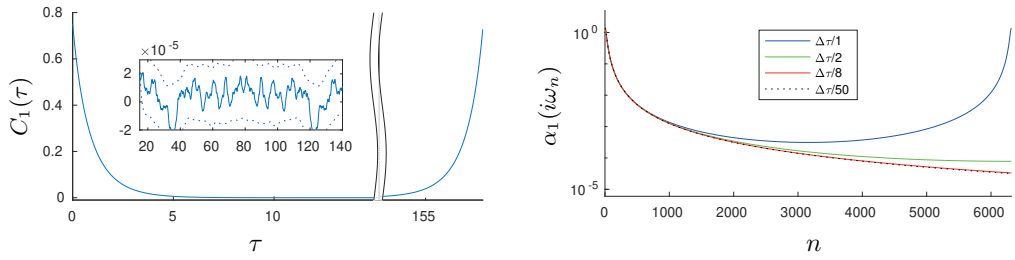

Figure 6.1 Dipole–dipole correlation function of He (BO) at $T = 2000$ K in imaginary time (left) and as a function of Matsubara frequencies (right) from Publication IV.

6.1 Multipole correlation in imaginary time

Earlier in this work, we have considered the properties and estimation of quantum correlation functions. The correlation function is a hugely important entity, because all the fine details of the thermal density matrix – electronic correlation, rovibration, nonadiabatic effects – are projected into its meaningful digits. Later, these features are extracted to form a spectrum and an estimate of a dynamic polarizability.

6.1.1 Symmetric 1-time correlation

For the rest of this chapter, we will discuss symmetric 1-time correlators, *i.e.* correlation functions involving two identical measurements. In particular, we consider electric multipole correlators up to the third order, namely $C_1 \equiv \langle\hat{\mu}(\tau)\hat{\mu}\rangle$, $C_2 \equiv \langle\hat{\Theta}(\tau)\hat{\Theta}\rangle$ and $C_3 \equiv \langle\hat{\Omega}(\tau)\hat{\Omega}\rangle$, where $0 \leq \tau \leq \beta$.

In PIMC simulation, the computation of 1-time correlation functions is straightforward and done according to Eq. (2.102). An example that is plotted in Fig. 6.1 demonstrates some of the typical features: the function is symmetric, *i.e.* $C(\tau) = C(\beta - \tau)$, and decreases rapidly down to the uncorrelated mean value. In atomic systems and AQ simulations the mean is always zero; that is, all of the aforementioned correlators have implicit normal ordering. Furthermore, around the mean there is statistical fluctuation, which can be decreased by providing more MC data, but never completely eliminated.

6.1.2 Fourier transform

Taking a Fourier transform according to Eq. (2.106) gives the imaginary-time correlation function in terms of discrete Matsubara frequencies. The transform is a continuous integral, but the correlation function is only known at discrete time-slices. To the first approximation, one can write the integral as the sum over the discrete time-steps:

$$\alpha(i\omega_n) \approx \Delta\tau \sum_{m=0}^{M-1} \mathrm{e}^{-i\omega_n \Delta\tau} C(m\Delta\tau), \tag{6.1}$$

which is equivalent of the discrete Fourier transform producing the M lowest Matsubara frequencies. The discrete transform is easy to implement, but there is an error due the finite sampling resolution $\Delta\tau$, which increases with the Matsubara frequency ω_n.

An example of Matsubara data thus produced is shown in Fig. 6.1. Since $C(\tau)$ is symmetric, $\alpha(i\omega_n)$ is purely real, and it should also be monotonically decreasing to 0. However, if the original data is used, the result becomes symmetric instead, due to the finite resolution error. Fortunately, the error can be controlled by using, for instance, cubic spine interpolation to increase the effective resolution. For instance, the resolution $\Delta\tau/8$ already produces quite a decent accuracy for the first M frequencies. In the limit of infinite resolution, the transform becomes continuous. Usually, this is not necessary, since contribution of the higher frequencies is negligible.

The Fourier transform is linear, which means that independent samples can be first transformed and then averaged. The benefit is that one can then estimate the statistical properties, such as the covariance matrix of the Matsubara data. An estimate of the covariance matrix $\langle C \rangle$ over N samples is given by

$$\langle C_{mk} \rangle = N^{-1} \sum_{n=1}^{N} (\alpha(i\omega_m) - \bar{\alpha}(i\omega_m))(\alpha(i\omega_k) - \bar{\alpha}(i\omega_k)),$$

where $\bar{\alpha}(i\omega_m)$ is the sample mean. An invertible $\langle C \rangle$ is later needed for reliable MaxEnt inversion.

6.1.3 Higher order correlation

Naturally, one is right to be curious about more exotic correlation functions and their implications on the response properties. The higher-order polarizabilities featured in this work are obviously related to specific 2-time correlators and beyond. The dynamic property makes them much more diverse and interesting than the static limit suggests. For instance, combinations between different spectral regions open up the analysis of interesting spectral properties, such as Raman spectroscopy. Yet, for the very same reason the complexity grows exponentially for the entire account of implementation concerns, such as memory layout and Fourier transforming, not to mention the analytic continuation. In this sense, this Thesis is not an exhaustive study, but a scratch on the surface.

6.2 van der Waals dispersion coefficients

Long-range interaction is one of the biggest challenges in quantum many-body simulations. Approaches such as DFT and MD, which are otherwise very scalable and efficient, struggle to model the correct van der Waals dispersion. The Lennard–Jones potential has been successful in modeling the asymptotic r^{-6}-dependence of the London dispersion: the interaction of quantum fluctuating dipole moments. However, not only can the higher multipoles be meaningful [33], but there are effects arising from quantum electrodynamics that are proportional to r^{-7} [163]. In the following, we will consider the London interaction, which is given for two spherically symmetric species A and B as

$$V(r) = -\frac{C_6^{AB}}{r^6} - \frac{C_8^{AB}}{r^8} - \frac{C_{10}^{AB}}{r^{10}} - \dots \tag{6.2}$$

where C_{2n}^{AB} are characteristic coefficients for the pair A and B. Three-body dispersion coefficients are discussed in Ref. [164], however, as usual the higher-order terms become rather tedious.

The dispersion coefficients from Eq. (6.2) can be expressed in terms of imaginary-fre-

quency polarizabilities. The general form is [165]

$$C_{2n}^{AB} = \sum_{l=1}^{n-2} \frac{(2n-2)!}{(l!)(l'!)} \frac{1}{2\pi} \int_0^\infty \mathrm{d}\omega\, \alpha_l^A(i\omega)\alpha_{l'}^B(i\omega), \tag{6.3}$$

where $n > 2$, $l' = n - l - 1$ and $\alpha_l(i\omega)$ are multipole–multipole polarizabilities of lth order (see Table 3.1). From Eq. (6.3) we can write down the first three terms:

$$C_6 = \frac{3}{\pi} \int_0^\infty \mathrm{d}\omega\, \alpha_1^A(i\omega)\alpha_1^B(i\omega) \tag{6.4}$$

$$C_8 = \frac{15}{2\pi} \int_0^\infty \mathrm{d}\omega \left[\alpha_1^A(i\omega)\alpha_2^B(i\omega) + \alpha_2^A(i\omega)\alpha_1^B(i\omega)\right] \tag{6.5}$$

$$\begin{aligned} C_{10} = &\frac{14}{\pi} \int_0^\infty \mathrm{d}\omega \left[\alpha_1^A(i\omega)\alpha_3^B(i\omega) + \alpha_3^A(i\omega)\alpha_1^B(i\omega)\right] \\ &+ \frac{35}{\pi} \int_0^\infty \mathrm{d}\omega\, \alpha_2^A(i\omega)\alpha_2^B(i\omega). \end{aligned} \tag{6.6}$$

The formulas such as these can be readily utilized, if the polarizabilities α_l are known for a reasonable number of Matsubara frequencies: the integral can be safely extrapolated or truncated, since the polarizability converges to zero.

In Table 6.1 we present a few coefficients that are matched with literature references, when available. Technical details, such as time-steps and temperatures can be found in Publication IV. Generally, the agreement is excellent but many of the results are also novel. Correlated ab initio methods are also successful in for calculating the dispersion coefficients [40, 41, 44, 45]. However, they overlook the thermal and nonadiabatic effects.

In some cases, such as C_8 between H and H_2, there is a mismatch, because the reference only treats the electronic polarizability and neglects the centrifugal and orientational effects. Moreover, the nuclear polarizabilities are subject to the finite temperature, and thus, one would expect thermal trends in those coefficients involving rotationally active polarizabilities. Accurate calculation of finite temperature dispersion coefficients is absolutely called for, because otherwise thermal simulation methods would depend on 0 Kelvin parameters.

Table 6.1 Dispersion coefficients (with 2SEM estimates) for pairs of atoms (BO), positron systems (AQ) and molecules (AQ) at 300 K from Publication IV, using $\Delta\tau = 0.02$. Available 0 K data is provided for reference.

	C_6	C_8	C_{10}
H–H	6.50(4)	124.7(4)	3300(9)
	6.4990267[a,c]	124.39908[a,c]	3285.8284[a,c]
H–He	2.82(4)	41.9(3)	873(4)
	2.8213439[a,c]	41.828[a,c]	871.23[a,c]
H–H_2	8.78(7)	164.8(8)[e]	4003(12)
	8.7843286[c]	161.31542[c]	
H–HD^+	6.35(12)[e]	135(5)[e]	2620(50)[e]
	5.3815691[b]	99.592513[b]	2023.6873[b]
H–Ps	34.8(3)	318(2)	11560(60)
	34.785[f]		
H–Ps_2	68.7(4)	4210(50)	$3.35(6) \times 10^5$
He–He	1.46(2)	14.09(9)	182.7(8)
	1.4609778[a,c]	14.117857[a]	183.69107[a]
He–H_2	4.01(5)	56.4(4)[e]	1008(4)
	4.0128132[c]	55.381453[c]	
He–HD^+	2.65(9)[e]	41(3)[e]	507(10)[e]
	2.3441447[b]	31.043629[b]	416.42889[b]
He–Ps	13.4(2)	60.9(6)	3040(30)
	13.37[f]		
He–Ps_2	26.4(4)	1520(30)	$1.17(3)\times10^5$
H_2–H_2	12.04(12)	219.1(1.3)	4870(20)
	12.058168[c]		
H_2–HD^+	8.4(3)	184(8)	3800(200)
H_2–Ps	45.2(4)	401(4)	13270(70)
H_2–Ps_2	89.2(8)	5470(70)	$4.32(8)\times10^5$
HD^+–HD^+	11.7(1.2)	530(70)	16000(3000)
HD^+–Ps	37(1)	510(40)	7940(120)
HD^+–Ps_2	74(3)	4800(200)	$3.7(2)\times10^5$
Ps–Ps	207.3(1.3)	0[d]	68400(400)
	207.97[g]		
Ps–Ps_2	410(3)	21000(300)	$1.59(4)\times10^5$
Ps_2–Ps_2	811(5)	83200(800)	$1.000(12)\times10^7$

[a] Yan *et al* [142], [b] Tang *et al* [161], [c] Bishop *et al* [166], [d] The quadrupole moment of Ps is zero by the symmetry of masses, [e] The mismatch is due to orientational and thermal effects that are missing from the reference, [f] Mitroy *et al* [167], [g] Martin *et al* [168]

6.3 Dynamic polarizability

Dynamic polarizability with a real-frequency argument ω is our most impressive result. It is directly involved in the observable response properties, such as the refractive index, Rayleigh scattering and many other linear and nonlinear optical phenomena mentioned in Chapter 1. Imaginary part of the complex polarizability is also directly related to spectral properties: infrared activity, Raman spectroscopy, electronic resonances, scattering cross-section *etc*. Unfortunately, the dynamic response is an out-of-equilibrium process, and thus, it can be extracted from PIMC results only with enormous difficulty.

Earlier we established that the response functions can be defined and calculated in either real or imaginary time. Furthermore, their analytic properties allow for analytic continuation between the domains. This leads to a scheme of integral transforms, which enable one to turn an imaginary-time correlation function into dynamic spectrum, and finally, the dynamic response. Unfortunately, the needed transforms involve highly challenging numerical problems that are scientific problems in their own right.

In the following, we will first discuss the numerical challenge and review solving it with the MaxEnt method. Then, we proceed to study atomic and molecular multipole spectra and the dynamic polarizabilities that they cause.

6.3.1 Numerical inversion of the spectrum

From Eqs. (2.110) or (2.111) we can generalize the analytic continuation with the following identity

$$G = \int_{-\infty}^{\infty} \mathrm{d}\omega\, K(\omega) A(\omega), \tag{6.7}$$

where A is the spectral function, and G and K are the imaginary-domain Green's function and the associated transformation kernel, respectively. The spectral function $A(\omega)$ is a convenient agent, because it is always real and positive-semidefinite, even though the mapping could probably be expressed in alternative forms. The forward mapping of Eq. (6.7), *i.e.*, calculating G from A, is easy. However, the inversion – calculating A

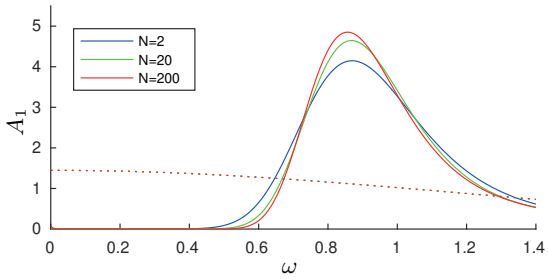

Figure 6.2 MaxEnt inversion of the dipole spectrum of He (BO) as function of the input data quality. Dotted line is the default model. From Publication IV.

from G – turns out to be a highly challenging numerical problem.

A QMC result of G is never perfectly accurate, but includes a degree of statistical fluctuation. Thus, even small errors can be magnified tremendously, because the transformation kernels K are highly nonlinear. For this reason, many methods have been developed to regulate the output [169, 170, 171, 172]. In this work, we use MaxEnt method, which uses Bayesian inference to choose *the most likely A to give G*. More details on MaxEnt are given in Appendix A. The particular software implementation is ΩMaxEnt (version 2018-01) by Bergeron and Tremblay Ref. [74]. More details on the workflow and practical instructions are given in Publication IV.

An example of MaxEnt on the dipole spectrum of helium is found in Fig. 6.2. The MaxEnt spectrum is reasonably accurate even with relatively bad data: the lower *moments* of the distribution, *i.e.* the weight and the alignment are correct. A degree of broadening is expected due to the fundamental spectral linewidth and thermal broadening; however, here the spectrum is excessively broad. The observed effect is artificial and arises from the used *default model*. The spectra can be systematically improved towards better detail by providing more MC data. The scaling appears to be exponential, and thus, obtaining accurate higher moments is practically impossible, unless the approach is fundamentally improved. Prominent strategies include preprocessing the input data and using more tailored default models. However, such tweaks may introduce uncontrollable biases and should be used with caution. Thus, we shall refrain from developing the MaxEnt method itself in this Thesis.

Nevertheless, we can produce the associated multipole polarizability from the spectrum

$A(\omega)$ by using Eq. (3.14). For spectra obeying the bosonic anti-symmetry, *i.e.* $A(\omega') = -A(-\omega')$, the equation is conveniently rewritten as

$$\begin{aligned}\alpha(\omega) &= \int_{-\infty}^{\infty} \mathrm{d}\omega' \, \frac{A(\omega')}{\omega - \omega' - i\eta} \\ &= \int_{0}^{\infty} \mathrm{d}\omega' A(\omega') \left[\frac{1}{\omega - \omega' - i\eta} + \frac{1}{\omega + \omega' + i\eta} \right]. \end{aligned} \tag{6.8}$$

The last form is natural for $A(\omega \geq 0)$, and it also represents the resonant and anti-resonant polarizabilities from Eq. (3.15). In the following, we present $\mathrm{Re}[\alpha(\omega)]$ and $\mathrm{Im}[\alpha(\omega)]$ separately, and refer to them as *polarizability* and *spectrum*, respectively.

6.3.2 Atomic spectra

Let us first study the atomic multipole spectra, which are simple: they only involve electronic excitations. Figure 6.3 contains results of BO simulations of H and He atoms at 2000 Kelvin: the spectra and the associated dynamic polarizabilities up to the quadrupole order. The atoms are essentially at the electronic ground states, and there are no notable thermal effects. One still recognizes that the main spikes of the dipole spectra for H are roughly between $0.375 < \omega < 0.5$, which is the interval between first dipole transition and dissociation of the electron. For He, the corresponding interval is approximately $0.76 < \omega < 0.90$, which also agrees with the known spectral data. Most of the higher excitations, and thus, the main spectral weight is within this interval. Beyond the dissociation limit, there is the spectral continuum, which decays fast and is related to the absorption cross-section.

Moreover, the data is in good agreement with the reference [166]. At the static limit, the results presented in Table 5.1 agree with the previous studies. The dispersive region, *i.e.*, the low frequencies before the spectral spikes, are also an excellent match. Near the absorptive region, there are small disagreements due to the artificial spectral broadening. No prior data exists for the resonant polarizability, which is probably due to a few reasons. On one hand, the resonant region is challenging to compute, because it is very sensitive to the exact spectral details. On the other hand, the resonant response is challenging to measure in experiments, and understanding it might require quantized fields, such as the Hopfield model [90].

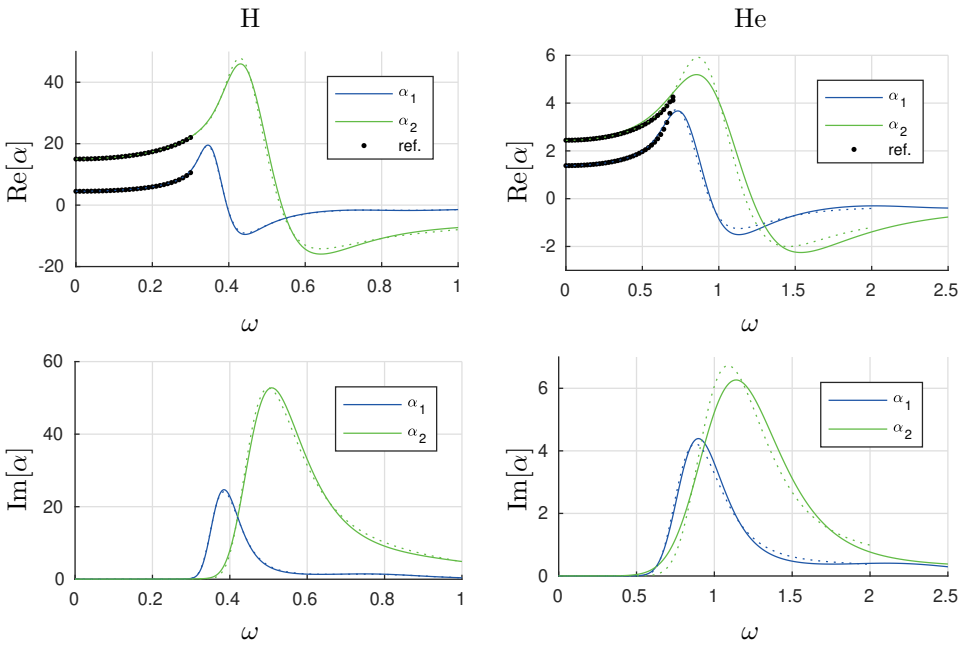

Figure 6.3 The dynamic multipole polarizability (top) and spectra (bottom) of H (BO) and He (BO) for dipole (left) and quadrupole (right) processes. Modified from Publication IV.

6.3.3 Positron systems

Positron systems are essentially similar to atoms, but we will present them separately for a few reasons. First, the simulations are fully nonadiabatic. Electrons and positrons have equal masses, and thus, the particles need to treated on equal footing. Second, the results for dipositronium Ps_2 are categorically novel in the literature.

The correlation functions and the dynamic properties are presented in Fig. 6.4, and the static values in Table 5.1. Logarithmic plots of the Matsubara data indicate that the correlation in different orders of multipole have different orders of magnitude but similar scaling towards zero. In the second figure, we show vanishing of the correlation in the imaginary domain: the multipole correlation of Ps_2 converges to that of 2Ps within the first ~ 2500 Matsubara frequencies at 300 K. However, we cannot compare the quadrupole order, because the quadrupole moment of Ps is always zero due to the symmetry. Last, we present the dynamic polarizabilities of Ps_2. The dipole spectrum is located roughly between $0.181\,60 < \omega < 0.242\,40$, as expected [173]. It is also very close

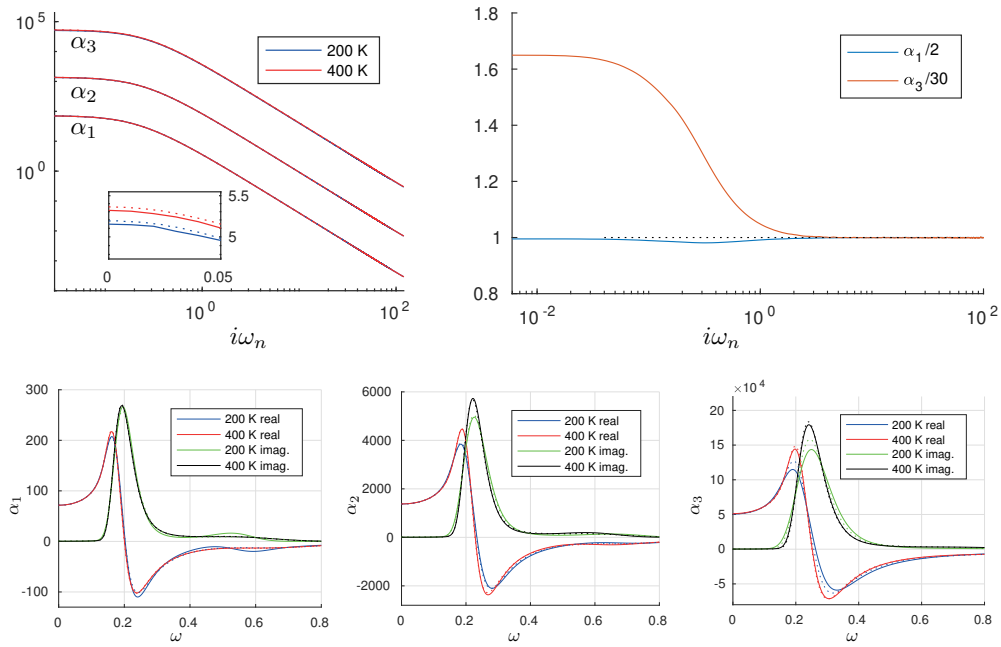

Figure 6.4 Results for Ps_2 (AQ). Top-left: Logarithmic plot of the multipole polarizabilities α_1, α_2 and α_3 in Matsubara frequencies. Top-right: Scaled fraction of the Matsubara data for $\alpha_1(i\omega_n)$ and $\alpha_3(i\omega_n)$ between Ps_2 and Ps. Bottom: Complex-valued dynamic polarizabilities α_1, α_2 and α_3 for real-frequency argument ω. Modified from Publication IV.

to the positron spectrum, $0.1875 < \omega < 0.25$. Similar to atoms, the higher multipole responses are stronger in magnitude and also slightly shifted towards higher frequencies.

6.3.4 Diatomic molecules

The molecular spectra are the most diverse, because they involve thermally active nuclear effects in addition to the electronic part. Therefore, we omit BO simulations and focus on AQ simulations including full accounts of rovibration, thermal averaging and nonadiabatic effects. Again, the response properties from AQ simulations are spherically symmetric and normally ordered.

The dynamic dipole and quadrupole polarizabilities H_2 are presented in Fig. 6.5. The results at the static limit are in Table 5.2, and complementary data in Publication IV.

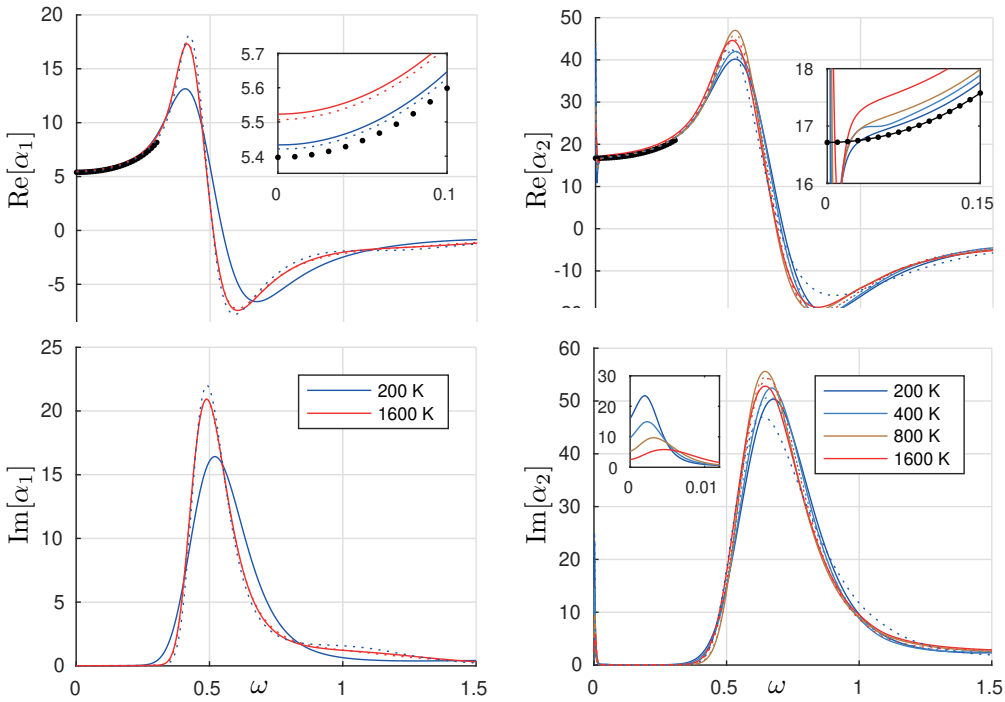

Figure 6.5 The dynamic multipole polarizability (top) and spectra (bottom) of H_2 (AQ) for dipole (left) and quadrupole (right) processes. Modified from Publication IV.

The dipole polarizability α_1 of H_2 shows the centrifugal effect: the polarizability increases from 0 K to $T = 200$ K and $T = 1600$ K. The quadrupole polarizability α_2 has a strong orientational effect because of the permanent quadrupole moment. The inset of polarizability shows that the familiar centrifugal effect also manifests, when the orientational effect has faded off. Thermal decay of the orientational effect is seen in the low-frequency inset of the quadrupole spectrum $A_2(\omega)$: specific rotational resonances cannot be distinguished, but the ensemble is clearly shifted towards higher occupations in higher temperatures. Consequently, the static rotational polarizability is decreased, but the rotational effect also wears off as a function of frequency.

Likewise, the dipole and quadrupole properties of HD^+ are presented in Fig. 6.6. Reasoning behind the thermal and rovibrational effects coincides with H_2. However, HD^+ is polar, and thus, rotationally active in all multipoles. Thus, spectral effects similar to H_2 are shown already in the low-frequency insets. The results also indicate that HD^+ has more exotic features and thermal effects in the electronic spectra. To probe for

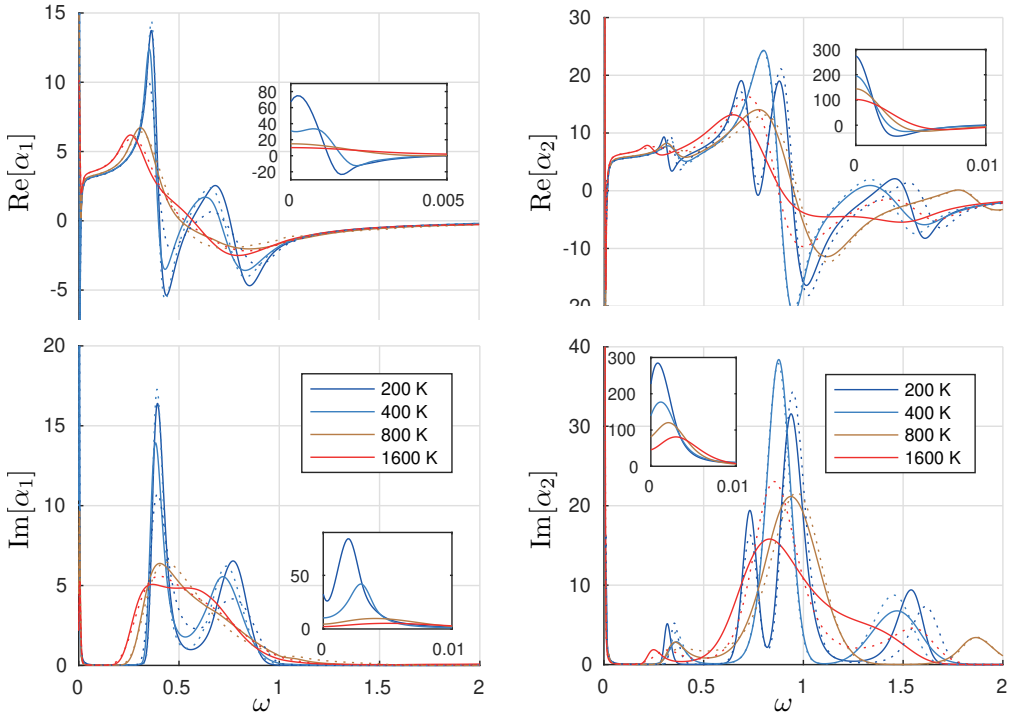

Figure 6.6 The dynamic multipole polarizability (top) and spectra (bottom) of HD^+ (AQ) for dipole (left) and quadrupole (right) processes. Modified from Publication IV.

systematic errors, all the simulations were repeated with two different time-steps, represented with solid and dotted lines. Good agreement between the independent studies makes a strong case for the repeatability of the results, but it does not completely rule out the possibility of numerical artifacts due to MaxEnt.

The spectra thus obtained are important developments both conceptually and practically. They present an estimate of the full active spectrum: although the results lack a lot of fine detail, the polarizabilities at off-resonant frequencies are accurate. The computational workflow, including the inversion problem and the straightforward account of nonadibatic coupling, can likely be optimized and further developed to yield better performance. In the era of high-performance computing, the PIMC approach has the prospects of a future benchmark.

7 CONCLUSIONS

This Thesis is a review of theory and methods involved in the estimation of static and dynamic polarizabilities with the PIMC method. The multipole polarizability describes the electric field response of localized quantum mechanical systems, such as atoms and small molecules. Thus, it is one of the most important and fundamental response properties, and accordingly, involved in a wide range of physical phenomena from nonlinear optics to spectroscopy and long-range interactions.

The main scientific contribution of this Thesis is a collection of different strategies to estimate polarizabilities from PIMC simulations. In particular, we introduce and demonstrate a finite-field approach, static field-derivative estimators, and finally, analytic continuation of quantum correlation functions. To summarize, all the approaches are functional and also, in different ways, exact and controllable. They are complementary to each other and make for a comprehensive toolbox. Yet, the most powerful strategy is the one involving quantum correlation functions. The pinnacle of the research was reached in the end.

There are numerous similar studies of polarizability in the literature, but the nonadiabatic approach of this Thesis is conceptually unique. The PIMC simulation is formally exact within the scope of nonrelativistic quantum mechanics and apart from a controllable systematic error due to finite time-step. Especially, the nonadiabatic or vibronic coupling is implicit, and there is no need for laborious treatments, such as diabatic transformations [174]. Thus, we can combine the electronic and nuclear response properties, while most other approaches have to treat them separately: For instance, PIMD methods are impressive in describing the nuclear quantum phenomena, such as Raman and IR spectra, in thermal conditions. However, description of the electronic response is inadequate. On the other hand, *ab initio* methods achieve great accuracy and numerical precision of the electronic polarizability but struggle with the rovibration and its thermal coupling.

The all-electron PIMC method has obvious benefits, but the use is scarce, unless the approach scales to bigger problems. The Fermion sign problem is especially hard on

fully quantum mechanical simulations, which involve many strongly interacting core electrons. Various solutions, such as RPIMC and PIGS, offer partial remedy to the efficiency. However, they pose extra restrictions that are likely to interfere with response properties. Another way to scale up is to use effective core potentials or pseudopotentials. The implementation of nonlocal pseudopotentials has additional challenges in real-space QMC [175, 176]. Besides, it turns out that most of the readily available parameterizations (*e.g.* [177]) are optimized for energy rather than density, while the latter plays a larger role in polarizabilities. The aim of this Thesis was measurement of the response rather than fundamental development of the simulation. Yet, an obvious and well motivated future avenue is to derive and benchmark estimators, which appreciate the special implications of fermionic simulations, and possibly, fixed-node schemes.

Another important challenge is the analytic continuation from the imaginary-time correlation to the dynamic response. The ill-posed nature of the problem stands against brute-force solutions and incremental development. A better method than MaxEnt is called for, but as of today, not readily available. Fundamentally different angles would be using propagators in real [94, 95, 178, 179] and complex times [180], but of course they are challenges on their own. On the bright side, the expertise accumulated in this research is not specific to polarizabilities but can be utilized in a plethora of similar physical response problems, such as the estimation of dynamic structure factor [83], magnetic susceptibility [181], density-of-states [169], NMR relaxation rate [182], absorption spectra and transport properties [183, 184], Compton profile [185, 186], polarons [170], and optical conductivity [187]. Relevance of the dynamic response problem is universal.

For the actual results, we provide figures and tabulated data on the multipole polarizabilities of several small Coulomb systems: H, H_2^+, H_2, H_3^+, HD^+, He, He^+, HeH^+, Li^+, Be^{2+}, Ps, PsH, and Ps_2. They are not equally suitable to adduce thermal and nonadiabatic effects, but most of them are very common species in both laboratories and the nature. We have successfully used the data for benchmarking the new methods, but we also complement the literature by many original pieces of data. On the other hand we have reproduced thermal behaviour of molecular polarizabilities at low and high temperatures, and more importantly, modeled the transient between the two regimes. We hardly discuss the quality and motivation behind individual results, because there are simply too many of them, and not all the numbers are relevant to applications. In

the broad picture, the novel data can prove useful in, *e.g.*, positron spectroscopy, stellar modeling, and van der Waals interactions. More specific natural follow-ups would be the PIMC studies of Hydrogen at finite [188] and even extreme pressure [66, 67, 68, 189].

Overall this Thesis captures the essence of method development and basic research. We started by leaping into a new territory – the question of electric field response – unaware of the problems and benefits it might introduce. To state the fundamentals and probe the limitations was an inevitable and educating struggle. Over time we learned to recognize many familiar phenomena but also to establish something completely new. Having found the path, it is easier to take the next step: to extend, approximate and utilize the results in the meaningful new horizons.

References

[1] J. Stark and G. Wendt. “Beobachtungen über den Effekt des elektrischen Feldes auf Spektrallinien. II. Längseffekt”. *Annalen der Physik* 348 (1914), 983–990.

[2] M. Javaid et al. “Band structure and giant Stark effect in two-dimensional transition-metal dichalcogenides”. *Electronic Structure* 1 (2018), 015005.

[3] P. S. Epstein. “Zur Theorie des Starkeffektes”. *Annalen der Physik* 355 (1916), 489–520.

[4] H. A. Kramers. “Über den Einfluß eines elektrischen Feldes auf die Feinstruktur der Wasserstofflinien”. *Zeitschrift für Physik* 3 (1920), 199–223.

[5] P. S. Epstein. “The Stark effect from the point of view of Schrödinger’s quantum theory”. *Physical Review* 28 (1926), 695–710.

[6] H. A. Kramers. “La diffusion de la lumiere par les atomes”. *Atti Cong. Intern. Fisica (Transactions of Volta Centenary Congress) Como*. Vol. 2. 1927, 545–557.

[7] B. Orr and J. Ward. “Perturbation theory of the non-linear optical polarization of an isolated system”. *Molecular Physics* 20 (1971), 513–526.

[8] A. D. Buckingham. *Permanent and Induced Molecular Moments and Long-Range Intermolecular Forces*. John Wiley & Sons, Inc., 1967, 107–142.

[9] N. Bloembergen and Y. R. Shen. “Quantum-theoretical comparison of nonlinear susceptibilities in parametric media, lasers, and Raman lasers”. *Physical Review* 133 (1964), A37–A49.

[10] D. M. Bishop. “Molecular vibrational and rotational motion in static and dynamic electric fields”. *Reviews of Modern Physics* 62 (1990), 343–374.

[11] J. Deiglmayr et al. “Calculations of static dipole polarizabilities of alkali dimers: Prospects for alignment of ultracold molecules”. *The Journal of Chemical Physics* 129 (2008), 064309.

[12] T. T. Tsong and G. Kellogg. “Direct observation of the directional walk of single adatoms and the adatom polarizability”. *Physical Review B* 12 (1975), 1343–1353.

[13] V. Jansson et al. “Adatom diffusion in high electric fields”. *2017 30th International Vacuum Nanoelectronics Conference (IVNC)*. IEEE, 2017.

[14] N. F. Allard et al. "Self-broadening of the hydrogen Balmer α line". *Astronomy & Astrophysics* 480 (2008), 581–587.

[15] A. Y. Potekhin, A. D. Luca, and J. A. Pons. "Neutron Stars—Thermal Emitters". *Space Science Reviews* 191 (2014), 171–206.

[16] J. Mitroy, M. S. Safronova, and C. W. Clark. "Theory and applications of atomic and ionic polarizabilities". *Journal of Physics B* 43 (2010), 202001.

[17] M. Saffman, T. G. Walker, and K. Mølmer. "Quantum information with Rydberg atoms". *Reviews of Modern Physics* 82 (2010), 2313–2363.

[18] A. Vela and J. L. Gazquez. "A relationship between the static dipole polarizability, the global softness, and the Fukui function". *Journal of the American Chemical Society* 112 (1990), 1490–1492.

[19] A. D. Headley. "Substituent effects on the basicity of dimethylamines". *Journal of the American Chemical Society* 109 (1987), 2347–2348.

[20] W. J. Hehre et al. "A scale of directional substituent polarizability parameters from ab initio calculations of polarizability potentials". *Journal of the American Chemical Society* 108 (1986), 1711–1712.

[21] J. F. Ward and I. J. Bigio. "Molecular second- and third-order polarizabilities from measurements of second-harmonic generation in gases". *Physical Review A* 11 (1975), 60–66.

[22] D. P. Shelton and J. J. Palubinskas. "Vibrational hyperpolarizabilities and the Kerr effect in CH_4, CF_4, and SF_6". *The Journal of Chemical Physics* 104 (1996), 2482–2487.

[23] J. Kerr. "XL. A new relation between electricity and light: Dielectrified media birefringent". *The London, Edinburgh, and Dublin Philosophical Magazine and Journal of Science* 50 (1875), 337–348.

[24] A. D. Buckingham and D. A. Dows. "Dipole moments and polarizabilities of electronically excited molecules through the Kerr effect". *Discussions of the Faraday Society* 35 (1963), 48.

[25] J. A. Leegwater and S. Mukamel. "Semiclassical Green function calculation of four wave mixing in polarizable clusters and liquids". *The Journal of Chemical Physics* 101 (1994), 7388–7398.

[26] F. Kajzar and J. Messier. “Third-harmonic generation in liquids”. *Physical Review A* 32 (1985), 2352–2363.

[27] A. Liu, S.-L. Chuang, and C. Z. Ning. “Piezoelectric field-enhanced second-order nonlinear optical susceptibilities in wurtzite GaN/AlGaN quantum wells”. *Applied Physics Letters* 76 (2000), 333–335.

[28] R. Eisenschitz and F. London. “Über das Verhältnis der van der Waalsschen Kräfte zu den homöopolaren Bindungskräften”. *Zeitschrift für Physik* 60 (1930), 491–527.

[29] F. London. “The general theory of molecular forces”. *Transactions of the Faraday Society* 33 (1937), 8b.

[30] K. Huang and A. E. García. “Effects of truncating van der Waals interactions in lipid bilayer simulations”. *The Journal of Chemical Physics* 141 (2014), 105101.

[31] M. Javanainen et al. “Atomistic model for nearly quantitative simulations of langmuir monolayers”. *Langmuir* 34 (2017), 2565–2572.

[32] I.-C. Lin et al. “Importance of van der Waals interactions in liquid water”. *The Journal of Physical Chemistry B* 113 (2009), 1127–1131.

[33] J. Tao and A. M. Rappe. “Communication: Accurate higher-order van der Waals coefficients between molecules from a model dynamic multipole polarizability”. *The Journal of Chemical Physics* 144 (2016), 031102.

[34] A. Holt et al. “A NEMO potential that includes the dipole-quadrupole and quadrupole-quadrupole polarizability”. *Journal of Computational Chemistry* (2010), 1583–1591.

[35] I. Leontyev and A. Stuchebrukhov. “Accounting for electronic polarization in non-polarizable force fields”. *Physical Chemistry Chemical Physics* 13 (2011), 2613–2626.

[36] I. V. Leontyev and A. A. Stuchebrukhov. “Polarizable mean-Field model of water for biological simulations with AMBER and CHARMM force fields”. *Journal of Chemical Theory and Computation* 8 (2012), 3207–3216.

[37] J. A. Lemkul et al. “An empirical polarizable force field based on the classical Drude oscillator model: Development history and recent applications”. *Chemical Reviews* 116 (2016), 4983–5013.

[38] I. Kylänpää et al. “Accuracy of ab initio electron correlation and electron densities in vanadium dioxide”. *Physical Review Materials* 1 (2017), 065408.

[39] B. Champagne et al. “Basis set and electron correlation effects on the polarizability and second hyperpolarizability of model open-shell π-conjugated systems”. *The Journal of Chemical Physics* 122 (2005), 114315.

[40] B. Sahoo. “An ab initio relativistic coupled-cluster theory of dipole and quadrupole polarizabilities: Applications to a few alkali atoms and alkaline earth ions”. *Chemical Physics Letters* 448 (2007), 144–149.

[41] L. W. Wansbeek et al. “Ab initio determination of polarizabilities and van der Waals coefficients of Li atoms using the relativistic coupled-cluster method”. *Physical Review A* 78 (2008), 012515.

[42] J. Friedrich et al. “Incremental evaluation of coupled cluster dipole polarizabilities”. *Physical Chemistry Chemical Physics* 17 (2015), 14284–14296.

[43] V. A. Dzuba, V. V. Flambaum, and M. G. Kozlov. “Combination of the many-body perturbation theory with the configuration-interaction method”. *Physical Review A* 54 (1996), 3948–3959.

[44] S. G. Porsev and A. Derevianko. “High-accuracy relativistic many-body calculations of van der Waals coefficientsC6for alkaline-earth-metal atoms”. *Physical Review A* 65 (2002).

[45] S. G. Porsev and A. Derevianko. “High-accuracy calculations of dipole, quadrupole, and octupole electric dynamic polarizabilities and van der Waals coefficients C 6, C 8, and C 10 for alkaline-earth dimers”. *Journal of Experimental and Theoretical Physics* 102 (2006), 195–205.

[46] S. Liu and C. E. Dykstra. “Multipole polarizabilities and hyperpolarizabilities of AH_2 and A_2H_n molecules from derivative Hartree-Fock theory”. *Journal of Physical Chemistry* 91 (1987), 1749–1754.

[47] D. Paschoal et al. “Gaussian basis sets for ab initio calculation of NLO properties of polyatomic molecules”. *J. Comp. Methods in Sci. and Eng.* 10 (2010), 239–256.

[48] C. Jamorski, M. E. Casida, and D. R. Salahub. “Dynamic polarizabilities and excitation spectra from a molecular implementation of time-dependent density-functional response theory: N_2 as a case study”. *The Journal of Chemical Physics* 104 (1996), 5134–5147.

[49] P. R. T. Schipper et al. “Molecular calculations of excitation energies and (hyper)polarizabilities with a statistical average of orbital model exchange-correlation potentials”. *The Journal of Chemical Physics* 112 (2000), 1344–1352.

[50] X. Chu and A. Dalgarno. “Linear response time-dependent density functional theory for van der Waals coefficients”. *The Journal of Chemical Physics* 121 (2004), 4083.

[51] G. Maroulis. *Atoms, Molecules, and Clusters in Electric Fields: Theoretical Approaches to the Calculation of Electric Polarizability*. Imperial College Press, 2006.

[52] M. Caffarel, M. Rérat, and C. Pouchan. “Evaluating dynamic multipole polarizabilities and van der Waals dispersion coefficients of two-electron systems with a quantum Monte Carlo calculation: A comparison with some ab initio calculations”. *Physical Review A* 47 (1993), 3704–3717.

[53] H. A. Kurtz, J. J. P. Stewart, and K. M. Dieter. “Calculation of the nonlinear optical properties of molecules”. *Journal of Computational Chemistry* 11 (1990), 82–87.

[54] U. Hohm and U. Trümper. “Temperature dependence of the dipole polarizability of xenon ($^1S_0$) due to dynamic non-resonant Stark effect caused by blackbody radiation”. *Chemical Physics* 189 (1994), 443–449.

[55] H. Montgomery and K. Sen. “Dipole polarizabilities for a hydrogen atom confined in a penetrable sphere”. *Physics Letters A* 376 (2012), 1992–1996.

[56] M. Chołuj et al. “On the calculations of the static electronic dipole (hyper)polarizability for the free and spatially confined H^-”. *The Journal of Chemical Physics* 146 (2017), 194301.

[57] D. M. Bishop and J. Pipin. “Temperature-dependence of the dynamic dipole polarizability of H_2”. *Molecular Physics* 72 (1991), 961–964.

[58] D. M. Bishop and B. Lam. “Hyperpolarizabilities of diatomic molecules: The effects of vibration and rotation”. *Chemical Physics Letters* 143 (1988), 515–520.

[59] C. E. Dykstra and D. J. Malik. “Derivative Numerov–Cooley theory. A method for finding vibrational state properties of diatomic molecules”. *The Journal of Chemical Physics* 87 (1987), 2806–2811.

[60] F. Bresme. “Equilibrium and nonequilibrium molecular-dynamics simulations of the central force model of water”. *The Journal of Chemical Physics* 115 (2001), 7564–7574.

[61] G. R. Medders and F. Paesani. “Infrared and Raman spectroscopy of liquid water through "first-principles" many-body molecular dynamics”. *Journal of Chemical Theory and Computation* 11 (2015), 1145–1154.

[62] A. Zen et al. “Ab initio molecular dynamics simulation of liquid water by quantum Monte Carlo”. *The Journal of Chemical Physics* 142 (2015), 144111.

[63] M. Shin D. Ho and J. Shumway. “Ab-initio path integral techniques for molecules”. *arXiv:quant-ph/0611105* (2006). eprint: arXiv,quant-ph/0611105.

[64] S. Habershon, B. J. Braams, and D. E. Manolopoulos. “Quantum mechanical correlation functions, maximum entropy analytic continuation, and ring polymer molecular dynamics”. *The Journal of Chemical Physics* 127 (2007), 174108.

[65] C. Pierleoni and D. Ceperley. “The coupled electron-ion Monte Carlo method”. *Computer Simulations in Condensed Matter Systems: From Materials to Chemical Biology Volume 1*. Springer Berlin Heidelberg, 2006, 641–683.

[66] C. Pierleoni et al. “Liquid–liquid phase transition in hydrogen by coupled electron–ion Monte Carlo simulations”. *Proceedings of the National Academy of Sciences* 113 (2016), 4953–4957.

[67] G. Rillo et al. “Optical properties of high pressure liquid hydrogen across molecular dissociation” (2018). arXiv: http://arxiv.org/abs/1810.08131v1 [cond-mat.mtrl-sci].

[68] V. Gorelov, C. Pierleoni, and D. M. Ceperley. “Benchmarking vdW-DF first-principles predictions against Coupled Electron-Ion Monte Carlo for high-pressure liquid hydrogen”. *Contributions to Plasma Physics* (2019), e201800185.

[69] I. Kylänpää, M. Leino, and T. T. Rantala. “Hydrogen molecule ion: Path-integral Monte Carlo approach”. *Physical Review A* 76 (2007), 052508.

[70] I. Kylänpää and T. T. Rantala. “Thermal dissociation of dipositronium: Path-integral Monte Carlo approach”. *Physical Review A* 80 (2009), 024504.

[71] I. Kylänpää and T. T. Rantala. "Finite temperature quantum statistics of H_3^+ molecular ion". *The Journal of Chemical Physics* 133, 044312 (2010), 044312.

[72] I. Kylänpää. "First-principles finite temperature electronic structure of some small molecules". PhD thesis. Tampere University of Technology, 2011.

[73] M. Jarrell and J. Gubernatis. "Bayesian inference and the analytic continuation of imaginary-time quantum Monte Carlo data". *Physics Reports* 269 (1996), 133–195.

[74] D. Bergeron and A.-M. S. Tremblay. "Algorithms for optimized maximum entropy and diagnostic tools for analytic continuation". *Physical Review E* 94 (2016), 023303.

[75] R. P. Feynman and A. R. Hibbs. *Quantum mechanics and path integrals*. International series in pure and applied physics. McGraw-Hill, 1965.

[76] H. Kleinert. *Path Integrals in Quantum Mechanics, Statistics, Polymer Physics, and Financial Markets*. World Scientific, 2006. 1547 pp.

[77] R. W. Boyd. *Nonlinear Optics*. Elsevier, 2008. 640 pp.

[78] G. Stefanucci and R. van Leeuwen. *Nonequilibrium Many-Body Theory of Quantum Systems: A Modern Introduction*. Cambridge University Press, 2013.

[79] S. S. Jha. "Nonlinear response theory—I". *Pramana* 22 (1984), 173–182.

[80] N. Evans and S. King. *Theories of Matter, Space, and Time: Quantum Theories*. IOP Concise Physics. Morgan & Claypool Publishers, 2018.

[81] H. F. Trotter. "On the product of semi-groups of operators". *Proceedings of the American Mathematical Society* 10 (1959), 545–551.

[82] M. Suzuki. "Generalized Trotter's formula and systematic approximants of exponential operators and inner derivations with applications to many-body problems". English. *Communications in Mathematical Physics* 51 (1976), 183–190.

[83] D. M. Ceperley. "Path integrals in the theory of condensed Helium". *Reviews of Modern Physics* 67 (1995), 279–355.

[84] J. S. Toll. "Causality and the dispersion relation: Logical foundations". *Physical Review* 104 (1956), 1760–1770.

[85] R. Kubo. "Statistical-mechanical theory of irreversible processes. I. General theory and simple applications to magnetic and conduction problems". *Journal of the Physical Society of Japan* 12 (1957), 570–586.

[86] D. R. Reichman et al. “A Feynman path centroid dynamics approach for the computation of time correlation functions involving nonlinear operators”. *The Journal of Chemical Physics* 113 (2000), 919–929.

[87] K. A. Jung, P. E. Videla, and V. S. Batista. “Inclusion of nuclear quantum effects for simulations of nonlinear spectroscopy”. *The Journal of Chemical Physics* 148 (2018), 244105.

[88] S. Kielich. “General molecular theory and electric field effects in isotropic dielectrics”. *Dielectric and Related Molecular Processes*. Royal Society of Chemistry, 1972, 192–387.

[89] B. J. Berne. “Path integral Monte Carlo methods: Static- and time-correlation functions”. *Journal of Statistical Physics* 43 (1986), 911–929.

[90] J. J. Hopfield. “Theory of the contribution of excitons to the complex dielectric constant of crystals”. *Physical Review* 112 (1958), 1555–1567.

[91] L. Knoll, S. Scheel, and D.-G. Welsch. “QED in dispersing and absorbing media” (2000). arXiv: `http://arxiv.org/abs/quant-ph/0006121v5 [quant-ph]`.

[92] A. Bechler. “Quantum electrodynamics of the dispersive dielectric medium–a path integral approach”. *Journal of Modern Optics* 46 (1999), 901–921.

[93] G. Maroulis and D. M. Bishop. “On the electric polarisabilities of $Li^+(^1S)$, $Li(^2S)$ and $Li^-(^1S)$”. *Journal of Physics B: Atomic and Molecular Physics* 19 (1986), 369–377.

[94] I. Ruokosenmäki and T. T. Rantala. “Numerical path integral approach to quantum dynamics and stationary quantum states”. *Communications in Computational Physics* 18 (2015), 91–103.

[95] I. Ruokosenmäki et al. “Numerical path integral solution to strong Coulomb correlation in one dimensional Hooke’s atom”. *Computer Physics Communications* 210 (2017), 45–53.

[96] T. J. H. Hele et al. “Boltzmann-conserving classical dynamics in quantum time-correlation functions: "Matsubara dynamics"”. *The Journal of Chemical Physics* 142 (2015), 134103.

[97] M. S. Safronova, W. R. Johnson, and A. Derevianko. “Relativistic many-body calculations of energy levels, hyperfine constants, electric-dipole matrix elements, and static polarizabilities for alkali-metal atoms”. *Physical Review A* 60 (1999), 4476–4487.

[98] B. Arora, M. S. Safronova, and C. W. Clark. “Determination of electric-dipole matrix elements in K and Rb from Stark shift measurements”. *Physical Review A* 76 (2007), 052516.

[99] R. P. Feynman. “Forces in Molecules”. *Physical Review* 56 (1939), 340–343.

[100] P. Pulay. “Ab initio calculation of force constants and equilibrium geometries in polyatomic molecules”. *Molecular Physics* 17 (1969), 197–204.

[101] A. Badinski, P. D. Haynes, and R. J. Needs. “Nodal Pulay terms for accurate diffusion quantum Monte Carlo forces”. *Physical Review B* 77 (2008), 085111.

[102] W. Ying and C. S. Henriquez. “Hybrid finite element method for describing the electrical response of biological cells to applied fields”. *IEEE Transactions on Biomedical Engineering* 54 (2007), 611–620.

[103] J. He, V. D. Noto, and S. J. Paddison. “The structure of water–methanol mixtures under an electric field: Ab initio molecular dynamics simulations”. *Chemical Physics Letters* 635 (2015), 99–106.

[104] J. Tiihonen. “Stark effect and polarizabilities of hydrogen with path integral Monte Carlo method”. MA thesis. Tampere University of Technology, 2014.

[105] D. L. Andrews and T. Thirunamachandran. “On three-dimensional rotational averages”. *The Journal of Chemical Physics* 67 (1977), 5026–5033.

[106] G. Wagnière. “The evaluation of three-dimensional rotational averages”. *The Journal of Chemical Physics* 76 (1982), 473–480.

[107] D. M. Bishop, B. Kirtman, and B. Champagne. “Differences between the exact sum-over-states and the canonical approximation for the calculation of static and dynamic hyperpolarizabilities”. *The Journal of Chemical Physics* 107 (1997), 5780–5787.

[108] D. M. Bishop, B. Lam, and S. T. Epstein. “The Stark effect and polarizabilities for a diatomic molecule”. *The Journal of Chemical Physics* 88 (1988), 337.

[109] W. Kolos and L. Wolniewicz. “Polarizability of the hydrogen molecule”. *The Journal of Chemical Physics* 46 (1967), 1426.

[110] P. Debye. “Polar molecules”. *Journal of the Society of Chemical Industry* 48 (1929), 1036–1037.

[111] W. L. McMillan. “Ground State of Liquid He^4”. *Physical Review* 138 (1965), 442–451.

[112] P. J. Reynolds et al. “Fixed-node quantum Monte Carlo for molecules”. *The Journal of Chemical Physics* 77 (1982), 5593–5603.

[113] D. L. Freeman and J. D. Doll. “Fourier path integral Monte Carlo method for the calculation of the microcanonical density of states”. *The Journal of Chemical Physics* 101 (1994), 848–849.

[114] P. E. Kornilovitch. “Ground-state dispersion and density of states from path-integral Monte Carlo: Application to the lattice polaron”. *Physical Review B* 60 (1999), 3237–3243.

[115] V. Linetsky. “The path integral approach to financial modeling and options pricing”. *Computational Economics* 11 (1997), 129–163.

[116] G. T. B. Mark Newman. *Monte Carlo Methods in Statistical Physics*. Oxford University Press, 1999. 496 pp.

[117] J. Hašík, E. Tosatti, and R. Martoňák. “Quantum and classical ripples in graphene”. *Physical Review B* 97 (2018), 140301.

[118] R. M. Martin, L. Reining, and D. M. Ceperley. *Interacting Electrons*. Cambridge University Press, 2016.

[119] N. Metropolis et al. “Equation of state calculations by fast computing machines”. *The Journal of Chemical Physics* 21 (1953), 1087.

[120] N. Hatano and M. Suzuki. “Finding exponential product formulas of higher orders”. *Quantum Annealing and Other Optimization Methods*. Springer Berlin Heidelberg, 2005, 37–68.

[121] R. G. Storer. “Path-Integral calculation of the quantum-statistical density matrix for attractive Coulomb forces”. *Journal of Mathematical Physics* 9 (1968), 964–970.

[122] K. Esler. “Advancements in the path integral Monte Carlo method for many-body quantum systems at finite temperature”. PhD thesis. University of Illinois at Urbana–Champaign, 2006.

[123] M. Boninsegni. "Permutation sampling in path integral Monte Carlo". *Journal of Low Temperature Physics* 141 (2005), 27–46.

[124] S. A. Chin. "High-order path-integral Monte Carlo methods for solving quantum dot problems". *Physical Review E* 91 (2015), 031301.

[125] D. M. Ceperley. "Fermion nodes". *J. Stat. Phys.* 63 (1991), 1237–1267.

[126] E. Y. Loh et al. "Sign problem in the numerical simulation of many-electron systems". *Physical Review B* 41 (1990), 9301–9307.

[127] M. Troyer and U.-J. Wiese. "Computational complexity and fundamental limitations to fermionic quantum Monte Carlo simulations". *Physical Review Letters* 94 (2005), 170201.

[128] T. Schoof et al. "Configuration path integral Monte Carlo". *Contributions to Plasma Physics* 51 (2011), 687–697.

[129] T. Dornheim et al. "Permutation blocking path integral Monte Carlo: a highly efficient approach to the simulation of strongly degenerate non-ideal fermions". *New Journal of Physics* 17 (2015), 073017.

[130] Z.-X. Li, Y.-F. Jiang, and H. Yao. "Majorana-time-reversal symmetries: A fundamental principle for sign-problem-free quantum Monte Carlo simulations". *Physical Review Letters* 117 (2016), 267002.

[131] D. M. Ceperley. "Path integral Monte Carlo methods for fermions". *Monte Carlo and molecular dynamics of condensed matter systems*. Ed. by K. Binder and G. Ciccotti. Conference proceedings (Società Italiana di Fisica). Italian Physical Society, 1996.

[132] D. M. Bishop and J. Pipin. "Static electric properties of H and He". *Chemical Physics Letters* 236 (1995), 15–18.

[133] C. D. Lin. "Hyperspherical coordinate approach to atomic and other Coulombic three-body systems". *Physics Reports* 257 (1995), 1–83.

[134] H. Nakashima and H. Nakatsuji. "Solving the Schrödinger equation for helium atom and its isoelectronic ions with the free iterative complement interaction (ICI) method". *J. Chem. Phys* 127 (2007), 224104.

[135] S. Kar and Y. K. Ho. "Dipole polarizabilities of plasma-embedded Ps^- and H^- ions". *Physics Letters A* 372 (2008), 4253–4256.

[136] J. Pipin and D. M. Bishop. "Dynamic polarizabilities and hyperpolarizabilities of the hydrogen negative ion". *Journal of Physics B: Atomic, Molecular and Optical Physics* 25 (1992), 17.

[137] W. Cencek, K. Szalewicz, and B. Jeziorski. "Breit-Pauli and direct perturbation theory calculations of relativistic helium polarizability". *Physical Review Letters* 86 (2001), 5675–5678.

[138] D. M. Bishop and M. Rérat. "Higher-order polarizabilities for the helium isoelectronic series". *The Journal of Chemical Physics* 91 (1989), 5489–5491.

[139] W. R. Johnson and K. T. Cheng. "Relativistic configuration-interaction calculation of the polarizabilities of heliumlike ions". *Physical Review A* 53 (1996), 1375–1378.

[140] S. Bubin et al. "Relativistic corrections to the ground-state energy of the positronium molecule". *Physical Review A* 75 (6 2007), 062504.

[141] A. M. Frolov and V. H. Smith. "Ground state of positronium hydride". *Physical Review A* 56 (1997), 2417–2420.

[142] Z.-C. Yan et al. "Variational calculations of dispersion coefficients for interactions among H, He, and Li atoms". *Physical Review A* 54 (1996), 2824–2833.

[143] P. Schwerdtfeger and J. K. Nagle. "2018 Table of static dipole polarizabilities of the neutral elements in the periodic table". *Molecular Physics* (2018), 1–26.

[144] P. M. Kiefer and J. T. Hynes. "Kinetic isotope effects for nonadiabatic proton transfer reactions in a polar environment. 1. Interpretation of tunneling kinetic isotopic effects". *The Journal of Physical Chemistry A* 108 (2004), 11793–11808.

[145] D. R. Yarkony. "Nonadiabatic quantum chemistry—Past, Present, and Future". *Chemical Reviews* 112 (2011), 481–498.

[146] S. L. Saito. "Is positronium hydride atom or molecule?" *Nuclear Instruments and Methods in Physics Research Section B: Beam Interactions with Materials and Atoms* 171 (2000), 60–66.

[147] W. Kolos and L. Wolniewicz. "Improved theoretical ground-state energy of the hydrogen molecule". *The Journal of Chemical Physics* 49 (1968), 404–410.

[148] D. M. Bishop, J. Pipin, and S. M. Cybulski. "Theoretical investigation of the nonlinear optical properties of H_2 and D_2: Extended basis set". *Physical Review A* 43 (1991), 4845–4853.

[149] A. V. Turbiner and H. Olivares-Pilon. "The H_2^+ molecular ion: A solution". *Journal of Physics B: Atomic, Molecular and Optical Physics* 44 (2011), 101002.

[150] T. Tsogbayar and M. Horbatsch. "Calculation of Stark resonance parameters for the hydrogen molecular ion in a static electric field". *Journal of Physics B: Atomic, Molecular and Optical Physics* 46 (2013), 085004.

[151] D. M. Bishop and B. Lam. "An analysis of the interaction between a distant point charge and H_2". *Molecular Physics* 65 (1988), 679–688.

[152] A. V. Turbiner and J. C. Lopez Vieyra. "Ground state of the H_3^+ molecular ion: Physics behind". *The Journal of Physical Chemistry A* 117 (2013), 10119–10128.

[153] K. Kawaoka. "Electric, magnetic, and spectral properties of H_3^+ ground state calculated from single-center wavefunctions". *The Journal of Chemical Physics* 55 (1971), 4637.

[154] K. Pachucki. "Born-Oppenheimer potential for HeH^+". *Physical Review A* 85 (2012), 042511.

[155] M. Pavanello et al. "Non-Born–Oppenheimer calculations of the pure vibrational spectrum of HeH^+". *The Journal of Chemical Physics* 123 (2005), 104306.

[156] J. D. Poll and L. Wolniewicz. "The quadrupole moment of the H_2 molecule". *The Journal of Chemical Physics* 68 (1978), 3053–3058.

[157] D. R. Bates and G. Poots. "Properties of the hydrogen molecular ion I: Quadrupole transitions in the ground electronic state and dipole transitions of the isotopic ions". *Proceedings of the Physical Society A* 66 (1953), 784.

[158] D. M. Bishop and L. M. Cheung. "Static higher polarisabilities of H_2^+". *Journal of Physics B* 12 (1979), 3135–3148.

[159] G. D. Carney and R. N. Porter. "H_3^+: Geometry dependence of electronic properties". *The Journal of Chemical Physics* 60 (1974), 4251–4264.

[160] V. Buch. "Path integral simulations of mixed para-D_2 and ortho-D_2 clusters: The orientational effects". *The Journal of Chemical Physics* 100 (1994), 7610–7629.

[161] L.-Y. Tang et al. "High-precision nonadiabatic calculations of dynamic polarizabilities and hyperpolarizabilities for low-lying vibrational-rotational states of hydrogen molecular ions". *Physical Review A* 90 (2014), 012524.

[162] W.-C. Tung, M. Pavanello, and L. Adamowicz. "Accurate potential energy curves for HeH^+ isotopologues". *The Journal of Chemical Physics* 137 (2012), 164305.

[163] H. B. G. Casimir and D. Polder. "The influence of retardation on the London-van der Waals forces". *Physical Review* 73 (1948), 360–372.

[164] A. McLachlan. "Three-body dispersion forces". *Molecular Physics* 6 (1963), 423–427.

[165] S. H. Patil and K. T. Tang. "Multipolar polarizabilities and two- and three-body dispersion coefficients for alkali isoelectronic sequences". *The Journal of Chemical Physics* 106 (1997), 2298–2305.

[166] D. M. Bishop and J. Pipin. "Dipole, quadrupole, octupole, and dipole–octupole polarizabilities at real and imaginary frequencies for H, He, and H_2 and the dispersion-energy coefficients for interactions between them". *International Journal of Quantum Chemistry* 45 (1993), 349–361.

[167] J. Mitroy and M. W. J. Bromley. "van der Waals coefficients for positronium-atom interactions". *Physical Review A* 68 (2003), 035201.

[168] D. W. Martin and P. A. Fraser. "The van der Waals force between positronium and light atoms". *Journal of Physics B: Atomic and Molecular Physics* 13 (1980), 3383–3387.

[169] C. E. Creffield et al. "Spectral weight function for the half-filled Hubbard model: A singular value decomposition approach". *Physical Review Letters* 75 (1995), 517–520.

[170] A. Mishchenko et al. "Diagrammatic quantum Monte Carlo study of the Fröhlich polaron". *Physical Review B* 62 (2000), 6317–6336.

[171] J. Nordström et al. "A GPU code for analytic continuation through a sampling method". *SoftwareX* 5 (2016), 178–182.

[172] K. S. D. Beach, R. J. Gooding, and F. Marsiglio. "Reliable Padé analytical continuation method based on a high-accuracy symbolic computation algorithm". *Physical Review B* 61 (2000), 5147–5157.

[173] J. Usukura and Y. Suzuki. "Resonances of positronium complexes". *Physical Review A* 66 (2002), 010502.

[174] A. Alijah and M. Baer. "The electronic adiabatic-diabatic transformation matrix: A theoretical and numerical study of a three-state system". *The Journal of Physical Chemistry A* 104 (2000), 389–396.

[175] M. Casula. "Beyond the locality approximation in the standard diffusion Monte Carlo method". *Physical Review B* 74 (2006).

[176] J. T. Krogel and P. R. C. Kent. "Magnitude of pseudopotential localization errors in fixed node diffusion quantum Monte Carlo". *The Journal of Chemical Physics* 146 (2017), 244101.

[177] M. Burkatzki, C. Filippi, and M. Dolg. "Energy-consistent pseudopotentials for quantum Monte Carlo calculations". *The Journal of Chemical Physics* 126 (2007), 234105.

[178] N. Makri. "On smooth Feynman propagators for real time path integrals". *The Journal of Physical Chemistry* 97 (1993), 2417–2424.

[179] L. Mühlbacher and E. Rabani. "Real-time path integral approach to nonequilibrium many-body quantum systems". *Physical Review Letters* 100 (2008), 176403.

[180] R. Rota et al. "Quantum Monte Carlo estimation of complex-time correlations for the study of the ground-state dynamic structure function". *The Journal of Chemical Physics* 142 (2015), 114114.

[181] F. C. Zhang and T. K. Lee. "Spectral density and magnetic susceptibility for the asymmetric degenerate Anderson model". *Physical Review B* 30 (1984), 1556–1558.

[182] A. W. Sandvik. "NMR relaxation rates for the spin-1/2 Heisenberg chain". *Physical Review B* 52 (1995), R9831–R9834.

[183] E. Gallicchio and B. J. Berne. "On the calculation of dynamical properties of solvated electrons by maximum entropy analytic continuation of path integral Monte Carlo data". *The Journal of Chemical Physics* 105 (1996), 7064–7078.

[184] G. Aarts and J. M. M. Resco. "Transport coefficients, spectral functions and the lattice". *The Journal of High Energy Physics* 2002 (2002), 053–053.

[185] L. Dobrzyński and A. Holas. "Reconstruction of the electron momentum density distribution by the Maximum Entropy Method". *Nuclear Instruments and Methods in Physics Research Section A: Accelerators, Spectrometers, Detectors and Associated Equipment* 383 (1996), 589–600.

[186] V. Olevano et al. “Momentum distribution and Compton profile by the ab initio GW approximation”. *Physical Review B* 86 (2012), 195123.

[187] O. Gunnarsson, M. W. Haverkort, and G. Sangiovanni. “Analytical continuation of imaginary axis data for optical conductivity”. *Physical Review B* 82 (2010), 165125.

[188] I. Kylänpää and T. T. Rantala. “First-principles simulation of molecular dissociation–recombination equilibrium”. *The Journal of Chemical Physics* 135 (2011), 104310.

[189] S. Azadi et al. “Dissociation of high-pressure solid molecular hydrogen: A quantum Monte Carlo and anharmonic vibrational study”. *Physical Review Letters* 112 (2014), 165501.

A MAXIMUM ENTROPY METHOD

The Maximum Entropy method (MaxEnt) is a popular means to regulate highly nonlinear inversion problems. In the first order, this means solving $A(\omega)$ for a given $G(\lambda)$ from

$$G(\lambda) = \int \mathrm{d}\omega' K_\lambda(\lambda, \omega') A(\omega'),$$

where λ is either imaginary time τ or Matsubara frequency $i\omega_n$. Instead of C, we have used G for Green's function, but the difference is cosmetic within the scope of this Thesis. The inversion is problematic when the kernel K_λ contains a highly nonlinear mapping, because then even small fluctuations in $G(\lambda)$ have large implications on the outcome. Consequently, any numerical transform becomes sensitive to the specific implementation, such as the finite-sized ω-grid.

This sensitivity can regulated with Bayesian inference. That is, picking the most probable A out of all possible solutions with a given G, based on the available *a priori* knowledge of the solution. This equals to maximizing

$$\mathbb{P}(A|G) = \frac{\mathbb{P}(G|A)\mathbb{P}(A)}{\mathbb{P}(G)}, \tag{A.1}$$

where the terms are different probabilities. First, $\mathbb{P}(G)$ can be considered fixed for a given inversion problem. Second, the relative probability of G given A can be quantified by the central limit theorem as

$$\mathbb{P}(G|A) \propto \mathrm{e}^{-\frac{X^2}{2}}, \tag{A.2}$$

where

$$\chi^2 = (G - \bar{G})^T C^{-1} (G - \bar{G}), \tag{A.3}$$

where C is covariance matrix and $\bar{G} = KA$ is resulting forward-mapping of the problem.

If the covariance is diagonal,

$$\chi^2 = \sum_i \frac{(G_i - \bar{G}_i)^2}{\sigma_i^2}, \tag{A.4}$$

where σ_i is the variance at the ith element of G. In other words, X^2 is a least-squares fitting error between the proposed mapping $\bar{G} = KA$ and the input G. Last, the prior probability can be defined as

$$\mathbb{P}(A) \propto e^{\alpha S} \tag{A.5}$$

where α is a scaling parameter and

$$S = -\int \frac{d\omega}{2\pi} A(\omega) \ln \frac{A(\omega)}{D(\omega)} \tag{A.6}$$

is the relative entropy. $D(\omega)$ is the so-called default model that sets an *a priori* bias for the entropy. The default model can be used to steer the fitting by setting it to resemble the expected shape of the spectral function.

Combining Eqs. (A.2) and (A.5), the inversion equals to maximizing

$$\ln \mathbb{P}(A|G) = \alpha S - X^2/2, \tag{A.7}$$

for a given ω-grid and α. The parameter α adjusts the balance the fit between the least-squares error and the default model: too small α favors overfitting to statistical noise, while too large α returns the default model and shuns any new information. There are several strategies to choose the optimal α, e.g. classical, historic and the Bryan's approach. In this work, we use ΩMaxEnt software by Bergeron and Tremblay [74], which uses maximum curvature of $\log(X^2)$–$\log(\alpha)$-plot to identify the optimal α. Their approach is relatively independent of the choice of $D(\omega)$, which makes for a good black box. For more details, we refer to [73] about MaxEnt and [74] about ΩMaxEnt, the implementation.

PUBLICATIONS

PUBLICATION I

Adiabatic and nonadiabatic static polarizabilities of H and H_2

Juha Tiihonen, Ilkka Kylänpää & Tapio T. Rantala

Physical Review A 91, 062503, 2015
DOI: 10.1103/PhysRevA.91.062503

Adiabatic and nonadiabatic static polarizabilities of H and H_2

Juha Tiihonen,* Ilkka Kylänpää, and Tapio T. Rantala
Department of Physics, Tampere University of Technology, P.O. Box 692, FI-33101 Tampere, Finland
(Received 24 March 2015; published 12 June 2015)

The path-integral Monte Carlo method is employed to evaluate static (hyper)polarizabilities of small hydrogen systems at finite temperature. Exact quantum statistics are obtained for hydrogen atom and hydrogen molecule immersed in homogeneous electric field. The method proves to be reliable and yields perfect agreement with known values of static polarizabilities in both adiabatic and nonadiabatic simulations. That is, we demonstrate how electronic, rotational, and vibrational contributions can be evaluated either separately or simultaneously. Indeed, at finite temperature and nonzero-field strengths we observe considerable rovibrational effects in the polarization of the hydrogen molecule. Given sufficient computational resources, the path-integral Monte Carlo method turns out to be a straightforward tool for describing and computing static polarizabilities for traditionally challenging regimes.

DOI: 10.1103/PhysRevA.91.062503 PACS number(s): 31.15.A−, 32.10.Dk, 33.15.Kr

I. INTRODUCTION

Polarizability is a fundamental property of matter, describing its response to the external electric fields. It has straightforward manifestations in linear and nonlinear optical phenomena and thus it has a significant role in the interpretation of experimental data and development of new technology [1]. Current *ab initio* methods for quantum scale modeling of polarizability result from many decades of development. Nevertheless, while these provide high accuracy at 0 K, their applicability is limited in many central real-world aspects such as high temperatures, finite particle densities, and rovibrational effects. Here we propose a different approach, which could overcome these problems in a straightforward manner for the benefit of, e.g., cold-atom physics [1], astrophysics [2], and spectroscopy [3] and thus make important bridges from *ab initio* to the practical world.

The polarizability is conventionally divided into components as a perturbation expansion. For example, in the Buckingham convention [4] the total energy of a system in a constant electric field (Stark effect) is expressed as

$$E^{(1)} = E^{(0)} - \mu_\alpha^{(0)} F_\alpha - \tfrac{1}{2}\alpha_{\alpha\beta} F_\alpha F_\beta - \tfrac{1}{6}\beta_{\alpha\beta\gamma} F_\alpha F_\beta F_\gamma - \tfrac{1}{24}\gamma_{\alpha\beta\gamma\delta} F_\alpha F_\beta F_\gamma F_\delta - \cdots \quad (1)$$

with permanent dipole moment $\mu_\alpha^{(0)}$, static dipole polarizability $\alpha_{\alpha\beta}$, and first and second hyperpolarizabilities $\beta_{\alpha\beta\gamma}$ and $\gamma_{\alpha\beta\gamma\delta}$, respectively. In addition, the expression for the induced dipole moment reduces to

$$\mu_\alpha^{(1)} = -\frac{\partial E^{(1)}}{\partial F_\alpha} = \mu_\alpha^{(0)} + \alpha_{\alpha\beta} F_\beta + \tfrac{1}{2}\beta_{\alpha\beta\gamma} F_\beta F_\gamma + \tfrac{1}{6}\gamma_{\alpha\beta\gamma\delta} F_\beta F_\gamma F_\delta + \cdots, \quad (2)$$

where indices $\alpha,\beta,\gamma,\delta,\ldots$ refer to Einstein summation of distinct tensor components.

The polarizabilities are usually calculated with either sum-over-states [5] or finite-field (FF) approaches [6]. Sum-over-states formulas are exact, but they become extensively complicated for higher-rank polarizabilities. Also, their computation typically involves limited basis sets. The FF principle is based on calculating the perturbations in multiple finite-field strengths and then extrapolating the differentials to zero field [7], e.g.,

$$\alpha_{\alpha\beta} = \left.\frac{\partial^2 E^{(1)}}{\partial F_\alpha \partial F_\beta}\right|_{F=0}. \quad (3)$$

This can be done with a variety of methods. Basically, the challenge is to approximate solutions to the system, which is fundamentally unstable in any nonzero constant electric field.

Moreover, electron-nucleus coupling and internuclear motion have to be treated in order to obtain total polarizabilities. This is commonly performed with the so-called clamped-nucleus approximation, i.e., supplementing electronic polarizability with rotational and vibrational components [8]:

$$\alpha^{\mathrm{tot}} = \alpha^{\mathrm{el}} + \alpha^{\mathrm{rot}} + \alpha^{\mathrm{vib}}, \quad (4)$$

where α^{tot} is the total polarizability. This cumbersome separation can be overcome with a nonadiabatic Hylleraas basis approach, which, however, is limited to three particles only [9].

Overall, the extent of the finite-field response is built upon increasingly complicated series of properties. This combined with finite-temperature statistics makes consideration of electric-field phenomena a formidable task with conventional methods. In this work we introduce a more holistic approach: the path-integral Monte Carlo (PIMC) approach [10–13] applied in the study of electric-field phenomena and calculation of polarizabilities. We were able to find only a couple of studies [14,15] vaguely geared in this direction.

Thus, we present a comprehensive and accurate study of static polarizabilities of neutral hydrogen atoms and molecules. These two- and four-particle systems are considered both adiabatically and nonadiabatically, i.e., with and without the Born-Oppenheimer (BO) approximation. Also, it should be emphasized that with the PIMC approach all the terms in Eqs. (1) and (2) are implicitly included. We will demonstrate that the nonrelativistic PIMC approach is a straightforward and efficient tool for studying electric-field effects including the inherent temperature dependence.

*Corresponding author: juha.tiihonen@tut.fi

II. METHOD

For interacting distinguishable particles the Feynman formulation of quantum-statistical mechanics [16] gives the partition function as a trace of the density matrix

$$Z = \mathrm{Tr}\hat{\rho}(\beta) = \int dR_0 dR_1 \cdots dR_{M-1} \prod_{i=0}^{M-1} e^{-S(R_i, R_{i+1};\tau)},$$

where $\hat{\rho}(\beta) = e^{-\beta\hat{H}}$, S is the action, $\beta = 1/k_B T$, $\tau = \beta/M$, $R_M = R_0$, and M is called the Trotter number. We use the pair approximation in the action [10,17] for the Coulomb interaction of charges. For neutral systems the external potential arising from the homogeneous finite electric field yields an additional diagonal term in the action, i.e., [18]

$$U_{\mathrm{ext}}(R;\tau) = -\tau\mu_\alpha F_\alpha = -\tau F_\alpha q_n r_{n\alpha}, \tag{5}$$

where R is the configuration at given time slice, F_α is the electric field, and q_n is the charge of the nth particle, where n denotes summation over all particles. Sampling in the configuration space is carried out using the Metropolis procedure [19] with multilevel bisection moves [20]. We use both the thermal estimator [10] and the virial estimator [21] in the calculation of total energy.

In our model all the particles are described as boltzmannons, i.e., they obey the Boltzmann statistics. Since we are dealing with the hydrogen atom and the ground state of the H_2 molecule the particles involved can accurately be treated as distinguishable particles. In the case of the hydrogen molecule this is possible in the singlet state by assigning spin up to one electron and spin down to the other one and applying the same for the positive particles. This is accurate enough, as long as the thermal energy is well below that of the lowest electronic triplet excitation. At $T \approx 160$ K this is the case for the hydrogen molecule [11]. This fact can also be exploited in the calculations of BO energetics at the equilibrium internuclear distance. Therefore, within our BO simulations we may use temperatures up to a few thousand Kelvin and still the system remains in its electronic ground state (see, for example, the BO results in Fig. 1 of Ref. [12]). The numerical gain is a smaller statistical error in less time.

It should be emphasized that for systems consisting of distinguishable particles the accuracy of the PIMC method is determined only by the imaginary-time time step τ. As τ approaches zero the exact many-body results are obtained within the numerical precision.

We use atomic units in this work and thus the lengths, energies, and masses are given in units of the Bohr radius a_0, hartree E_h, and free-electron mass m_e, respectively. Therefore, we have $m_e = 1$ as the mass of the electrons and for the protons we use $m_p = 1836.152\,672\,48 m_e$. We use the imaginary-time time step $\tau = \beta/M = 0.03 E_\mathrm{h}^{-1}$, which ensures very good accuracy [13]. Our Trotter number $M = 2^{16}$ together with the time step τ result in a 160.6 K simulation temperature. For the BO calculations we use higher temperature for better statistics, but as discussed above we are still sampling the correct electronic state. The statistical standard error of the mean with 2σ limits is used as an error estimate for the observables. The simulations are carried out in a periodic cubic simulation cell $V = (150a_0)^3$, where we apply the minimum image convention.

III. RESULTS

We present PIMC results for the hydrogen atom H and hydrogen molecule H_2 both adiabatically and nonadiabatically. The adiabatic calculations are carried out with fixed nuclei and will be referred as electronic BO calculations. The nonadiabatic calculations with freely moving quantum nuclei include full account of electron-nuclei coupling and are called all quantum (AQ). In general, we are able to separate electronic, rotational, and vibrational contributions by restricting motion of the chosen degrees of freedom.

We have chosen a few finite-field strengths F_z ($E_h e^{-1} a_0^{-1}$), in which we compute the induced perturbations in dipole moment and total energy. We confirm that a reasonably weak strength of the field ensures a *metastable* equilibrium state, where quantum statistics can be sampled without risk of dissociation, i.e., electrons tunneling apart from the nuclei due to the electric field.

The results are compared with finite-field reference models constructed from Eqs. (1) and (2) (as in Ref. [7]) and known values for polarizabilities from the literature [22–26]. For atoms and molecules with a zero permanent dipole moment, i.e., $\mu^{(0)} = 0$, also $\beta_{zzz} = 0$ [8]. It should be emphasized that the reference model is for 0 K temperature, it is only exact at the zero-field limit, and while considered only up to γ_{zzzz}, it is subject to a truncation error.

We begin with computation of the H atom. The only difference between the BO and AQ cases is in the ground-state

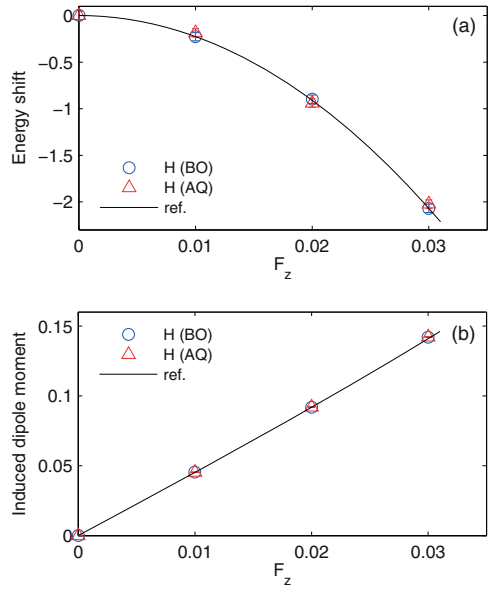

FIG. 1. (Color online) (a) Stark shift (in mhartree) and (b) induced dipole moment (ea_0) of the hydrogen atom as functions of the external electric field. The energy shift is the difference between perturbed and unperturbed total energies $\Delta E^{(1)} = E^{(1)} - E^{(0)}$. Blue circles represent BO results, red triangles represent AQ results, and the solid line is the reference model (see Table I).

TABLE I. Energy shift $\Delta E^{(1)} = E^{(1)} - E^{(0)}$ (in mhartree) and induced dipole moment (ea_0) of the H atom, also visualized in Fig. 1. The column labeled "Difference" represents the difference between values from the closest available reference model [22,23] and the PIMC results.

Calculation	F_z	$\Delta E^{(1)}$	ΔE^{ref}	Difference	$\Delta\mu^{(1)} \times 10^2$	$\Delta\mu^{\text{ref}} \times 10^2$	Difference
BO	0.0	0.000(52)	0.0	0.000(52)	0.004(15)	0.0	−0.004(15)
	0.01	−0.227(39)	−0.2256	0.002(39)	4.530(12)	4.5222	−0.008(12)
	0.02	−0.898(39)	−0.9089	−0.011(39)	9.197(14)	9.1778	−0.019(14)
	0.03	−2.069(39)	−2.0700	−0.001(39)	14.203(16)	14.099	−0.103(16)
AQ	0.0	0.000(50)		0.000(50)	−0.008(17)		0.008(17)
	0.01	−0.185(45)		−0.040(45)	4.536(13)		−0.013(13)
	0.02	−0.939(45)		0.030(45)	9.195(15)		−0.018(15)
	0.03	−2.023(45)		−0.047(45)	14.208(18)		−0.109(18)

energy: With a virial estimator we get (in zero field) $E^{(0)}(\text{BO}) = -0.499\,97(5)$ and $E^{(0)}(\text{AQ}) = -0.499\,71(5)$ against exact $E^{\text{ref}}(\text{BO}) = -0.5$ and $E^{\text{ref}}(\text{AQ}) = -0.499\,727\,8$, respectively. In Fig. 1(a) we present the energy shift and in Fig. 1(b) we give the induced dipole moment for a few finite-field values. We employ the same BO reference model to both cases and they both yield excellent agreement. However, in stronger fields, e.g., $F_z = 0.03$, the truncation error, i.e., exclusion of the fourth hyperpolarizability $\epsilon_{zzzzzz} = 3.533\,595 \times 10^6$ [23], is large enough to be observed as a small difference between our result and the reference. These results are also given numerically in Table I.

The static (hyper)polarizabilities are obtained by nonlinear regression on our results. We use the data for the induced dipole moment because its estimator is statistically more precise compared to those of the total energy. The fitted polarizabilities for hydrogen are shown in Table II. Our static dipole polarizabilities α are accurate within 95% confidence estimates and second hyperpolarizabilities γ are slightly overestimated due to truncation error. Generally, the static dipole polarizabilities have much smaller error than the second hyperpolarizabilities.

The adiabatic simulations of the H_2 molecule are performed at the equilibrium distance $R_e = 1.40a_0$ [24] and, unlike other calculations, using a thermal estimator for the total energy [10]. To compensate for the high variance of the thermal estimator, we boost the efficiency by computing at higher temperature $T = 2500$ K, which, as argued earlier, is still close enough to the low-temperature clamped-nuclei density matrix. Our ground-state energy without the external field is $E^{(0)}(\text{BO}) = -1.174\,34(18)$, which is close to the highly accurate quantum chemistry estimate of $E^{\text{ref}}(\text{BO}) = -1.174\,474\,77$ [25]. The adiabatic hydrogen molecule is considered in the two extreme orientations in laboratory coordinates: perpendicular $\perp$ or parallel $\parallel$ to the external field. Computation of intermediate orientation angles could be done just as easily, but it is not considered here. Changes in total energy and induced dipole moment are presented in Figs. 2(a) and 2(b), respectively, and corresponding numerical values are given in Table III. These results demonstrate good agreement in both orientations. Using the procedure similar to that for the H atom, we obtain

TABLE II. Static dipole polarizabilities and second hyperpolarizabilities of H with 95% confidence intervals are obtained using nonlinear regression on our PIMC results. They are compared to the 0 K references found in the literature.

	α_{zz} (BO)	$\bar{\alpha}$ (AQ)
H	4.496(23)[a]	4.496(39)[a]
	4.500[b]	
	γ_{zzzz} (BO)	$\bar{\gamma}$ (AQ)
	1586(184)[a]	1592(316)[a]
	1333.125[c]	

[a]This work (160 K).
[b]Reference [22].
[c]Reference [23].

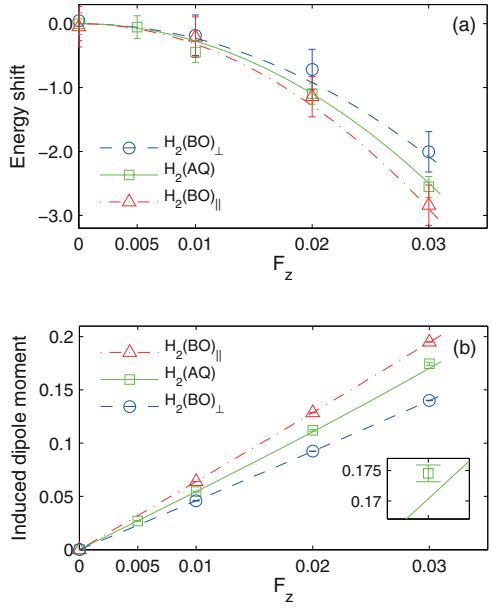

FIG. 2. (Color online) (a) Stark shift (in mhartree) and (b) induced dipole moment (ea_0) of the hydrogen molecule as functions of the external electric field. The energy shift is the difference between perturbed and unperturbed total energies $\Delta E^{(1)} = E^{(1)} - E^{(0)}$. Blue circles represent BO ($\perp$) results, red triangle represent BO ($\parallel$) results, green squares represent AQ results, and lines are the corresponding reference models (see Table III).

TABLE III. Energy shift $\Delta E^{(1)} = E^{(1)} - E^{(0)}$ (in mhartree) and induced dipole moment (ea_0) of the H_2 molecule, also visualized in Fig. 2. The column labeled "Difference" represents the difference between values from the closest available reference model [24–26] and the PIMC results.

Calculation	F_z	$\Delta E^{(1)}$	ΔE^{ref}	Difference	$\mu_z^{(1)} \times 10^2$	$\mu_z^{\mathrm{ref}} \times 10^2$	Difference
$BO_\parallel$	0.0	−0.048(317)	0.0	0.048(317)	−0.003(11)	0.0	0.003(11)
	0.01	−0.211(316)	−0.3196	−0.109(316)	6.399(11)	6.3984	−0.001(11)
	0.02	−1.141(316)	−1.2820	−0.141(316)	12.867(11)	12.865	−0.002(11)
	0.03	−2.841(316)	−2.8972	−0.057(316)	19.468(11)	19.468	−0.034(11)
$BO_\perp$	0.0	0.048(317)	0.0	−0.048(317)	0.002(11)	0.0	−0.002(11)
	0.01	−0.181(317)	−0.2292	−0.048(317)	4.590(11)	4.5886	−0.002(11)
	0.02	−0.717(317)	−0.9196	−0.202(317)	9.236(11)	9.2348	−0.001(11)
	0.03	−2.006(317)	−2.0800	−0.074(317)	13.996(11)	13.996	−0.022(11)
AQ	0.0	0.000(170)		0.000(170)	0.019(48)		−0.019(48)
160 K	0.005	−0.054(179)		−0.013(179)	2.699(28)		−0.012(28)
	0.01	−0.443(165)		0.172(165)	5.453(41)		−0.010(41)
	0.02	−1.095(166)		0.000(166)	11.205(91)		−0.143(91)
	0.03	−2.554(163)		0.058(163)	17.453(138)		−0.419(138)
AQ	0	0.000(296)	0.0	0.000(296)	0.037(47)	0.0	−0.037(47)
295 K	0.005	−0.082(322)	−0.0677	0.014(322)	2.738(53)	2.7106	−0.028(53)
	0.01	−0.494(250)	−0.2714	0.222(250)	5.443(51)	5.4433	0.001(51)
	0.02	−1.316(253)	−1.0945	0.222(253)	11.063(81)	11.063	−0.052(81)
	0.03	−2.686(247)	−2.4958	0.190(247)	17.148(131)	17.035	−0.113(131)

static dipole polarizabilities and second hyperpolarizabilities, which are shown in Table IV. The error bars can be made smaller by additional computational labor.

Nonadiabatic calculations of H_2 include rovibrational effects arising from the chosen finite temperature and influenced by the external electric field. It should be pointed out that with the nonadiabatic PIMC approach the electron-nuclei coupling is exactly included and thus in our simulations we sample an accurate many-body density matrix at finite temperature and in an external electric field. For the nonadiabatic molecule the equilibrium distance is slightly larger compared to the case of static nuclei and this is also accurately taken into account [11]. To compare ground-state energies, we extrapolate our finite-temperature energy to 0 K, which yields $E^{(0)}_{0\,\mathrm{K(AQ)}} = -1.163\,87(18)$, which coincides with the 0 K reference value $E^{\mathrm{ref}}(\mathrm{AQ}) = -1.164\,025\,018\,5$ [27]. Our simulations at $T = 160.6$ K demonstrate good agreement in the shift of the total energies, in the induced dipole moment, and in the fitted polarizabilities (see Fig. 2 and Tables IV and III).

It is important to understand that the exact polarizabilities in finite-temperature equilibrium obey the Maxwell-Boltzmann distribution of excited-state contributions. With the adiabatic and the monatomic cases, these reduce to electronic ground states at low temperatures, but this is not the case with H_2(AQ), whose excited rotational states are considerably occupied at $T = 160.6$ K. By thermal averaging [8] it can be shown that the total hyperpolarizability may vary significantly with temperature. This can be seen from from Fig. 2 and Table III, where the induced dipole moment of H_2(AQ) has a slightly higher value at 160.6 K (PIMC approach) than at the 295 K reference [26]. Indeed, comparison of the obtained hyperpolarizabilities in Table IV shows that $\bar{\gamma}(160.6\ \mathrm{K}) =$

TABLE IV. Static dipole polarizabilities and second hyperpolarizabilities of H_2 with 95% confidence intervals are obtained using nonlinear regression on 160 K PIMC results. They are compared to the 0 K references found in the literature.

	α_{zz} $(\mathrm{BO})_\parallel$	α_{xx} $(\mathrm{BO})_\perp$	$\bar{\alpha}$ (AQ)
H_2	6.382(13)[a]	4.577(10)[a]	5.417(37)[a]
	6.387493[c]	4.57861[c]	5.4139[d]
			5.428(59)[b]
	γ_{zzzz} $(\mathrm{BO})_\parallel$	γ_{xxxx} $(\mathrm{BO})_\perp$	$\bar{\gamma}$ (AQ)
	787(100)[a]	640(73)[a]	2678(298)[a]
	682.5[c]	575.9[c]	1763[e]
			1918(479)[b]

[a]This work (160 K).
[b]This work (295 K).
[c]Reference [24].
[d]Reference [25].
[e]Reference [26] (295 K).

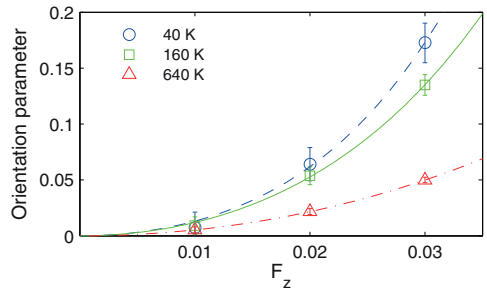

FIG. 3. (Color online) Orientation parameter of H_2 plotted against the external field strength at different temperatures. Blue circles represent 40 K, green squares 160 K, and red triangles 640 K results. Solid lines are quadratic fits to guide the eye.

TABLE V. Orientation parameter of the hydrogen molecule H_2 as a function of T (visualized in Fig. 3).

		F_z		
	T (K)	0.01	0.02	0.03
H_2	40	0.007(14)	0.064(15)	0.173(18)
	160	0.009(8)	0.054(8)	0.135(9)
	640	0.005(3)	0.021(3)	0.050(3)

2678(298) is considerably higher than $\bar{\gamma}(295\ \mathrm{K}) = 1918(479)$ or the reference value $\bar{\gamma}^{\mathrm{ref}}(295\ \mathrm{K}) = 1763$ [26], which is estimated according to Eq. (4). Static dipole polarizability $\bar{\alpha}$ is predicted to increase slightly with the temperature [25], however, the effect is lost here within error boundaries.

The rotational coupling with the electric field can be further examined by the orientation parameter

$$S = \tfrac{1}{2}\langle 3\cos^2\theta - 1\rangle, \tag{6}$$

where θ is the angle between the laboratory axis (electric field) and that of the diatomic H_2. The perpendicular configuration gives the lower limit $S = -\frac{1}{2}$ and the parallel configuration the upper limit $S = 1$; random orientation gives the expectation value of $\langle S\rangle = 0$. The parameter is computed for H_2(AQ) in different field strengths and temperatures using lower accuracy ($\tau \approx 1$) for feasible efficiency. Our results are presented in Fig. 3 and in Table V. While the static total polarizability peaks at parallel orientation, the estimate of S increases towards 1 in stronger fields and more so at lower temperatures, where thermal distortion is smaller.

IV. CONCLUSION

In this work we presented a path-integral Monte Carlo study of the hydrogen atom and hydrogen molecule in a weak homogeneous static electric field. We demonstrated accurate finite-field results for the Stark shift and induced dipole moment, which agree excellently with the Buckingham perturbation expansion, i.e., Eqs. (1) and (2) in the low-temperature regime. Also, our extrapolated values for static (hyper)polarizabilities match within confidence bounds the most accurate ones found in the literature.

We showed that with path integrals it is straightforward to extend the conventional analysis by taking into account the nonadiabatic effects and those from finite temperature. This also supports the extensive work by Bishop on finite-temperature effects on polarizabilities [8]. To this end, we also demonstrated how the orientation of the hydrogen molecule behaves as a function of the electric-field strength. While we do not yet report any nonequilibrium statistics or comprehensive finite-temperature dependences, it is evident that this approach permits access to *ab initio* study of unexplored electric-field phenomena.

ACKNOWLEDGMENTS

We acknowledge CSC–IT Center for Science Ltd. and Tampere Center for Scientific Computing for the allocation of computational resources. We gratefully acknowledge support from the Academy of Finland.

[1] J. Mitroy, M. S. Safronova, and C. W. Clark, J. Phys. B **43**, 202001 (2010).
[2] G. J. Harris, A. E. Lynas-Gray, S. Miller, and J. Tennyson, Astrophys. J. **600**, 1025 (2004).
[3] N. Subramanian, A. F. Goncharov, M. Somayazulu, and R. J. Hemley, J. Phys.: Conf. Ser. **215**, 012057 (2010).
[4] A. D. Buckingham, *Advances in Chemical Physics* (Wiley, New York, 2007), pp. 107–142.
[5] D. P. Shelton and J. E. Rice, Chem. Rev. **94**, 3 (1994).
[6] H. D. Cohen and C. C. J. Roothaan, J. Chem. Phys. **43**, S34 (1965).
[7] J. Kobus, Phys. Rev. A **91**, 022501 (2015).
[8] D. M. Bishop, Rev. Mod. Phys. **62**, 343 (1990).
[9] L.-Y. Tang, Z.-C. Yan, T.-Y. Shi, and J. F. Babb, Phys. Rev. A **90**, 012524 (2014).
[10] D. M. Ceperley, Rev. Mod. Phys. **67**, 279 (1995).
[11] I. Kylänpää, T. T. Rantala, and D. M. Ceperley, Phys. Rev. A **86**, 052506 (2012).
[12] I. Kylänpää and T. T. Rantala, J. Chem. Phys. **133**, 044312 (2010).
[13] I. Kylänpää and T. T. Rantala, J. Chem. Phys. **135**, 104310 (2011).
[14] D. Shin, M.-C. Ho, and J. Shumway, arXiv:quant-ph/0611105.
[15] H. Nagao, K. Ohta, M. Nakano, and K. Yamaguchi, Int. J. Quantum Chem. **65**, 697 (1997).
[16] R. P. Feynman, *Statistical Mechanics* (Perseus, Reading, 1998).
[17] R. G. Storer, J. Math. Phys. **9**, 964 (1968).
[18] J. Tiihonen, Master's thesis, Tampere University of Technology, 2014.
[19] N. Metropolis, A. W. Rosenbluth, M. N. Rosenbluth, A. H. Teller, and E. Teller, J. Chem. Phys. **21**, 1087 (1953).
[20] C. Chakravarty, M. C. Gordillo, and D. M. Ceperley, J. Chem. Phys. **109**, 2123 (1998).
[21] M. F. Herman, E. J. Bruskin, and B. J. Berne, J. Chem. Phys. **76**, 5150 (1982).
[22] I. Waller, Z. Phys. **38**, 635 (1926).
[23] G. L. Sewell, Math. Proc. Camb. Philos. Soc. **45**, 631 (1949).
[24] D. M. Bishop, J. Pipin, and S. M. Cybulski, Phys. Rev. A **43**, 4845 (1991).
[25] W. Kolos and L. Wolniewicz, J. Chem. Phys. **49**, 404 (1968).
[26] D. M. Bishop and B. Lam, Chem. Phys. Lett. **143**, 515 (1988).
[27] M. Stanke, D. Kędziera, S. Bubin, M. Molski, and L. Adamowicz, J. Chem. Phys. **128**, 114313 (2008).

PUBLICATION II

General polarizability and hyperpolarizability estimators for the path-integral Monte Carlo method applied to small atoms, ions, and molecules at finite temperatures

Juha Tiihonen, Ilkka Kylänpää & Tapio T. Rantala

Physical Review A 94, 032515, 2016
DOI: 10.1103/PhysRevA.94.032515

General polarizability and hyperpolarizability estimators for the path-integral Monte Carlo method applied to small atoms, ions, and molecules at finite temperatures

Juha Tiihonen, Ilkka Kylänpää, and Tapio T. Rantala
Department of Physics, Tampere University of Technology, P.O. Box 692, FI-33101 Tampere, Finland
(Received 27 July 2016; published 26 September 2016)

The nonlinear optical properties of matter have a broad relevance and many methods have been invented to compute them from first principles. However, the effects of electronic correlation, finite temperature, and breakdown of the Born-Oppenheimer approximation have turned out to be challenging and tedious to model. Here we propose a straightforward approach and derive general field-free polarizability and hyperpolarizability estimators for the path-integral Monte Carlo method. The estimators are applied to small atoms, ions, and molecules with one or two electrons. With the adiabatic, i.e., Born-Oppenheimer, approximation we obtain accurate tensorial ground state polarizabilities, while the nonadiabatic simulation adds in considerable rovibrational effects and thermal coupling. In both cases, the 0 K, or ground-state, limit is in excellent agreement with the literature. Furthermore, we report here the internal dipole moment of PsH molecule, the temperature dependence of the polarizabilities of H^-, and the average dipole polarizabilities and the ground-state hyperpolarizabilities of HeH^+ and $H_3{}^+$.

DOI: 10.1103/PhysRevA.94.032515

I. INTRODUCTION

Obtaining nonlinear optical properties (NOP) of matter by computational simulation is particularly important in such environments that are out of reach with experimental studies. For instance, this applies to exotic light-nucleus molecules like $H_3{}^+$ and HeH^+ in hot and dense stars and gas planets [1–3], or short lifetime particles like Ps or PsH [4–6]. Quite a different but trending regime is that of computational biophysics, where the accurate effects of polarization, finite temperature, and dielectric solvents are required of the molecular interaction models [7]. Motivations for the computational study of the NOP are diverse, and they are properly summarized in dedicated reviews [8–11].

The first-principles treatment of dielectric response comes down to dipole and multipole moments and polarizabilities. Basically, the computation of tensorial polarizabilities is straightforward, and a lot of methods have been developed for this purpose over the years, e.g., Refs. [12–23]. The significance of polarizabilities is pronounced in many physical scales starting from microscopic interactions, such as van der Waals [24], to macroscopic properties, like dielectric constant and refractive index. Transformation from the molecular to the optical level is typically an emergent procedure that loses some of the tensorial detail to statistical averaging of properties. The density of the effective polarizable medium is then related to the bulk with Clausius-Mossotti or Lorentz-Lorenz relations. Thus, in principle, one could build up macroscopic NOP in specific conditions simply by computing and combining the right set of microscopic polarizabilities. In practice, this can get tedious.

For example, consider a diatomic homonuclear molecule, like H_2, that has two distinct dipole polarizabilities α_{zz} and α_{xx}. Combined, they make up a rotationally averaged, effective polarizability $\bar{\alpha}$ that is well suited for the macroscopic transformation. However, anisotropy of the electronic polarizability is strongly coupled with the rovibrational state of the system, and to address this, the breakdown of the Born-Oppenheimer approximation is needed. The conventional way is to form the total polarizability out of the electronic, rotational, and vibrational parts [8], the latter of which are unique for every rovibrational state. When it comes to modeling the thermal coupling of properties, the relevant ensemble of excited states is required. This has lead to systematic tabulation of rovibrational state contributions, e.g., Ref. [25], which is surely informative but becomes quickly overwhelming with higher temperatures and more complicated systems. Thus, for simulating the NOP in thermal conditions, the most reasonable course of action is to reduce complexity. This can be done by making approximations or using semiempirical methods, e.g., Refs. [26,27]. The more controllable way is to give up the tensorial character and concentrate directly on the average properties [28] or the exact thermal ensemble.

In this paper, we provide a tangible interface between tensorial distinction and thermal averaging of molecular polarizabilities. We perform a series of path-integral Monte Carlo (PIMC) simulations on a variety of small atoms and molecules: H, Ps, He, H^-, Li^+, PsH, $H_2{}^+$, H_2, $H_3{}^+$, and HeH^+. Similar study for H and H_2 was done earlier with finite field approach [29], but this time we propose field-free static polarizability and hyperpolarizability estimators for imaginary-time path-integral methods. The exact account of particle correlations in PIMC is a useful feature for two reasons: electronic correlation is important to the accurate evaluation of polarizabilities [30], and nuclear correlation allows a controlled breakdown of the Born-Oppenheimer approximation. Also, inherent account of thermal ensemble allows direct sampling in finite temperature and, in principle, at finite density. That being said, PIMC is probably the most straightforward way to simulate thermal coupling of polarizabilities from first principles.

II. THEORY

Consider a quantum statistical system with N distinguishable particles in phase space R. The state of the system is described by finite-temperature density matrix ρ. The density operator is

$$\hat{\rho} = e^{-\hat{H}/k_B T}, \tag{1}$$

where $\hat{H}$ is the Hamiltonian operator. In the path-integral picture, we identify $\hbar/k_B T = \beta = i(t - t_0)$ as an imaginary-time interval, so that we can write Eq. (1) in terms of action $\hat{S} = \beta\hat{H}$. Any diagonal observable $\langle O\rangle$ can be obtained by integrating the relevant operator $\hat{O}$ over the phase space

$$\langle O\rangle = Z^{-1}\int dR\langle R|\hat{\rho}|R\rangle O(R), \tag{2}$$

where

$$Z = \int dR\langle R|\hat{\rho}|R\rangle \tag{3}$$

is the partition function.

Now, consider a perturbation caused by a uniform external electric field F_α, where indices $\alpha,\beta,\gamma,\delta,\ldots$, follow the Einstein summation over the axes x, y, and z. In uniform field, the perturbation of the Hamiltonian is completely described by

$$\hat{H}^{(1)} = \hat{H}^{(0)} - \hat{\mu}_\alpha F_\alpha, \tag{4}$$

where $\hat{H}^{(0)}$ is the unperturbed Hamiltonian and $\hat{\mu}_\alpha$ is the dipole moment operator. According to the Buckingham convention [31], the change in total energy is written as a perturbation expansion of coefficients

$$E^{(1)} = E^{(0)} + \mu_\alpha F_\alpha + \tfrac{1}{2}\alpha_{\alpha\beta}F_{\alpha\beta} + \tfrac{1}{6}\beta_{\alpha\beta\gamma}F_{\alpha\beta\gamma} + \tfrac{1}{120}\gamma_{\alpha\beta\gamma\delta}F_{\alpha\beta\gamma\delta} + \cdots. \tag{5}$$

Hence, in the zero-field limit, we can solve the individual properties:

$$\mu_\alpha = \lim_{F\to 0}\frac{\partial}{\partial F_\alpha}E^{(1)}, \tag{6}$$

$$\alpha_{\alpha\beta} = \lim_{F\to 0}\frac{\partial}{\partial F_\alpha}\frac{\partial}{\partial F_\beta}E^{(1)} = \lim_{F\to 0}\frac{\partial}{\partial F_\beta}\mu_\alpha, \tag{7}$$

$$\beta_{\alpha\beta\gamma} = \lim_{F\to 0}\frac{\partial}{\partial F_\alpha}\frac{\partial}{\partial F_\beta}\frac{\partial}{\partial F_\gamma}E^{(1)} = \lim_{F\to 0}\frac{\partial}{\partial F_\gamma}\alpha_{\alpha\beta}, \tag{8}$$

$$\gamma_{\alpha\beta\gamma\delta} = \lim_{F\to 0}\frac{\partial}{\partial F_\alpha}\frac{\partial}{\partial F_\beta}\frac{\partial}{\partial F_\gamma}\frac{\partial}{\partial F_\delta}E^{(1)} = \lim_{F\to 0}\frac{\partial}{\partial F_\delta}\beta_{\alpha\beta\gamma}, \tag{9}$$

and so on. Bearing in mind that $\frac{\partial\hat{S}}{\partial F_\alpha} = \beta\hat{\mu}_\alpha$, direct differentiation eventually leads to the following exact tensorial estimators:

$$\alpha_{\alpha\beta} = \beta[\langle\mu_\alpha\mu_\beta\rangle - \langle\mu_\alpha\rangle\langle\mu_\beta\rangle], \tag{10}$$

$$\beta_{\alpha\beta\gamma} = \beta^2\left[\langle\mu_\alpha\mu_\beta\mu_\gamma\rangle + 2\langle\mu_\alpha\rangle\langle\mu_\beta\rangle\langle\mu_\gamma\rangle - \sum_{\alpha\beta,\gamma}\langle\mu_\alpha\mu_\beta\rangle\langle\mu_\gamma\rangle\right], \tag{11}$$

$$\gamma_{\alpha\beta\gamma\delta} = \beta^3\left[\langle\mu_\alpha\mu_\beta\mu_\gamma\mu_\delta\rangle - 6\langle\mu_\alpha\rangle\langle\mu_\beta\rangle\langle\mu_\gamma\rangle\langle\mu_\delta\rangle - \sum_{\alpha\beta\gamma,\delta}\langle\mu_\alpha\mu_\beta\mu_\gamma\rangle\langle\mu_\delta\rangle - \sum_{\alpha\beta,\gamma\delta}\langle\mu_\alpha\mu_\beta\rangle\langle\mu_\gamma\mu_\delta\rangle + 2\sum_{\alpha\beta,\gamma,\delta}\langle\mu_\alpha\mu_\beta\rangle\langle\mu_\gamma\rangle\langle\mu_\delta\rangle\right], \tag{12}$$

where shorthand notation is used for unique terms with cyclic permutation over comma-separated indices, e.g.,

$$\sum_{\alpha\beta,\gamma}\langle\mu_\alpha\mu_\beta\rangle\langle\mu_\gamma\rangle = \langle\mu_\alpha\mu_\beta\rangle\langle\mu_\gamma\rangle + \langle\mu_\gamma\mu_\alpha\rangle\langle\mu_\beta\rangle + \langle\mu_\beta\mu_\gamma\rangle\langle\mu_\alpha\rangle.$$

It should be pointed out that the bracketed terms on the right-hand side, e.g., $\langle u_\alpha\rangle$, are the relevant observables for a path-integral simulation. That is, in this form the polarizability estimates, e.g., $\langle\alpha_{\alpha\beta}\rangle$, cannot be computed directly from a single sample trajectory. Rather, they emerge from the correct addition of the long-time expectation values of different dipole moment products.

III. METHOD

In path-integral Monte Carlo scheme, integration of phase space is carried out by Monte Carlo sampling of discrete imaginary-time paths. The path of length β is discretized according to the expansion [32], which divides the length into small intervals: $\beta = M\tau$, where M is the Trotter number. Calculation of diagonal properties can then be done by taking average of each time slice:

$$\langle O\rangle = M^{-1}Z^{-1}\sum_{i=1}^{M}\langle R_{i-1}|\rho(R_{i-1},R_i;\tau)|R_i\rangle O(R_i), \tag{13}$$

where R_i are the coordinates of particles at the ith time slice, and $R_0 = R_M$. This is exact in the limit of $\tau\to 0$, or $M\to\infty$, but for practical reasons finite time step is used. The best accuracy is obtained by using the so-called pair approximation to describe Coulomb interaction [33]. Correct and efficient sampling of the density operator $\rho(R_{i-1},R_i;\tau)$ near the thermal equilibrium is obtained by Metropolis Monte Carlo with multilevel bisection procedure [34]. In this paper, only systems with up to two electrons are considered. Thus opposite spins are assumed, and all the particles obey Boltzmann statistics [5].

The total energies are obtained by thermal or virial estimators [35]. The virial estimator is preferred, because it has smaller variance. However, for convenience the thermal estimator is used for adiabatic simulations with more than one fixed nucleus. The polarizabilities are computed according to the dipole moment products that appear in Eqs. (10)–(12). The dipole moment is unambiguously defined for the neutral systems, where the effect of the origin cancels out. For the systems with a nonzero net charge, we set the origin at the

center-of-mass of the nuclei, or that of all the particles, in adiabatic or nonadiabatic simulations, respectively.

IV. RESULTS

We investigate a few well-known small atoms, ions, and molecules with up to two electrons by performing parallel PIMC simulations. By fixing or freeing the nuclear motion we demonstrate the breakdown of the Born-Oppenheimer approximation. The inclusion of the electron-nuclei coupling reveals the rovibrational effects, and thus, together with finite temperature, also the thermal coupling of properties. This allows us to report the total energies and relevant tensorial polarizabilities corresponding to both the electronic ground state and the finite-temperature rovibrational ensemble. Due to the exponential nature of thermal effects, we approach the observed thermal trends with an *ad hoc* exponential least-squares fit of the form

$$O = a\,\exp(bT) + c, \tag{14}$$

where O is the observable and a, b, and c are the fitting parameters.

In any case, the number of nonvanishing and distinguishable tensor properties is greatly reduced by symmetry. To best convey with the literature, we use z to mark the principal direction, and, when suitable, x for a perpendicular direction. None of the studied systems require more than two simultaneous directions. Capital Z is used to denote the laboratory axis, which is used in freely rotating nonadiabatic simulations. Statistical standard error of the mean (SEM) with 2σ, i.e., 2SEM confidence boundaries are used unless otherwise stated.

When relevant, we use $m_p = 1836.15267248 m_e$ for proton mass and $m_{\mathrm{He}} = 7294.2995363 m_e$ for that of He nucleus. Generally, the time step of $\tau = 0.03$ is sufficient for the systems with only hydrogen, and any small discrepancy with the literature is due to the high temperature. For heavier nuclei, i.e., He and Li^+, also smaller time step of $\tau = 0.01$ is used, but it accounts for a small error in total energy. In some simulations, especially the nonadiabatic, $\tau = 0.1$ is used for computational feasibility, but also to demonstrate the time-step effect, or lack thereof.

A. Adiabatic simulations

The adiabatic, i.e., fixed-nuclei calculations, are good to begin with, since they exhibit no thermal coupling by default: the most stable systems, i.e., the neutral and the positive, are effectively at their electronic ground states at thousands of kelvins [48]. High temperature is preferred for computational feasibility, and thus 2000 K is used for the simulation of H, Ps, He, H_2, Li^+, H_2^+, H_3^+, and HeH^+. PsH is less stable because of the highly mobile positron and is simulated at 1000 K. The most special case is the hydrogen negative ion, whose polarizabilities show notable temperature dependency at relatively low temperatures; H^- is simulated at 25–500 K and the results are extrapolated to 0 K.

For each adiabatic simulation we report the time step, the total energy, and all the relevant polarizability tensors depending on the symmetry. Also, the best available 0 K references from the literature are shown for comparison

TABLE I. Time steps τ, total energies E, and static dipole polarizabilities α_{zz} and second hyperpolarizabilities γ_{zzzz} obtained from the adiabatic calculations of atoms and ions are matched with suitable literature references.

	τ	E	α_{zz}	γ_{zzzz}
Ps	0.03	−0.24999(2)[a]	36.00(4)[a]	$1.70(4) \times 10^5$[a]
		−0.25[b]	36[b]	1.7067×10^5[b]
H	0.03	−0.49996(2)[a]	4.502(4)[a]	1331(28)[a]
	0.03	−0.49997(5)[c]	4.496(23)[c]	1586(184)[c]
		−0.5[d]	4.5[d]	1333.1[e]
H^-	0.1	−0.52799(6)[f]	206(2)[f]	$7.4(2.9) \times 10^7$[f]
	0.03	−0.52781(7)[f]	209(5)[f]	$5.9(7.0) \times 10^7$[f]
		−0.52775[g]	206.15[h]	8.03×10^7[i]
PsH	0.03	−0.78932(7)[a]	42.27(7)[a]	$1.60(8) \times 10^5$[a]
		−0.78913[j]	42.2836[k]	
He	0.01	−2.9036(2)[a]	1.382(4)[a]	42(6)[a]
		−2.90372[l]	1.38319217[m]	43.104[m]
Li^+	0.01	−7.2810(4)[a]	0.1923(4)[a]	0.24(8)[a]
		−7.279913[n]	0.192453[n]	0.2427[p]

[a]This work.
[b]E, α_{zz}, and γ_{zzzz} of Ps are half, 8-fold, and 128-fold of those of H, respectively.
[c]Tiihonen *et al.* [29].
[d]Waller [36].
[e]Sewell [37].
[f]This work (extrapolated to 0 K).
[g]Lin [38]; Nakashima *et al.* [39].
[h]Kar *et al.* [40].
[i]Pipin *et al.* [41].
[j]Frolov *et al.* [42].
[k]Yan [43].
[l]Pekeris [44]; Nakashima *et al.* [39].
[m]Cencek *et al.* [45].
[n]Johnson *et al.* [46].
[p]Grasso *et al.* [47].

[29,36–47,49–59]. The simplest group is presented in Table I; atoms and ions with a single fixed nucleus are isotropic and have no permanent dipole moment, and thus they only have nonvanishing dipole polarizability α_{zz} and second hyperpolarizability γ_{zzzz}. The total energies match at least with three, and most of the polarizabilities at least with two significant digits. The biggest discrepancies are with the extrapolated values of H^-, which could stem from the choice of the extrapolation function (14). The temperature dependencies of α_{zz} and γ_{zzzz} of H^- are presented in Fig. 1, and it is likely that instead of exponential decay, α_{zz} would saturate towards the reference value. Also, to our knowledge, γ_{zzzz} has been reported for neither of the positron systems, Ps and PsH, prior to this work.

Table II contains homonuclear molecules and molecular ions made of protons and electrons. They also lack the permanent dipole moment, but now the geometry gives rise to optical anisotropy, i.e., difference between the response in z and x directions. Consequently, the nonvanishing terms are $\alpha_{zz} \neq \alpha_{xx}$ and $\gamma_{zzzz} \neq \gamma_{xxxx} \neq \gamma_{zzxx} \neq \gamma_{xxyy}$ [31]. The simulations of the diatomic molecules were carried out at the approximate equilibrium bond lengths $R_{H_2^+} = 2.0 a_0$ and $R_{H_2} = 1.4 a_0$ so that the nuclei were connected by the z axis.

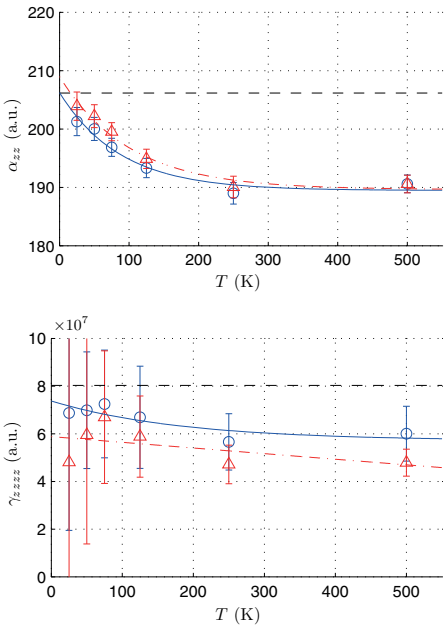

FIG. 1. Finite temperature data for α_{zz} and γ_{zzzz} of H^- is plotted against temperature for two time steps: $\tau = 0.1$ (blue circle) and $\tau = 0.03$ (red triangle). Exponential fit is used to extrapolate to 0 K. The black dashed lines mark reference values at 0 K [40,41].

The nuclei in triangular H_3^+ molecule were fixed equilaterally $R_{H_3^+} = 1.65a_0$ apart so that the z axis was perpendicular to the plane. Again, the agreement of the total energy is good. With H_2^+ and H_2, the agreement is also good with the polarizabilities. The latest and the only references of the dipole polarizability of H_3^+ are from Ref. [57], where they are assumed inaccurate lower-bound estimates. Indeed, our results for α_{zz} and α_{xx} are somewhat larger. We also present estimates for the higher static polarizabilities of H_3^+.

The most complicated of our systems is HeH^+, because it contains a permanent dipole moment μ_z, which also induces nonzero first hyperpolarizabilities $\beta_{zzz} \neq \beta_{zxx}$. With nonzero net charge, the choice of origin for the dipole moment is ambiguous. Here, we use the center-of-mass of the nuclei, which places the origin $0.293609a_0$ apart from the He nucleus with the equilibrium bond length of $R_{HeH^+} = 1.46a_0$. All of the properties are presented in Table III, and up to the dipole polarizabilities they match well with the literature. None of the hyperpolarizabilities have been reported before, although the error boundaries are very dominant with any of the z-dependent components.

Vaguely in the spirit of Ref. [60], we also performed a simulation of PsH as sort of a molecule consisting of two electrons and two "nuclei," proton and positron. By replacing the laboratory axis with the local axis between the nuclei, we were able to compute a nonzero dipole moment of $\mu_z = 0.0305(6)$. In principle, such treatment of PsH causes slight alterations to the properties of PsH found in Table I and a symmetry similar to that of HeH^+. To demonstrate such small effects, more laborious calculations would be required, but we omit the opportunity for now. The essence of this work is to show that the proposed estimators give decent values for polarizabilities and hyperpolarizabilities, and so far this requirement has been amply met.

B. Nonadiabatic simulations

An important step towards realistic and more meaningful simulation of nonlinear optical properties is the breakdown of the Born-Oppenheimer approximation. In PIMC, this is done by allowing quantum statistical description of the nuclei, i.e., replacing fixed-point charges with imaginary-time trajectories similar to the electrons. Besides reduced mass correction to electron-nucleus interaction, this enables the exact account

TABLE II. Time step τ, total energies E, and static anisotropic dipole polarizabilities $\alpha_{zz} \neq \alpha_{xx}$ and second hyperpolarizabilities $\gamma_{zzzz} \neq \gamma_{xxxx} \neq \gamma_{zzxx} \neq \gamma_{xxyy}$ obtained from the adiabatic calculations of homonuclear molecules and molecular ions are matched with suitable literature references.

	τ	R	E	α_{zz}	α_{xx}	γ_{zzzz}	γ_{xxxx}	γ_{zzxx}	γ_{xxyy}
H_2^+	0.03	2.0	−0.60259(10)[a]	5.080(4)[a]	1.7586(8)[a]	−43(17)[a]	73(2)[a]	27(2)[a]	24.2(5)[a]
			−0.602634214[b]	5.0776490[c]	1.757648[c]	−193.76[d]	83.87[d]	29.73[d]	
H_2	0.03	1.4	−1.1746(4)[a]	6.388(7)[a]	4.574(5)[a]	700(49)[a]	572(26)[a]	211(10)[a]	191(7)[a]
	0.03		−1.17434(18)[e]	6.382(13)[e]	4.577(10)[e]	787(100)[e]	640(73)[e]		
			−1.17447477[f]	6.387493[g]	4.57861[g]	682.5[g]	575.9[g]	211.9[g]	192.0[g]
H_3^+	0.03	1.65	−1.3438(3)[a]	2.202(2)[a]	3.549(3)[a]	51(4)[a]	58(11)[a]	19(2)[a]	19(3)[a]
			−1.3438356[h]	1.7322[i]	3.2923[i]				

[a]This work.
[b]Turbiner *et al.* [49]; Laaksonen *et al.* [50]; Madsen *et al.* [51].
[c]Tsogbayar *et al.* [52].
[d]Bishop *et al.* [53].
[e]Tiihonen *et al.* [29].
[f]Kolos *et al.* [54].
[g]Bishop *et al.* [55].
[h]Turbiner *et al.* [56].
[i]Kawaoka [57].

TABLE III. Permanent dipole moment and static dipole polarizabilities and hyperpolarizabilities from the adiabatic simulation of HeH^+ molecular ion with $\tau = 0.01$.

E	μ_z	α_{zz}	α_{xx}	β_{zzz}	β_{zxx}	γ_{zzzz}	γ_{xxxx}	γ_{zzxx}	γ_{xxyy}
−2.9785(6)[a]	0.6788(1)[a]	1.544(21)[a]	0.8515(7)[a]	−2(4)[a]	−0.17(7)[a]	11(507)[a]	7.2(8)[a]	3(8)[a]	2.4(2)[a]
−2.978706[b]	0.655[b]	1.5421[c]	0.85070[c]						

[a]This work.
[b]Pachucki [58].
[c]Pavanello *et al.* [59].

of rovibrational motion in thermal bath. On the downside, we are not able to distinguish between rotational, vibrational, and electronic components directly, unless we use artificial constraints and internal coordinates. Yet, here we aim at skipping the tedious tabulation and explicit summation of rovibrational properties and, instead, get the accurate and thermally averaged estimates served on a silver platter.

We simulated four isolated molecules, namely H_2^+, H_2, H_3^+ and HeH^+, in various temperatures. The maximum temperature was 1600 K (3200 K for H_2), where molecular stability is still sustained; dissociation of molecules would result in an undesired explosion in the variance of the dipole moment products. In Table IV we summarize the obtained total energies and make polynomial extrapolations to 0 K. Comparison with the literature [28,58,61–65] shows that the agreement in total energies is good at least with the smaller time step $\tau = 0.03$, although the results of HeH^+ might be improved by a smaller time step still. The average bond lengths are altered by the rovibrational motion. Extrapolation to 0 K gives $R_{H_2^+} = 2.0630(9)a_0$, $R_{H_2} = 1.4482(4)a_0$, $R_{H_3^+} = 1.7231(6)a_0$, and $R_{HeH^+} = 1.5167(4)a_0$ with $\tau = 0.03$.

In laboratory coordinates with freely moving nuclei, all the odd terms, i.e., μ and β, vanish due to symmetry and the anisotropic properties, i.e., α and γ, reduce to orientational averages. In Fig. 2, we present the temperature dependencies of the average dipole polarizability α_{ZZ} and second hyperpolarizability γ_{ZZZZ} for each molecule. The data points are accompanied with a least-squares nonlinear fit according to Eq. (14). Extrapolated values, i.e., $\alpha_{ZZ}(0) = a + c$, are presented in Table V and compared with the literature, when possible. It appears that all of the homonuclear systems exhibit similar behavior: α_{ZZ} increases by the temperature in linear or quadratic fashion, and the effect is to some extent countered with exponential decay of γ_{ZZZZ}. The explanation is simple, if we assume that the primary contribution to γ_{ZZZZ} is given by the rotational states. The rotational hyperpolarizability emerges from the anisotropy between α_{zz} and α_{xx}: the molecule has a tendency to assume more favorable orientation, which is that of higher α. Typically, the lowest rotational states have the highest hyperpolarizabilities [25], and thus the dominant part γ_{ZZZZ} is decreased as the thermal ensemble shifts towards higher temperatures. Out of the homonuclear systems, H_2^+ goes through the most drastic change in γ_{ZZZZ}, and it has indeed the highest anisotropy.

HeH^+ has different response to the temperature: α_{ZZ} decays by the temperature and γ_{ZZZZ} seems to tend to zero as the temperature is increased. This is surely influenced by the permanent dipole moment μ_z. Even though μ_Z and β_{ZZZ}

TABLE IV. Total energies from nonadiabatic calculations of molecules with two time steps $\tau = 0.1$ and $\tau = 0.03$. The values are extrapolated to 0 K and compared values from the literature.

	τ	0 K	200 K	400 K	800 K	1600 K	3200 K
H_2^+	0.1	−0.5972(8)[a]	−0.59668(6)[b]	−0.59599(6)[b]	−0.59445(9)[b]	−0.59007(9)[b]	
	0.03	−0.5975(12)[a]	−0.59682(9)[b]	−0.59599(9)[b]	−0.59438(12)[b]	−0.59006(15)[b]	
		−0.597139[c]					
H_2	0.1	−1.16518(12)[a]	−1.16456(9)[b]	−1.16394(10)[b]	−1.16256(8)[b]	−1.15952(16)[b]	−1.15050(13)[b]
	0.03	−1.16436(16)[a]	−1.16374(15)[b]	−1.16300(12)[b]	−1.16163(12)[b]	−1.15850(19)[b]	−1.14340(21)[b]
		−1.164025[d]					
H_3^+	0.1	−1.3245(2)[a]	−1.3239(2)[b]	−1.3228(2)[b]	−1.3207(2)[b]	−1.3133(3)[b]	
	0.03	−1.3233(3)[a]	−1.3226(3)[b]	−1.3217(3)[b]	−1.3192(3)[b]	−1.3118(3)[b]	
		−1.323568[e]					
HeH^+	0.1	−2.9827(3)[a]	−2.9823(3)[b]	−2.9815(2)[b]	−2.9803(2)[b]	−2.9761(3)[b]	
	0.03	−2.9722(5)[a]	−2.9717(4)[b]	−2.9712(4)[b]	−2.9697(4)[b]	−2.9656(5)[b]	
		−2.96627[f]					

[a]This work (extrapolated to 0 K).
[b]This work.
[c]Tang *et al.* [28].
[d]Stanke *et al.* [61].
[e]Kylänpää *et al.* [62] ([63]).
[f]Calculated based on Refs. [58] and [64].

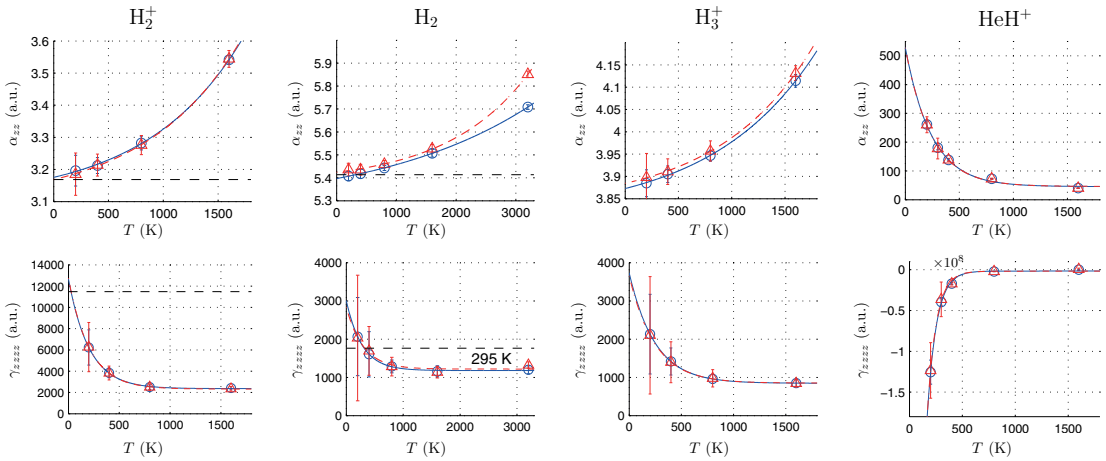

FIG. 2. Nonadiabatic dipole polarizabilities α_{ZZ} and second hyperpolarizabilities γ_{ZZZZ} are plotted against the temperature. Blue circles and red triangles mark the simulated data points associated with $\tau = 0.1$ and $\tau = 0.03$, respectively. Least-squares nonlinear fits have been made according to Eq. (14). When available, the black dashed lines mark reference values at 0 K [28,65] or 295 K [25].

vanish in the nonadiabatic ensemble, the existence of μ_z induces large rotational component for α_{ZZ}, likewise to the previous paragraph. Thus, when the anisotropy of μ gets decreased by higher-order rotational motion, so does the rotational part of α_{ZZ}.

At this point it is fair to note, however, that any qualitative ideas concerning the rotational or vibrational components are inspired by previous works, and no such conclusions can be drawn solely from the raw simulation data of this work. What is evident, though, is that the difference between the adiabatic and the nonadiabatic results is huge. This is not an implication of error but of the importance of nonadiabatic effects and thermal coupling.

V. SUMMARY

We have derived general estimators of static dipole polarizabilities and hyperpolarizabilities for the path-integral Monte Carlo method. Using the field-free estimators is straightforward in any kind of molecular simulation, and it surpasses our previous finite-field approach in simplicity and speed [29]. In principle, the computation of nonlinear optical properties of matter can be done with PIMC directly at any finite temperature.

As a reference, a variety of well-known one- and two-electron atoms and molecules were simulated with PIMC: H, Ps, H^-, He, Li^+, H_2^+, H_2, PsH, H_3^+, and HeH^+. Agreement with the literature is mostly excellent, with the exceptions of H^- and H_3^+, whose static dipole polarizabilities are being improved in this work. Also, we provide tensorial estimates of the second hyperpolarizabilities of PsH, H_3^+, and HeH^+ and hyperpolarizabilities of HeH^+. While our list of two-electron systems is not exhaustive, the efficiency and universality of our method is still amply demonstrated.

Beyond the computation of adiabatic, or fixed-nuclei polarizabilities, we take two important steps with unprecedented ease: the breakdown of the Born-Oppenheimer approximation brings in dielectric contributions emerging from nuclear motion, and the sampling of thermal ensemble couples them directly to finite temperature. We estimate the temperature dependencies of the polarizabilities of four molecules: H_2^+, H_2, H_3^+, and HeH^+ between 0 and 1600 kelvin (3200 K for H_2). Again, we demonstrate good agreement with the literature, if one exists. The explicit treatment of thermal averaging gives rise to interesting relationships between the anisotropic and the average quantities, e.g., anisotropy $\alpha_{zz} \neq \alpha_{xx}$ induces large rotational component to γ_{ZZZZ}, which then decays rapidly by the temperature.

Clearly, PIMC is a special method that allows exact simulation of polarizabilities in novel regimes. The accuracy of results is controllable by computational effort, whose limitations are evident but not really imminent in the scope of our work. Partly for this reason but mainly for the

TABLE V. Polarizabilities and hyperpolarizabilities from nonadiabatic calculations of atoms are extrapolated to 0 K by using Eq. (14).

	τ	α_{ZZ}	γ_{ZZZZ}
H_2^+	0.1	3.175(34)[a]	12674(1006)[a]
	0.03	3.168(49)[a]	12750(1403)[a]
	ref.	3.168725[b]	11479.805[b]
H_2	0.1	5.397(19)[a]	3012(604)[a]
	0.03	5.424(24)[a]	2839(894)[a]
	ref.	5.4139[c]	
H_3^+	0.1	3.873(24)[a]	3738(642)[a]
	0.03	3.884(39)[a]	3656(950)[a]
HeH^+	0.1	529(8)[a]	$-1.128(8)\times 10^9$[a]
	0.03	528(23)[a]	$-1.202(21)\times 10^9$[a]

[a]This work (extrapolated to 0 K).
[b]Tang *et al.* [28].
[c]Kolos *et al.* [65].

simplicity, the higher multipole properties and the effects of finite density and pressure were left out of this work. Same goes for solids and more complicated molecules, such as H_2O or CO_2, even though the power of PIMC resides in the accurate many-body correlations. This work is best reviewed as a necessary first step on the path of understanding the quantum statistical dielectric properties with PIMC.

ACKNOWLEDGMENTS

We thank David Ceperley for insightful discussions. For financial support we gratefully acknowledge the Jenny and Antti Wihuri Foundation, and the Academy of Finland. Also, we acknowledge CSC–IT Center for Science Ltd. and Tampere Center for Scientific Computing for the allocation of computational resources.

[1] G. J. Harris, A. E. Lynas-Gray, S. Miller, and J. Tennyson, Astrophys. J. **600**, 1025 (2004).
[2] G. J. Harris, A. E. Lynas-Gray, S. Miller, and J. Tennyson, Astrophys. J. **617**, L143 (2004).
[3] E. A. Engel, N. Doss, G. J. Harris, and J. Tennyson, Mon. Not. R. Astron. Soc. **357**, 471 (2005).
[4] D. B. Cassidy and A. P. Mills, Nature (London) **449**, 195 (2007).
[5] I. Kylänpää, T. T. Rantala, and D. M. Ceperley, Phys. Rev. A **86**, 052506 (2012).
[6] A. P. Mills, J. Phys.: Conf. Ser. **488**, 012001 (2014).
[7] I. V. Leontyev and A. A. Stuchebrukhov, J. Chem. Theory Comput. **8**, 3207 (2012).
[8] D. M. Bishop, Rev. Mod. Phys. **62**, 343 (1990).
[9] D. P. Shelton and J. E. Rice, Chem. Rev. **94**, 3 (1994).
[10] G. Maroulis, *Atoms, Molecules, and Clusters in Electric Fields: Theoretical Approaches to the Calculation of Electric Polarizability* (Imperial College Press, London, 2006).
[11] J. Mitroy, M. S. Safronova, and C. W. Clark, J. Phys. B **43**, 202001 (2010).
[12] A. Dalgarno and J. T. Lewis, Proc. R. Soc. A **233**, 70 (1955).
[13] D. W. Norcross and M. J. Seaton, J. Phys. B: At. Mol. Phys. **9**, 2983 (1976).
[14] A. Hibbert, M. L. Dourneuf, and V. K. Lan, J. Phys. B: At. Mol. Phys. **10**, 1015 (1977).
[15] R. McWeeny, Int. J. Quantum Chem. **23**, 405 (1983).
[16] B. Kirtman, J. M. Luis, and D. M. Bishop, J. Chem. Phys. **108**, 10008 (1998).
[17] K. Pachucki and J. Sapirstein, Phys. Rev. A **63**, 012504 (2000).
[18] C. C. Cannon and A. Derevianko, Phys. Rev. A **69**, 030502 (2004).
[19] X. Chu and A. Dalgarno, J. Chem. Phys. **121**, 4083 (2004).
[20] M. Safronova and W. Johnson, Adv. At., Mol., Opt. Phys. **55**, 191 (2008).
[21] L.-Y. Tang, Z.-C. Yan, T.-Y. Shi, and J. F. Babb, Phys. Rev. A **79**, 062712 (2009).
[22] A. L. Hickey and C. N. Rowley, J. Phys. Chem. A **118**, 3678 (2014).
[23] J. Kobus, Phys. Rev. A **91**, 022501 (2015).
[24] J. C. Slater and J. G. Kirkwood, Phys. Rev. **37**, 682 (1931).
[25] D. M. Bishop and B. Lam, Chem. Phys. Lett. **143**, 515 (1988).
[26] S. Nir, J. Chem. Phys. **59**, 3341 (1973).
[27] A. V. Gubskaya and P. G. Kusalik, J. Chem. Phys. **117**, 5290 (2002).
[28] L.-Y. Tang, Z.-C. Yan, T.-Y. Shi, and J. F. Babb, Phys. Rev. A **90**, 012524 (2014).
[29] J. Tiihonen, I. Kylänpää, and T. T. Rantala, Phys. Rev. A **91**, 062503 (2015).
[30] B. Champagne, E. Botek, M. Nakano, T. Nitta, and K. Yamaguchi, J. Chem. Phys. **122**, 114315 (2005).
[31] A. D. Buckingham, in *Permanent and Induced Molecular Moments and Long-Range Intermolecular Forces* (John Wiley & Sons, Inc., New York, 2007), pp. 107–142.
[32] H. F. Trotter, Proc. Am. Math. Soc. **10**, 545 (1959).
[33] R. G. Storer, J. Math. Phys. **9**, 964 (1968).
[34] C. Chakravarty, M. C. Gordillo, and D. M. Ceperley, J. Chem. Phys. **109**, 2123 (1998).
[35] D. M. Ceperley, Rev. Mod. Phys **67**, 279 (1995).
[36] I. Waller, Z. Phys. **38**, 635 (1926).
[37] G. L. Sewell, Math. Proc. Cambr. Philos. Soc. **45**, 631 (1949).
[38] C. D. Lin, Phys. Rep. **257**, 1 (1995).
[39] H. Nakashima and H. Nakatsuji, J. Chem. Phys **127**, 224104 (2007).
[40] S. Kar and Y. K. Ho, Phys. Lett. A **372**, 4253 (2008).
[41] J. Pipin and D. M. Bishop, J. Phys. B: At., Mol. Opt. Phys. **25**, 17 (1992).
[42] A. M. Frolov and V. H. Smith, Phys. Rev. A **56**, 2417 (1997).
[43] Z.-C. Yan, J. Phys. B: At., Mol. Opt. Phys. **35**, L345 (2002).
[44] C. L. Pekeris, Phys. Rev. **112**, 1649 (1958).
[45] W. Cencek, K. Szalewicz, and B. Jeziorski, Phys. Rev. Lett. **86**, 5675 (2001).
[46] W. R. Johnson and K. T. Cheng, Phys. Rev. A **53**, 1375 (1996).
[47] M. N. Grasso, K. T. Chung, and R. P. Hurst, Phys. Rev. **167**, 1 (1968).
[48] I. Kylänpää and T. T. Rantala, J. Chem. Phys. **135**, 104310 (2011).
[49] A. V. Turbiner and H. Olivares-Pilon, J. Phys. B: At., Mol. Opt. Phys. **44**, 101002 (2011).
[50] L. Laaksonen, P. Pyykkö, and D. Sundholm, Int. J. Quantum Chem. **23**, 309 (1983).
[51] M. M. Madsen and J. M. Peek, At. Data Nucl. Data Tables **2**, IN3 (1970).
[52] T. Tsogbayar and M. Horbatsch, J. Phys. B: At., Mol. Opt. Phys. **46**, 085004 (2013).
[53] D. M. Bishop and B. Lam, Mol. Phys. **65**, 679 (1988).
[54] W. Kolos and L. Wolniewicz, J. Chem. Phys. **49**, 404 (1968).
[55] D. M. Bishop, J. Pipin, and S. M. Cybulski, Phys. Rev. A **43**, 4845 (1991).
[56] A. V. Turbiner and J. C. Lopez Vieyra, J. Phys. Chem. A **117**, 10119 (2013).
[57] K. Kawaoka, J. Chem. Phys. **55**, 4637 (1971).
[58] K. Pachucki, Phys. Rev. A **85**, 042511 (2012).
[59] M. Pavanello, S. Bubin, M. Molski, and L. Adamowicz, J. Chem. Phys. **123**, 104306 (2005).

[60] S. L. Saito, Nucl. Instrum. Methods Phys. Res., Sect. B **171**, 60 (2000).
[61] M. Stanke, D. Kçedziera, S. Bubin, M. Molski, and L. Adamowicz, J. Chem. Phys. **128**, 114313 (2008).
[62] I. Kylänpää and T. T. Rantala, J. Chem. Phys. **133**, 044312 (2010).
[63] M. Pavanello and L. Adamowicz, J. Chem. Phys. **130**, 034104 (2009).
[64] W.-C. Tung, M. Pavanello, and L. Adamowicz, J. Chem. Phys. **137**, 164305 (2012).
[65] W. Kolos and L. Wolniewicz, J. Chem. Phys. **46**, 1426 (1967).

Erratum: General polarizability and hyperpolarizability estimators for the path-integral Monte Carlo method applied to small atoms, ions, and molecules at finite temperatures [Phys. Rev. A 94, 032515 (2016)]

Juha Tiihonen, Ilkka Kylänpää, and Tapio T. Rantala

(Received 7 July 2017; published 19 July 2017)

DOI: 10.1103/PhysRevA.96.019902

In our recent work we derived field-free estimators for static polarizabilities and hyperpolarizabilities for the path-integral Monte Carlo method. Our derivation contained some unconventional practices of notation and sign. For example, we had replaced $F_\alpha F_\beta$ with $F_{\alpha\beta}$, etc., whereas the latter is commonly used for a field gradient, i.e., $F_{\alpha\beta} = (\nabla F_\alpha)_\beta$. Also, in Eqs. (5)–(9) there were some sign errors in contrast to Ref. [1]. However, these signs cancel out in either case, leaving the resulting estimators and the data unaffected. The correct way to write the equations would be the following:

$$E^{(1)} = E^{(0)} - \mu_\alpha F_\alpha - \tfrac{1}{2}\alpha_{\alpha\beta} F_\alpha F_\beta - \tfrac{1}{6}\beta_{\alpha\beta\gamma} F_\alpha F_\beta F_\gamma - \tfrac{1}{24}\gamma_{\alpha\beta\gamma\delta} F_\alpha F_\beta F_\gamma F_\delta - \cdots , \tag{5}$$

$$\mu_\alpha = -\lim_{F\to 0} \frac{\partial}{\partial F_\alpha} E^{(1)}, \tag{6}$$

$$\alpha_{\alpha\beta} = -\lim_{F\to 0} \frac{\partial}{\partial F_\alpha}\frac{\partial}{\partial F_\beta} E^{(1)} = \lim_{F\to 0} \frac{\partial}{\partial F_\beta}\mu_\alpha, \tag{7}$$

$$\beta_{\alpha\beta\gamma} = -\lim_{F\to 0} \frac{\partial}{\partial F_\alpha}\frac{\partial}{\partial F_\beta}\frac{\partial}{\partial F_\gamma} E^{(1)} = \lim_{F\to 0} \frac{\partial}{\partial F_\gamma}\alpha_{\alpha\beta}, \tag{8}$$

$$\gamma_{\alpha\beta\gamma\delta} = -\lim_{F\to 0} \frac{\partial}{\partial F_\alpha}\frac{\partial}{\partial F_\beta}\frac{\partial}{\partial F_\gamma}\frac{\partial}{\partial F_\delta} E^{(1)} = \lim_{F\to 0} \frac{\partial}{\partial F_\delta}\beta_{\alpha\beta\gamma}. \tag{9}$$

Furthermore, we want to publish one more nonvanishing property that was left out in the original article. Namely, $\beta_{yyy} = 1.12(14)$ for H_3^+ in the adiabatic (fixed-nuclei) simulation.

[1] A. D. Buckingham, in *Advances in Chemical Physics: Intermolecular Forces*, edited by J. O. Hirschfelder, Advances in Chemical Physics Vol. 12 (Wiley, Hoboken, NJ, 2007), pp. 107–142.

PUBLICATION III

Static field-gradient polarizabilities of small atoms and molecules at finite temperature

Juha Tiihonen, Ilkka Kylänpää & Tapio T. Rantala

The Journal of Chemical Physics 147, 204101, 2017
DOI: 10.1063/1.4999840

Static field-gradient polarizabilities of small atoms and molecules at finite temperature

Juha Tiihonen,[a] Ilkka Kylänpää,[b] and Tapio T. Rantala
Laboratory of Physics, Tampere University of Technology, P.O. Box 692, FI-33101 Tampere, Finland

(Received 11 August 2017; accepted 6 November 2017; published online 22 November 2017)

In this work, we propose new field-free estimators of static field-gradient polarizabilities for finite temperature path-integral Monte Carlo method. Namely, dipole–quadrupole polarizability A, dipole–dipole–quadrupole polarizability B, and quadrupole–quadrupole polarizability C are computed for several up to two-electron systems: H, H^-, He, Li^+, Be^{2+}, Ps_2, PsH, H_2^+, H_2, H_3^+, and HeH^+. We provide complementary data for ground state electronic properties within the adiabatic approximation and demonstrate good agreement with available values in the literature. More importantly, we present fully non-adiabatic results from 50 K to 1600 K, which allow us to analyze and discuss strong thermal coupling and rovibrational effects in total field-gradient polarizabilities. These phenomena are most relevant but clearly overlooked, e.g., in the construction of modern polarizable force field models. However, our main purpose is demonstrating the accuracy and simplicity of our approach in a problem that is generally challenging. *Published by AIP Publishing.* https://doi.org/10.1063/1.4999840

I. INTRODUCTION

Computation of the electric field response at quantum mechanical level—polarizability—is a fundamental problem in electronic structure theory. Approaching it from the first-principles is challenging but well motivated: polarizabilities have implications in many physical properties and modeling aspects, such as optical response and atomic and molecular interactions. Method development and understanding of polarizability has been vast over the past several decades, but the main focus has always been on the bare ground state properties.[1–3] While the finite temperature regime is formally well established,[4] explicit results beyond the Born–Oppenheimer approximation are scarce. By introducing efficient polarizability estimators for the finite temperature path-integral Monte Carlo (PIMC) method, we are aiming to change that.

In our recent article,[5] we proposed a scheme for estimating static dipole polarizabilities in a field-free PIMC simulation. This was an improvement to our earlier finite-field approach.[6] The resulting properties, including substantial rovibrational effects, were those corresponding to an isolated molecule in low density gas. However, the dipole-induced polarizabilities only describe the effects of a uniform electric field.

In this work, we complement our tools by introducing similar estimators for the field-gradient polarizabilities. According to the definitions of Buckingham,[1] the foremost properties are dipole–quadrupole polarizability A, dipole–dipole–quadrupole polarizability B, and quadrupole–quadrupole polarizability C. As the names suggest, they have a direct consequence in treating the long-range interactions between atoms or molecules. There is emerging interest in polarizable force field models[7,8] and van der Waals coefficient formulae[9] employing polarizabilities of all orders. However, the employed properties are often only electronic averages or fully empirical fits, while rovibrational coupling is completely overlooked. Here, we show that finite temperature has an immense effect on total molecular field-gradient polarizabilities.

At first, we present the analytic forms of the field-free PIMC estimators. After this, we demonstrate their capability in a series of simulations for different small atoms, ions, and molecules. The results are compared against values available in the literature. However, to the best of our knowledge, many of them are presented here for the first time. This is most pronounced in the non-adiabatic simulations, which include all rovibrational and electronic effects at finite temperature.

II. THEORY

Let us consider a system of N distinguishable particles in coordinate-space R and at inverse temperature $\beta = \hbar/k_B T$. Later, $\hbar = 1$. The thermal density matrix $\rho(R, R'; \beta)$ is given by the density operator

$$\rho(R, R'; \beta) = \langle R|\hat{\rho}(\beta)|R'\rangle, \tag{1}$$

where $\hat{\rho}$ is also identified as a retarded propagator in imaginary-time,

$$\hat{\rho}(\beta) = e^{-\beta\hat{H}} = e^{-i(t-t_0)\hat{H}} = \hat{G}(t - t_0), \tag{2}$$

where $i(t - t_0) = \beta = 1/k_B T$.

[a]tiihonen@iki.fi
[b]Present address: Materials Science and Technology Division, Oak Ridge National Laboratory, Oak Ridge, Tennessee 37831, USA.

A. Perturbation of properties

The expectation value $\langle O\rangle$ of a property $\hat{O}$ is given by a weighted trace of the density matrix

$$\begin{aligned}\langle O\rangle &= Z^{-1}\int dR\left\langle R\left|\hat{O}\hat{\rho}(\beta)\right|R\right\rangle \\ &= Z^{-1}\int dRdR'\left\langle R\left|\hat{O}\right|R'\right\rangle\langle R'|\hat{\rho}(\beta)|R\rangle,\end{aligned} \tag{3}$$

where

$$Z = \int dR\langle R|\hat{\rho}(\beta)|R\rangle \tag{4}$$

is the partition function. If $\hat{O}$ is diagonal, then

$$\int dR'\left\langle R\left|\hat{O}\right|R'\right\rangle = \int dR'\langle R|R'\rangle O(R') = O(R) \tag{5}$$

and Eq. (3) simplifies to

$$\langle O\rangle = Z^{-1}\int dRO(R)\rho(R,R;\beta). \tag{6}$$

Now, consider a perturbation λ_1. The response of $\hat{O}$ with respect to this perturbation is given to the first order by a differential of Eq. (3),

$$\begin{aligned}\frac{\partial}{\partial\lambda_1}\langle O\rangle &= \frac{\partial}{\partial\lambda_1}Z^{-1}\int dR\left\langle R\left|\hat{O}\hat{\rho}(\beta)\right|R\right\rangle \\ &= Z^{-1}\int dR\left\langle R\left|\hat{O}\frac{\partial}{\partial\lambda_1}\hat{\rho}(\beta)\right|R\right\rangle \\ &\quad - Z^{-2}\int dR\left\langle R\left|\hat{O}\hat{\rho}(\beta)\right|R\right\rangle\int dR\left\langle R\left|\frac{\partial}{\partial\lambda_1}\hat{\rho}(\beta)\right|R\right\rangle \\ &= \left\langle O\frac{\partial\rho}{\partial\lambda_1}\right\rangle - \langle O\rangle\left\langle\frac{\partial\rho}{\partial\lambda_1}\right\rangle,\end{aligned} \tag{7}$$

where we have used the Hellman–Feynman theorem and assumed no dependence between λ and $\hat{O}$ or $|R\rangle$. The higher order responses, i.e., differentials of the form $\frac{\partial}{\partial\lambda_1}\frac{\partial}{\partial\lambda_2}\ldots$ can be easily derived similar to Eq. (7). In particular, the second order is given by

$$\begin{aligned}\frac{\partial}{\partial\lambda_1}\frac{\partial}{\partial\lambda_2}\langle O\rangle &= \frac{\partial}{\partial\lambda_1}\left[\left\langle O\frac{\partial\rho}{\partial\lambda_2}\right\rangle - \langle O\rangle\left\langle\frac{\partial\rho}{\partial\lambda_2}\right\rangle\right] \\ &= \left\langle O\frac{\partial\rho}{\partial\lambda_2}\frac{\partial\rho}{\partial\lambda_1}\right\rangle - \left\langle\frac{\partial\rho}{\partial\lambda_1}\right\rangle\left\langle\frac{\partial\rho}{\partial\lambda_2}O\right\rangle \\ &\quad - \left\langle O\frac{\partial\rho}{\partial\lambda_1}\right\rangle\left\langle\frac{\partial\rho}{\partial\lambda_2}\right\rangle - \langle O\rangle\left\langle\frac{\partial\rho}{\partial\lambda_2}\frac{\partial\rho}{\partial\lambda_1}\right\rangle \\ &\quad + 2\langle O\rangle\left\langle\frac{\partial\rho}{\partial\lambda_2}\right\rangle\left\langle\frac{\partial\rho}{\partial\lambda_1}\right\rangle,\end{aligned} \tag{8}$$

and so on. Clearly, the calculation of the response boils down to the differential of the density operator. Using the exact density matrix from Eqs. (1) and (2), the derivative is given by

$$\frac{\partial}{\partial\lambda_1}\hat{\rho}(\beta) = \beta\hat{\rho}(\beta)\left(-\frac{\partial\hat{H}}{\partial\lambda_1}\right). \tag{9}$$

However, in practical calculations, the exact density matrix is rarely available. Therefore, it becomes necessary to approximate $\hat{\rho}(\beta)$ by dividing it to small intervals. That is, we consider $\hat{\rho}(\tau)$, where $\tau = \beta/M$ and M is an arbitrary large integer. Based on the properties of Green's functions,[11] we may then rewrite the propagator from R to R' as

$$\langle R|\hat{\rho}(\beta)|R'\rangle = \prod_{i=0}^{M-1}\langle R_i|\hat{\rho}(\tau)|R_{i+1}\rangle, \tag{10}$$

where $R_0 = R$ and $R_M = R'$ and whose full phase-space path-integral is written as $\int dR_1\ldots dR_M$. The differential of Eq. (10) is now given by

$$\begin{aligned}\frac{\partial}{\partial\lambda_1}\prod_{i=0}^{M-1}\langle R_i|\hat{\rho}(\tau)|R_{i+1}\rangle &= \sum_{j=1}^{M}\prod_{i=0,i\neq j}^{M-1}\left\langle R_j\left|\frac{\partial}{\partial\lambda_1}\hat{\rho}(\tau)\right|R_{j+1}\right\rangle \\ &\quad\times\langle R_i|\hat{\rho}(\tau)|R_{i+1}\rangle \\ &= \sum_{j=1}^{M}\prod_{i=0,i\neq j}^{M-1}\left\langle R_j\left|\tau\hat{\rho}(\tau)\left(-\frac{\partial\hat{H}}{\partial\lambda_1}\right)\right|R_{j+1}\right\rangle \\ &\quad\times\langle R_i|\hat{\rho}(\tau)|R_{i+1}\rangle \\ &= \frac{\beta}{M}\sum_{j=1}^{M}\prod_{i=0,i\neq j}^{M-1}\left\langle R_j\left|\hat{\rho}(\tau)\hat{D}_1\right|R_{j+1}\right\rangle \\ &\quad\times\langle R_i|\hat{\rho}(\tau)|R_{i+1}\rangle,\end{aligned} \tag{11}$$

where $\hat{D}_1 = -\frac{\partial\hat{H}}{\partial\lambda_1}$. If $\hat{D}_1$ is a diagonal operator, we may use Eq. (5) such that under the path-integration, each time-slice yields $\int dR_{j+1}\langle R_j|\hat{D}|R_{j+1}\rangle = O(R_j)$. This allows us to express the expectation value of the derivative as

$$\begin{aligned}\left\langle\frac{\partial\hat{\rho}(\beta)}{\partial\lambda_1}\right\rangle &= \frac{\beta}{M}\sum_{j=0}^{M-1}\int dR_1\ldots dR_M\prod_{i=1}^{M}\rho(R_{i-1},R_i;\tau)D_1(R_j) \\ &= \beta\left\langle\bar{D}_1(\beta)\right\rangle,\end{aligned} \tag{12}$$

where $\bar{D}_1(\beta)$ means the average over a sample path with the total length of $M\tau = \beta$. It is important to appreciate this property: for a discrete sample path, the correct result can only be obtained by taking the average over all time-slices rather than measuring just one. In fact, the latter is only possible, when $\hat{D}_1$ commutes with $\hat{\rho}$ (that is, $\hat{H}$), but even then using the average is more efficient in a practical implementation. Finally, we note that the result of Eq. (12) can be generalized to the product of multiple derivatives (and, optionally, a diagonal observable $\hat{O}$) such that

$$\left\langle\frac{\partial\hat{\rho}(\beta)}{\partial\lambda_1}\cdots\frac{\partial\hat{\rho}(\beta)}{\partial\lambda_L}\hat{O}\right\rangle = \beta^L\left\langle\bar{D}_1(\beta)\ldots\bar{D}_L(\beta)\bar{O}(\beta)\right\rangle, \tag{13}$$

as long as $\hat{O}$ and all of the $\hat{D}$ commute with each other. For convenience and efficiency, the path-average property has been applied to $\hat{O}$ also. This can be done when the density matrix is symmetric in the phase-space and imaginary-time.[11]

B. Field-gradient polarizabilities

Now, let us consider higher order responses to the electric field, that is, polarizabilities. Let $H^{(0)}$ be the unperturbed many-body Hamiltonian with full interactions. A perturbation caused by a uniform external electric field F_α and the field-gradient $F_{\alpha\beta} = (\nabla F_\alpha)_\beta$ gives the total Hamiltonian as

$$\hat{H}^{(1)} = \hat{H}^{(0)} - \hat{\mu}_\alpha F_\alpha - \tfrac{1}{3}\hat{\Theta}_{\alpha\beta}F_{\alpha\beta} - \cdots, \tag{14}$$

where $\hat{\mu}_\alpha$ and $\hat{\Theta}_{\alpha\beta}$ are the dipole and (traceless) quadrupole moment operators, respectively. Indices α, β, γ, δ, ... refer to the Einstein summation of the combinations of x, y, and z. According to the Buckingham convention,[1] the change in total energy is written as a perturbation expansion of coefficients

$$\begin{aligned} E^{(1)} = E^{(0)} &- \mu_\alpha F_\alpha - \frac{1}{2}\alpha_{\alpha\beta}F_\alpha F_\beta - \frac{1}{6}\beta_{\alpha\beta\gamma}F_\alpha F_\beta F_\gamma \\ &- \frac{1}{24}\gamma_{\alpha\beta\gamma\delta}F_\alpha F_\beta F_\gamma F_\delta - \frac{1}{3}\Theta_{\alpha\beta}F_{\alpha\beta} \\ &- \frac{1}{3}A_{\gamma,\alpha\beta}F_\gamma F_{\alpha\beta} - \frac{1}{6}B_{\alpha\beta,\gamma\delta}F_\alpha F_\beta F_{\gamma\delta} \\ &- \frac{1}{6}C_{\alpha\beta,\gamma\delta}F_{\alpha\beta}F_{\gamma\delta} - \cdots . \end{aligned} \tag{15}$$

Here, μ_α and $\Theta_{\alpha\beta}$ are the permanent dipole and quadrupole moments, respectively. Coefficients α, β, and γ are static dipole polarizabilities of different orders. They have been treated earlier.[5] In this work, we focus on the field-gradient polarizabilities A, B, and C, which are called dipole–quadrupole, dipole–dipole–quadrupole, and quadrupole–quadrupole polarizabilities, respectively.

We can solve for the individual properties by differentiating Eq. (15) with respect to the perturbation in the zero-field limit. In particular, we get

$$A_{\alpha,\beta\gamma} = -3\lim_{F\to 0}\frac{\partial}{\partial F_{\beta\gamma}}\frac{\partial}{\partial F_\alpha}E^{(1)} = 3\lim_{F\to 0}\frac{\partial}{\partial F_{\beta\gamma}}\mu_\alpha, \tag{16}$$

$$B_{\alpha\beta,\gamma\delta} = -3\lim_{F\to 0}\frac{\partial}{\partial F_{\gamma\delta}}\frac{\partial}{\partial F_\alpha}\frac{\partial}{\partial F_\beta}E^{(1)} = 3\lim_{F\to 0}\frac{\partial}{\partial F_{\gamma\delta}}\frac{\partial}{\partial F_\beta}\mu_\alpha, \tag{17}$$

$$C_{\alpha\beta,\gamma\delta} = -3\lim_{F\to 0}\frac{\partial}{\partial F_{\gamma\delta}}\frac{\partial}{\partial F_{\alpha\beta}}E^{(1)} = \lim_{F\to 0}\frac{\partial}{\partial F_{\gamma\delta}}\Theta_{\alpha\beta}, \tag{18}$$

where we have used $\frac{\partial}{\partial F_\alpha}E^{(1)} = -\mu_\alpha$ and $\frac{\partial}{\partial F_{\alpha\beta}}E^{(1)} = -\frac{1}{3}\Theta_{\alpha\beta}$.

Equations (16)–(18) already give away how the field-free estimators can be derived in the density-matrix picture. Using Eq. (14) as the Hamiltonian, the perturbations $\lambda_1 = F_{\alpha\beta}$ and $\lambda_2 = F_\beta$ yield

$$\begin{aligned} -\frac{\partial\hat{H}}{\partial F_{\alpha\beta}} &= \frac{1}{3}\hat{\Theta}_{\alpha\beta} + \mathcal{O}(F), \\ -\frac{\partial\hat{H}}{\partial F_\alpha} &= \hat{\mu}_\alpha + \mathcal{O}(F), \end{aligned}$$

where $\mathcal{O}(F)$ refers to higher-order terms that vanish as $F \to 0$. Based on Eqs. (7), (9), and (13), A is now given by

$$\begin{aligned} A_{\alpha,\beta\gamma} &= 3\lim_{F\to 0}\frac{\partial}{\partial F_{\beta\gamma}}\langle\mu_\alpha\rangle \\ &= 3\left[\left\langle\mu_\alpha\frac{\partial\rho}{\partial F_{\beta\gamma}}\right\rangle - \langle\mu_\alpha\rangle\left\langle\frac{\partial\rho}{\partial F_{\beta\gamma}}\right\rangle\right] \\ &= \beta\left[\langle\bar{\mu}_\alpha\bar{\Theta}_{\beta\gamma}\rangle - \langle\bar{\mu}_\alpha\rangle\langle\bar{\Theta}_{\beta\gamma}\rangle\right]. \end{aligned} \tag{19}$$

Similarly, we get

$$\begin{aligned} C_{\alpha\beta,\gamma\delta} &= \lim_{F\to 0}\frac{\partial}{\partial F_{\gamma\delta}}\langle\Theta_{\alpha\beta}\rangle \\ &= \frac{\beta}{3}\left[\langle\bar{\Theta}_{\alpha\beta}\bar{\Theta}_{\gamma\delta}\rangle - \langle\bar{\Theta}_{\alpha\beta}\rangle\langle\bar{\Theta}_{\gamma\delta}\rangle\right]. \end{aligned} \tag{20}$$

Finally, using Eq. (8), we can write B as

$$\begin{aligned} B_{\alpha\beta,\gamma\delta} &= 3\lim_{F\to 0}\frac{\partial}{\partial F_{\gamma\delta}}\frac{\partial}{\partial F_\beta}\langle\mu_\alpha\rangle \\ &= \beta^2\left[\langle\bar{\Theta}_{\gamma\delta}\bar{\mu}_\alpha\bar{\mu}_\beta\rangle - \langle\bar{\Theta}_{\gamma\delta}\rangle\langle\bar{\mu}_\alpha\bar{\mu}_\beta\rangle + 2\langle\bar{\Theta}_{\gamma\delta}\rangle\langle\bar{\mu}_\alpha\rangle\langle\bar{\mu}_\beta\rangle \right. \\ &\quad \left. - \langle\bar{\Theta}_{\gamma\delta}\bar{\mu}_\alpha\rangle\langle\bar{\mu}_\beta\rangle - \langle\bar{\Theta}_{\gamma\delta}\bar{\mu}_\beta\rangle\langle\bar{\mu}_\alpha\rangle\right]. \end{aligned} \tag{21}$$

We stress that bar denotes the average over a sample path. Besides that, the implementation of Eqs. (19)–(21) is very straightforward because β is a chosen parameter and $\hat{\mu}_\alpha$ and $\hat{\Theta}_{\alpha\beta}$ are diagonal observables.

III. METHOD

Our method of choice is the path-integral Monte Carlo (PIMC), where the density matrix ρ of N distinguishable particles is obtained by stochastic sampling. In general, we cannot express $\rho(R, R; \beta)$ analytically. Instead, we need to use a discrete path as defined in Eq. (10), which allows us to decompose the full many-body Hamiltonian accurately at a reasonably small time step $\tau = \beta/M$. The method is very accurate, when the finite time step is chosen small enough to eliminate many-body errors. However, this also implies either large path-size M or high temperature, and thus, probing of the low temperature regime is computationally more demanding. In fact, proper integration over the M dimensions of dR_i is a formidable task at any discretization. Thus, it is necessary to use Metropolis sampling and other advanced algorithms for efficient Monte Carlo integration. This involves nothing out of the ordinary from an implementation of PIMC, and thus, we shall direct a curious reader to more dedicated resources, e.g., Refs. 10 and 11.

The convenience of the Metropolis algorithm also emerges in the sampling of any spatial degrees of freedom, including the rovibrational motion of the nuclei. In particular, we can easily differentiate between adiabatic and non-adiabatic simulations. We will refer to these as Born–Oppenheimer (BO) and all-quantum (AQ), respectively. In BO simulation, the nuclei are fixed in space, whereas in AQ simulation they are free to move confined only by the implicit interaction of the electronic bonding. The resulting nuclear motion yields the correct rovibrational sampling, including the zero-point motion.[12] Likewise, the simulation of positrons is only a matter of choosing the charge and mass because full explicit correlation is already included in the density matrix.

However, the situation is more complicated for identical particles, especially Fermions. In simulations involving the exchange interaction, a numerical sign problem arises from the antisymmetry. Various schemes have been developed to approach the Fermion sign problem (e.g., Ref. 13), but they will likely have implications on the polarizability estimators proposed in this work. Therefore, we will leave that as a subject for another study and only concentrate on the simulation of up to two Fermions (effectively, electrons or positrons), whose spin states we can safely sample using the Boltzmann statistics.

IV. RESULTS

We demonstrate the finite temperature computation of the field-gradient polarizabilities with our path-integral Monte Carlo code and the estimators based on Eqs. (19)–(21). The simulations are exact apart from a small time step error from the many-body correlations. At longer time steps τ, extrapolating $\tau \to 0$ helps us to improve the result and provide upper bound estimates for properties that are converging from below and vice versa. However, in the adiabatic simulation with the Boltzmann statistics, the error is most effectively eliminated by simply using a reasonably small τ. In the following adiabatic (BO) simulations, we shall use $\tau = 0.025$ for H and Ps systems, $\tau = 0.006\,25$ for He and Li systems, and $\tau = 0.003\,125$ for Be^{2+}. The non-adiabatic (AQ) results have been extrapolated linearly to $\tau \to 0$, using $\tau = 0.025$, 0.0125 for HeH^+ and $\tau = 0.05$, 0.025 otherwise. The statistical error estimate is given by standard error of the mean (SEM) with 2σ, i.e., 2SEM. All results are given in atomic units.

In the following, we present polarizability data and discussion for a variety of isolated one or two-electron systems: H, H^-, Li^+, Be^{2+}, H_2^+, H_2, PsH, Ps_2, H_3^+, and HeH^+. We run two kinds of simulations: adiabatic and non-adiabatic. In the adiabatic or Born–Oppenheimer approximation (BO), the nuclei are fixed in space, reducing symmetry and producing various directional components to polarizabilities. The adiabatic approximation inhibits the rovibrational motion, and thus, at reasonably low temperatures, the difference to absolute zero is negligible. Therefore, we start by establishing the validity of our method by comparing our BO results to the available 0 K reference data.

An excellent summary of independent tensorial polarizabilities for each point group is given in Ref. 1. In Table I, we present BO results for all of the spherically symmetric systems: $B_{zz,zz}$, $C_{zz,zz}$ and the total energy E. Furthermore, the results for the molecular systems, i.e., H_2^+, H_2 H_3^+, and HeH^+, are given in Table II. Each molecular system has one independent quadrupole moment Θ_{zz} and four independent dipole–dipole–quadrupole polarizabilities: $B_{zz,zz}$, $B_{xx,xx}$, $B_{zz,xx}$, and $B_{xz,xz}$. Similarly, there are three independent components

TABLE I. Total energies E, dipole–dipole–quadrupole polarizabilities B, and quadrupole–quadrupole polarizabilities C of spherically symmetric systems, matched with suitable literature references. All results in atomic units.

	E	$B_{zz,zz}$	$C_{zz,zz}$
H	−0.499 95(3)[a]	−106.5(3)[a]	5.003(4)[a]
	−0.5	−106.5[b]	5.0[b]
H^-	−0.527 66(10)[a]	$-4.78(87) \times 10^5$[a]	2568(136)[a]
	−0.527 75[c]	-4.843×10^5[d]	2591.6[d]
He	−2.903 7(2)[a]	−7.32(9)[a]	0.814(2)[a]
	−2.903 72[c]	−7.326 7[e]	0.815 0[e]
Li^+	−7.280 0(7)[a]	−0.121(3)[a]	0.037 97(9)[a]
	−7.279 913[f]	−0.121 4[e]	0.037 96[e]
Be^{2+}	−13.654 7(12)[a]	−0.008 3(3)[a]	0.005 106(15)[a]
	−13.655 566[f]	−0.008 393[e]	0.005 106 7[e]
PsH	−0.789 3(3)[a]	5300(260)[a]	260(3)[a]
	−0.789 13[g]		
Ps_2	−0.515 97(7)[a]	0(440)[h]	460(7)[a]
	−0.516 003 8[i]		

[a]This work.
[b]Bishop and Pipin.[14]
[c]Nakashima and Nakatsuji.[15]
[d]Pipin and Bishop.[27]
[e]Bishop and Rérat.[16]
[f]Johnson and Cheng.[17]
[g]Frolov and Smith.[28]
[h]This work; estimating anything other than 0 is unfeasible because of the large fluctuations.
[i]Bubin *et al.*[29]

TABLE II. Total energies E, independent quadrupole moments Θ, dipole–dipole–quadrupole polarizabilities B, and quadrupole–quadrupole polarizabilities C of molecular systems at fixed orientation, matched with suitable literature references. All results in atomic units.

	E	Θ_{zz}	$B_{zz,zz}$	$B_{xx,xx}$	$B_{xx,zz}$	$B_{xz,xz}$	$C_{zz,zz}$	$C_{xx,xx}$	$C_{xz,xz}$
H_2^+	−0.602 7(2)[a]	1.530 71(8)[a]	−41.9(9)[a]	−13.24(14)[a]	7.3(3)[a]	−18.10(4)[a]	1.913(12)[a]	1.268(5)[a]	1.1946(7)[a]
	−0.602 634[b]	1.530 7[c]	−41.869[d]	−13.249[d]	7.3052[d]	−18.099[d]	1.9113[d]	1.2670[d]	1.1945[d]
H_2	−1.174 6(4)[a]	0.456 3(2)[a]	−90.7(10)[a]	−66.8(8)[a]	34.5(10)[a]	−58.7(3)[a]	5.99(2)[a]	4.930(13)[a]	4.176(6)[a]
	−1.174 474[e]	0.456 84[f]	−90.29[g]	−66.83[g]	34.37[g]	−59.00[g]	5.983[g]	4.927[g]	4.180[g]
H_3^+	−1.344 0(4)[a]	−0.919 53(10)[a]	−11.7(3)[a]	−19.0(2)[a]	9.1(4)[a]	−11.07(4)[a]	1.557(10)[a]	2.078(6)[a]	1.2441(10)[a]
	−1.343 835 6[h]								
	−1.335 18[i]	−0.926 13[i]							
HeH^+	−2.978(2)[a]	1.249 56(13)[a]	−5(8)[a]	−2.07(12)[a]	1.0(3)[a]	−2.25(9)[a]	0.59(2)[a]	0.396(6)[a]	0.3382(5)[a]
	−2.978 706[j]								

[a]This work.
[b]Turbiner and Olivares-Pilon.[18]
[c]Bates and Poots.[19]
[d]Bishop and Cheung.[20]
[e]Kolos and Wolniewicz.[21]
[f]Poll and Wolniewicz.[22]
[g]Bishop *et al.*[23]
[h]Turbiner and Lopez Vieyra.[25]
[i]Carney and Porter.[24] ($R = 1.6504$).
[j]Pachucki.[26]

of quadrupole–quadrupole polarizabilities: $C_{zz,zz}$, $C_{xx,xx}$, and $C_{xz,xz}$. Distinct symmetries also lead to a few non-zero dipole–quadrupole polarizabilities A: for H_3^+, $A_{y,yy} = -0.653(7)$ and for HeH^+ $A_{z,zz} = -0.48(4)$ and $A_{x,zx} = -0.0660(9)$. The principal axis z is by default the line connecting the two nuclei, but for triangular H_3^+, it is perpendicular to the plane of protons. In BO simulation, the molecules are placed at the equilibrium geometries, namely, $R_{H_2^+} = 2.0$, $R_{H_2} = 1.4$, $R_{H_3^+} = 1.65$, and $R_{HeH^+} = 1.46$. The dipole and quadrupole moments are calculated with respect to the center-of-mass. By default, the temperature is set to $T = 2000$ K, which still corresponds to the electronic ground state for most systems. However, to be certain, we use $T = 1000$ K for H_2, $T = 500$ K for PsH, and $T = 100$ K for H^- and Ps_2. The data for positronium, Ps, are missing because the symmetry of masses $m_{\bar{e}} = m_e$ makes its quadrupole moment vanish. The largest discrepancy is in Θ_{zz} of H_3^+: based on our calculations and the reference energy, the cause is more likely in the basis functions of Ref. 24 than in the effects of temperature, time step, or equilibrium distance. Otherwise, the agreement is good with most of the available 0 K literature Refs. 14–26. Many properties of the molecular ions and the positron systems are also reported for the first time.

To non-adiabatic simulations, we refer as *all-quantum* (AQ) since they include all rovibrational and electronic quantum effects. Switching off the adiabatic approximation is simple: the nuclei are simulated and allowed to move like electrons, only with bigger mass. For atoms, the difference is negligible, but in molecules, this arouses considerable thermal coupling of properties, such as the polarizabilities. We use $m_p = 1836.152\,672\,48 m_e$ for proton mass and $m_{He} = 7294.299\,536\,3 m_e$ for that of He-nucleus. The AQ simulations are done in the laboratory coordinates, which is denoted by capital Z. The results are exact rovibrationally averaged quantities and therefore spherically symmetric. Consequently, $A_{Z,ZZ}$ are zero for all systems. The resulting temperature-dependent data for $B_{ZZ,ZZ}$ and $C_{ZZ,ZZ}$ for H_2^+, H_2, H_3^+, and HeH^+ are presented in Fig. 1 in order to show that any time step effects are negligible. The actual numerical and extrapolated data can be found in the supplementary material.

Any non-zero electric moments of a quantum system couple to its rotational states, and then this coupling is manifested in the rotational parts of higher order polarizabilities. At high temperatures, this rotational coupling is proportional to the inverse temperature, which has already been proposed[4,34] and demonstrated.[5] Now, for homonuclear molecules, H_2^+, H_2, H_3^+, the first non-zero electric moment is the quadrupole moment Θ, and thus, all of these systems show $\sim 1/T$ decay on B and C. For HeH^+ with non-zero dipole moment μ, the dipole polarizability α is also affected by the coupling.[5] Thus, it makes sense that B of HeH^+, involving both α and Θ, is in fact proportional to $\sim 1/T^2$.

However, the rotational polarizabilities do not diverge at low temperatures because it takes some energy to activate the rotational states. To model the temperature dependence of the total B and C, we propose an *ad hoc* nonlinear function of the form

$$f(T) = \left(\frac{a_1 \cdot \mathrm{erf}(a_2 T)}{T} \right)^x + a_3, \tag{22}$$

where a_1, a_2, and a_3 are coefficients and the error function $\mathrm{erf}(y)$ is used to saturate the values in a robust way as $T \to 0$. As argued earlier, a natural choice for the characteristic exponent describing the rotational coupling is $x = 1$ ($x = 2$ for B of HeH^+). However, we also present x optimized by the root-mean-squared error (RMSE) as a crude means of considering nontrivial thermal effects originating from the electronic and vibrational polarizabilities. Nonlinear fitting to time step extrapolated data has been done using fitnlm function in Matlab, which also provides 95% confidence intervals. Inversed squares of SEM estimates of the PIMC data were used as weights.

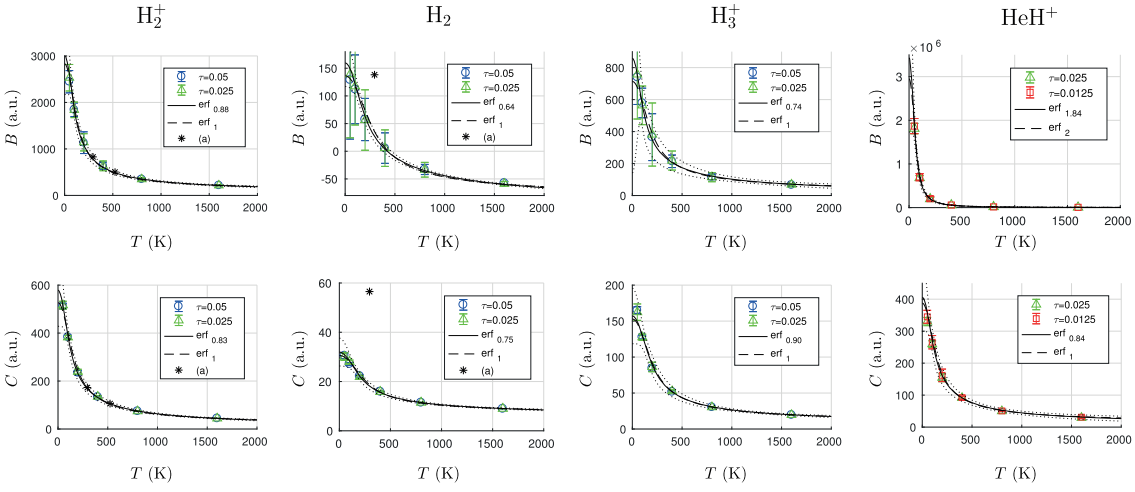

FIG. 1. Rovibrationally averaged dipole–dipole–quadrupole polarizabilities $B_{ZZ,ZZ}$ and quadrupole–quadrupole polarizabilities $C_{ZZ,ZZ}$ for nonadiabatic simulations of molecular systems plotted at different temperatures. A few data points from Ref. 34 have been marked with (a). Fits to Eq. (22) are presented with solid line for optimal exponent x and dashed line for integer exponent. Dotted lines are 95% confidence boundaries given by the fitting algorithm.

TABLE III. Total energies, dipole–dipole–quadrupole polarizabilities, and quadrupole–quadrupole polarizabilities extrapolated to 0 K. Quadratic fit is used for E, and Eq. (22) with optimal x for B and C. All results in atomic units.

	E	$B_{ZZ,ZZ}$	$C_{ZZ,ZZ}$
H_2^+	−0.596(2)[a]	3000(850)[a]	580(150)[a]
	−0.597 139[b]		
H_2	−1.162 5(11)[a]	160(35)[a]	32(6)[a]
	−1.164 025[c]		
H_3^+	−1.323(5)[a]	860(720)[a]	157(39)[a]
	−1.323 568[d]		
HeH^+	−2.967 0(8)[a]	$3.4(1.7) \times 10^6$[a]	406(110)[a]
	−2.966 27[e]		

[a]This work (extrapolated to 0 K).
[b]Tang *et al.*[30]
[c]Stanke *et al.*[31]
[d]Kylänpää and Rantala.[32]
[e]Calculated based on Refs. 26 and 33.

Extrapolation of Eq. (22) to $T = 0$ is given by $\frac{2}{\sqrt{\pi}} a_1 a_2 + a_3$. The corresponding data for B and C are presented in Table III together with quadratically extrapolated total energies and appropriate Refs. 26 and 30–33. The raw data and the fitting coefficients can be found in the supplementary material. Besides Fig. 1, the fitted curves are presented on a logarithmic scale in Fig. 2. It is easier to see that the rotational polarizability is saturated at low T but decays as T^{-x} as the rotational states get activated. Also, it can be observed that the magnitudes of the rotational parts of B (except for HeH^+) and C are clearly in the same order as the corresponding lower order moments, Θ_{zz}, from Table II.

The high-temperature limit of the fit is given by a_3. It gives the ballpark of the sum of the vibrational and electronic polarizabilities, whose thermal coupling is much smaller but not negligible. This is manifested in the characteristic exponent x: the optimal x in a least-squares fit appears to be slightly smaller than a natural integer, 1 or 2. While the exponent in T^{-x} is probably not the most natural way to model this, it shows evidence on how the vibrational and electronic parts compensate on the decay of rotational polarizability. Furthermore, to first approximation, the electronic part of AQ polarizability should equal to the isotropic average (see Ref. 4) of the BO values. One delusive example would be correlating the isotropic average $\langle B \rangle_{ZZ,ZZ} = -74.65$ of H_2 to its high-temperature limit, −82.828. Unfortunately, a quick survey reveals that the high-temperature limit seldom agrees with the averaged electronic quantities from 0 K. This underlines the difficulty of decomposing the dielectric properties under strong thermal influence, and we attempt to do it no further.

As a final remark, we discuss the only explicit reference for the finite temperature total polarizabilities given by Bishop and Lam.[34] As shown in Fig. 1, their results are a good match for H_2^+ but severely overestimated for H_2. We suggest that this is caused by inaccuracy of the vibrational wave function basis used by the authors. Due to the electronic correlations, their ground state is not exact but rather an uncontrollable mixture involving higher excited vibrational eigenstates. According to their own tables, such vibrational bias leads to unintended overestimation of properties, which can be substantial in case of polarizabilities. This example discloses the inherent sensitivity of estimating higher order electric properties in many-body systems.

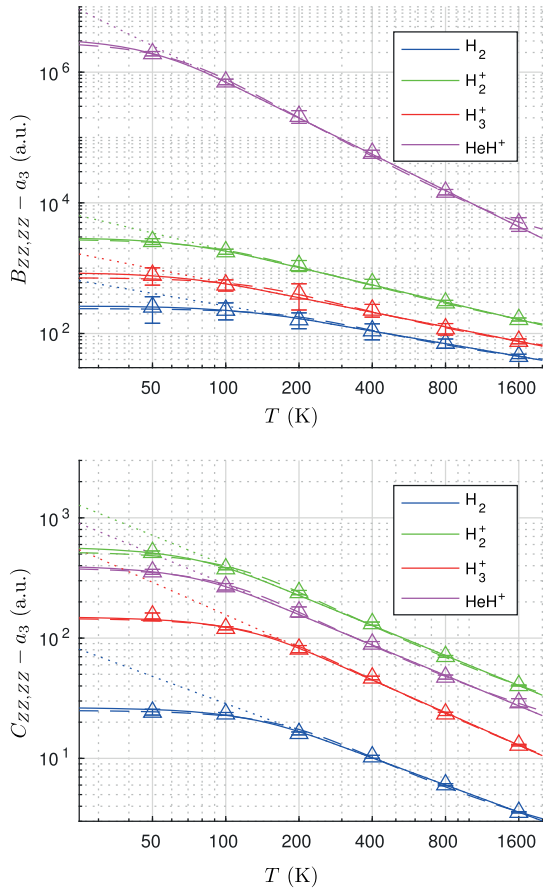

FIG. 2. Time step extrapolated data and nonlinear fits for B and C of H_2^+, H_2, H_3^+, and HeH^+ on a logarithmic scale. The fits to Eq. (22) are done with $x = 1$ (dashed) or the optimal x (solid). Dotted lines show the effect of replacing the error function with unity.

V. SUMMARY

As a natural continuation to our previous work, we present a scheme to estimate static field-gradient polarizabilities in a field-free PIMC simulation. We apply it on a range of small atoms, ions, and molecules, namely, H, H^-, He, Li^+, Be^{2+}, Ps_2, PsH, H_2^+, H_2, H_3^+, and HeH^+. The simulations with the adiabatic approximation and equilibrium geometries are done in the low temperature limit, and they indeed agree well with the 0 K literature references. However, we do not try to push the limits of statistical precision in this study, but rather, we want to give an ample demonstration of our method.

With the given set of systems, the variation in dielectric properties is already large. For instance, H^- or PsH are very diffuse compared to the heavier ions, Li^+ and Be^{2+}. On the

other hand, HeH^+ has a permanent dipole moment and thus much more diverse dielectric response than the homonuclear molecules. We want to emphasize that all these properties were obtained with the same PIMC procedure varying nothing else than the fundamental properties of the particles.

One of the most advantageous treats of the PIMC method is the exact simulation of the canonical ensemble. Molecules have geometrical anisotropy and thus permanent dipole or quadrupole moments, which then reflect in the higher order rotational polarizabilities. Our data indicate that the rotational parts of $B_{ZZ,ZZ}$ and $C_{ZZ,ZZ}$ are dominant at low temperatures but decay drastically when the temperature is increased. The latter effect has been anticipated in the literature,[4] but even our overly simplistic model in Eq. (22) shows that there is plenty of room for improvement. Indeed, the requirements of explicit correlations and non-adiabatic thermal averaging render results of this kind very scarce. By this work, we are hoping to inspire a change to that.

SUPPLEMENTARY MATERIAL

See supplementary material for the raw data of non-adiabatic PIMC simulations and the non-linear fitting.

ACKNOWLEDGMENTS

We thank Jenny and Antti Wihuri Foundation and Tampere University of Technology for financial support. Also, we acknowledge CSC–IT Center for Science Ltd. and Tampere Center for Scientific Computing for providing us with computational resources.

[1] A. D. Buckingham, *Permanent and Induced Molecular Moments and Long-Range Intermolecular Forces* (John Wiley & Sons, Inc., 2007), pp. 107–142.
[2] G. Maroulis, *Computational Aspects of Electric Polarizability Calculations: Atoms, Molecules and Clusters* (IOS Press, 2006).
[3] J. Mitroy, M. S. Safronova, and C. W. Clark, J. Phys. B: At., Mol. Opt. Phys. **43**, 202001 (2010).
[4] D. M. Bishop, Rev. Mod. Phys. **62**, 343 (1990).
[5] J. Tiihonen, I. Kylänpää, and T. T. Rantala, Phys. Rev. A **94**, 032515 (2016).
[6] J. Tiihonen, I. Kylänpää, and T. T. Rantala, Phys. Rev. A **91**, 062503 (2015).
[7] I. Leontyev and A. Stuchebrukhov, Phys. Chem. Chem. Phys. **13**, 2613 (2011).
[8] C. M. Baker, Wiley Interdiscip. Rev.: Comput. Mol. Sci. **5**, 241 (2015).
[9] J. Tao and A. M. Rappe, J. Chem. Phys. **144**, 031102 (2016).
[10] D. M. Ceperley, Rev. Mod. Phys. **67**, 279 (1995).
[11] I. Kylänpää, "First-principles finite temperature electronic structure of some small molecules," Ph.D. thesis, Tampere University of Technology, 2011.
[12] I. Kylänpää, M. Leino, and T. T. Rantala, Phys. Rev. A **76**, 052508 (2007).
[13] W. R. Magro, B. Militzer, D. M. Ceperley, B. Bernu, and C. Pierleoni, "Restricted Path Integral Monte Carlo Calculations of Hot, Dense Hydrogen," in *Strongly Coupled Coulomb Systems* (Springer, 2002), pp. 337–340.
[14] D. M. Bishop and J. Pipin, Chem. Phys. Lett. **236**, 15 (1995).
[15] H. Nakashima and H. Nakatsuji, J. Chem. Phys. **127**, 224104 (2007).
[16] D. M. Bishop and M. Rérat, J. Chem. Phys. **91**, 5489 (1989).
[17] W. R. Johnson and K. T. Cheng, Phys. Rev. A **53**, 1375 (1996).
[18] A. V. Turbiner and H. Olivares-Pilon, J. Phys. B: At., Mol. Opt. Phys. **44**, 101002 (2011).
[19] D. R. Bates and G. Poots, Proc. Phys. Soc. A **66**, 784 (1953).
[20] D. M. Bishop and L. M. Cheung, J. Phys. B: At., Mol. Opt. Phys. **12**, 3135 (1979).
[21] W. Kolos and L. Wolniewicz, J. Chem. Phys. **49**, 404 (1968).
[22] J. D. Poll and L. Wolniewicz, J. Chem. Phys. **68**, 3053 (1978).
[23] D. M. Bishop, J. Pipin, and S. M. Cybulski, Phys. Rev. A **43**, 4845 (1991).
[24] G. D. Carney and R. N. Porter, J. Chem. Phys. **60**, 4251 (1974).
[25] A. V. Turbiner and J. C. Lopez Vieyra, J. Phys. Chem. A **117**, 10119 (2013).
[26] K. Pachucki, Phys. Rev. A **85**, 042511 (2012).
[27] J. Pipin and D. M. Bishop, J. Phys. B: At., Mol. Opt. Phys. **25**, 17 (1992).
[28] A. M. Frolov and V. H. Smith, Phys. Rev. A **56**, 2417 (1997).
[29] S. Bubin, M. Stanke, D. Kędziera, and L. Adamowicz, Phys. Rev. A **75**, 062504 (2007).
[30] L.-Y. Tang, Z.-C. Yan, T.-Y. Shi, and J. F. Babb, Phys. Rev. A **90**, 012524 (2014).
[31] M. Stanke, D. Kçedziera, S. Bubin, M. Molski, and L. Adamowicz, J. Chem. Phys. **128**, 114313 (2008).
[32] I. Kylänpää and T. T. Rantala, J. Chem. Phys. **133**, 044312 (2010).
[33] W.-C. Tung, M. Pavanello, and L. Adamowicz, J. Chem. Phys. **137**, 164305 (2012).
[34] D. M. Bishop and B. Lam, Chem. Phys. Lett. **143**, 515 (1988).

PUBLICATION IV

Computation of dynamic polarizabilities and van der Waals coefficients from path-integral Monte Carlo

Juha Tiihonen, Ilkka Kylänpää & Tapio T. Rantala

The Journal of Chemical Theory and Computation 14, 5750, 2018
DOI: 10.1021/acs.jctc.8b00859

JCTC Journal of Chemical Theory and Computation

Article

Cite This: J. Chem. Theory Comput. 2018, 14, 5750−5763

pubs.acs.org/JCTC

Computation of Dynamic Polarizabilities and van der Waals Coefficients from Path-Integral Monte Carlo

Juha Tiihonen,* Ilkka Kylänpää,† and Tapio T. Rantala

Laboratory of Physics, Tampere University of Technology, P. O. Box 692, FI-33101 Tampere, Finland

ABSTRACT: We demonstrate computation of total dynamic multipole polarizabilities using path-integral Monte Carlo method (PIMC). The PIMC approach enables accurate thermal and nonadiabatic mixing of electronic, rotational, and vibrational degrees of freedom. Therefore, we can study the thermal effects, or lack thereof, in the full multipole spectra of the chosen one- and two-electron systems: H, Ps, He, Ps_2, H_2, and HD^+. We first compute multipole−multipole correlation functions up to octupole order in imaginary time. The real-domain spectral function is then obtained by analytical continuation with the maximum entropy method. In general, sharpness of the active spectra is limited, but the obtained off-resonant polarizabilities are in good agreement with the existing literature. Several weak and strong thermal effects are observed. Furthermore, the polarizabilities of Ps_2 and some higher multipole and higher frequency data have not been published before. In addition, we compute isotropic dispersion coefficients C_6, C_8, and C_{10} between pairs of species using the simplified Casimir−Polder formulas.

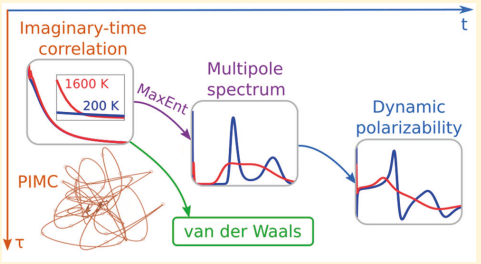

1. INTRODUCTION

Computing dynamic response functions from quantum correlation functions is a popular challenge among quantum Monte Carlo methods, such as path-integral Monte Carlo (PIMC),[1,2] diffusion Monte Carlo (DMC),[3] path-integral molecular dynamics (PIMD),[4,5] and their many derivatives. Purely imaginary-time methods are known to treat quantum many-body correlations very accurately.[6−9] Furthermore, they enable controllable simulation of equilibrium properties, nuclear quantum phenomena, and other nonadiabatic effects—typical banes of the traditional ab initio methods.[10−12] Unfortunately, the strategy of analytic continuation to real-time domain remains a formidable challenge.

A quantum correlation function of a causal process is analytic in the complex plane,[13] and thus, it can be transformed between purely imaginary and real axes by Kubo transform.[14] Unfortunately, numerical implementation of such an inversion is an infamous ill-posed problem: even small noise in the imaginary-time data maps large fluctuations onto the real-time response. Different strategies have been developed to get around this problem: complex time propagators,[15,16] Pade approximants,[17] SVD sampling[18] and Mishchenko's method.[19,20] None of the approaches is superior, yet one of the most popular approaches is maximum entropy (MaxEnt),[21,22] which optimizes the balance between prior information and a least-squares fit. It will be used in this work, too.

Fortunately, the same means of solution can be applied to a wide variety of physical problems. For dedicated reviews, see refs 1, 5, and 23. Quantum correlation functions and analytic continuation have been employed in the computation of, e.g., magnetic susceptibility,[24] density of states,[18] NMR relaxation rate,[25] absorption spectra and transport properties,[26,27] polarons,[19] and optical conductivity.[28]

In this work, we focus on the electric field response: dynamic multipole polarizability. Polarizability is, arguably, the most important of all electronic properties. It is an important parameter in nonlinear optics, spectroscopy, and a wide variety of other physical experiments.[29] Furthermore, it is gaining popularity in molecular interaction models and polarizable force fields.[30,31] Most importantly, the accurate computation of polarizability is a theoretical challenge and a powerful benchmark for any electronic structure methods.[32−38]

Our purpose is to demonstrate the computation of dynamic polarizabilities from PIMC simulations. Similar approaches in imaginary time have been exercised before for static polarizabilities,[39−43] but, to the best of our knowledge, this work is the first one featuring real-time response of the given problem. Explicit all-electron simulation is not the most typical application of the PIMC method, because of its computational cost. However, it provides some obvious benefits over the traditional ab initio methods, such as inherent accounts of finite temperature and exact many-body correlations. Besides the electronic structure, PIMC also enables fully nonadiabatic and quantum mechanical treatment of the nuclear degrees of freedom: rotation and vibration. All of these have different thermal effects on polarizability.[42,44,45] Especially, the infrared (IR)-active species have huge thermal effects on rotational polarizabilities,[46,47] which are also closely associated with IR and Raman spectroscopy.[48,49]

Received: August 23, 2018
Published: October 2, 2018

DOI: 10.1021/acs.jctc.8b00859
J. Chem. Theory Comput. 2018, 14, 5750−5763

We provide exemplary results, i.e., dynamic polarizabilities and dispersion coefficients up to octupole order, for several isolated atoms and molecules: H, He, HD^+, H_2, Ps, and Ps_2. The chosen species feature accurate reference data for validation[47,50−55] but also some exotic properties that have barely been studied before. In particular, we are able to reproduce known electronic polarizabilities at low frequencies and provide an estimate for the rest of the whole power spectrum, where no prior reference data exist. All the electronic, nuclear, and nonadiabatic effects are included in these total polarizabilities. Especially, we can easily quantify the dielectric properties of an ultimately nonadiabatic problem, Ps_2. Finally, we provide dispersion coefficients C_6, C_8, and C_{10} between pairs of the considered species.

The work is organized as follows. First, we review the theoretical background by using linear response theory and properties of Green's functions. We associate first-order dynamic polarizabilities with spectral functions, which are obtained from electric multipole correlation functions by a nonlinear inversion. In section 3, we review the practical aspects of computing the imaginary-time correlation functions with PIMC and performing the numerical inversion with MaxEnt. Finally, we present and discuss the results with suitable literature references.

2. THEORY

We consider a quantum system in an external optical perturbation, that is, a classical electric field $\mathbf{F}(t)$. The total Hamiltonian can be written as

$$\hat{H}(t) = \hat{H}_0 + \hat{H}_{\text{ext}}(t) \tag{1}$$

where $\hat{H}_0$ is a time-independent part

$$\hat{H}_0 = \hat{T} + \sum_{i>j} \hat{V}_{ij}(r) \tag{2}$$

where $\hat{T}$ and $\hat{V}_{ij}(r)$ are operators for kinetic energy and Coulomb interaction energy, respectively. The time-dependent perturbation is

$$\hat{H}_{\text{ext}}(t) = -\theta(t - t')\, \mathbf{F}(t)\cdot\hat{\mathbf{Q}} \tag{3}$$

where the Heaviside step function $\theta(t-t')$ denotes switching on the perturbation at time t'. The interaction $\hat{\mathbf{Q}}$ with the vector field $\mathbf{F}$ can be decomposed in the multipole expansion as[56]

$$\mathbf{F}\cdot\hat{\mathbf{Q}} = -\sum_{n=0}^{\infty} \frac{2^n n!}{(2n)!} F^{(n)}[n]\hat{Q}^{(n)} \tag{4}$$

where we have the net charge $F^{(0)} = q$ in electrostatic potential $\hat{Q}^{(0)} = \phi$. The electric multipole moments (dipole, quadrupole, and octupole, etc.)

$$\hat{Q}^{(1)} = \hat{\mu}, \quad \hat{Q}^{(2)} = \hat{\mathbf{\Theta}}, \quad \hat{Q}^{(3)} = \hat{\mathbf{\Omega}}, \quad \text{etc.} \tag{5}$$

and field gradients

$$F^{(1)} = \mathbf{F}, \quad F^{(2)} = \nabla\mathbf{F}, \quad F^{(3)} = \nabla\nabla\mathbf{F}, \quad \text{etc.} \tag{6}$$

are typically defined according to the center of mass. The n-dot product $[n]$ consists of the summation of corresponding tensorial components to produce a scalar potential, e.g., $Q^{(2)}[2]F^{(2)} = \sum_{ij}\nabla\Theta_{ij}(\nabla F)_{ij}$. Thus, the perturbation up to the third order is written as

$$\hat{H}_{\text{ext}}(t) = -\theta(t - t') \times \left[\hat{\mu}\cdot\mathbf{F}(t) + \frac{1}{3}\hat{\mathbf{\Theta}}\vdots(\nabla\mathbf{F}(t)) + \frac{1}{15}\hat{\mathbf{\Omega}}\vdots(\nabla\nabla\mathbf{F}(t))\right] \tag{7}$$

In the following treatment of spherically symmetric systems, we will omit the tensorial character and only consider scalar electric moments and field gradients.

2.1. Linear Response Theory. In many-body quantum mechanics, the linear response of some property P can be summarized as follows. $\hat{Q}$ denotes any of the perturbing operators in eq 5 and $F(t)$ a corresponding field term. In a causal scenario, the perturbation starts at time t' and the response is measured at time $t > t'$. The linear deviation can be written as

$$\delta P(t) = \frac{i}{\hbar}\int_{-\infty}^{t} \mathrm{d}t' \,\langle[\hat{H}_{ext}(t'),\, \hat{P}(t)]\rangle \tag{8}$$

$$= \frac{i}{\hbar}\int_{-\infty}^{t} \mathrm{d}t' \,\theta(t - t')\langle[\hat{P}(t - t'),\, \hat{Q}(0)]\rangle F(t') \tag{9}$$

$$= \int_{-\infty}^{\infty} \mathrm{d}t' \,\chi^R(t - t')\, F(t') \tag{10}$$

where square brackets denote a commutator and angle brackets a thermal average, $\langle\hat{A}\rangle \equiv \mathrm{Tr}[\hat{\rho}\hat{A}]/\mathrm{Tr}[\hat{\rho}]$, where $\hat{\rho} = \mathrm{e}^{-\beta\hat{H}_0}$ and $\beta = 1/k_B T$. On the second line we have used the time invariance of thermal equilibrium, and on the third line we have inserted the retarded susceptibility

$$\chi^R(t) = \frac{i}{\hbar}\theta(t)\langle[\hat{P}(t),\, \hat{Q}(0)]\rangle = -G^R(t) \tag{11}$$

where G^R is the retarded Green's function of $\hat{P}$ and $\hat{Q}$ and the negative sign follows from the usual convention of electric field perturbation. Frequency-dependent response is given by the Fourier transform

$$\delta P(\omega) = \mathcal{F}\delta P(t) = \chi^R(\omega)\, F(\omega) \tag{12}$$

based on the convolution theorem in eq 10. We can without loss of generality treat eq 12 in terms of a single frequency ω, because arbitrary signals and responses can be superposed from the harmonic waves.[57]

The subject of interest is the constant of proportionality, the complex susceptibility $\chi^R(\omega)$. It is also analytic in the upper complex plane, and thus, it can be expressed with the Kramers−Kronig relations as[21]

$$\chi^R(\omega) = -\int_{-\infty}^{\infty} \frac{\mathrm{d}\omega'}{\pi}\frac{\mathrm{Im}[\chi^R(\omega')]}{\omega - \omega' + i\eta} \tag{13}$$

where η is a positive infinitesimal. For reasons that will become apparent, we shall write it in terms of a spectral function $A(\omega)$:

$$\chi^R(\omega) = -\int_{-\infty}^{\infty} \frac{\mathrm{d}\omega'}{2\pi}\frac{A(\omega')}{\omega - \omega' + i\eta} \tag{14}$$

where we defined[58]

$$A(\omega) = i[G^R(\omega) - [G^R(\omega)]^\dagger] = -2\mathrm{Im}[G^R(\omega)] = 2\mathrm{Im}[\chi^R(\omega)] \tag{15}$$

where the advanced Green's function $[G^R]^\dagger$ is the Hermitian conjugate of G^R. The spectral function $A(\omega)$ has real and positive-semidefinite values, which are related to transition probabilities. Outside the spectral region, i.e., when $A(\omega) \sim 0$, $\chi^R(\omega)$ is effectively real and equal to the dielectric response of the system, i.e., polarizability. Within a spectral peak, $\chi^R(\omega)$

DOI: 10.1021/acs.jctc.8b00859
J. Chem. Theory Comput. 2018, 14, 5750−5763

becomes complex, and the imaginary part is related to the absorption/emission probability.

2.2. Imaginary-Time Correlation. Most quantum Monte Carlo methods operate in imaginary time: $-it \rightarrow \tau$, because imaginary-time propagators are well-behaved and the acquisition of correlation functions along an imaginary-time trajectory is straightforward. The imaginary-time Green's functions are defined as

$$\mathcal{G}(\tau) = \langle \mathcal{T}_\tau \hat{P}(0)\, \hat{Q}(\tau)\rangle \tag{16}$$

where $\mathcal{T}_\tau$ is a time-ordering operator in the imaginary axis. Equation 16 is the equivalent of $\chi^R(t)$ with a purely imaginary argument. At finite temperature, the Green's function is periodic over the inverse temperature β. That is, $0 \le \tau \le \beta$ and eq 16 satisfy $\mathcal{G}(\tau) = \pm\mathcal{G}(\tau + \beta)$, where the positive (negative) sign is for bosons (fermions). The Fourier transform is given in discrete Matsubara frequencies ω_n:

$$\mathcal{G}(i\omega_n) = \int_0^\beta \mathrm{d}\tau\ \mathrm{e}^{-i\omega_n\tau}\, \mathcal{G}(\tau) \tag{17}$$

which are $(2n+1)\pi/\beta$ for fermions and $2n\pi/\beta$ for bosons.

As before, $\mathcal{G}$ is analytic in the upper complex plane and can be represented with the spectral function:[21,22]

$$\mathcal{G}(\tau) = \int_{-\infty}^{\infty} \frac{\mathrm{d}\omega}{2\pi}\, K(\tau,\, \omega)\, A(\omega) \tag{18}$$

$$\mathcal{G}(i\omega_n) = \int_{-\infty}^{\infty} \frac{\mathrm{d}\omega}{2\pi}\, K(i\omega_n,\, \omega)\, A(\omega) \tag{19}$$

where the respective kernels for time and frequency domains are $K(\tau,\omega) = \mathrm{e}^{-\tau\beta}/(1 \pm \mathrm{e}^{-\beta\omega})$ (plus for bosons, minus for fermions) and $K(i\omega_n,\omega) = 1/(i\omega_n - \omega)$. That is, imaginary-time Green's functions can be analytically continued to the real domain by inverting eq 18 or 19. For that, the spectral function is a good agent, because it is (usually) positive-semidefinite and regularized. However, as both kernels are highly nonlinear, numerical inversion is challenging, to say the least.

2.3. Multipole Polarizability. Dynamic multipole polarizability α is by definition the linear response of an electric moment P to a perturbation F that couples to Q, i.e., $\alpha(\omega) = \chi^R(\omega)$. In particular, one can calculate the Fourier transform of eq 9 for a harmonic perturbation $F(t') = \mathrm{e}^{i\omega t'}F$:

$$\begin{aligned}\delta P(\omega) &= \frac{i}{\hbar}\int_{-\infty}^{\infty} \mathrm{d}t\ \mathrm{e}^{-i\omega t} \\ &\quad \times \int_{-\infty}^{t} \mathrm{d}t'\theta(t-t')\langle[\hat{P}(t-t'),\, \hat{Q}(0)]\rangle \mathrm{e}^{i\omega t'}F \\ &= \frac{i}{\hbar}\int_0^{\infty} \mathrm{d}(t-t')\ \mathrm{e}^{-i\omega(t-t')}\langle[\hat{P}(t-t'),\, \hat{Q}(0)]\rangle F\end{aligned} \tag{20}$$

where F is an amplitude. The integral can be calculated, when the correlation function is expanded in the energy eigenstates:

$$\begin{aligned}&\langle[\hat{P}(t-t'),\, \hat{Q}(0)]\rangle \\ &= \sum_n^\infty \frac{\mathrm{e}^{-\beta E_n}}{Z} \sum_m^\infty \left(P_{nm}Q_{mn}\mathrm{e}^{-i\omega_{mn}(t-t')} - Q_{mn}P_{nm}\mathrm{e}^{+i\omega_{nm}(t-t')}\right)\end{aligned} \tag{21}$$

where $\omega_{mn} = (E_m - E_n)/\hbar$ and, e.g., $Q_{mn} = \langle m|\hat{Q}|n\rangle$. Assuming that $F(t') \rightarrow 0$ as $t - t' \rightarrow \infty$, one can then identify the susceptibility as

$$\chi^R(\omega) = \sum_n^\infty \frac{\mathrm{e}^{-\beta E_n}}{\hbar Z} \sum_m^\infty \left[\frac{P_{nm}Q_{mn}}{\omega_{mn} - \omega} + \frac{Q_{mn}P_{nm}}{\omega_{mn} + \omega}\right] \tag{22}$$

$$\equiv \langle \alpha^-(\omega)\rangle + \langle \alpha^+(\omega)\rangle \tag{23}$$

$$\equiv \langle \alpha(\omega)\rangle \tag{24}$$

where $\alpha^-(\omega)$ and $\alpha^+(\omega)$ are the so-called resonant and antiresonant polarizabilities. In the zero Kelvin limit, i.e., $\beta \rightarrow \infty$, one recovers the usual sum-over-states definition of polarizability from eq 23.

In this work, we will consider isotropic polarizabilities, such as those of gaseous atoms and molecules. Consequently, all polarizabilities with an "odd" degree, such as $\chi^R_{\mu\Theta}$, cancel out in spherical averaging. We will thus consider the following even first-order properties (but omit $\chi^R_{\mu\Omega}$ for simplicity)

$$\alpha_1 \equiv \chi^R_{\mu\mu} \quad \text{(dipole−dipole)} \tag{25}$$

$$\alpha_2 \equiv \chi^R_{\Theta\Theta} \quad \text{(quadrupole−quadrupole)} \tag{26}$$

$$\alpha_3 \equiv \chi^R_{\Omega\Omega} \quad \text{(octupole−octupole)} \tag{27}$$

where P and Q are in turn replaced by μ, Θ, and Ω. These are scalar polarizabilities, meaning that the tensorial character is also lost in isotropic sampling.

Alternatively, one could compute polarizability in the internal coordinates of a molecule and find anisotropy, which leads to a tensorial response. While it goes against the measurable realm, moving to internal coordinates has some virtues: the first-order anisotropy adds insight into the optical response of the molecule, and it also reflects strongly to the rotational higher-order perturbations, the hyperpolarizabilities.[41−43,46] Often, only tensorial electronic polarizabilities have been reported, which omit the nuclear effects or treat them separately. In that case, isotropic averaging is required to make such results comparable with those in the "laboratory coordinates". For diatomic molecules, it is given in the first two degrees by[46,59]

$$\langle \alpha_1\rangle = (2\alpha_{xx} + \alpha_{zz})/3 \tag{28}$$

$$\langle \alpha_2\rangle = (\alpha_{zz,zz} + 8\alpha_{zx,zx} + 8\alpha_{xx,xx})/15 \tag{29}$$

where z is the principal axis.

2.4. Dispersion Coefficients. Lastly, we use polarizabilities in the computation of van der Waals, or more precisely, London dispersion coefficients. The coefficients are used to model attractive interactions between atoms and molecules due to quantum fluctuations of electric moments. After spherical averaging, the radial pair interaction between species A and B is quantified as

$$V^{AB}(r) = -\frac{C_6^{AB}}{r^6} - \frac{C_8^{AB}}{r^8} - \frac{C_{10}^{AB}}{r^{10}} - \ldots \tag{30}$$

where C_6, C_8, and C_{10} are the dispersion coefficients. Accurate calculation of the higher-order terms C_8 and C_{10} can be especially challenging, while their effect can be considerable.[60] According to the simplified Casimir−Polder formulas, the coefficients are defined in terms of dynamic polarizabilities with imaginary-frequency argument:[50]

DOI: 10.1021/acs.jctc.8b00859
J. Chem. Theory Comput. 2018, 14, 5750−5763

$$C_6^{AB} = \frac{3}{\pi}\int_0^\infty \mathrm{d}\omega\ \alpha_1^A(i\omega)\ \alpha_1^B(i\omega) \tag{31}$$

$$C_8^{AB} = \frac{15}{2\pi}\int_0^\infty \mathrm{d}\omega\ (\alpha_1^A(i\omega)\ \alpha_2^B(i\omega) + \alpha_2^A(i\omega)\ \alpha_1^B(i\omega)) \tag{32}$$

$$C_{10}^{AB} = \frac{14}{\pi}\int_0^\infty \mathrm{d}\omega\ (\alpha_1^A(i\omega)\ \alpha_3^B(i\omega) + \alpha_3^A(i\omega)\ \alpha_1^B(i\omega)) + \frac{35}{\pi}\int_0^\infty \mathrm{d}\omega\ \alpha_2^A(i\omega)\ \alpha_2^B(i\omega) \tag{33}$$

Based on eq 17, the required polarizabilities are obtained from the imaginary-time correlation functions at discrete Matsubara frequencies by a regular Fourier transform. The continuous integral can be evaluated with good accuracy by interpolating the smooth Matsubara data.

3. METHOD

The workflow of this study can be summarized in five steps:

1. PIMC computation of imaginary-time correlation function $\mathcal{G}(\tau)$;
2. Fourier transform to imaginary Matsubara frequencies $\mathcal{G}(i\omega_n)$;
3. MaxEnt inversion of eq 19 to obtain $A(\omega)$;
4. transformation with eq 14 to obtain dynamic polarizability $\alpha(\omega)$;
5. calculation of dispersion coefficients from $\alpha(i\omega_n)$.

We will provide an overview and some practical details in the following subsections.

3.1. Path-Integral Monte Carlo. To compute imaginary-time correlation functions $\mathcal{G}(\tau)$, we use a private implementation of the standard path-integral Monte Carlo method (PIMC).[1,2,61] Depending on the nature of the problem, other methods could be used as well; e.g., see refs 5 and 39. Measuring the correlation function itself is straightforward; the important factors are the accuracy and efficiency of the simulation. All-electron simulation of atomic species is not yet common with the PIMC method, because of its computational cost. However, it is needed to properly extract electronic properties, such as polarizabilities, in combination with the nuclear quantum effects: rotation, vibration, and, in principle, nonadiabatic coupling.

In thermal equilibrium defined by $\beta = 1/kT$, expectation values are given by

$$\langle O\rangle = Z^{-1}\mathrm{Tr}[\hat{\rho}(\beta)\hat{O}] \tag{34}$$

where $Z = \mathrm{Tr}\hat{\rho}(\beta)$ and $\hat{\rho}(\beta) = \mathrm{e}^{-\beta\hat{H}}$. The essence of PIMC is expansion of the density matrix $\rho(\beta)$ into a discrete imaginary-time path

$$\begin{aligned}\rho(R, R; \beta) &= \int \mathrm{d}R\ \langle R|\hat{\rho}(\beta)|R\rangle \\ &= \int \mathrm{d}R\ \langle R|\hat{\rho}(\Delta\tau)^M|R\rangle \\ &= \int \mathrm{d}R_1 \dots \mathrm{d}R_M\ \langle R_0|\hat{\rho}(\Delta\tau)|R_1\rangle \dots \langle R_{M-1}|\hat{\rho}(\Delta\tau)|R_M\rangle\end{aligned} \tag{35}$$

where R is a position representation of the many-body state, $M = \beta/\Delta\tau \gg 1$ is the Trotter number, and $R = R_M = R_0$ closes the ring polymer. Accuracy of the propagator $\mathrm{e}^{-\Delta\tau\hat{H}}$ can be controlled by adjusting the short time step $\Delta\tau$. In this work, we use exact pair-density matrices that are obtained from the Coulomb potential by matrix squaring,[61,62] and $\Delta\tau$ dictates the validity of the pair approximation.

In particular, a correlation function between $\hat{P}$ and $\hat{Q}$ is given by

$$\begin{aligned}\langle\mathcal{G}(m\Delta\tau)\rangle &= \langle\mathcal{T}_\tau P(0)\ Q(\tau)\rangle \\ &= Z^{-1}\int \mathrm{d}R_1 \dots \mathrm{d}R_M \\ &\quad \times \langle R_0|\hat{\rho}(\Delta\tau)|R_1\rangle \dots \langle R_{M-1}|\hat{\rho}(\Delta\tau)|R_M\rangle P(R_0)\ Q(R_m)\end{aligned} \tag{36}$$

$$\begin{aligned}&= Z^{-1}M^{-1}\sum_{k=0}^{M-1}\int \mathrm{d}R_1 \dots \mathrm{d}R_M \\ &\quad \times \langle R_0|\hat{\rho}(\Delta\tau)|R_1\rangle \dots \langle R_{M-1}|\hat{\rho}(\Delta\tau)|R_M\rangle P(R_k)\ Q(R_{m+k})\end{aligned} \tag{37}$$

where $0 \le m$ and $m + k \le M - 1$ are periodic in M and $O(R_m)$ denotes a measurement at a particular time slice. Equation 37 also utilizes symmetry of the equilibrium so that the average correlation can be measured with respect to any, or every, time slice. In practice, careless computation of all $M \times M$ correlations can be very costly in terms of both performance and data storage. A lot of efficiency can be recovered by utilizing the symmetry properties and optimizing loops and memory usage of the implementation. More details and an optimized pseudocode are provided in Appendix A.

Another computationally intensive part is sampling the integral $\int \mathrm{d}R$ over all possible paths. In PIMC, the many-body trajectory R is a Markovian walker that is sampled in thermal equilibrium using the Metropolis algorithm. Sampling efficiency is a result of many factors, such as the temperature, density, number of particles, fermion/boson statistics, and the finite time step $\Delta\tau$. In this work, we use the bisection method[2] in combination with random rotations. Also, for now we only simulate systems with distinguishable particles that can be solved exactly using the so-called boltzmannon statistics. By choosing to exclude identical fermions, we avoid having to treat self-canceling permutations that lead to degradation of efficiency due to the infamous sign problem.[63]

3.2. Fourier Transforming $\mathcal{G}(\tau)$. When a satisfactory estimate of $\langle\mathcal{G}(\tau)\rangle$ has been produced, it is time for postprocessing. The first follow-up step is Fourier transforming $\mathcal{G}(\tau)$ to give $\mathcal{G}(i\omega_n)$ in terms of discrete Matsubara frequencies ω_n. The alternative would be using eq 18 for the MaxEnt inversion, but the frequency kernel $K(i\omega_n,\omega)$ is considered better behaving.[22] The Matsubara data are also equated with the polarizability; i.e., $\mathcal{G}(i\omega_n) = \alpha(i\omega_n)$, which will be used in eqs 31−33).

The Fourier transform can be performed discretely; i.e.,

$$\mathcal{G}(i\omega_n) = \int_0^\beta \mathrm{d}\tau\ \mathrm{e}^{i\omega_n\tau}\,\mathcal{G}(\tau) \tag{38}$$

$$= \lim_{M\to\infty}\sum_{m=0}^{M-1}\Delta\tau\mathrm{e}^{i\omega_n m\Delta\tau/M}\,\mathcal{G}(m\Delta\tau) \tag{39}$$

where $\Delta\tau = \beta/M$ defines the sampling resolution. Practically, $\Delta\tau$ needs not to be zero, but a small finite value provides enough accuracy for a reasonable number of Matsubara frequencies. A typical process is visualized in Figure 1: fast Fourier transform (FFT) maps M original MC values of $\langle\mathcal{G}(m\tau)\rangle$ into equally many Matsubara frequencies. Beyond a fraction of the frequencies, there will be an error, unless $\Delta\tau$ is artificially decreased by some integer factor, e.g., 8. This consists of numerical interpolation of the data, which can be done for example with cubic splines. Alternatively, the spline-interpolated data can be Fourier transformed analytically,[22] but the practical difference is negligible. Furthermore, due to the linearity of

DOI: 10.1021/acs.jctc.8b00859
J. Chem. Theory Comput. 2018, 14, 5750−5763

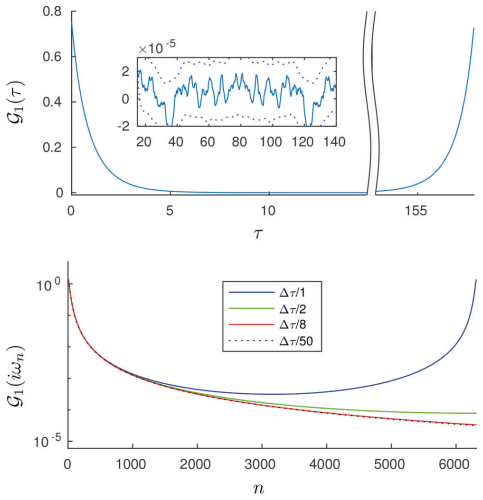

Figure 1. Top, total $\mathcal{G}_1(\tau)$ of He at 2000 K. Noisy fluctuation near $\langle\mu\rangle^2 = 0$ is depicted in the inset. Bottom, same data given in discrete Matsubara frequencies, $\alpha_1(i\omega_n)$. Discrete Fourier transform wrongfully produces periodic data. One way to approach the true Matsubara data is to increase the period by adjusting the relative interpolation density from $1/\Delta\tau$ to infinity. Since the absolute magnitude of $\alpha_l(i\omega_n)$ drops fast, and only a fraction of Matsubara frequencies contribute to $\alpha_l(\omega)$ or dispersion coefficients, we have chosen $\Delta\tau/8$ as a safe interpolation frequency.

Fourier transform, it does not matter, whether we transform the sample average or average over transforms of samples; i.e.,

$$\langle\mathcal{G}(i\omega_n)\rangle = \mathcal{F}\langle\mathcal{G}(\tau)\rangle = \langle\mathcal{F}\mathcal{G}(\tau)\rangle \tag{40}$$

We prefer the right-hand side (rhs) of eq 40, because it provides a tangible interface to the statistics of $\langle\mathcal{G}(i\omega_n)\rangle$.

In conclusion, using FFT with the original $\Delta\tau$ is tempting but only realiable for the lowest fraction of Matsubara frequencies. This can be resolved by boosting the sampling resolution of $\mathcal{G}(\tau)$ and, thus, reaching even higher frequencies. On the other hand, FFT is exact at the static limit, i.e., $\alpha(i\omega_n{=}\omega{=}0)$. There we have, for instance

$$\begin{aligned}\alpha_1(0) &= \sum_{m=0}^{M-1} \Delta\tau e^{i\omega_n m\Delta\tau/M} \langle\mathcal{G}_1(m\Delta\tau)\rangle \\ &= \sum_{m=0}^{M-1} \Delta\tau \left\langle M^{-1} \sum_{k=0}^{M-1} \mu(R_k)\,\mu(R_{k+m}) \right\rangle \\ &= M\Delta\tau \left\langle M^{-2} \sum_{m=0}^{M-1} \mu(R_m) \sum_{k=0}^{M-1} \mu(R_k) \right\rangle \\ &= \beta\langle\bar{\mu}^2\rangle\end{aligned}$$

where bar denotes an average over a sample path. The last form eclipses the static field-derivative estimators that have been proposed earlier.[42,43] The relative number of independent measurements needed by these static estimators is reduced from M^{d+1} to $(d+1)M$, where d is the degree of polarizability, here 1.

3.3. Maximum Entropy Method. Solving integral eq 18 or 19 is challenging, when $\mathcal{G}$ on the left-hand side is noisy or incomplete. While quantum Monte Carlo results can be, in principle, improved indefinitely, the statistical noise cannot be fully eliminated. Thus, even minor fluctuations in the high values of τ or ω can reflect strongly in the resulting spectral function $A(\omega)$. Normally, one could discretize τ or ω and solve the resulting linear system

$$\mathbf{G} = \mathbf{K}\mathbf{A} \tag{41}$$

where $\mathbf{G}$ and $\mathbf{A}$ are discrete input and output vectors, respectively, and $\mathbf{K}$ is a transformation matrix to be inverted. Unfortunately, here the kernel producing $\mathbf{K}$ is highly nonlinear. We could end up with very diverse results just by using different grids or MC samples.

Therefore, a robust method is needed for the inversion, and one of the most popular is maximum entropy (MaxEnt).[21,22] MaxEnt uses Bayesian inference to pick the most probable $\mathbf{A}$ out of all possible solutions with a given $\mathbf{G}$. This is equal to maximizing

$$P(\mathbf{A}|\mathbf{G}) = \frac{P(\mathbf{G}|\mathbf{A})\,P(\mathbf{A})}{P(\mathbf{G})} \tag{42}$$

First, $P(\mathbf{G})$ can be considered fixed. Second, the relative probability of $\mathbf{G}$ given $\mathbf{A}$ can be quantified by the central limit theorem as

$$P(\mathbf{G}|\mathbf{A}) \propto e^{-\chi^2/2} \tag{43}$$

where

$$\chi^2 = (\mathbf{G}-\bar{\mathbf{G}})^{\mathrm{T}}\mathbf{C}^{-1}(\mathbf{G}-\bar{\mathbf{G}}) \tag{44}$$

where $\bar{\mathbf{G}} = \mathbf{K}\mathbf{A}$ is the proposed forward mapping and $\mathbf{C}$ is the covariance matrix. In other words, χ^2 is a least-squares fitting error between the input and the proposed mapping. Lastly, the prior probability can be defined as

$$P(\mathbf{A}) \propto e^{aS} \tag{45}$$

where

$$S = -\int \frac{d\omega}{2\pi} A(\omega) \ln\left(\frac{A(\omega)}{D(\omega)}\right) \tag{46}$$

is called the relative entropy. $D(\omega)$ is the so-called default model that sets an a priori bias for the entropy. It can be used to steer the fitting by setting it to resemble the expected shape of the spectral function.

Combining eqs 43 and 45, the inversion boils down to maximizing

$$\ln P(A|G) = aS - \chi^2/2 \tag{47}$$

for a given frequency grid and a. Again, a is an adjustable parameter that balances the fit between the least-squares error and the default model: too small a favors overfitting to statistical noise, while too large a returns the default model and shuns any new information. There are several strategies for identifying the optimal a, e.g., classical, historic, and the Bryan's approach. It is indeed one of the most important practical choices, along with specifying the ω-grid and the default model $D(\omega)$.

In this work, we use OmegaMaxEnt software (ΩMaxEnt, version 2018-01) by Bergeron and Tremblay.[22] It uses fitted spectral moments to regulate the output and maximum curvature of the $\log(\chi^2)-\log(a)$ plot to identify the optimal a.

DOI: 10.1021/acs.jctc.8b00859
J. Chem. Theory Comput. 2018, 14, 5750−5763

It is thus relatively independent of the choice of $D(\omega)$, which makes for a good black box. For further details on the implementation and techniques, we refer to ref 22 and the user documentation.

A few practical notes on the use of ΩMaxEnt are in order. First, for first-order polarizabilities we choose a *bosonic calculation*, which enforces the problem to positive frequencies, only. For the input, we use a real-valued $\mathcal{G}(i\omega_n \geq 0)$ and its *re-re covariance matrix* **C**, which are estimated from a set of Fourier transformed PIMC results. In practice, the input data must be truncated to n_{max} lowest Matsubara frequencies based on a few rules of thumb: there has to be many enough high frequencies to converge the estimation of spectral moments; yet, for too large n_{max}, the inputs become unreliable due to random noise. A particular problem is the covariance matrix **C**, which will be inverted and needs to be nonsingular. However, by increasing the number of MC samples, we get a more accurate estimate of **C**, and enable more Matsubara frequencies to be used. In this work, the number is usually between 50 and 800.

A *non-uniform grid in main spectral range* is manually adjusted to promote resolution in the active spectral regions: the electronic peaks and, with some molecules, the low-frequency rotational spectra. We choose not to modify $D(\omega)$ from the software default, which is a normalized Gaussian function centered at $\omega = 0$, whose variance depends on the estimated spectral moments. Finally, the output data are given in the form $\frac{1}{2}A(\omega)/\omega$, where the negative frequencies obey antisymmetry $A(\omega) = -A(-\omega)$. Unfortunately, we cannot reliably estimate the error of $A(\omega)$, but the typical qualitative error is that collections of sharp peaks are replaced by a single soft form. This is exemplified in Figure 2, which also demonstrates one of the

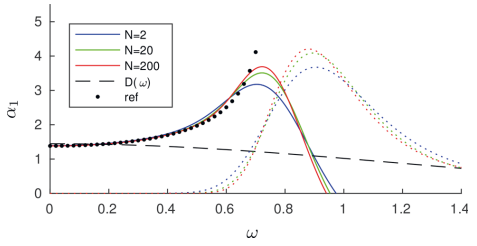

Figure 2. Improvement of the MaxEnt spectrum of He at 2000 K as a function of input data quality. The real (solid) and imaginary (dotted) components of the dynamic polarizability $\alpha_1(\omega)$ are plotted using a variable number of data blocks N, an arbitrary measure of computational effort. Even low-quality data produce a qualitatively meaningful spectrum. The off-resonant data are good, but near the active spectral region the MaxEnt data divert from the 0 K reference.[50] Providing better input data improves the sharpness systematically. However, using this means to achieve narrow peaks with purely physical spectral broadening leads to ill-conditioned scaling of computation. A better strategy would be improving the default model $D(\omega)$ (dashed), which is rather plain in this work.

integral properties of MaxEnt: while increasingly tedious, providing better input improves the result by sharpening the spectrum while roughly maintaining its original weight.

3.4. Integral Transforms. The last two steps only involve integral transforms of discrete numerical data. For both, the actual integration is done numerically using the trapezoidal rule with dense cubic spline interpolation.

The first transform, eq 14, can be rewritten as

$$\alpha(\omega) = -\int_{-\infty}^{\infty} \frac{d\omega'}{2\pi} \frac{A(\omega')}{\omega - \omega' + i\eta} = \int_0^{\infty} \frac{d\omega'}{2\pi} A(\omega') \left[\frac{1}{\omega' - \omega - i\eta} + \frac{1}{\omega + \omega' + i\eta} \right] \quad (48)$$

which is convenient, because the input is given as $A(\omega \geq 0)$. It also represents the resonant and antiresonant terms of polarizability. Practically, the integration can be truncated after the main spectral region, at around $\hbar\omega' \sim 10$ at maximum. Setting the dissipation term to $\eta = 0.001$ appears to produce convergent results.

The calculation of dispersion coefficients involves products of polarizabilities for two species (or just one paired with itself). Thus, the integrand is nonlinear in the MC data, which has a few consequences: First, random fluctuations in $\langle \alpha(i\omega_n) \rangle$ may not exactly cancel out. This cannot be eliminated completely, but some of the noise can be filtered out by smoothing the data before integration with the moving average technique. Second, the error estimate for each integrated term ΔC_* is written as

$$(\Delta C_*)^2 = \int_0^{\infty} d\omega \, (\alpha_{l_1}^A(i\omega) \, \Delta\alpha_{l_2}^B(i\omega))^2 + (\Delta\alpha_{l_1}^A(i\omega) \, \alpha_{l_2}^B(i\omega))^2 + \alpha_{l_1}^A(i\omega) \, \alpha_{l_2}^B(i\omega) \, \Delta\alpha_{l_1}^A(i\omega) \, \Delta\alpha_{l_2}^B(i\omega) \quad (49)$$

where l_1 and l_2 take values of 1, 2, and 3, and the integral is in practice replaced by a sum over the components of $\Delta\omega$. As before, $\langle \alpha(i\omega_n) \rangle$ decays fast in the growing n, and thus, the integration can be safely truncated at, e.g., $n = M$.

4. RESULTS

We estimate dynamic polarizability for a collection of systems with one or two electrons: H, He, Ps, Ps_2, HD^+, and H_2. The list is not exhaustive, but diverse enough to demonstrate the most important physical effects and features of the method. The results involve three quantities, $\mathcal{G}_l(\tau)$, $\alpha_l(i\omega_n)$, and complex $\alpha_l(\omega)$ computed for three multipole processes: dipole−dipole ($l = 1$), quadrupole−quadrupole ($l = 2$), and octupole−octupole ($l = 3$). Each system is simulated independently with two time steps $\Delta\tau$ to probe for time-step error and to rule out the possibility of numerical artifacts. The smaller time step is used for the main results (solid line), while the bigger provides a "sanity check" (dotted line): the results are roughly as reliable as the two independent results are inseparable. The molecular simulations are repeated at various temperatures between 200 and 1600 K to probe for weak and strong thermal effects. Finally, we use $\alpha_l(i\omega_n)$ to compute dispersion coefficients between pairs of species at 300 K. For reference, Table 1 contains a compilation of all static polarizabilities and total energies, and their statistical error estimates: 2σ standard error of the mean (2SEM). Agreement with the available references is excellent. All results are given in atomic units.

4.1. H and He. To establish computation of purely electronic spectra, we start with atomic species: isolated H and He. The systems are simulated in clamped-nuclei approximation at $T = 2000$ K. At low temperatures, they are effectively in their electronic ground states. Hence, the spectra and polarizabilities

DOI: 10.1021/acs.jctc.8b00859
J. Chem. Theory Comput. 2018, 14, 5750−5763

Table 1. Comparison of Total Energies and Static Polarizabilities (with 2SEM Estimates) from the PIMC Simulations and Available 0 K References[a]

	T (K)	E	$\Delta\tau$	$\alpha_1(0)$	$\alpha_2(0)$	$\alpha_3(0)$
H	2000	−0.49993(2)	0.05	4.5023(9)	15.011(7)	131.4(2)
	300	−0.5000(2)	0.02	4.50(3)	15.03(12)	132(3)
	0	−0.5		4.5[b]	15.0[b]	131.25[b]
He	2000	−2.9036(4)	0.0125	1.382(3)	2.435(9)	10.49(9)
	300	−2.904(2)	0.02	1.38(4)	2.43(6)	10.5(4)
	0	−2.90372[c]		1.383192[d]	2.445083[d]	10.620329[d]
H_2	1600	−1.15855(9)	0.05	5.519(5)	26.83(5)	125.7(7)
	800	−1.16168(12)	0.05	5.463(6)	34.38(9)	123.0(8)
	400	−1.1630(2)	0.05	5.424(10)	47.7(3)	121.4(9)
	300	−1.1633(8)	0.02	5.42(6)	53.4(10)	118(3)
	200	−1.1637(3)	0.05	5.43(3)	66.1(5)	121(2)
	0	−1.164025[e]		5.395708[f]	12.455708[f]	
	0			5.4139[g]		
HD^+	1600	−0.59047(12)	0.05	11.96(3)	152.5(5)	156.7(6)
	800	−0.59493(12)	0.05	19.04(4)	257(2)	214.9(9)
	400	−0.59663(12)	0.05	33.73(7)	468(4)	345(2)
	300	−0.5968(3)	0.02	43.6(4)	601(14)	426(8)
	200	−0.5972(2)	0.05	62.3(3)	848(10)	557(6)
	0	−0.597898[h]		395.306326[h]	2050.233354[h]	773.42727[h]
Ps_2	400	−0.51598(8)	0.05	71.57(8)	1390(20)	$5.3(4)\times10^4$
	300	−0.5158(2)	0.02	71.9(3)	1390(30)	$5.2(4)\times10^4$
	200	−0.51593(12)	0.05	71.7(2)	1370(20)	$5.1(3)\times10^4$
	0	−0.516004[i]				

[a]For H and He, the results are adiabatic, i.e., from clamped-nuclei simulations; otherwise, the results are fully nonadiabatic including rovibrational motion. All values are given in atomic units. [b]Bishop and Pipin.[50] [c]Pekeris,[51] [d]Yan et al.[52] (data truncated). [e]Pachucki and Komasa[53] (data truncated). [f]Bishop and Pipin[50] (isotropic averaging; separation $R = 1.449$; mismatch of α_2 is due to the missing rotational component). [g]Kolos and Wolniewicz[54] (isotropic averaging; separation $R = 1.4$). [h]Tang et al.[47] (data truncated). [i]Usukura and Suzuki[55] (data truncated).

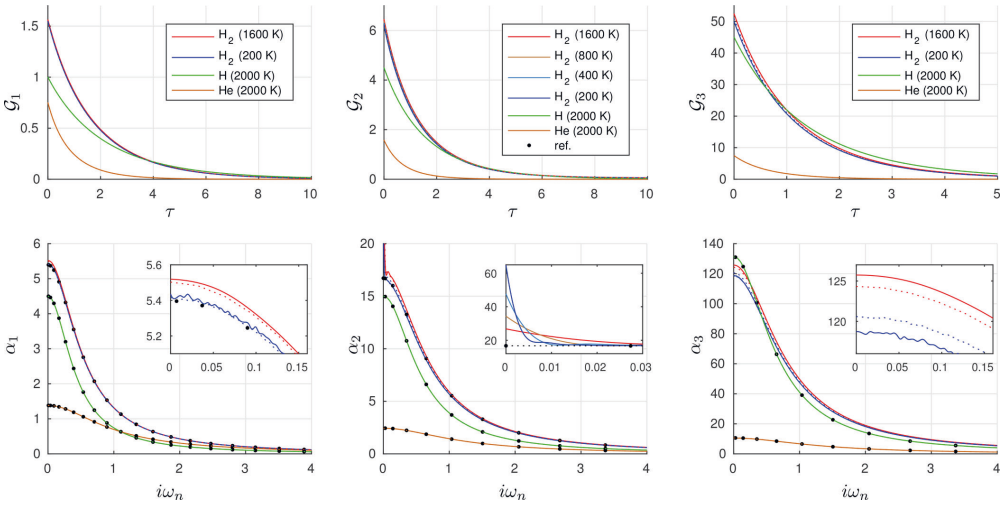

Figure 3. Correlation functions $\mathcal{G}_l(\tau)$ and Fourier transforms $\alpha_l(i\omega_n)$ of H, He, and H_2. With atoms, the thermal dependence is negligible, and the results match with 0 K reference values.[50] With H_2, there is a weak centrifugal effect that separates 200 and 1600 K results from each other and the reference in the dipole and octupole processes. On the other hand, a permanent quadrupole correlation causes a huge and thermally dependent orientational effect that is shown in the inset of α_2. It overrides the centrifugal effect and is also missing from the reference.

are in good agreement with 0 K references.[50,64] The time steps are $\Delta\tau = 0.05$, 0.1 for H and $\Delta\tau = 0.0125$, 0.025 for He. The correlation functions $\mathcal{G}_l(\tau)$ and their Fourier transforms $\alpha_l(i\omega_n)$ are presented in Figure 3. Real-domain dynamic polarizabilities $\alpha_l(\omega)$ are obtained by analytic continuation and presented in Figures 4 and 5. The imaginary part $\mathrm{Im}[\alpha_l(\omega)]$ and the spectrum

DOI: 10.1021/acs.jctc.8b00859
J. Chem. Theory Comput. 2018, 14, 5750−5763

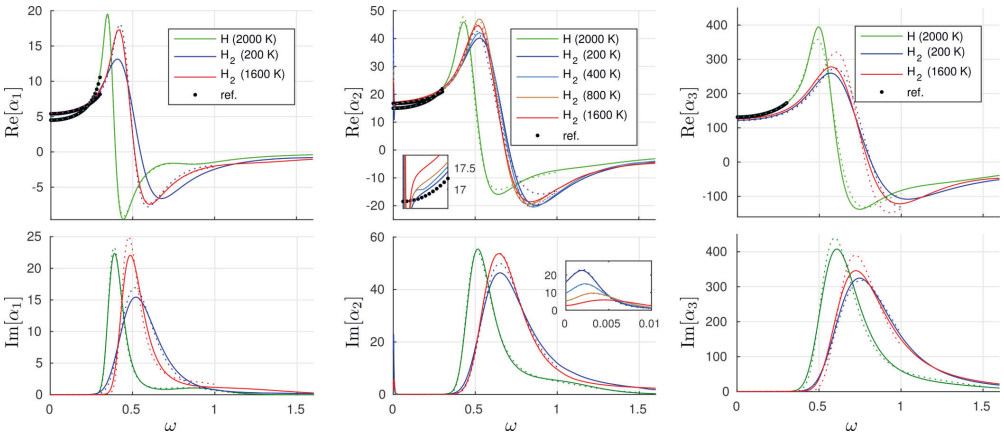

Figure 4. Dynamic polarizabilities $\alpha(\omega)$ of H and H_2. The spectral peaks of H are lower than those of H_2, but their proportions remain approximately the same in higher multipoles. While the results for H are in good agreement, H_2 shows thermal and nuclear effects that are missing from the 0 K references.[50] The quadrupole polarizability $\alpha_2(\omega)$ of H_2 has a large thermal effect due to rotational coupling: the low-frequency (IR) spectrum spreads out, and the huge orientational polarizability decreases toward higher temperatures. At higher frequencies, the difference to 0 K is explained by vibrational and centrifugal effects, and a different bond length used in ref 50. Unfortunately, different shapes of the electronic peaks are not entirely due to electron−nucleus coupling: the spectral broadening due to MaxEnt inversion is worse with the heavier, low-temperature simulations. Consequently, the results are generally sharper with the longer time step (dotted) than the shorter one (solid).

$A_l(\omega)$ are related, so the latter is not presented separately. The real part $\mathrm{Re}[\alpha_l(\omega)]$ provides the optical response.

Overall, agreement with the references is excellent at low frequencies, but the amount of detail is limited in the active spectral region (see Table 1 and Figures 3, 4, and 5). The same holds for all of the simulated electronic spectra. The lower moments of the MaxEnt spectrum, weight and alignment, are generally accurate. However, the higher moments providing sharpness and distinction between bound transitions are lost in the noise. Spectral weight of the continuum is relatively small for the dipole process but increases substantially with the higher multipole transitions. Our polarizabilities are slightly higher than the reference near the first electronic excitation. This mismatch results from "spilling" of the spectrum to inappropriate frequencies due to the artificial spectral broadening. The true frequency ranges between the lowest multipole transition and continuum are $0.375 < \hbar\omega < 0.5$ for H and around $0.76 < \hbar\omega < 0.90$ for He.

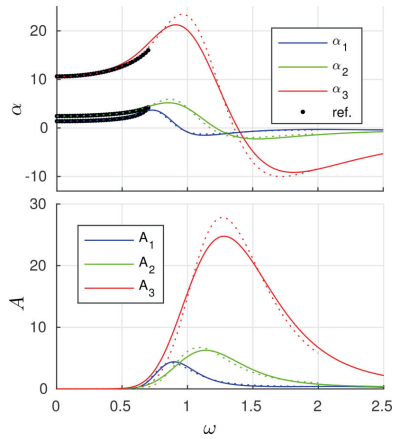

Figure 5. Real dynamic polarizabilities $\mathrm{Re}[\alpha(\omega)]$ and spectral functions $A(\omega)$ of He at 2000 K. In higher multipoles, the spectral moments grow in magnitude and frequency. The results are in good agreement between big (dotted) and small (solid) time steps and the 0 K reference.[50]

4.2. Ps_2. Next, we consider the nonadiabatic regime with dipositronium, Ps_2: an exotic system, whose dielectric properties, to the best of our knowledge, have not been simulated before. The positron mass equals that of electron $m_{\bar{e}} = m_e$, and the simulation is thus fully nonadiabatic. Annihilation is not considered. Ps_2 is likely to dissociate at $T > 800$ K,[65] so we simulate it at temperatures $T = 200$ and 400 K with time steps $\Delta\tau = 0.05$ and 0.1. We have compiled the results of correlation functions and imaginary-frequency polarizability to Figure 6 and real-frequency dynamic polarizabilities to Figure 7. Total energies and static polarizabilities are found in Table 1. Pure positronic systems have much larger dielectric response than regular atoms, but otherwise they act similarly. As seen in the figures, all the imaginary-domain correlations have similar scaling and only different orders of magnitude.

An interesting question is the relationship between Ps_2 and Ps, the latter of which can be solved analytically. First, the bound dipole spectrum ranges of Ps ($0.1875 < \hbar\omega < 0.25$) agree with those of Ps_2 ($0.18160 < \hbar\omega < 0.24240$[55]) and the results of this work. The higher multipole spectra are shifted to higher frequencies. Second, the imaginary-time dipole correlation of Ps_2 at 300 K is approximately twice that of Ps, as shown in Figure 8. For two completely uncorrelated positroniums, this quotient would be exactly 2. The small difference is related to the binding energy of Ps_2. The quadrupole correlations cannot be compared,

DOI: 10.1021/acs.jctc.8b00859
J. Chem. Theory Comput. 2018, 14, 5750−5763

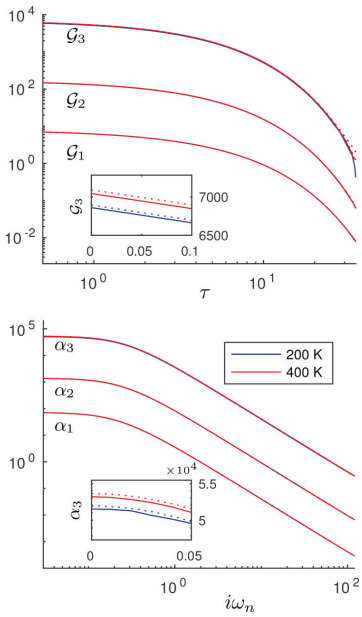

Figure 6. Logarithmic plots of $\mathcal{G}(\tau)$ and $\alpha(i\omega_n)$ of Ps_2 at 200 and 400 K. Different multipole correlations have similar scaling but different orders of magnitude. A small thermal effect increment is observed at the higher temperature. This is most pronounced in the octupole order, which is depicted in the insets.

because α_2 is zero for Ps. The octupole processes converge to a quotient of approximately 30, but the response at low Matsubara frequencies does not show any intuitive behavior. The transient occurs at $\hbar\omega_n < 15$, which involves the first ∼2500 Matsubara frequencies at 300 K.

4.3. H_2 and HD^+. Finally, we study combined electronic, nonadiabatic, thermal, and nuclear quantum effects featured in two molecular systems: H_2 and HD^+. For both systems, the temperatures are T = 200, 400, 800, and 1600 K and time steps $\Delta\tau$ = 0.05 and 0.1. The simulation is nonadiabatic with fully quantized nuclei, using m_p = 1836.15267248m_e and m_d = 3670.480492233m_e for the respective masses of proton and deuteron. The correlation functions and imaginary-frequency polarizabilities are presented in Figures 3 and 9 depending on the multipole symmetry. Dynamic polarizabilities are shown in Figures 4 for H_2 and 10 for HD^+.

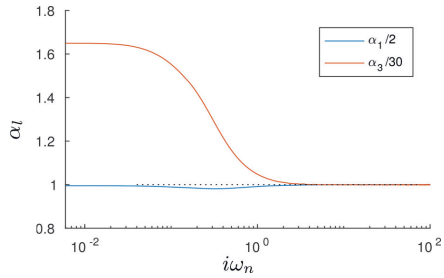

Figure 8. Scaled quotients between $\alpha_l(i\omega_n)$ of Ps_2 and Ps at 300 K. The scaling factor is chosen such that the fraction converges to unity as $i\omega_n \to \infty$. For instance, it is understandable that the dipole polarizability of Ps_2 almost equals twice that of Ps.

While the molecules are effectively in their electronic ground states, their nuclear motion depends on the temperature. This may cause a weak or a strong effect on the total molecular polarizability. The weak effect is related to centrifugal distortion: the bond becomes longer, if a molecule is in a high rotational ensemble (high temperature); hence, the electric moments usually get slightly larger.[42] This is most readily seen by comparing 200 and 1600 K data of $\mathcal{G}_l(\tau)$ in Figures 3 and 9.

The strong effect is caused by nonzero electric moments. The molecule pursues a favorable orientation with the perturbing field, which causes a dominant, orientational contribution to the average polarizability.[41] High rotational ensemble interferes with the orientation, and hence, the rotational effect fades off as the temperature increases.[42,43,46] In higher orders, this effect is reproduced between nonzero anisotropy of tensorial polarizability and an associated hyperpolarizability.[42,43,46] Here, permanent moments are present in α_2 of H_2 and each α_l of HD^+, whose figures also have insets showing the strong decay of the rotational polarizability as T increases. At the low-temperature limit, all rotational motion is deactivated and the static polarizability saturates to a finite value.[43] Beyond the static limit, the rotational effect fades off rapidly in terms of both real

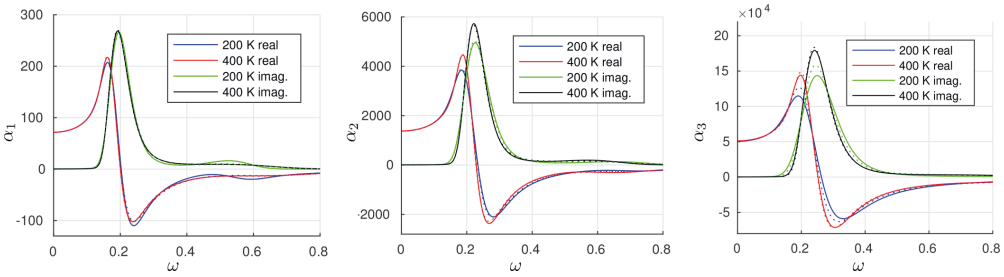

Figure 7. Dynamic polarizabilities $\alpha(\omega)$ of Ps_2 at 200 and 400 K. Here, all the spectra are located roughly at the same frequency interval, but the spectral weights escalate in higher multipoles. There is a small thermal increment in the higher multipole polarizabilities, as supported by Figure 6. The differences in spectral sharpness, however, are mostly due to the numerics.

DOI: 10.1021/acs.jctc.8b00859
J. Chem. Theory Comput. 2018, 14, 5750−5763

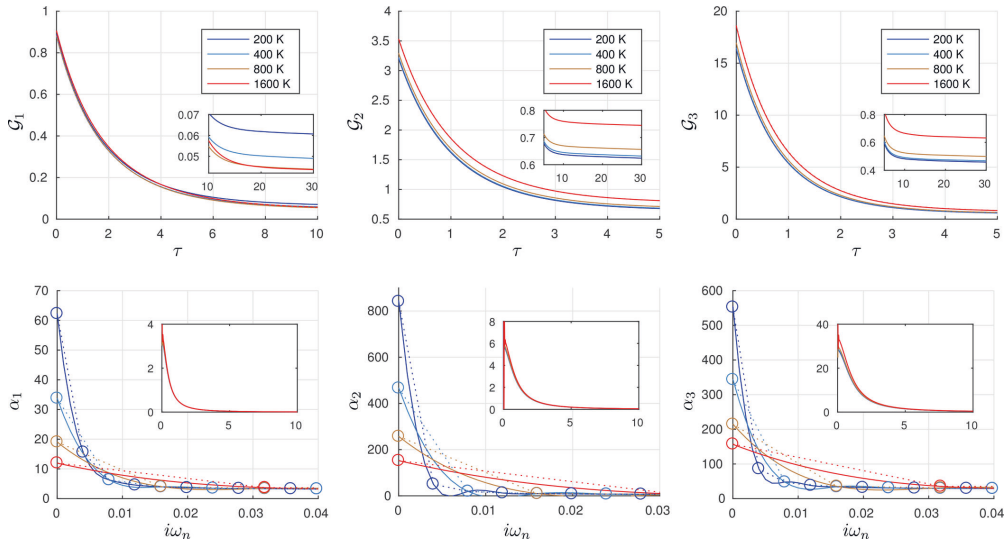

Figure 9. Correlation functions $\mathcal{G}(\tau)$ and Fourier transforms $\alpha(i\omega_n)$ of HD^+ at variable temperatures. A weak centrifugal effect is seen as $\mathcal{G}_l(\tau)$ saturates to slightly different finite values: the effect is also inverted between the dipole and the higher orders. On the other hand, $\alpha(i\omega_n)$ exhibits a strong rotational effect, which decays fast in both the temperature and the Matsubara frequencies. Thermal and time-step effects are not as complex as they first seem: rather, the error of cubic spline interpolation is demonstrated by applying it for the smaller time step (solid) but not the bigger one (dotted). The actual data points are marked with circles. The large-scale data of $\alpha(i\omega_n)$ are shown in the insets and do not have notable thermal effects at higher frequencies.

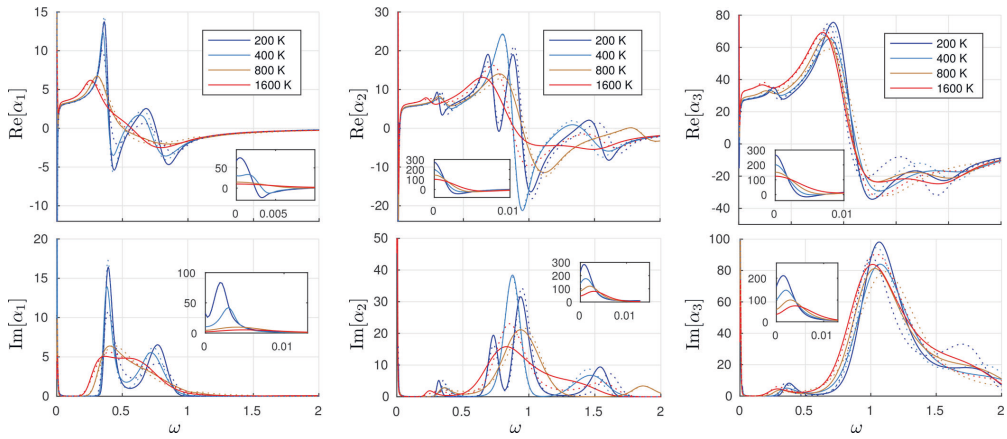

Figure 10. Dynamic polarizabilities $\alpha(\omega)$ of HD^+ at variable temperatures. HD^+ is IR-active in all multipoles, and thus, in each plot, we can see broadening of the IR spectrum and thermal decay of the orientational effect. The temperature causes considerable shifting and broadening also to the electronic spectra, only a part of which is explained by the numerical deficiency of MaxEnt. There is a reasonable agreement between the bigger (dotted) and the smaller (solid) time steps.

and imaginary frequencies. This limits the spectral activity of rotation to infrared frequencies. At higher frequencies, the optical properties are dictated by the electronic spectra. Therefore, our results for H_2 beyond infrared agree with isotropic averages computed with eqs 28 and 29, and the available electronic reference data.[50]

4.4. Dispersion Coefficients. Lastly, we demonstrate an additional use of imaginary-frequency polarizability data: computing London dispersion coefficients using eqs 31−33. For this purpose, we simulated H, He, H_2, HD^+, Ps, and Ps_2, the same as before but using compatible temperature and time step:

DOI: 10.1021/acs.jctc.8b00859
J. Chem. Theory Comput. 2018, 14, 5750−5763

$T = 300$ K and $\Delta\tau = 0.02$. Proof-of-concept results between each pair of species are presented in Table 2.

Table 2. Dispersion Coefficients (with 2SEM Estimates) for Pairs of Atoms and Molecules at 300 K, Using $\Delta\tau = 0.02$[a]

	C_6	C_8	C_{10}
H−H	6.50(4)	124.7(4)	3300(9)
	6.4990267[b,d]	124.39908[b,d]	3285.8284[b,d]
H−He	2.82(4)	41.9(3)	873(4)
	2.8213439[b,d]	41.828[b,d]	871.23[b,d]
H−H_2	8.78(7)	164.8(8)[f]	4003(12)
	8.7843286[d]	161.31542[d]	
H−HD^+	6.35(12)[f]	135(5)[f]	2620(50)[f]
	5.3815691[c]	99.592513[c]	2023.6873[c]
H−Ps	34.8(3)	318(2)	11560(60)
H−Ps_2	68.7(4)	4210(50)	$3.35(6) \times 10^5$
He−He	1.46(2)	14.09(9)	182.7(8)
	1.4609778[b,d]	14.117857[b]	183.69107[b]
He−H_2	4.01(5)	56.4(4)[f]	1008(4)
	4.0128132[d]	55.381453[d]	
He−HD^+	2.65(9)[f]	41(3)[f]	507(10)[f]
	2.3441447[c]	31.043629[c]	416.42889[c]
He−Ps	13.4(2)	60.9(6)	3040(30)
He−Ps_2	26.4(4)	1520(30)	$1.17(3)\times10^5$
H_2−H_2	12.04(12)	219.1(1.3)	4870(20)
	12.058168[d]		
H_2−HD^+	8.4(3)	184(8)	3800(200)
H_2−Ps	45.2(4)	401(4)	13270(70)
H_2−Ps_2	89.2(8)	5470(70)	$4.32(8) \times 10^5$
HD^+−HD^+	11.7(1.2)	530(70)	16000(3000)
HD^+−Ps	37(1)	510(40)	7940(120)
HD^+−Ps_2	74(3)	4800(200)	$3.7(2) \times 10^5$
Ps−Ps	207.3(1.3)	0[e]	68400(400)
Ps−Ps_2	410(3)	21000(300)	$1.59(4) \times 10^5$
Ps_2−Ps_2	811(5)	83200(800)	$1.000(12) \times 10^7$

[a]Available 0 K data provided for reference. [b]Yan et al.[52] [c]Tang et al.[47] [d]Bishop and Pipin.[50] [e]The quadrupole moment of Ps is zero by the symmetry of masses. [f]The mismatch is due to orientational and thermal effects that are missing from the reference.

Most results match the available 0 K references,[47,50,52] because as we have shown, the thermal dependency of polarizabilities is negligible for most of the systems considered here. Exceptions are the polarizabilities associated with permanent electric moments: α_2 of H_2 and all α_1 of HD^+. As seen in Figures 3 and 9, they have quickly vanishing and thermally dependent rotational peaks at low Matsubara frequencies. This leads to a small yet noticeable difference between our 300 K results and the 0 K electron-only references: the peaks effectively increase the values of the dispersion coefficients; the effect of rotational coupling is attractive. Otherwise (e.g., Ps systems) the coefficients are being reported for the first time. Our approach provides a rather direct but accurate interface for incorporating nuclear quantum effects, orientational averaging, and thermal trends into weak molecular interactions.

5. SUMMARY

We have given a detailed demonstration of estimating dynamic multipole polarizabilities from all-electron PIMC simulations. In particular, we have computed autocorrelation functions of the three lowest electric multipoles and analytically continued them with the MaxEnt method. We have validated our approach by reproducing well-known reference values for some one- and two-electron systems: H, He, and H_2. However, we have also provided new complementary data, such as the higher-moment spectra and polarizabilities of H_2, HD^+, and Ps_2. Similarly, we have provided van der Waals dispersion coefficients between the aforementioned species. The coefficients are spherically averaged and include a full thermal ensemble of electric interactions at 300 K.

Indeed, the paradigm of our approach is to provide mixing, as opposed to separation, of the degrees of freedom. Of course, explicit decomposition of the electronic, rovibrational, non-adiabatic, and thermal problems can be very insightful in simple systems, such as those featured in this work. For instance, the existing models for rotational spectrum, zero-point vibration, and absorption cross-section, etc., are very intuitive and precise. Such quantum phenomena we can merely pinpoint from the PIMC results, but not quite reverse engineer. The electronic spectrum itself is a challenge to reproduce at the sharpness and precision of ab initio methods. However, for the purpose of exact mixing of all the degrees of freedom, PIMC provides a rather unique and controllable interface. This will be useful in more complex environments, where harmonic and adiabatic approximations start to fail.

The shortcomings of our approach are mostly due to the ill-posed nature of analytic continuation. A method beoynd MaxEnt is called for but, as of today, not readily available. A universal remedy is increasing computation: "to solve an ill-posed problem, nothing beats good data", as stated by Jarrell and Gubernatis.[21] After all, what counts as heavy today can well be the standard of tomorrow. In that sense, all-electron simulation with PIMC holds the future prospect of a high-accuracy electronic structure benchmark. A natural follow-up for the future will be the simulation of systems that are challenged with the exchange interaction, the fermion sign problem.

In the end, polarizability itself is rather a single example of dynamic response based on quantum correlation functions; the proposed scheme works as a template to numerous similar problems, and vice versa. A lot more will be learned and achieved by developing better practices for producing and processing QMC data, and here we have only taken a first step.

APPENDIX A: OPTIMIZING AUTOCORRELATION IN PIMC

Computation of an imaginary-time autocorrelation function can be the bottleneck of a PIMC simulation, when the number of time slices is large. It is thus reasonable to briefly discuss optimization of such a procedure.

We consider measurement of a correlation function from a sample trajectory R, which has M time slices separated by a time step $\Delta\tau$. A single measurement means choosing a reference time slice R_k and correlating it with another time slice R_{k+m} such that

$$C_{PQ}(m\Delta\tau) = P(R_k)\, Q(R_{k+m}) \tag{50}$$

where $k + m$ goes from 0 to $M - 1$ and symmetry $C_{PQ}(m\Delta\tau) = C_{PQ}(-m\Delta\tau)$ is assumed. As pointed out in eq 37, the imaginary time slices are equivalent: by shifting the reference time slice, i.e., k goes from 0 to $M-1$, we get M independent correlation functions from a single sample trajectory R. While efficient in terms of sampling, making M^2 measurements is an intensive computational task.

DOI: 10.1021/acs.jctc.8b00859
J. Chem. Theory Comput. 2018, 14, 5750−5763

A few optimizations can make the practical calculation significantly faster. First, rather than measuring P or Q on the fly, an array of measurements should be stored into memory, e.g., $P_k = P(R_k)$. If the observable is tensorial, a contiguous memory layout should be preferred for the imaginary-time dimension. Second, unnecessary checkups and modification of indices should be avoided. The following pseudocode achieves this:

```
Initialize(C)
for k=0,M-1
  C(0) = C(0) + P(k)*Q(k)
  for m=k+1,M-1
    C(m-k) = C(m-k) + P(k)*Q(m) + Q(k)*P(m)
  end
end
  D(0) = C(0)/M
  for k=1,(M-1)/2  # if M is even, round up
    D(k) = ( C(k) + C(M-k-1) )/(2*M)
  end
```

where D is another array that only has $M/2$ indices. Namely, only half the data needs to be recorded because of the symmetry. Moreover, if we are computing an autocorrelation function, i.e., $Q = P$, the previous code simplifies to

```
Initialize(C)
for k=0,M-1
  for m=k,M-1
    C(m-k) = C(m-k) + P(k)*P(m)
  end
end
D(0) = C(0)/M
for k=1,(M-1)/2  # if M is even, round up
  D(k) = ( C(k) + C(M-k-1) )
end
```

The previous loops are also easy to parallelize. Third, using a finite stride is advised between the measurements and subsequent sample trajectories: e.g., only every 100th sample is measured. However, a stride in imaginary time should not be used, because it could resonate with the statistical properties of the data. Finally, using a compressed binary data format, such as the hierarchical data format (HDF), and storing the data in average bins or blocks over a large number of measurements are strongly recommended.

AUTHOR INFORMATION

Corresponding Author

*E-mail: tiihonen@iki.fi.

ORCID

Juha Tiihonen: 0000-0003-2107-911X
Ilkka Kylänpää: 0000-0002-7941-3216
Tapio T. Rantala: 0000-0001-8581-502X

Present Address

†Materials Science and Technology Division, Oak Ridge National Laboratory, Oak Ridge, TN 37831, USA.

Notes

The authors declare no competing financial interest.

ACKNOWLEDGMENTS

Juha Tiihonen has received financial support from Jenny and Antti Wihuri Foundation and Tampere University of Technology. Also, we acknowledge CSC—IT Center for Science Ltd. and Tampere Center for Scientific Computing for providing us with computational resources.

REFERENCES

(1) Berne, B. J. Path integral Monte Carlo methods: Static- and time-correlation functions. *J. Stat. Phys.* **1986**, *43*, 911—929.
(2) Ceperley, D. M. Path integrals in the theory of condensed Helium. *Rev. Mod. Phys.* **1995**, *67*, 279—355.
(3) Foulkes, W. M. C.; Mitas, L.; Needs, R. J.; Rajagopal, G. Quantum Monte Carlo simulations of solids. *Rev. Mod. Phys.* **2001**, *73*, 33—83.
(4) Cao, J.; Voth, G. A. The formulation of quantum statistical mechanics based on the Feynman path centroid density. II. Dynamical properties. *J. Chem. Phys.* **1994**, *100*, 5106—5117.
(5) Habershon, S.; Braams, B. J.; Manolopoulos, D. E. Quantum mechanical correlation functions, maximum entropy analytic continuation, and ring polymer molecular dynamics. *J. Chem. Phys.* **2007**, *127*, 174108.
(6) Weiss, S.; Egger, R. Path-integral Monte Carlo simulations for interacting few-electron quantum dots with spin-orbit coupling. *Phys. Rev. B: Condens. Matter Mater. Phys.* **2005**, *72*, 245301.
(7) Shee, J.; Zhang, S.; Reichman, D. R.; Friesner, R. A. Chemical Transformations Approaching Chemical Accuracy via Correlated Sampling in Auxiliary-Field Quantum Monte Carlo. *J. Chem. Theory Comput.* **2017**, *13*, 2667—2680.
(8) Kylänpää, I.; Räsänen, E. Path integral Monte Carlo benchmarks for two-dimensional quantum dots. *Phys. Rev. B: Condens. Matter Mater. Phys.* **2017**, *96*, 205445.
(9) Kylänpää, I.; Balachandran, J.; Ganesh, P.; Heinonen, O.; Kent, P. R. C.; Krogel, J. T. Accuracy of ab initio electron correlation and electron densities in vanadium dioxide. *Phys. Rev. Materials* **2017**, *1*, 065408.
(10) Mitroy, J.; Bubin, S.; Horiuchi, W.; Suzuki, Y.; Adamowicz, L.; Cencek, W.; Szalewicz, K.; Komasa, J.; Blume, D.; Varga, K. Theory and application of explicitly correlated Gaussians. *Rev. Mod. Phys.* **2013**, *85*, 693—749.
(11) Tubman, N. M.; Kylänpää, I.; Hammes-Schiffer, S.; Ceperley, D. M. Beyond the Born-Oppenheimer approximation with quantum Monte Carlo methods. *Phys. Rev. A: At., Mol., Opt. Phys.* **2014**, *90*, 042507.
(12) Yang, Y.; Kylänpää, I.; Tubman, N. M.; Krogel, J. T.; Hammes-Schiffer, S.; Ceperley, D. M. How large are nonadiabatic effects in atomic and diatomic systems? *J. Chem. Phys.* **2015**, *143*, 124308.
(13) Toll, J. S. Causality and the Dispersion Relation: Logical Foundations. *Phys. Rev.* **1956**, *104*, 1760—1770.
(14) Kubo, R. Statistical-Mechanical Theory of Irreversible Processes. I. General Theory and Simple Applications to Magnetic and Conduction Problems. *J. Phys. Soc. Jpn.* **1957**, *12*, 570—586.
(15) Thirumalai, D.; Berne, B. J. Time correlation functions in quantum systems. *J. Chem. Phys.* **1984**, *81*, 2512—2513.
(16) Rota, R.; Casulleras, J.; Mazzanti, F.; Boronat, J. Quantum Monte Carlo estimation of complex-time correlations for the study of the ground-state dynamic structure function. *J. Chem. Phys.* **2015**, *142*, 114114.
(17) Beach, K. S. D.; Gooding, R. J.; Marsiglio, F. Reliable Padé analytical continuation method based on a high-accuracy symbolic computation algorithm. *Phys. Rev. B: Condens. Matter Mater. Phys.* **2000**, *61*, 5147—5157.

DOI: 10.1021/acs.jctc.8b00859
J. Chem. Theory Comput. 2018, 14, 5750—5763

(18) Creffield, C. E.; Klepfish, E. G.; Pike, E. R.; Sarkar, S. Spectral Weight Function for the Half-Filled Hubbard Model: A Singular Value Decomposition Approach. *Phys. Rev. Lett.* **1995**, *75*, 517−520.
(19) Mishchenko, A.; Prokof'ev, N.; Sakamoto, A.; Svistunov, B. Diagrammatic quantum Monte Carlo study of the Fröhlich polaron. *Phys. Rev. B: Condens. Matter Mater. Phys.* **2000**, *62*, 6317−6336.
(20) Nordström, J.; Schött, J.; Locht, I. L.; Di Marco, I. A GPU code for analytic continuation through a sampling method. *SoftwareX* **2016**, *5*, 178−182.
(21) Jarrell, M.; Gubernatis, J. Bayesian inference and the analytic continuation of imaginary-time quantum Monte Carlo data. *Phys. Rep.* **1996**, *269*, 133−195.
(22) Bergeron, D.; Tremblay, A.-M. S. Algorithms for optimized maximum entropy and diagnostic tools for analytic continuation. *Phys. Rev. E: Stat. Phys., Plasmas, Fluids, Relat. Interdiscip. Top.* **2016**, *94* (3), 023303.
(23) Zwanzig, R. Time-Correlation Functions and Transport Coefficients in Statistical Mechanics. *Annu. Rev. Phys. Chem.* **1965**, *16*, 67−102.
(24) Zhang, F. C.; Lee, T. K. Spectral density and magnetic susceptibility for the asymmetric degenerate Anderson model. *Phys. Rev. B: Condens. Matter Mater. Phys.* **1984**, *30*, 1556−1558.
(25) Sandvik, A. W. NMR relaxation rates for the spin-1/2 Heisenberg chain. *Phys. Rev. B: Condens. Matter Mater. Phys.* **1995**, *52*, R9831−R9834.
(26) Gallicchio, E.; Berne, B. J. On the calculation of dynamical properties of solvated electrons by maximum entropy analytic continuation of path integral Monte Carlo data. *J. Chem. Phys.* **1996**, *105*, 7064−7078.
(27) Aarts, G.; Resco, J. M. M. Transport coefficients, spectral functions and the lattice. *J. High Energy Phys.* **2002**, *2002*, 053−053.
(28) Gunnarsson, O.; Haverkort, M. W.; Sangiovanni, G. Analytical continuation of imaginary axis data for optical conductivity. *Phys. Rev. B: Condens. Matter Mater. Phys.* **2010**, *82*, 165125.
(29) Mitroy, J.; Safronova, M. S.; Clark, C. W. Theory and applications of atomic and ionic polarizabilities. *J. Phys. B: At., Mol. Opt. Phys.* **2010**, *43*, 202001.
(30) Baker, C. M. Polarizable force fields for molecular dynamics simulations of biomolecules. *Wiley Interdiscip. Rev. Comput. Mol. Sci.* **2015**, *5*, 241−254.
(31) Leontyev, I.; Stuchebrukhov, A. Accounting for electronic polarization in non-polarizable force fields. *Phys. Chem. Chem. Phys.* **2011**, *13*, 2613−2626.
(32) Liu, S.; Dykstra, C. E. Multipole polarizabilities and hyperpolarizabilities of AHn and A2Hn molecules from derivative Hartree-Fock theory. *J. Phys. Chem.* **1987**, *91*, 1749−1754.
(33) Kurtz, H. A.; Stewart, J. J. P.; Dieter, K. M. Calculation of the nonlinear optical properties of molecules. *J. Comput. Chem.* **1990**, *11*, 82−87.
(34) Dzuba, V. A.; Flambaum, V. V.; Kozlov, M. G. Combination of the many-body perturbation theory with the configuration-interaction method. *Phys. Rev. A: At., Mol., Opt. Phys.* **1996**, *54*, 3948−3959.
(35) Jamorski, C.; Casida, M. E.; Salahub, D. R. Dynamic polarizabilities and excitation spectra from a molecular implementation of time-dependent density-functional response theory: N2as a case study. *J. Chem. Phys.* **1996**, *104*, 5134−5147.
(36) Schipper, P. R. T.; Gritsenko, O. V.; van Gisbergen, S. J. A.; Baerends, E. J. Molecular calculations of excitation energies and (hyper)polarizabilities with a statistical average of orbital model exchange-correlation potentials. *J. Chem. Phys.* **2000**, *112*, 1344−1352.
(37) Chu, X.; Dalgarno, A. Linear response time-dependent density functional theory for van der Waals coefficients. *J. Chem. Phys.* **2004**, *121*, 4083.
(38) Quinet, O.; Liégeois, V.; Champagne, B. TDHF Evaluation of the dipole-quadrupole polarizability and its geometrical derivatives. *J. Chem. Theory Comput.* **2005**, *1*, 444−452.
(39) Caffarel, M.; Rérat, M.; Pouchan, C. Evaluating dynamic multipole polarizabilities and van der Waals dispersion coefficients of two-electron systems with a quantum Monte Carlo calculation: A comparison with someab initio calculations. *Phys. Rev. A: At., Mol., Opt. Phys.* **1993**, *47*, 3704−3717.
(40) Shin, D.; Ho, M.-C.; Shumway, J. Ab-initio path integral techniques for molecules. 2006, *arXiv.org ePrint archive*, arXiv:quant-ph/0611105. https://arxiv.org/abs/quant-ph/0611105.
(41) Tiihonen, J.; Kylänpää, I.; Rantala, T. T. Adiabatic and nonadiabatic static polarizabilities of H and H_2. *Phys. Rev. A: At., Mol., Opt. Phys.* **2015**, *91*, 062503.
(42) Tiihonen, J.; Kylänpää, I.; Rantala, T. T. General polarizability and hyperpolarizability estimators for the path-integral Monte Carlo method applied to small atoms, ions, and molecules at finite temperatures. *Phys. Rev. A: At., Mol., Opt. Phys.* **2016**, *94*, 032515.
(43) Tiihonen, J.; Kylänpää, I.; Rantala, T. T. Static field-gradient polarizabilities of small atoms and molecules at finite temperature. *J. Chem. Phys.* **2017**, *147*, 204101.
(44) Hohm, U.; Trümper, U. Temperature dependence of the dipole polarizability of xenon (1S0) due to dynamic non-resonant Stark effect caused by black-body radiation. *Chem. Phys.* **1994**, *189*, 443−449.
(45) Bishop, D. M.; Pipin, J. Temperature-dependence of the dynamic dipole polarizability of H2. *Mol. Phys.* **1991**, *72*, 961−964.
(46) Bishop, D. M. Molecular vibrational and rotational motion in static and dynamic electric fields. *Rev. Mod. Phys.* **1990**, *62*, 343−374.
(47) Tang, L.-Y.; Yan, Z.-C.; Shi, T.-Y.; Babb, J. F. High-precision nonadiabatic calculations of dynamic polarizabilities and hyperpolarizabilities for low-lying vibrational-rotational states of hydrogen molecular ions. *Phys. Rev. A: At., Mol., Opt. Phys.* **2014**, *90*, 012524.
(48) Bloembergen, N.; Shen, Y. R. Quantum-Theoretical Comparison of Nonlinear Susceptibilities in Parametric Media, Lasers, and Raman Lasers. *Phys. Rev.* **1964**, *133*, A37−A49.
(49) Bresme, F. Equilibrium and nonequilibrium molecular-dynamics simulations of the central force model of water. *J. Chem. Phys.* **2001**, *115*, 7564−7574.
(50) Bishop, D. M.; Pipin, J. Dipole, quadrupole, octupole, and dipoleoctupole polarizabilities at real and imaginary frequencies for H, HE, and H2 and the dispersion-energy coefficients for interactions between them. *Int. J. Quantum Chem.* **1993**, *45*, 349−361.
(51) Pekeris, C. L. Ground State of Two-Electron Atoms. *Phys. Rev.* **1958**, *112*, 1649−1658.
(52) Yan, Z.-C.; Babb, J. F.; Dalgarno, A.; Drake, G. W. F. Variational calculations of dispersion coefficients for interactions among H, He, and Li atoms. *Phys. Rev. A: At., Mol., Opt. Phys.* **1996**, *54*, 2824−2833.
(53) Pachucki, K.; Komasa, J. Schrdinger equation solved for the hydrogen molecule with unprecedented accuracy. *J. Chem. Phys.* **2016**, *144*, 164306.
(54) Kolos, W.; Wolniewicz, L. Improved Theoretical Ground-State Energy of the Hydrogen Molecule. *J. Chem. Phys.* **1968**, *49*, 404−410.
(55) Usukura, J.; Suzuki, Y. Resonances of positronium complexes. *Phys. Rev. A: At., Mol., Opt. Phys.* **2002**, *66*, 010502.
(56) Kielich, S. *Dielectric and Related Molecular Processes*, Vol. *1*; Royal Society of Chemistry: Cambridge, U.K., 1972; pp 192−387, DOI: 10.1039/9781847555878.
(57) Berne, B. J. Time-Dependent Properties of Condensed Media. In *Physical Chemisry: An Advanced Treatise. Liquid State*, Vol. *VIIIB*; Henderson, D.Elsevier, 1971; pp 539−716, DOI: 10.1016/B978-0-12-245658-9.50010-9.
(58) Stefanucci, G.; van Leeuwen, R. *Nonequilibrium Many-Body Theory of Quantum Systems: A Modern Introduction*; Cambridge University Press: Cambridge, U.K., 2013; DOI: 10.1017/CBO9781139023979.
(59) Wagnière, G. The evaluation of three-dimensional rotational averages. *J. Chem. Phys.* **1982**, *76*, 473−480.
(60) Tao, J.; Rappe, A. M. Communication: Accurate higher-order van der Waals coefficients between molecules from a model dynamic multipole polarizability. *J. Chem. Phys.* **2016**, *144*, 031102.
(61) Kylänpää, I. First-principles Finite Temperature Electronic Structure of Some Small Molecules. Ph.D. thesis, Tampere University of Technology, Tampere, Finland, 2011.

DOI: 10.1021/acs.jctc.8b00859
J. Chem. Theory Comput. 2018, 14, 5750−5763

(62) Kylänpää, I.; Rantala, T. T. First-principles simulation of molecular dissociation−recombination equilibrium. *J. Chem. Phys.* **2011**, *135*, 104310.
(63) Ceperley, D. M. Path integral Monte Carlo methods for fermions. *Monte Carlo and molecular dynamics of condensed matter systems*; Euroconference on Computer Simulation Condensed Matter Physics and Chemistry; Itailian Physical Society: Bologna, Italy, 1996.
(64) Bishop, D. M.; Pipin, J. Calculation of the polarizability and hyperpolarizability tensors, at imaginary frequency, for H, He, and H2 and the dispersion polarizability coefficients for interactions between them. *J. Chem. Phys.* **1992**, *97*, 3375−3381.
(65) Kylänpää, I.; Rantala, T. T. Thermal dissociation of dipositronium: Path-integral Monte Carlo approach. *Phys. Rev. A: At., Mol., Opt. Phys.* **2009**, *80*, 024504.

DOI: 10.1021/acs.jctc.8b00859
J. Chem. Theory Comput. 2018, 14, 5750−5763